NOVA SCHOOL OF SCIENCE & TECHNOLOGY

DEPARTMENT OF PHYSICS

PARP1 inhibitors for cancer combination therapy: merging liposome encapsulation and UVC irradiation

CARLOTA JOSÉ FERNANDES DA CONCEIÇÃO

Master in

Technologic, Comparative and Molecular Genetics

DOCTORATE IN RADIATION BIOLOGY AND BIOPHYSICS

NOVA University Lisbon

September, 2023

DEPARTMENT OF
PHYSICS

PARP1 inhibitors for cancer combination therapy: merging liposome encapsulation and UVC irradiation

CARLOTA JOSÉ FERNANDES DA CONCEIÇÃO

Master in Technologic, Comparative and Molecular Genetics

Adviser: Maria de Fátima Guerreiro da Silva Campos Raposo
Associate Professor with Aggregation, NOVA School of Science and Technology, NOVA University Lisbon

Co-advisers: Paulo António Matins Ferreira Ribeiro
Associate Professor, NOVA School of Science and Technology, NOVA University Lisbon

Elin Moe
Researcher, ITQB, NOVA University Lisbon

Examination Committee:

Chair: Orlando Manuel Neves Duarte Teodoro,
Full Professor, NOVA School of Science and Technology, NOVA University Lisbon

Rapporteurs: Ana Margarida Moutinho Grenha,
Associate Professor with Aggregation, Faculty of Science and Technology, University of Algarve

Ana Paula Costa dos Santos Peralta Leandro,
Associate Professor with Aggregation, Faculty of Pharmacy, University of Lisbon

Adviser: Maria de Fátima Guerreiro da Silva Campos Raposo,
Associate Professor with Aggregation, NOVA School of Science and Technology, NOVA University Lisbon

Members: Miguel Ângelo dos Santos Machuqueiro,
Assistant Researcher, Faculty of Science, University of Lisbon

Orlando Manuel Neves Duarte Teodoro,
Full Professor, NOVA School of Science and Technology, NOVA University Lisbon

DOCTORATE IN RADIATION BIOLOGY AND BIOPHYSICS

NOVA University Lisbon
September, 2023

PARP1 inhibitors for cancer combination therapy: merging liposome encapsulation and UVC irradiation

To my parents.

ACKNOWLEDGMENTS

Throughout this journey I was fortunate to encounter and work with many people that made me grow as a person and as a researcher. So, I would like to convey and express my regards and deep appreciation to all of them.

First and foremost, I would like to express my sincere gratitude to my supervisor Prof. Dr. Maria Raposo, without whom this work would not have been possible. I deeply appreciate her leadership and wisdom as a person, mentor and researcher. Thank you for supporting and believing in me and the work that we set out to do. Thank you for guiding and giving me freedom to explore different fields. I am truly grateful for the incredible opportunities that were given to me, which were crucial for my growth as a scientist. But mostly, I will never forget the kindness, comprehension, conversations, and advice, that always helped me all this time.

To my co-supervisor Prof. Dr. Paulo Ribeiro for all the support, guidance, and assistance all these years. Without them, the completion of this work would not be possible. Thank you for always being available to help with any issue that appeared along the way, and for always maintaining a positive outlook and joy in the work environment. It was truly enjoyable working in this kind environment and group.

To my co-supervisor Dr. Elin Moe, without whom any of this work would be possible. I am truly grateful for accepting to embark on this journey and for giving support, help and guidance all these years. Thank you for always backing up my work and giving me freedom to explore different things and make my own mistakes. Thank you for all the opportunities that were given, for the kindness and supportive words, because they helped in my growth as a person and a scientist. I will never forget this amazing time together and all our conversations. It was truly a wonderful and enjoyable journey.

I would like to acknowledge Prof. Dr. Pedro Tavares who, as coordinator of the Radiation Biology and Biophysics Doctoral Training Programme and Prof. Dr. Paulo Limão-Vieira and

Prof. Dr. Alice Pereira from the Executive Committee of the Doctoral Training Programme for giving me the opportunity to pursue this PhD.

Also, want to acknowledge Prof. Dr. Maria Arménia Carrodo, to Dr. Pedro Matias, Dr. Carlos Frazão, Dr. Margarida Archer, Dr. Colin McVey, Dr. João Vicente, Dr. Célia Romão, Dr. Tiago Bandeiras, and all members from the Macromolecular Crystallography Unit (Mx-Unit) for kindly receiving me at their facilities and providing the opportunity to work in an outstanding research environment.

To Dr. João Vicente for facilitating the contact between our group and Dr. Elin Moe, for providing access and training to the circular dichroism and UV-vis instruments, and for the help and guidance given.

To Dr. Colin McVey for the help and training with the purification equipment Akta Explorer.

To Dr. Tiago Bandeiras for providing access to the Nano-DSF and Tecan Instruments and to Dr. Sandra Santos, Dr. Carolina Cassona and Catarina Paiva for the training given.

To Dr. Paula Chicau for providing access and training to the dynamic light scattering instrument at ITQB.

To Dr. Américo Duarte, from the Bacterial Energy Metabolism group at ITQB, for providing access to the tip-sonicator instrument used in this thesis.

To Dr. Célia Silveira for providing the training needed for usage of the Fourier transform infrared instrument at ITQB.

To Dr. Teresa da Silva and Dr. João Carita for training and technical support within the ITQB research facility.

The Department of Physics of NOVA School of Science and Technology, Universidade NOVA de Lisboa and CEFITEC through UIDB/00068/2020. To the financial support from the Portuguese National Funding Agency FCT-MCTES through the grants PD/BD/142765/2018 and COVID/BD/152660/2022 (to Carlota J.F. Conceição). This work was also supported by the Radiation Biology and Biophysics Doctoral Training Programme (RaBBiT, PD/00193/2012); Applied Molecular Biosciences Unit - UCIBIO (UIDB/04378/2020); UIDB/04559/2020 (LIBPhys) and UIDP/04559/2020 (LIBPhys).

Thanks to the secretariat of the Physics Department for helping with the orders, quotes, and other bureaucracies. A special thanks to Mrs. Ana Cruz for all the help, support, assistance, and friendship throughout the years.

To my colleagues and friends from the Molecular Functional Systems group, namely Paulo Zagalo and Thais Pivetta that were always available, helpful, and supportive all the time. We have had a great time together and thank you for your friendship.

To my colleagues and friends from the Mx-Unit, Filipe Rollo, Andreia Fernandes, André Gouveia, Dalila Fernandes, Sara Santos and Patricia Borges, for receiving me so well and for all the support, help, laughter and friendship.

To Bruno Salgueiro, for all the help and support that you gave me this time. Thank you for listening to my nonsense and for making me laugh all the time. I don't know how to thank you enough for all the friendship, but surely, we will continue with our nonsense and fun times.

To Filipa Pires, words are not enough to express how grateful I am for your friendship. Thank you for all the help, support and assistance. Thank you for all the meetings, dinners and conversations, even though we should have had more.

Lastly, to my parents that I deeply adore and cherish. Thank you for your immense and constant support throughout my life and these last years. Thank you for believing in me and for your unconditional love.

“When you come out of the storm you won't be the same person who walked in.
That's what this storm is all about." (Haruki Murakami).

ABSTRACT

Cancer is a multifactorial disease that constitutes a serious health problem worldwide, and its standardized treatments, such as radiation therapy, present major cytotoxic side effects, which can be circumvent by alternative approaches. The efficiency of cancer therapy can be maximized with molecules that modulate radiation effect, such as PARP1 inhibitors (PARPi). Even though it was proved that PARPi increases cell sensitization to UV radiation and that combination of UVC and PARPi leads to cancer cell death, the combined effect of PARPi + liposomes + UVC irradiation remains to be described in literature and no information can be found in relation to the effect of UVC exposure on PARPi. Thus, the main goals of this work were to 1) produce, purify and stabilize a human PARP1 protein; 2) uncover best liposome formulation or lipid content for maximal encapsulation of PARP1 inhibitors Veliparib, Rucaparib and Niraparib; 3) understand the physical interactions of PARPi and liposomes; 4) determine the effect of UVC exposure on PARPi inhibitor capability and finally 5) unveil the potential of combining PARPi + liposomes + UVC. For this, a production and purification protocol was developed and optimized for human PARP1, and protein maximal stabilization was attempted, for further assessments regarding PARPi + radiation therapy. It was uncovered that liposome formulations containing negatively charged lipids, such as DPPG, were the best choice for PARPi encapsulation and that interaction with lipid membrane was done preferentially through the carbonyl groups. This constitutes the first evidence that points DPPG as the lipid of choice for PARPi liposome formulations. Moreover, this work provides the first evidence on the effect of UVC exposure and DPPG encapsulation on Veliparib's inhibitory capability, and unveils the degradation process and products, thus helping in how to continue with the maximization of PARPi combination therapy and unveiling its therapeutic potential.

Keywords: PARP1, activity inhibitors, Veliparib, Rucaparib, Niraparib, liposomes, UVC, cancer combination therapy.

RESUMO

O cancro é uma doença multifatorial e representa um sério problema de saúde em todo o mundo. Uma vez que o seu tratamento por radioterapia apresenta graves efeitos secundários citotóxicos, alguns métodos alternativos são tidos em conta para os ultrapassar. Por sua vez, a eficiência da terapia pode ser maximizada através do uso de moléculas que modelam o efeito da radiação, tais como os inibidores da PARP1 (PARPi). Embora tenha sido provado que PARPi aumenta a sensibilidade das células para a radiação UV, e que UVC e PARPi conduzem à morte das células cancerígenas, o efeito combinado de PARPi + lipossomas + UVC permanece por ser descrito e nenhuma informação é encontrada sobre o efeito da exposição a UVC em PARPi. Como tal, os principais objetivos deste trabalho foram 1) produzir, purificar e estabilizar a proteína PARP1 humana; 2) determinar a melhor formulação lipídica para o encapsulamento dos inibidores Veliparib, Rucaparib e Niraparib; 3) compreender as interações físicas de PARPi + lipossomas; 4) determinar o efeito da exposição UVC em PARPi e 5) revelar o potencial da terapia de combinação PARPi + lipossomas + UVC. Para tal, foi desenvolvido e otimizado um protocolo de produção e purificação da PARP1 humana, e tentada a sua estabilização, por forma a ser usada em ensaios relativos à combinação de PARPi + radioterapia. Foi também verificado que lipossomas contendo lípidos negativamente carregados, como DPPG, são a melhor opção para o encapsulamento de PARPi, e que a interação com a membrana lipídica é feita através dos grupos carbonilo. Desta forma, constituindo a primeira evidência que aponta DPPG como o lípido de escolha para a formulação de lipossomas para PARPi. Adicionalmente, este trabalho fornece a primeira evidência sobre o efeito de UVC e DPPG, na capacidade inibitória de Veliparib. É revelado também o processo e produtos de degradação do mesmo, ajudando assim no processo futuro de maximização da terapia combinada de PARPi e revelando o seu potencial terapêutico.

Palavras-chave: PARP1, inibidores de atividade, Veliparib, Rucaparib, Niraparib, liposomes, UVC, terapia de combinação em cancro.

CONTENTS

LIST OF FIGURES

List of Tables

ACRONYMS

AF2	AlphaFold 2
AI	Artificial intelligence
AIF	Apoptosis inducing factor
ALC1	Chromodomain helicase/ATPase DNA binding protein 1-like
ALDH	Aldehyde dehydrogenase
APC	Adenomatous polyposis coli
ARH	ADP-ribosyl hydrolase
ART	ADP-ribosyl transferase
ARTDs	ART diphteria toxin like enzymes
ATM	Ataxia telangiectasia mutated
ATP	Adenosine triphosphate
ATR	Ataxia telangiectasia and rad3-related protein
ATRIP	ATR-interacting protein
BER	Base excision repair
BRCA1/2	Breast cancer type 1/2 susceptibility protein
BRCT	BRCA-C-terminus domain
BSA	Bovine serum albumin
CAMKII	Calcium-dependent protein kinase

CAT	Catalytic domain
CD	Circular dichroism
CHD2	DNA-binding protein 2
CHK1/2	Check-point kinase 1/2
Chol	Cholesterol
CIB2	Calcium and integrin binding protein 2
cryo-EM	cryo- Electron microscopy
CSR	Class-switch recombination
DDB	DNA damage-binding proteins
DLS	Dynamic light scattering
DMSO	Dimethylsulfoxide
DNA	Deoxyribonucleic acid
DNA-PK	DNA-dependent protein kinases
DNA-PKcs	DNA-dependent protein kinases catalytic subunit
DPPC	1,2-dipalmitoyl-sn-glycero-3-phosphocholine
DPPG	1,2-dipalmitoyl-sn-glycero-3-phospho-rac-(1'-glycerol) sodium salt
DSB	Double strand break
dsDNA	Double-strand DNA
EDTA	Ethylenediamine tetraacetic acid
EE	Encapsulation efficiency
EGFR	Epidermal growth factor receptor
EMSA	Electrophoretic mobility shift assay
ESM	Egg sphingomyelin
EWS	Ewing sarcoma protein
EXO1	Exonuclease 1
FEN1	Flap endonuclease 1

FTIR	Fourier-transform infrared spectroscopy
GG-NER	global genome-NER
GUV	giant unilamellar vesicles
H1 and H2B	histones
HD	Alpha-helical domain
HDAC	histone deacetylase
HIF1α/2A	hypoxia-inducible factor 1α/2A
HPF1	Histone PARylation factor 1
HR	Homologous recombination
HSP	heat-shock protein
IDP/IDR	Intrinsic disordered protein/region
IGF-1	Insulin-like growth factor 1
IL6	Interleukin 6
IMAC	Immobilized-metal affinity chromatography
IPTG	isopropyl β-D-1- thiogalactopyranoside
ITF	Intrinsic tryptophan fluorescence
LB	Luria broth
LC	Loading capacity
LC-MS	Liquid chromatography-mass spectrometry
LIG3/4	DNA ligase 3/4
LUV	large unilamellar vesicles
MacroD	Macro domain
MAR	Mono (ADP-ribosyl) modification
MITF	Melanocyte-lineage survival transcriptional factor
MLV	Multilamellar vesicles
MMR	Mismatch repair

MRN	MRE11 nuclease-RAD50-NSB1 complex
mRNA	Messenger RNA
MS	Mass spectrometry
MWCO	Molecular weight cutoff
NAD^+	Nicotinamide adenine dinucleotide
Nano-DSF	Nano-Differential Scanning fluorimetry
NER	Nucleotide excision repair
NF-κB	Nuclear factor kappa B
NHEJ	Non-homologous end joining
NMNAT	Nuclear nicotinamide mononucleotide adenylyltransferase
NMR	Nuclear magnetic spectroscopy
NSCLC	Non-small cell lung carcinoma
NUPR1	Nuclear stress protein
OB	Oligonucleotide/oligosaccharide
PAR	poly (ADP-ribosyl) modification
PARG	poly (ADP-ribose) glycohydrolase
PARP1	Poly (ADP-ribose) polymerase
PB	Power broth
PBM	PAR binding motif
PBZ	PAR binding zinc finger
PCA	principal component analysis
PCAF	lysine acetyltransferase 2B
PCNA	Proliferating cell nuclear antigen
PCR	polymerase chain reaction
PDB	Protein Data Bank
PdI	polydispersity index

PECAM1/CD3	platelet/endothelial cell adhesion molecule
PEG	Poly(ethylene glycol)
PKC	protein kinase C
PNKP	Polynucleotide kinase 3'-phosphatase
Pol θ	DNA polymerase θ
POPC	1-palmitoyl-2-oleoyl-sn-glycero-3-phosphocholine
PTMs	post-translational modifications
RFC	Replication factor C
RNA	Ribonucleic acid
RNF4	Ubiquitin ligase ring finger protein 4
ROS	Reactive oxygen species
RPA	Replication protein A
SCLC	Small cell lung carcinoma
SDS-PAGE	Sodium dodecyl-sulfate polyacrylamide gel electrophoresis
SEC	Size-exclusion chromatography
SIRT	Sirtuin
snoRNA	Small nucleolar RNA
SSA	Single strand break annealing
SSB	Single strand break
SUV	Small unilamellar vesicles
TARG1	Terminal ADP-ribose protein glycohydrolase
TCEP	tris(2-carboxyethyl)phosphine
TDP1	Tyrosyl-DNA phosphodiesterase 1
TFIIH	Transcription factor IIH
TNFα	Tumor necrosis factor α
TNKS	Tankyrase

TOP1	DNA topoisomerase 1
TSF	Thermal Shift Assay
UV	Ultraviolet
UV-Vis	Ultraviolet and visible
VEGFR1	Vascular endothelial growth factor receptor 1
WGR	Tryptophan (W) - glycine (G) - arginine (R)
WWP2	WW domain containing E3 Ubiquitin protein ligase 2
XPC	*Xerodema pigmentosum* complementation group C
XRCC1/4	X-ray repair cross-complementing protein 1/4
Zn1-3 or ZF	Zinc fingers 1 to 3

SYMBOLS

<	Below or lower than
>	higher than
≈ or ~	Approximately
≥	Equal or higher than
Å	Angstrom metric unit
a and b	Constants
$Å^2$	Angstrom squared
aa	Aminoacid(s)
Ab	Abasic site
AIC	Akaike information criterion
A_{xnm}	Absorbance at x nanometers
c	Concentration
Ca^{2+}	Calcium ion
$CaCl_2$	Calcium chloride
CaF_2	Calcium fluoride
C_{encap}	Concentration of inhibitor encapsulated after dialysis
CH_2	Methylene
CH_3	Methyl

c_L	Speed of light in vacuum
C_{lipid}	Lipid concentration
C_{total}	Concentration of inhibitor before dialysis
d.nm	particle diameter size in nanometers
$D\tau$	Diffusion behavior
Em_{Xnm}	Emission intensity at x nanometers
Fe^{2+}/Fe^{3+}	Iron ions
g	Centrifugal/gravitational force
$g_{2(t)}$	Autocorrelation function
H_2O_2	hydrogen peroxide
h_p	Planck constant
I	Intensity
I	Intensity of the transmitted light
I_0	Intensity of the incident light
IC50	Half maximal inhibitory concentration
K^+	Potassium ion
Kav	gel-phase distribution coefficient
KCl	potassium chloride
kDa	Kilodaltons
K_I	Inhibition constant or binding affinity
l	path length
Li^+	Lithium ion
Mg^{2+}	Magnesium ion
$MgCl_2$	Magnesium chloride
Mn^{2+}	Manganese ion
$MnSO_4$	Manganese sulphate

Mw	Molecular weight
n	Release exponent
Na^+	Sodium ion
NaCl	Sodium chloride
Ni^{2+}	Nickel ion
$NiCl_2$	Nickel chloride
nt	Nucleotide(s)
OD_{600nm}	Optical density at 600 nanometers
OH	hydroxyl
p	p-value
Q	Amount of drug released
q	Bragg wave vector
Q_0	Start value
Q_{max}	Maximum value of Q
R^2	Empirical confidence criteria
RFU	Relative fluorescence units
rpm	Revolutions per minute
T	Temperature
T	Absolute temperature
t	Time
T_{LAG}	Lag time
Tm	Melting temperature
T_{onset}	Onset temperature
V total	Total volume of the SEC column
v/v	Volume per volume
Ve	Elution volume

V_o	Void volume
y_{AV}	Average output value
y_I	Observed value
$\hat{y}_I$	Model-predicted
Zn^{2+}	Zinc ion
$ZnSO_4$	Zinc sulphate
β	Coherence factor or beta letter
ΔE	Planck-Einstein equation
ε	Molar extinction coefficient
η	Medium viscosity
θ	Angle
κ_B	Boltzmann coefficient
λ	wavelength
τ	Delay time
υ	Frequency

1

General Introduction

Cancer is a multifactorial disease that still in the present moment constitutes as serious health problem all over the world. Standardized treatments resort to the use of radiation therapy coupled with surgical intervention and chemotherapy [1]. However, cytotoxic side effects to normal cells are also reported, and involves the generation of DNA moieties and reactive oxygen species (ROS) [2,3].

The efficiency of cancer radiation therapy can be maximized with the use of molecules that modulate radiation effects [4,5]. Among those DNA repair inhibitors appear as some with the most interesting potential [4,5]. These molecules have specific cellular targets that are involved in signaling pathways related to homologous repair (HR), base excision repair (BER), and non-homologous end joining (NHEJ), such as poly (ADP-ribose) polymerase1 (PARP1) [1,4,6,7].

PARP1 belongs to an extensive family of proteins and due to its many cellular roles, it is regarded as of great interest for cancer therapy [8-10]. This protein belongs to a DNA dependent sub-group of PARP proteins, but its localization is not exclusive to the nuclear compartment [8]. Because of this and its flexible nature, PARP1 is found to be involved directly and/or indirectly in DNA repair, transcription, replication, cell cycle progression and other intracellular pathways [9,10].

This is why PARP1 inhibitor (PARPi) therapy is often employed as a complement to more conventional cancer therapies. PARPi are molecules that were designed as analogous to the protein NAD^+ activity cofactor, thus leading to the hinderance of PARP1's enzymatic activity [4,11]. Molecules such as Veliparib, Rucaparib and Niraparib interact with the catalytic domain of PARP1 and prevent its auto- and hetero-modification capability (PARylation) [4,5]. This therapeutic route takes advantage of the compromised DNA repair pathways in cancer cells, and

therefore prevent the repair of DNA strand breaks [4,5]. The inhibition of PARP1's auto-modification prevents its release from the DNA strand breaks and consequently hinders the allocation of BER proteins for damage repair [4,5]. Moreover, PARPi can be employed in synergistic lethal strategies, through combinational therapy with DNA damage agents (e.g. radiation or chemotherapeutics), or even as mono-therapy agents [12-14]. Conventional PARPi therapy was proved to increase cell sensitization to UV radiation and positive feedback was reported when both were combined, thus leading to cancer cell death [12-18]. Furthermore, it was verified that even low-energy sources, such as UVC light, were capable of activating PARylation due to intracellular DNA damage, and in turn PARP1 inhibition further sensitized cells to UVC irradiation [19].

Because radiation and PARPi therapeutic approaches comes with some drawbacks (e.g. cytotoxic effect, off-target effect, high compound clearance rates, among others) [20,21], the use of liposome nano-delivery systems comes as a natural mean to circumvent these issues [22]. Liposomes are one of the best-known nano delivery systems and can be safely used to decrease off-target toxicity and increase therapeutic efficiency [23]. Some liposome systems were described with PARP1 inhibitors (majority with Talazoparib and Olaparib), that usually follow conventional lipid formulations (e.g. use of PC lipids) [22,24-27]. However, the combined effect of PARPi + liposomes + UVC irradiation remains to be described and no information can be found regarding the effect of radiation exposure on PARPi and its inhibitory capacity.

Thus, our main goals were: 1) produce, purify and stabilize a human PARP1 protein close to its native state; 2) uncover the best liposome formulation or lipid constituents that permitted maximal inhibitor encapsulation of Veliparib, Rucaparib and Niraparib; 3) understand the interaction mode of set PARPi and liposomes; 4) determine the effect of UVC exposure on PARPi inhibitor capability; and ultimately 5) unveil the potential of combining liposome + PARPi + UVC irradiation.

This thesis consists of seven more chapters, beyond this. The second chapter is related to the state of the art, where it is showcased the importance of PARP1 and its framework in the PARP protein family. Moreover, the intracellular role of PARP1 is emphasized by the presentation of the various DNA repair pathways where it is involved, as well as how its function is regulated. In this section the involvement of PARP1 in cancer development and progression is also debated, as a mean to confer to the reader the biological importance of the protein. Additionally, therapeutic approaches targeting PARP1 are debated, namely the use of PARPi in combination therapy with radiation and nano-systems.

In chapter 3, experimental concepts and methodology are presented. Fundamental information is given regarding the type of methodology involved in PARP1 gene cloning, protein expression, purification, and spectroscopic characterization. Moreover, liposome's production process is explained, as well as the spectroscopic techniques used for biophysical characterization.

Chapter 4 consists of the development and optimization of a production and purification protocol for recombinant human PARP1, since protein samples were needed to access the inhibitory capability of PARPi. Moreover, PARP1 intrinsic nature, oligomerization and stabilization is extensively analyzed and debated in Chapter 5. This was done to guarantee high sample quality and stability for the experiments in this thesis and future assessments.

Chapter 6 comprises the protocol optimization of liposome production and PARPi encapsulation. Moreover, spectroscopic analysis was done to unveil the interaction mode of PARPi and liposomes. This chapter serves as a mean to unveil best liposome formulation for PARPi encapsulation, understand the encapsulation mode, drug release rates and mechanisms.

In Chapter 7, the effect of UVC irradiation on PARPi Veliparib was assessed. This was done with and without compound encapsulation in the best liposome formulation unveiled in Chapter 6. Moreover, samples of irradiated Veliparib were analyzed for their inhibitory capability on PARP1 (protein that was produced and stabilized following Chapters 4 and 5). A putative degradation process and products of irradiated Veliparib is presented in Chapter 7.

The eighth and final chapter encompasses the main conclusions of this thesis and debates potential future routes in PARP1 study and PARP1 cancer therapies.

References

[1] D.E. Citrin, J.B. Mitchell, Altering the Response to Radiation: Sensitizers and Protectors, Semin. Oncol. 41 (2014) 848–859. https://doi.org/10.1053/j.seminoncol.2014.09.013.

[2] S.K. Liu, P.L. Olive, R.G. Bristow, Biomarkers for DNA DSB inhibitors and radiotherapy clinical trials, Cancer Metastasis Rev. 27 (2008) 445–458. https://doi.org/10.1007/s10555-008-9137-8.

[3] G.-I. Mun, S. Kim, E. Choi, C.S. Kim, Y.-S. Lee, Pharmacology of natural radioprotectors, Arch. Pharm. Res. 41 (2018) 1033–1050. https://doi.org/10.1007/s12272-018-1083-6.

[4] C.J. Lord, A. Ashworth, PARP Inhibitors: The First Synthetic Lethal Targeted Therapy Europe PMC Funders Group, Science (80-.). 355 (2017) 1152–1158. https://doi.org/10.1126/science.aam7344.PARP.

[5] G. O'Sullivan Coyne, A. Chen, S. Kummar, Delivering on the promise: Poly ADP ribose polymerase inhibition as targeted anticancer therapy, Curr. Opin. Oncol. 27 (2015) 475–481. https://doi.org/10.1097/CCO.0000000000000238.

[6] J.D. Steffen, M.M. McCauley, J.M. Pascal, Fluorescent sensors of PARP-1 structural dynamics and allosteric regulation in response to DNA damage, Nucleic Acids Res. 44 (2016) 9771–9783. https://doi.org/10.1093/nar/gkw710.

[7] H.H.W. Chen, M.T. Kuo, Improving radiotherapy in cancer treatment: Promises and challenges, Oncotarget. 8 (2017) 62742–62758. https://doi.org/10.18632/oncotarget.18409.

[8] S. Vyas, M. Chesarone-Cataldo, T. Todorova, Y. Huang, P. Chang, A systematic analysis of the PARP protein family identifies new functions critical for cell physiology, Nat. Commun. 4 (2013) 1–13. https://doi.org/10.1038/ncomms3240.

[9] F.G. Sousa, R. Matuo, D.G. Soares, A.E. Escargueil, J.A.P. Henriques, A.K. Larsen, J. Saffi, PARPs and the DNA damage response, Carcinogenesis. 33 (2012) 1433–1440. https://doi.org/10.1093/carcin/bgs132.

[10] J.D. Steffen, R.M. Tholey, M. Langelier, J.L. Planck, J. Schiewer, S. Lal, N.A. Bildzukewicz, C.J. Yeo, K.E. Knudsen, J.R. Brody, J.M. Pascal, Targeting PARP-1 allosteric regulation offers therapeutic potential against cancer, Cancer Res. 74 (2015) 31–37. https://doi.org/10.1158/0008-5472.CAN-13-1701.

[11] C. Qin, Z. Ji, E. Zhai, K. Xu, Y. Zhang, Q. Li, H. Jing, X. Wang, X. Song, PARP inhibitor olaparib enhances the efficacy of radiotherapy on XRCC2-deficient colorectal cancer cells, Cell Death Dis. 13 (2022). https://doi.org/10.1038/s41419-022-04967-7.

[12] B. Carney, S. Kossatz, T. Reiner, Molecular imaging of PARP, J. Nucl. Med. 58 (2017) 1025–1030. https://doi.org/10.2967/jnumed.117.189936.

[13] S. Boussios, P. Karihtala, M. Moschetta, A. Karathanasi, A. Sadauskaite, E. Rassy, N. Pavlidis, Combined Strategies with Poly (ADP-Ribose) Polymerase (PARP) Inhibitors for the Treatment of Ovarian Cancer: A Literature Review, Diagnostics. 9 (2019) 87. https://doi.org/10.3390/diagnostics9030087.

[14] M. Yi, B. Dong, S. Qin, Q. Chu, K. Wu, S. Luo, Advances and perspectives of PARP inhibitors, Exp. Hematol. Oncol. 8 (2019) 29. https://doi.org/10.1186/s40164-019-0154-9.

[15] N. V Malyuchenko, E.Y. Kotova, O.I. Kulaeva, M.P. Kirpichnikov, V.M. Studitskiy, PARP1 Inhibitors: antitumor drug design., Acta Naturae. 7 (2015) 27–37. http://www.ncbi.nlm.nih.gov/pubmed/26483957.

[16] T. Hirai, S. Saito, H. Fujimori, K. Matsushita, T. Nishio, R. Okayasu, M. Masutani, Radiosensitization by PARP inhibition to proton beam irradiation in cancer cells, Biochem. Biophys. Res. Commun. 478 (2016) 234–240. https://doi.org/10.1016/j.bbrc.2016.07.062.

[17] S.A. Jannetti, B.M. Zeglis, M.R. Zalutsky, T. Reiner, Poly(ADP-Ribose)Polymerase (PARP) Inhibitors and Radiation Therapy, Front. Pharmacol. 11 (2020) 170. https://doi.org/10.3389/fphar.2020.00170.

[18] S.J. Derby, A.J. Chalmers, R.D. Carruthers, Radiotherapy-Poly(ADP-ribose) Polymerase Inhibitor Combinations: Progress to Date, Semin. Radiat. Oncol. 32 (2022) 15–28. https://doi.org/10.1016/j.semradonc.2021.09.005.

[19] J.M.F. Fischer, O. Popp, D. Gebhard, S. Veith, A. Fischbach, M. Scheffner, E. Ferrando-may, S. Beneke, A. Leitenstorfer, Poly (ADP-ribose) -mediated interplay of XPA and PARP1 leads to reciprocal regulation of protein function, 281 (2014) 3625–3641. https://doi.org/10.1111/febs.12885.

[20] C.E. Knezevic, G. Wright, L.L. Remsing Rix, W. Kim, B.M. Kuenzi, Y. Luo, J.M. Watters, J.M. Koomen, E.B. Haura, A.N. Monteiro, C. Radu, H.R. Lawrence, U. Rix, Proteome-wide Profiling of Clinical PARP Inhibitors Reveals Compound-Specific Secondary Targets, Cell Chem. Biol. 23 (2016) 1490–1503. https://doi.org/10.1016/j.chembiol.2016.10.011.

[21] N. Gan, Q. Sun, P. Tang, D. Wu, T. Xie, Y. Zhang, H. Li, Determination of interactions between human serum albumin and niraparib through multi-spectroscopic and computational methods, Spectrochim. Acta - Part A Mol. Biomol. Spectrosc. 206 (2019) 126–134. https://doi.org/10.1016/j.saa.2018.07.100.

[22] L. Cai, X. Xu, W. Chen, The Current State of the Art in PARP Inhibitor-Based Delivery Nanosystems, Pharmaceutics. 14 (2022) 1647. https://doi.org/10.3390/pharmaceutics14081647.

[23] Y. Cheng, P. Zhao, S. Wu, T. Yang, Y. Chen, X. Zhang, C. He, C. Zheng, K. Li, X. Ma, G. Xiang, Cisplatin and curcumin co-loaded nano-liposomes for the treatment of hepatocellular

carcinoma, Int. J. Pharm. 545 (2018) 261–273. https://doi.org/10.1016/j.ijpharm.2018.05.007.

[24] B. Singh, S. Yang, A. Krishna, S. Sridhar, Nanoparticle Formulations of Poly (ADP-ribose) Polymerase Inhibitors for Cancer Therapy, Front. Chem. 8 (2020). https://doi.org/10.3389/fchem.2020.594619.

[25] J. Li, Q. Sun, C. Lu, H. Xiao, Z. Guo, D. Duan, Z. Zhang, T. Liu, Z. Liu, Boron encapsulated in a liposome can be used for combinational neutron capture therapy, Nat. Commun. 13 (2022) 2143. https://doi.org/10.1038/s41467-022-29780-w.

[26] J.A. Perez-Fidalgo, A. Cortés, E. Guerra, Y. García, M. Iglesias, U. Bohn Sarmiento, E. Calvo García, L. Manso Sánchez, A. Santaballa, A. Oaknin, A. Redondo, M.J. Rubio, A. González-Martín, Olaparib in combination with pegylated liposomal doxorubicin for platinum-resistant ovarian cancer regardless of BRCA status: a GEICO phase II trial (ROLANDO study), ESMO Open. 6 (2021) 100212. https://doi.org/10.1016/j.esmoop.2021.100212.

[27] J.A. Magalhães, D.C. Arruda, M.S. Baptista, D.B. Tada, Co-Encapsulation of Methylene Blue and PARP-Inhibitor into Poly(Lactic-Co-Glycolic Acid) Nanoparticles for Enhanced PDT of Cancer, Nanomaterials. 11 (2021) 1514. https://doi.org/10.3390/nano11061514.

2

PARP1 A DESIRABLE TARGET FOR CANCER TREATMENT: THE BIOLOGICAL FUNDAMENT

Poly (ADP-ribose) polymerase 1 (PARP1): more than a simple DNA repair player[1]

Abstract

Currently, standardize cancer treatment strategy resorts to the use of radiation therapy coupled with surgical intervention and chemotherapeutic agents. However, regardless of radiation therapy representing a powerful tool to destroy cancer cells, its cytotoxic effects to normal cells represents a major drawback. The therapeutic efficiency can be maximized with the use of molecules that can modulate radiation effects, such as DNA repair inhibitors (e.g. PARP1 inhibitors - PARPi). With this approach tumor cell viability can be undermined by targeting DNA repair mechanisms. These molecules have specific cellular targets, such as Poly (ADP-ribose) polymerase-1 (PARP1), which are involved in signaling pathways related to the homologous repair (HR), base excision repair (BER) and non-homologous end joining (NHEJ). Thus, treatment using PARPi represent a new era for cancer therapy, and even new horizons can be attained by coupling these molecules with a nano-delivery system. For this, liposomes encompass all the required features due to its excellent biocompatibility, biodegradability, and low toxicity. Realizing the high usefulness and vast possibilities offered by combined PARPi cancer

[1] This chapter is based on a manuscript that is in preparation for submission for publication:

Conceição, C.J.F., Moe, E., Ribeiro, P. A. and Raposo, M.. Poly (ADP-ribose) polymerase 1 (PARP1): more than a simple DNA repair player

therapy, we will present here a comprehensive overview on PARP1 biological features, its role in cancer development and PARPi-mediated cancer therapies.

2.1 Introduction

Cancer as a multifactorial disease represents nowadays the human pathology with highest incidence and lethal consequences for the world population. This pathology is described as a disease from the genetic field, where the deregulation of tumor cells englobes multiple levels of genetic and epigenetic controls [1–3]. Common genetic alterations associated with cancer are structural alterations (e.g. inversions, translocations, among others) and numeric chromosomal alterations, punctual mutations and epigenetic variations. During cancer progression, such mutations will accumulate and be transmitted to the cell progeny [1]. This disease includes more than 200 forms, with environmental (e.g. radiation and exposure to chemical compounds), genetic and epigenetic factors being involved in its development and progression [2,3].

A comprehensive overview of the complexity involved in tumor development and progression is described by Hanahan and Weinberg, in their 2011's hallmarks of cancer [4]. In this work the authors include the overall molecular features that provide a solid base to start to grasp the intricacy of cancer biology. However, the hallmarks are disputed and other defend the "tissue organization" theory as the most comprehensive, where: (1) cancer cells must be understood in their complex tissue environment, (2) assume cellular proliferation and motility as the cell default state, as well as realize the (3) importance of cellular microenvironment interplay [5].

Nevertheless, the steppingstone for carcinogenesis is the hallmark associated with genomic instability and mutation [4]. In this category, mutations or epigenetic alterations to specific genes may lead to the activation of oncogenes and/or silencing of genome caretakers. These caretakers are usually responsible for the maintenance of genome stability and cellular homeostasis by their intrinsic role in DNA damage detection and repair [4].

Several DNA repair mechanisms are in action in normal cells, through which cell viability is preserved and achieved by the maintenance of genomic integrity. The innate repair mechanisms that operate to preserve genome integrity are dependent and activated based on the type of damage sustained. For vertebrates, double strand breaks (DSBs) are usually repaired by homologous repair (HR), but this is not the only repair route. Non-homologous end joining (NHEJ) (e.g. C-NHEJ and A-NHEJ) and single strand annealing (SSA) can also repair these types

of damages, however they are error-prone mechanisms that lead to DNA loss and rearrangements. This in turn due to excessive DNA damage/alteration accumulation, can lead to cell cycle arrest and cell death [6]. As for single strand break (SSB) repair, different mechanisms come into play, namely the base excision repair (BER), nucleotide excision repair (NER) and mismatch repair (MMR). If not repaired in time of replication, SSB can evolve to DSB damage [6], which in turn can only be repaired by the HR pathway [7].

Among the extensive number of proteins involved in the repair pathways, the one in the "first line of action" and with great preponderance in cancer progression/survival belongs to the poly (adenosine diphosphate-ribose) polymerase (PARP) enzyme family, more specifically the Poly (ADP-ribose) polymerase 1 (PARP1) [8].

In this work one intends to review the multiple aspects of PARP1 performance in DNA repair and cancer and show how this protein is involved in multiple biological processes. Additionally, we want to give an overview of how PARP1 may be used as a therapeutic target for cancer therapy, and what is known, done and available in this regard.

2.2 The extensive PARP Protein Family

The human PARP family includes a total of 17 proteins [9]. Originally, this superfamily was referred as consisting of 18 members, however the Tankyrase 3 protein proved to be a splice variant of Tankyrase 2 [10]. PARP homologous proteins have also been detected across the three domains (bacteria, archea, higher eukaryotes) of life and in double-stranded DNA (dsDNA) viruses (*Aeromonas phage* Aeh1, *Anticarsia gemmatalis nucleopolyhedrovirus*, *Invertebrate iridescent virus 6* and *Cellulophaga phage phi4:1*) [11]. In eukaryotes, PARP expression spans from plants to vertebrates' cells. Relatively to the human PARP family members, they have all been grouped and catalogued by their intrinsic cellular roles in the following subfamilies: DNA dependent (3 proteins), tankyrase (TNKS) (2 proteins), CCCH Zn Finger (3 proteins), MacroDomain members (3 proteins) and the unclassified members (6 proteins) [9]. Due to the homology of the CAT domain with the diphteria toxin ART fold, PARP members are also named as ART diphteria toxin-like enzymes (ARTDs) (Table 2.1) [12].

Table 2.1 — Human PARP superfamily depiction and additional information regarding cellular compartment localization, enzymatic activity, and function.

Subfamily	Protein Name	Alternative name	Cellular Compartment Localization	Enzymatic Activity	Function	References
DNA dependent	PARP1	ARTD1	Nucleus and mitochondria	MARylation PARylation, with branching	DNA repair, transcription, chromatin structure modulation - epigenetics, cell cycle, programmed cell death, membrane repair, adipogenesis, innate immunity and cell stress response	[9,13–24]
	PARP2	ARTD2	Nucleus and cytoplasm (centrosome in G_0/G_1)	PARylation	DNA repair, chromatin structure modulation - epigenetics	[9,13,17,25–27]
	PARP3	ARTD3	Nucleus and cytoplasm (centrosome in G_0/G_1)	MARylation	DNA repair regulator, DNA damage surveillance network, chromatin structure modulation - epigenetics, transcription regulation, epigenetics, and link to the mitotic fidelity checkpoint	[9,12,17,26,28,29]
Tankyrase	PARP5a	TNKS1 ARTD5	Cytoplasm (centrosome)	PARylation	DNA repair and telomere length	[9,12,17,30]
	PARP5b	TNKS2 ARTD6	Cytoplasm (mitotic spindle and spindle pole)	PARylation	DNA repair, signalling pathway, telomere length and intracell vesicle traffic	[9,12,17,31–35]
CCCH Zn Finger	PARP7	tiPARP ARTD14 RM1	Nucleus and cytoplasm	MARylation	Transcription regulation, Cell structure, adhesion and motility, innate immunity, and cell stress response	[9,12,17,27]
	PARP12	ARTD12 ZC3HDC1	Cytoplasm (Golgi)	MARylation	Cell stress response	[9,12,17,27]
	PARP13	ZAP1 ARTD13 ZC3HAV1	Cytoplasm	No activity reported	Innate immunity	[9,12,17,27]
MacroDomain	PARP9	BAL1 ARTD9	Nucleus and cytoplasm (primarily)	No activity reported	Innate immunity	[9,12,17,27,36]
	PARP14	BAL2 ARTD8 CoaSt6	Nucleus and cytoplasm (primarily)	MARylation	Focal adhesion, actin cytoskeleton, transcription regulation, signal transduction pathways, cell motility and innate immunity	[9,12,17,27,36]

	PARP15	BAL3 ARTD7	Nucleus (nucleosome)	MARylation	Post-translational modification of proteins and negative regulator of transcription	[9,12,17,36,37]
Unclassified	PARP4	vPARP ARTD4	Nucleus and cytoplasm	MARylation	Cell transportation and vault particle regulation	[9,12,17,27]
	PARP6	ARTD17	Cytoplasm	MARylation	Cell structure, adhesion, motility, spindle pole regulation and cell replication	[9,12,17,27]
	PARP8	ARTD16	Nucleus (nuclear envelop and centrosome spindle poles)	MARylation	Membrane (organelles) and nuclear envelope formation	[9,12,17,27]
	PARP10	ARTD10	Cytoplasm	MARylation	Signal transduction pathways, spindle pole regulation and cell replication	[9,12,17,27]
	PARP11	ARTD11	Nucleus and cytoplasm (centriole)	MARylation	Spermatogenesis	[9,12,17,27]
	PARP16	ARTD15	Cytoplasm (endoplasmic reticulum)	MARylation	Unfolded protein response, cell stress response, membrane, and nuclear envelope formation	[9,12,17,27]

Chapter 2. PARP1 a desirable target for cancer treatment: the biological fundament

Many of the PARP proteins are capable of catalyzing ADP-ribosyl post-translational modifications onto specific cellular targets [38]. The ADP-ribose is a signaling molecule that is produced by the transferase activity of PARPs, while using the NAD^+ as a substrate [39]. The attachment of ADP-ribose is primally done to proteins; however, evidence has shown that it can also be found on DNA/RNA ends and small chemical groups (e.g. acetate or phosphate) [39,40]. Usually, the PARPs transferase activity is linked to mono- or poly (ADP-ribosyl) modifications (MARylation and PARylation, respectively), but most of these members transfer only a single ADP-ribose molecule to their targets [41], as seen in Table 2.1. The protein members 1, 2, 5a and 5b are responsible for the addition of large polymer chains of ADP-ribose [17], but only PARP1 can promote branching points onto the PAR chain [39]. In Figure 2.1a it is depicted the array of possible patterns for ADP-ribosylation on target proteins.

The cofactor nicotinamide adenine dinucleotide (NAD^+) molecule is usually covalently linked to the acceptor protein, primarily to the glutamate (E) and aspartate (D) residues [9,17,40], but further studies have proved that serine (S), arginine (R), lysine (K) and cysteine (C) amino acid residues can also be involve [9,17,42–45], as seen in Figure 2.1b. In the case of arginine, ADP-ribosylation has been in part or completely associated with non-PAR ARTs, such as the human arginine ADP-ribosyltransferase 1 (ART1) [45,46], that mediates mono-ADP-ribosylation [17]. However, some indications point to a possible involvement of PARP10, which still needs further validation [17]. Nevertheless, the majority of the identified ADP-ribosylation modifications in cytoplasmatic and nuclear proteins, is substantially associated to the PARP family members [45]. More recently, threonine and tyrosine have also been pointed out as novel PAR acceptors [43,45,47,48]. The ADP-ribosyl modification of each amino acid residue involves a specific set of proteins [42–45,47,48], and some of these associations are depicted in Figure 2.1b, as well as the acceptor (Figure 2.1b1) and donor bond (Figure 2.1b2) molecules involved. The ADP-ribose modifications are essential in the regulation of multiple cellular processes such as DNA repair, transcription, cell fate and stress response [39]. Through the addition of poly (ADP-ribose) modifications, the biochemical properties and biological activity of the target proteins are modified, facilitating processes such as protein ubiquitination and degradation [41].

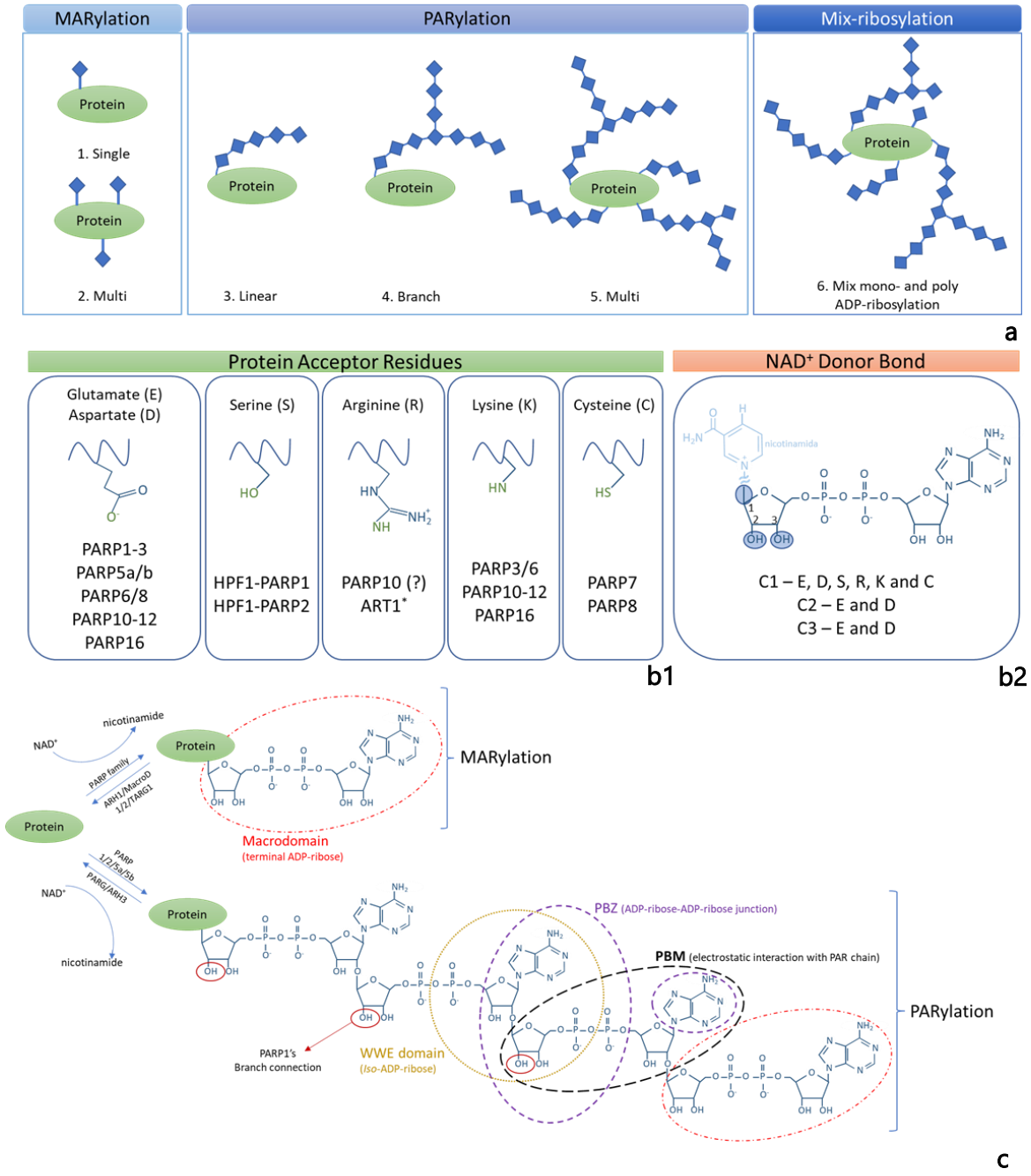

Figure 2.1 — Illustrations of NAD⁺ polymer chains formation and NAD⁺ bonding with protein residues. a) Representation of possible patterns for MARylation and chain patterns PARylation taking into consideration [49]; b) Identification of possible donor and acceptor bond in NAD⁺ (b2) and common amino acid residues (b1), that are involved in ADP-ribosylation. PARP proteins responsible for bond formation, and subsequent residue modification, are identified in their respective target, taking into consideration [42–45,47,48,50]; c) Schematics of MARylation and PARylation reactions, with indication of PARP family members involved. Additional identification of *readers* recognition sites in the ADP-ribosylation mono/polymer, taking into consideration [41,50–52].

Chapter 2. PARP1 a desirable target for cancer treatment: the biological fundament

Like other tightly regulated post-translational modifications, PARylation employs several players, that are classified as *writers*, *readers,* and *erasers*. The first englobes the overall PARP family members, the second includes proteins that are capable to recognize and bind to the PAR chains, and the later encompasses enzymes that are capable to trim and remove the ADP-ribose chains [39,50,51,53]. PARylation is known to facilitate protein-protein interactions, with the branched chains serving as scaffolds for the binding of proteins that present WWE domain (e.g. PARP14, PARP11 and PARP12), PAR-binding motif (PBM) (e.g. *Xeroderma pigmentosum* complementation group A (XPA), DNA ligase III, X-ray repair cross complementing1 (XRCC1), Ku70, ataxia telangiectasia mutated (ATM), p21 and p53), PAR-binding zinc finger (PBZ) (e.g. CHFR and APLF) or Macro domains (MacroH2A variants, PARP15 and PARP14). On the other hand, MARylation only promotes the binding of proteins that contain Macro domains [41,50–52], as depicted in Figure 2.1c.

The use of the NAD^+ cofactor has a profound effect at multiple cellular levels, and because of this the enzymatic activity of PARP proteins is tightly regulated in its activation, in order to avoid complete NAD^+ depletion from the cellular energy centers (e.g. mitochondria) [39].

In human cells, PAR and MAR modifications are reversed by a specific set of hydrolase proteins (Figure 2.1c). The first is reversed by the poly (ADP-ribose) glycohydrolase (PARG) isoforms (99, 102 and 111 kDa isoforms) and ADP-ribosyl hydrolase 3 (ARH3), while single modifications are reversed by the ARH1, MacroD1, MacroD2 and terminal ADP-ribose protein glycohydrolase 1 (TARG1 or OARD1) [40,49,50]. Moreover, several evidence have shown that some phosphodiesterases (e.g. NUDT9, NUDT16 and ENPP1) present ADP-ribose *eraser* capability [49]. Further information regarding ADP-ribose hydrolases activity, specificity and cellular localization can be found in Table 2.2.

Table 2.2 — Compilation of human PAR and MARylation erasers, with information regarding cellular localization, substrate, bond, type of reversal and catalytic activity.

Name	Alternative Names	Classification	Cellular Localization	Substrate	Target bond	Type of reversal	Catalytic Activity	References
PARG (99, 102, 111 kDa isoforms)	---	Macrodomain	Nucleus (111 kDa) Cytoplasm (60, 99, 102 kDa) Mitochondrial (60, 55 kDa)	PAR	O-glycosidic	Partial	Yes (99, 102 and 111 kDa) No (55 and 60 KDa)	[49–51,54,55]
MacroD1	LRP16	Macrodomain	Nucleus Cytoplasm (primarily mitochondrial)	MAR (D/E)	Carboxyl ester	Complete	Yes	[49–51,56,57]
MacroD2	C20orf133	Macrodomain	Nucleus Cytoplasm	MAR (D/E)	Carboxyl ester	Complete	Yes	[49–51,56,57]
TARG1	OARD1 C6of130	Macrodomain	Nucleus Cytoplasm (Stress granules)	MAR (E) PAR	Carboxyl ester	Complete	Yes	[49,50,57,58]
ARH1	ADPRH	ARH fold	Cytoplasm	MAR (R)	N-glycosidic	Complete	Yes	[49,50,59]
ARH3	ADPRHL2	ARH fold	Nucleus Cytoplasm Mitochondria	MAR PAR	O-glycosidic	Complete	Yes	[49,50,58,59]
NUDT9	ADPR-PPase	NUDIX	Mitochondria	PAR	Phosphodiester	Partial	Yes	[49,50,60]
NUDT16	IDPase U8 snoRNA-binding protein H29K	NUDIX	Nucleus Cytoplasm	MAR PAR	Phosphodiester	Partial	Yes	[49,50,61–63]
ENPP1	Plasma-cell membrane glycoprotein PC1	ENPP (PDNP)	Cell Membrane	MAR PAR	Phosphodiester	Partial	Yes	[49,50,64–66]

Note: E- glutamate; R – arginine; ADPRH – ADP-ribosylarginine hydrolase; ADPR-PPase – adenosine diphosphoribose pyrophosphatase; NUDIX – nucleoside diphosphates linked to moiety-X; ENPP1 – ectonucleotide pyrophosphatase/phosphodiesterase family member 1; IDPase – IDP phosphatase

2.2.1 The DNA repair PARPs - PARP1, PARP2 and PARP3

The PARP family was first presented 60 years ago by Chambon et al., [67,68], with the first report of immediate ADP-ribosylation response to DNA damage, induced by alkylating agents, ionizing radiation, or oxygen/nitrogen radicals. Over the years the cellular role and localization of these members revealed to be far more complex, and wider than what was initially perceived (Table 2.1).

Among the 17 members, PARP1, PARP2 and PARP3 are the ones more commonly associated with repair of DNA damage [39,69].

In structural terms these proteins present several similarities in two main domains, as seen in Figure 2.2. The catalytic domain (CAT) of the three PARPs includes a regulatory alpha-helical domain (HD) and an ADP-ribosyl transferase (ART) fold, that are conserved and responsible for the addition of the ADP-ribosyl chains [70–73]. The PAR polymer addition is done using the NAD^+ cofactor as a substrate, and results in the subsequent release of a nicotinamide molecule per NAD^+ (Figure 2.1c) [69,74]. Besides the CAT domain, PARP1, 2 and 3 share a common tryptophan (W) – glycine (G) – arginine (R) motif, that is generally called the WGR domain. This domain can interact with DNA and works as a key regulator of DNA dependent catalytic activity [39,69,73]. Furthermore, PARP1 presents four additional domains; three zinc fingers (Zn1, 2 and 3) and a BRCA-C-terminus (BRCT) domain, while PARP2 and 3 presents only a small N-terminal tail [39,71–73], as depicted in Figure 2.2. This tail is not essential for PARP 2 and 3 enzymatic activity; however, it is involved in the DNA binding interface [75,76]. For these two proteins the WGR domain acts as the regulatory center for DNA binding, sensing the nature of the DNA break [76,77]. Their enzymatic activity can be triggered by DNA breaks carrying a phosphate group in the 5′ end [76,77]. However, PARP3 activity appears to be most sensitive and reactive to 5′ phosphorylated single strand nicks [76,78]. Recent crystal structure data revealed that PARP2's WGR domain links two DNA breaks, which has led to the understanding that this protein may serve as a connecting bridge between DNA ends [78].

In the case of PARP1, the DNA binding capability is primarily triggered by the zinc finger domains, and contrary to PARP2 and 3 its DNA binding capability and enzymatic activity is insensitive to the DNA phosphorylation state [73,75,76]. PARP1 indiscriminately binds DNA, however the interaction stoichiometry depends on the type of damage [18,79–81]. Previous reports have shown that PARP1's binding affinity/stoichiometry is dependent on DSBs, with the protein's DNA binding domain presenting a stoichiometry of two proteins to one DNA

molecule with 5′-recessed DNA ends, and a 1:1 stoichiometry to 3′-recessed ends and dsDNA. Protein dimerization was found to be a requisite for high enzymatic activity [79].

PARP1's BRCT domain is viewed as the protein center for auto-modification and the WGR domain for DNA binding/interaction and allosteric activation [70–73].

It is proposed that the overall structure of PARP1 resembles a "beads-on-a-string" assembly in the absence of DNA damage [8], and the detection of strand breaks leads to the partial displacement and unfolding of the HD sub-domain [72]. In this way, the access to the ART pocket is granted to NAD^+, leading to the activation of PARP1's enzymatic activity. PARP2 and 3 activation appears to be governed by the same allosteric mechanism [70].

Even though PARP1 and 2 present overlapping functions in DNA damage response, the first prevails over all the family members, since it is responsible for 80 – 90 % of DNA repair related PAR modifications [82,83]. Among the PARP family, PARP1 is the best characterized and studied isoform [82].

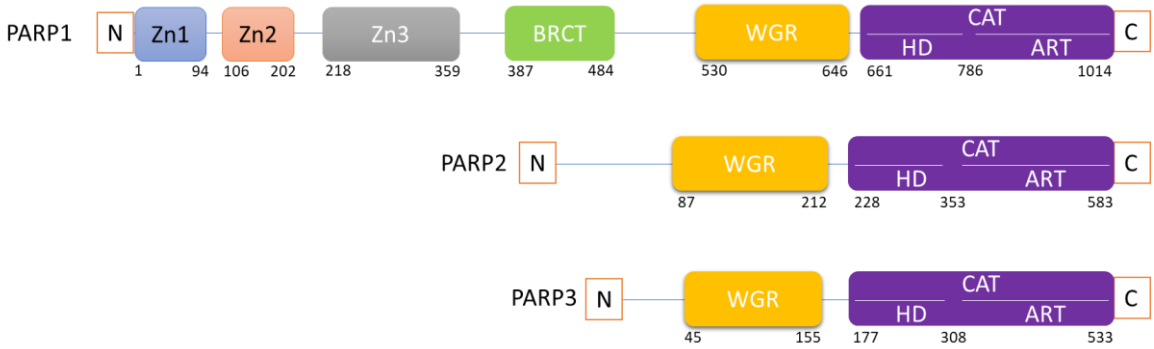

Figure 2.2 — Schematic illustration of DNA dependent PARP1, PARP2 and PARP3 domains, with indication of amino acid boundaries in accordance with suggestions of Suskiewicz et al., 2023 [84], van Beek et al., 2021 [69] and Steffen et al., 2014 [85].

2.3 PARP1 the Canonical PARP protein

Poly (ADP-ribose) polymerase 1 (PARP1) is an abundant nuclear enzyme, which primarily acts as a transferase and is closely associated with DNA repair, mostly Base Excision Repair (BER) [9]. The key involvement of this protein in the repair pathways has led to its denomination as the DNA "guardian angel" [86].

Solely in the nuclear compartment, where the PARP representation is high, PARP1 concentration values were reported to be around 7-100 μM ($2 \times 10^5 – 10^6$ copies/nucleus), which translates into a nuclear-cell ratio of 0.08 [69]. These values are a clear indication of PARP1s

great nuclear representation and its importance in maintaining genomic stability and cellular homeostasis.

PARP1, a 114 kDa multi-domain protein, orchestrates vital biological processes such as inflammation, hypoxic response, transcriptional regulation, maintenance of chromosome stability, DNA repair, and cell death [71,82]. The most extensively studied property so far is the response of this protein to DNA damage and subsequent repair of genomic anomalies. PARP1 is also capable of binding to chromatin ends in a DNA strand break, stabilize the site and recruit repair and chromatin remodeling factors to the break loci [71,73]. The catalytic activity of PARP1 is stimulated by 500-fold, either from SSB or DSB recognition [87]. Upon damage recognition and binding, PARP1's six main domains (Figure 2.2) reorganize, change its folding and trigger enzymatic activity. This activity translates into the formation and increase of PAR chains onto specific targets (either DNA/RNA, other proteins such as histones – *trans*/hetero-modification – or PARP1 itself – *cis*/auto-modification) [69,74,82]. Through an overall change in surface charge, subsequent steps are triggered thus leading to strand break repair [72]. PARP1 auto-modification occurs predominantly on E/D and S residues, namely in E488, E491, S499, S507 and S519 [44,88–90], and promotes the release of PARP1 from the break sites through electrostatic and steric repulsion [45,72].

The removal of PAR modifications is essential to prevent the trapping of PAR recruited proteins and permit the access by downstream repair effectors to the damage site. For the turn-over of PARP1's PAR chains, the two main human proteins involved are the PARG and ARH3, which are responsible for the cleavage of the O-glycosidic bond between ADP-ribosyl subunits [58], as depicted in Table 2.2 and Figure 2.1c.

The inhibition of PARP1's transferase activity in the repair of SSB, is met with the accumulation of these damages, that through the collision with the replication fork will evolve into a DSB [91]. Thus, demonstrating how PARP1 auto-modification may have a profound impact in genome integrity.

The key function of PARP1's auto-modification activity is closely related to the release of the protein from the damage sites, where the bind interaction between PARP1 and DNA breaks serves as a stabilizing element, until repair effectors are recruited [92,93]. As previously explained in subsection 2.2, PAR chains also serve as a scaffold for effector recruitment and for protein complex building blocks. Any type of interference with PARP1's PAR activity has profound consequences in cellular homeostasis, that leads to PARP entrapment and DNA repair prevention. This mechanism is described as the one behind clinical PARP1 inhibitors, that are used in cancer therapy. These catalytic inhibitor molecules are employed to promote PARP1

trapping on the chromatin matrix, thus preventing DNA break repair and promote cytotoxicity in cells that have their repair systems already compromised [45,58]. PARP1 is viewed as an attractive target for cancer therapy since this protein is usually upregulated in several tumors and is critical for cell survival [94]. Data regarding PARP1 inhibitors, and their therapeutic potential will be explained and discussed in another subsection.

Even though among the PARP family, the PARP1 isoform is the member most studied and characterized, some questions remain to be answered regarding its full-length structure. Due to its flexible multi-domain nature and the presence of several linkers, only X-ray crystal structures of truncated or engineered versions of this protein have been published [73,95]. These structures comprise mainly interaction studies of CAT with known therapy inhibitors [74,95–97], as well as some interesting new potential molecules [98–114]. Besides inhibitor interactions, several attempts were made to understand PARP1 and DNA interaction at a structural level, however all the structures remain to be of single domain or truncated versions of PARP1 [73,115–117]. Furthermore, the structures of PARP1 bound to NAD and BAD co-factors were also determined, but still no full-length protein structure was assessed [70,101]. In other inquiries the focus was on putative PARP1 protein interactors, where published structures include PARP1 CAT and PARP1-CAT ΔHD interacting with TIMELESS [118] and HPF1 [119], respectively. Even though attempts to determine native human PARP1 X-ray crystal structure have rendered results for single domains and truncated protein versions [120], in other organisms single domain structures have been determined from *Gallus gallus* [101] and *Rattus norvegicus* [121].

The history behind the PARP family structural unwinding can be referred to the first publishing of PARP1 in 2004 [104], followed by PARP2 in 2010 [122] and PARP3 [123], with these being the central focus for the majority of PAR transferase activity.

Structures of PARP1 domains were also determined by nuclear magnetic spectroscopy (NMR), namely the Zn1-Zn2 interacting with SSB and Zn1-Zn2-Zn3 [80,124], full-length with dumbbell DNA [70,84], the BRCT domain [84], the WGR domain [124] and CAT in complex with inhibitors (Veliparib, Olaparib and Talazoparib) [96].

In 2019, an electron density map of a dimeric form of PARP1 associated to DNA (dsDNA and nicked-dsDNA) was described using single-particle electron microscopy (EM). However, the resolution was very low (28Å) [125]. Nevertheless, these results gave a reinforcement of the hypothesis that PARP1 forms a dimer upon binding to DNA. Using the same technique, the structure of full-length PARP2 associated to the histone PARylation factor 1 (HPF1) was unveiled in 2020 [126]. The cryo-EM structure of PARP1 has yet to be determined.

Chapter 2. PARP1 a desirable target for cancer treatment: the biological fundament

In recent years, the rise of the artificial intelligence (AI) structural prediction systems AlphaFold (with its new released AF2) [127] and RoseTTAFold [128], have presented an enormous advancement in the prediction of structured and unstructured (or intrinsically disordered) protein regions. These tools can predict models of highly complex and large proteins, with an elevated degree of accuracy [127-129]. Predictions are made taking into consideration the amino acid sequence and, for example the AF2, may resort to deposited Protein Data Bank (PDB) structures and multiple sequence alignment to detect evolutionary relationships in the protein of interest [127,129].

Taking advantage of this tool, and coupling it with experimental assays, Suskiewicz et al., 2023 [84], presents an in-depth analysis of PARP family structural models and unveil possible new information regarding biological functions (possible PARP14's RNA-binding and RNA ADP-ribosylation). The AF2 models of PARP1 suggest that its BRCT domain is relative flexible and independent to the remaining domains (Figure 2.3a) [84]. Moreover, the authors state that the predicted model appears to be more consistent to PARP1's multi-domain DNA-bound crystal structures [84]. However, due to the experimental analysis done by the authors, it is stated that the "free" form of PARP1 behaves as a "beads-on-a-string" (that is the consensus idea over many years) (Figure 2.3b) and that it collapses into a more rigid form upon DNA binding, with BRCT being excluded from this bound form (Figure 2.3c) [84].

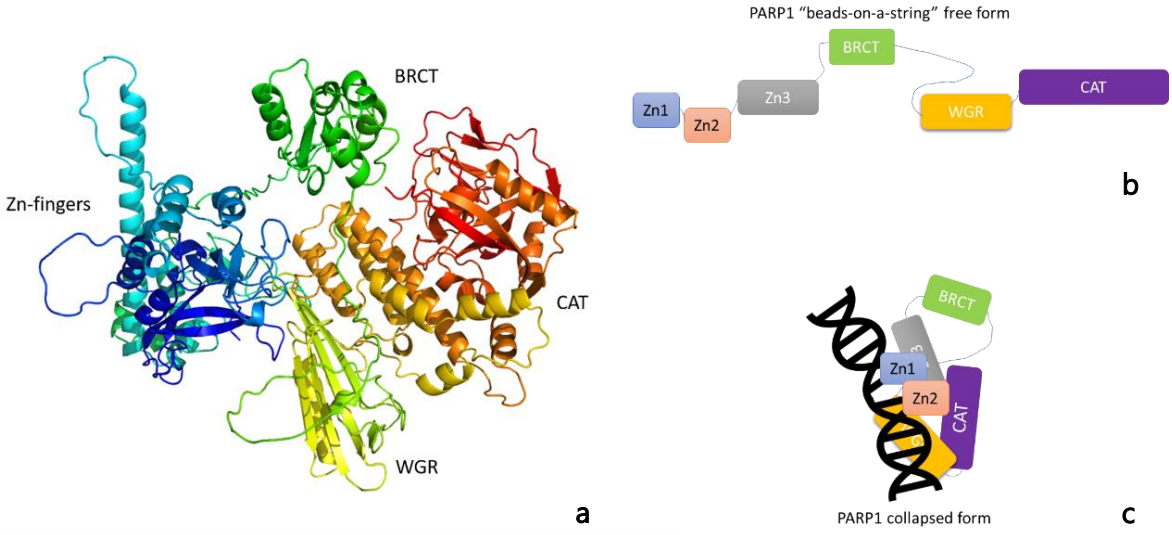

Figure 2.3 — Insights into PARP1 structure. a) PARP1 full-length predicted structure retrieved from AlphaFold (AF) [127,130] and figure prepared in PyMOL [131]; b) Model of PARP1 "beads-on-a-string" free form, taking into consideration [84]; c) Model of PARP1collapsed/rigid form when bound to a DNA break, taking into consideration [84].

2.4 PARP1s vast intracellular functions, partners and regulation

PARP1 through its ADP-ribosylation activity, either on itself and other targets, can modulate and orchestrate several intracellular pathways. In these pathways some of the most important cellular functions are included: chromatin modification, transcription regulation, DNA damage repair and cell death [132,133]. However, due to the nature of the PAR modification, the accumulation of these chains is met with cytotoxic effects if not properly regulated. Studies in mice verified that target disruption of PARG had lethal consequences, with activation of apoptotic cell death in blastocysts [132,134]. Thus, the PARP1 interactors are vast and can be rationalized into 3 categories: 1) PARP1 ligands and activity regulators; 2) enzymes that modify PARP1 and 3) PARP1 substrates and binding partners. In Figure 2.4 all the players involved in PARP1 biological functions are summarized.

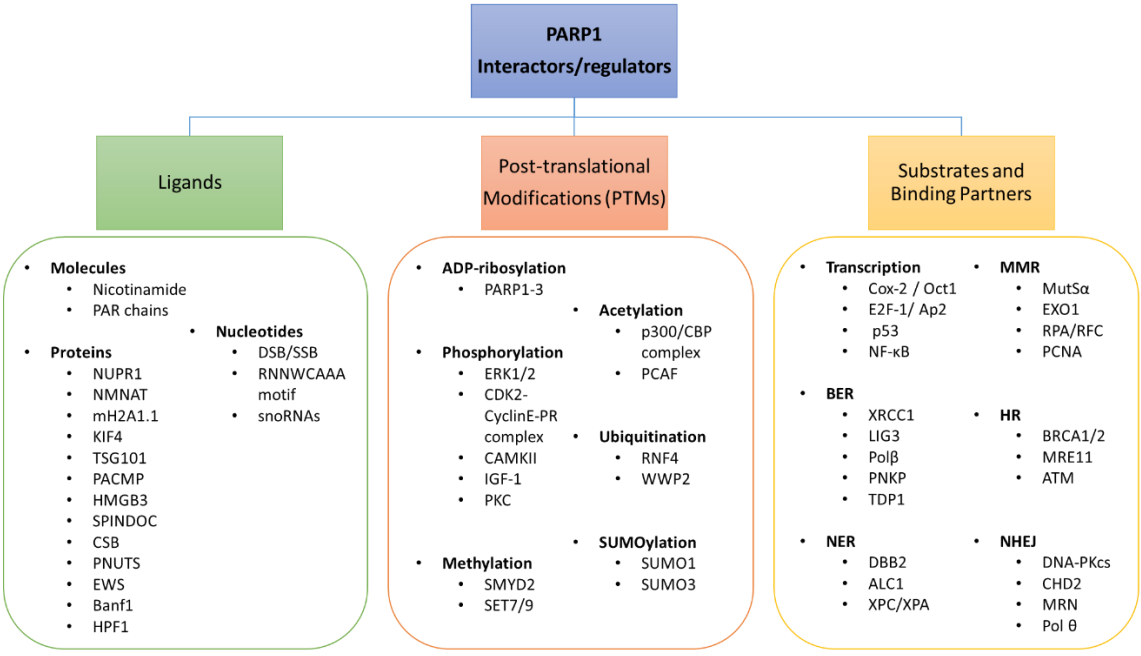

Figure 2.4 — Schematic summarizing the various levels of PARP1 regulation and regulator effect on multiple biological levels. It is identified the molecules that bind and regulate PARP1 activity (green box), enzymes that regulate PARP1 activity through post-translational modifications (PTMs) (orange box) and PARP1's catalytic activity targets or binding partners in transcription regulation and DNA repair pathways (yellow box).

2.4.1 Ligands and regulators of the enzymatic activity of PARP1

One of the ligands and regulators of PARP1's enzymatic activity is the nicotinamide by-product from NAD^+ consumption [132]. These molecules are known to have a mild inhibitory

effect on PARP1's transferase activity, and it is from this interference that clinical PARP1 inhibitors were first conceived and later optimized [132,135,136].

Moreover, the size of the added PAR chains helps in reducing PARP1's activity, through their excessive negative charge. When PAR chains become very long and branched, repulson forces from DNA lead to the release of PARP1 and NAD^+ consumption is thus limited [132]. Also, another negative regulator of the enzymatic activity of PARP1 is the nuclear stress protein (NUPR1), which is done by physical interaction with the protein [137].

Another off-switch of PARP1's enzymatic activity is the presence in DNA of the motif 5'-RNNWCAAA-3' (where R is adenine (A) or guanine (G), N can be any nucleotide base and W is A or thymine (T)). This sequence is present in the promoters of several genes and the interaction with PARP1 suppresses the enzymatic activity and other dependent functions of the later [138]. Here it is proved that other than its affinity to and DSB/SSB dependent activity, PARP1 is regulated by other nucleotide singularities.

For example, small nucleolar RNAs were shown to affect PARP1 activity, more specifically the SNORA74A and SNORA73 [139,140]. The first was reported to interact with PARP1 and serve as positive regulator of PARP1 activity [139], while the second restrains PARP1's auto-PARylation and leads to genome instability in hematopoietic malignancies [140].

Some proteins can be included in this section such as the nuclear nicotinamide mononucleotide adenylyltransferase (NMNAT), that enhances PARP1 activity. This protein associates with PAR chains and is capable of synthesizing new NAD^+ molecules, which are then fed into the transferase cycle of PARP1 [141]. Other proteins, that are also involved in the regulation of PARP1's catalytic activity, are the histone variant mH2A1.1, KIF4, TSG101, PACMP, HMGB3, SPINDOC, and CSB [142–148]. The PNUTS protein was also reported to aid PARP1 in its DNA repair activity [149]. This protein acts as a binding partner, and it is required for the recruitment of PARP1 to DSBs and for damage site PARylation, in NHEJ repair pathway [149]. Moreover, Lee et al., verified that the Ewing sarcoma protein (EWS) promoted the dissociation of PARP1 from the chromatin, thus suppressing its enzymatic activity, and leads to the prevention of excessive accumulation of PARP1 on DNA [150]. In the case of the DNA-binding protein Banf1, Bolderson and colleagues verified that the activity of PARP1 was inhibited by direct interaction with the NAD^+ binding domain, which translated in the flawed repair of oxidative lesions [151].

One of the most important discoveries that set a new stage on PARP1 activity regulation was the description of the interactor histone PARylation factor 1 (HPF1), that was revealed to be the major mediator of PARP1's serine target modifications [89,126,152]. HPF1 proved to be able to model the activity of PARP1, at micromolecular concentrations (in vitro assays), and to

form a joint active site with PARP1/2, that leads to the aa specificity switch of PARP1/2 from E/D to S [89,90,119,126,152,153] (Figure 1b1). HPF1 was also proved to influence PARP1's enzymatic activity towards histone modification, instead of it being mostly directed to auto-PARylation [154].

2.4.2 Enzymes that are able to modify PARP1

Various post-translational modifications (PTMs) are known to regulate PARP1 enzymatic activity; phosphorylation, acetylation, methylation, ADP-ribosylation, SUMOylation and ubiquitination [132,155]. Among these, disruption/dysregulation of PARP1's phosphorylation, acetylation and methylation are met with severe cellular consequences [155].

PARP1's ADP-ribosylation is carried out by itself, PARP2 and PARP3. Even though, evidence have shown that PARP1 auto-modification occurs predominantly on E/D and S residues (E488, E491, S499, S507 and S519) [44,88–90], the K498, K521 and K524 (all within the auto-modification loop – 466-525 aa), were also reported to be potential auto-modification sites [155,156]. Extensive auto-modification (chains greater than 200 units in length) inhibits the DNA binding capability and enzymatic activity of PARP1, while less extensive chains are suggested to affect exclusively the enzymatic activity [155,156]. PARP1 and 2 can form a heterodimer and through this association PTMs are exerted onto each other. On the other hand, PARP3 promotes mono (ADP)-ribosylation of PARP1, and by direct physical interaction the first can activate PARP1's transferase activity in the absence of DNA [155].

Phosphorylation may have positive and negative impacts on the cellular activity of PARP1. Modification of the serine and threonine residues (S372 and T373) by the extracellular signal-regulated kinases 1/2 (ERK1/2) [157], and S785/786 by the hormone-activated kinase CDK2, cyclin E and progesterone receptor complex (CDK2-cyclin E-PR) [158], produces activation or further enhancement of PARP1's enzymatic activity. The phosphorylation of PARP1 in S785 and S786 results in the loosening of the NAD^+-binding pocket, within the CAT domain [158], thus making indispensable the enzymatic activities of PARP1 and CDK2 for their hormone-dependent recruitment to the chromatin and Histone 1 (H1) displacement in the chromatin [155,158]. Similarly, phosphorylation of PARP1 by the calcium-dependent protein kinase (CAMKII) activates its enzymatic activity in neuronal development, and consequently leads to nuclear export of KIF4 [159]. On the other hand, the phosphorylation of PARP1 by the insulin-like growth factor-1 (IGF-1) and protein kinase C (PKC), is linked to the inhibition of PARP1's ADP-ribosylation activity and attenuation of its DNA binding capability and enzymatic activity, respectively [155].

Methylation of PARP1 amino acids was reported in the K528 and K508 residues. The first was associated with the activity of the lysine methyltransferase SMYD2 and the second to SET7/9 [160,161]. Methylation of the mentioned lysine residues was associated with significant enhancements of PARP1 enzymatic activity [160,161]. Negative feedback on SET7/9 methylation of K508 was verified upon auto-PARylation of PARP1 [160].

Acetylation of PARP1's lysine residues (K498, K505, K508, K521 and K524) was demonstrated by Hassa et al. [162]. These modifications are conducted by the p300/CBP protein complex and are considered of essence for PARP1 interaction and coactivation (with p300 and CDK8/MED14 complex) of the NF-κB protein complex, in inflammatory response [155,162]. On the other hand, protein acetylation by lysine acetyltransferase 2B (PCAF) was reported to enhance auto- and hetero-modification activities of PARP1, and it was deemed as essential for stress-induced cell death pathways [155,163]. Deacetylation of PARP1 promotes cell survival [163] and can be conducted by sirtuin 1 (SIRT1), in the 1-214 aa and 477-524 aa regions, or by histone deacetylase 1 (HDAC1) in the 477-524 aa region [162,163]. HDAC 2 and 3 were also proved efficient in PARP1 deacetylation [160].

Crosstalk between PARP1 acetylation and SUMOylation was observed, with the modifications promoted by SUMO1 and 3 contributing to the prevention of PARP1 acetylation by p300 [164]. Additionally, crosstalk between PARP1's ubiquitination and SUMOylation hint to a possible regulation mechanism on PARP1's transcriptional role. Martin et al. [165] verified that SUMO-targeted ubiquitin ligase ring finger protein 4 (RNF4) mediates heat-shock-inducible ubiquitination of PARP1 (that is SUMOylated) and functions as a positive regulator of *HSP70.1* gene [165]. The authors state that the results obtained pointed to a novel mechanism that regulates PARP1 transcriptional function, in response to heat-shock, where the SUMOylation and RNF4-mediated ubiquitination of the protein is in rule [165].

Moreover, Zhang et al., [166,167] uncovered that the Nedd4 family member WWP2 was a specific E3 ubiquitin ligase of PARP1, contributing to the discovery of a new ubiquitin-proteasome degradation pathway of PARP1. The authors verified that WWP2 mediated ubiquitination occurred in K418 and K249, in mouse myocardium tissue and cells [167].

PARP1 activity is also regulated by proteases in various cell death pathways, where protein degradation is conducted by caspase 3 and 7 in apoptosis, granzyme A and B in immune responses and cathepsins in autophagic and necrotic cell death [132].

2.4.3 PARP1 protein substrates and binding partners

Over the years, many proteins were described as PARylated by PARP1 and have contributed to a better understanding of the many biological functions of PARP1. Beside proteins, nucleic acids are also depicted as PARP1's catalytic targets and a comprehensive review can be found in [168]. The focus in this section is going to be on proteins that PARP1 regulates by either physical interaction or by the PARylation activity.

Even thought, PARP1's major acceptor of PAR chains is itself; this protein has long been associated with several intracellular players [132]. The extensive PAR chains act as scaffolds to attract and assist in the assembly of large protein complexes, which are usually involved in chromatin remodeling, DNA repair and cell cycle checkpoints [132]. The role of PARP1 in chromatin remodeling is varied, where chromatin relaxation or condensation is promoted by interaction with nucleosomes and PARylation of histones H1 and H2B [133]. Also, PARP1 is closely associated to transcription regulation by direct interaction with transcription factors or by PAR activity [132,133]. In the first are included Cox-2, Oct1, E2F-1 and Ap2, and in the second are englobed p53 and RNA polymerases I/II [133]. In the case of NF-κB, PARP1 may act in both manners with p50 and p65 sub-units, thus regulating the transcriptional function of NF-κB [132].

However, one of the best described functions of PARP1 is its role in detecting and initiating DNA repair, which will be discussed further in this section. This protein initially was associated exclusively with BER pathway, where PARP1 role is best characterized, but over the years it has been proved its involvement in other repair pathways, such as MMR, HR and NHEJ [133,169,170].

Single base modifications or nucleotide damage are the most common types of damage that can be found on DNA. SSB lesions arise spontaneously, or from base modifications such as oxidated bases, abasic sites and others [169]. On the other hand, DSBs are produced upon exposure to DNA-damaging agents, such as ionizing radiation, replication forks collapse or genome rearrangements (e.g. class-switch recombination (CSR), V(D)J recombination and meiosis) [132,169].

SSBs are readily repaired by BER, with PARP1 recognizing damage loci and promoting the recruitment of effector protein complexes. However, even though it is known that DSBs are repaired either by HR or NHEJ, PARP1 mechanistic involvement in these two pathways is still not fully understood. Nevertheless, the choice between HR or NHEJ is known to be ruled by cell cycle phase and chromatin context [132,169].

2.4.3.1 Base Excision Repair (BER)

BER serves as a route to repair SSBs and small lesions that may appear in DNA. The latter are first transformed into SSBs through the action of DNA glycosylases and APE1 [133,169]. The SSBs are sensed and bound by PARP1, that after auto-modification recruits the repair effector X-ray repair cross-complementing protein 1 (XRCC1) (Table 2.3). The rapid recruitment of XRCC1 is dependent on PARP1 and PARP2 enzymatic activity, and serves as a signal for the recruitment of repair effectors such as DNA ligase 3 (LIG3), DNA polymerase β and bifunctional polynucleotide kinase 3'-phosphatase (PNKP). Only after the recruitment and formation of the protein complex is the repair process stimulated [132,133,169].

Additionally, it was shown that PARP1-mediated repair in "nick" lesions requires the involvement of tyrosyl-DNA phosphodiesterase 1 (TDP1) [171] (Table 2.3). TDP1 is a target of PARP1's catalytic activity, and after PARylation the protein stability and recruitment is enhanced. Nick lesions are known to result from the abortion of DNA topoisomerase 1 (TOP1) activity, with TDP1 hydrolyzing the existing bond between TOP1 and DNA. This action helps in exposing the lesion to PARP1 and repair is carried out through BER [171].

However, some reports suggest that PARP1 may not be essential for BER repair in a specific subset of DNA lesions [172]. In the case of purine base damage, it has been pointed out that the repair may require the presence of PARP1, however in the case of pyrimidine damage the repair may be independent of PARP1 [173].

Moreover, it is important to refer that PARP1s intracellular signaling may act as a double-edged-sword, since in inflammatory processes, chronically activated repair pathways can induce DNA damage [133].

2.4.3.2 Nucleotide Excision Repair (NER)

UV irradiation is known to generate distorted DNA structures (e.g. thymine dimers) and the repair is done through the NER pathway [132]. This repair route involves a large set of proteins that are responsible for damage recognition, damaged-DNA stretch removal, gap filling and strand ligation [133]. Also, in recent studies it has been proved that PARP1 is involved in the initial stages of the NER sub-pathway named as global genome (GG)-NER, and that PARP1's catalytic activity is triggered by UVB radiation [174].

The UV damages are initially recognized by the *Xerodema pigmentosum* complementation group C (XPC) and RAD23B (XPC-HHRAD23B) complex, that subsequently associates with the DNA damage-binding proteins 1 and 2 (DDB1-DDB2) complex. This induces the ubiquitylation of core histones and leads to nucleosome displacement [169]. DDB2 promotes the

recruitment of PARP1, by physical interaction, and stimulates histones' PARylation [174,175] (Table 2.3), which results in further chromatin relaxation by the recruitment of the chromatin-remodeling helicase amplified liver cancer protein 1 (ALC1) [175,176]. Additionally, because XPC binds to PAR, through its specific binding-motif (PBM), its recruitment to the damage site is further enhanced [177]. Chromatin relaxation facilitates the access of the remaining NER proteins and further stimulates the repair. Moreover, PAR synthesis was also suggested to be central in the recruitment of NER damage recognition factor XPA [169] (Table 2.3).

Final repair steps involve the 1) DNA unwinding by the transcription factor IIH (TFIIH) and verification by XPA and RPA; 2) damaged-DNA stretch removal by endonucleases XPG and ERCC1/XPF (23-30 nt fragment); 3) gap filling by DNA polymerases δ and ε with PCNA, RPA and RFC. Strand ligation (4) is done by DNA ligase I or DNA ligase III-XRCC1, depending on the cell cycle stage [132,178].

The role of PARP1 in NER is biologically significant, more specifically its interaction with DDB2 and ALC1, since inhibition of PARP1 activity was revealed to induce cellular sensitization to UV irradiation [175].

2.4.3.3 Mismatch Repair (MMR)

DNA mismatch repair is activated when single/double mismatch bases and loops, arise from insertions/deletion in the DNA strand [132]. This pathway is initiated by the recognition heterodimer MSH2-MSH6 (MUTSα) and recruitment of the PMS2-MLH1 heterodimer (MUTLα). The MUTSα-MUTLα complex slides and nicks the DNA strand near the damage site, thus promoting Exonuclease 1 (EXO1) activity [132]. Afterwards, the recruitment of the replication clamp PCNA and the clamp loader RFC (replication factor C) to the protein complex, promotes mismatch-excision directed by 3′ or 5′ strand break [179]. In the final stages DNA polymerases δ and ε promote gap filling, and DNA ligation I leads to strand ligation [132,179].

In vitro studies revealed that PARP1 enhances mismatch dependence of 5′-directed excision in MMR, and that PARP1's DNA binding and BRCT domains are involved in MMR excision specificity [179]. It was also revealed that PARP1 physically interacts with several MMR proteins such as MUTSα, EXO1, replication protein A (RPA), RFC and PCNA [179] (Table 2.3). Additionally, MSH6 protein was presented as a target of PARP1 enzymatic activity [180]. Even with this data, much is still uncertain about the exact role of PARP1 in MMR and further characterization studies are needed.

2.4.3.4 Homologous Repair (HR)

HR repair is known as the high-fidelity repair route and is characterized by the usage of the sister chromatid or homologous chromosome as a DNA template for damage repair [132]. Moreover, homologous repair is required to prevent the deleterious effect of perturbed replication forks, either stalled or collapsed [174].

After DSB end recognition, the MRE11 nuclease-RAD50-NBS1 (MRN) complex jointly with the CtIP-BRCA1 complex cooperate in the generation of 3'-overhangs on DBSs blunt ends. The generated structure is then stabilized by the replication protein A1 (RPA1) and PARP1 is also pointed to help in stabilizing these DNA structures [169,174,181].

Activation of MRN complex contributes to cell cycle arrest, as well as to DNA damage repair by activation of the ataxia telangiectasia mutated (ATM) signaling, through phosphorylation [181]. Afterwards, BRCA2 mediates the exchange of RPA1 for RAD51, which promotes the search for a homologous DNA template (strand invasion) for lesion repair [179]. DNA polymerase extends the 3'-overhang strand, DNA ligase I connects the strand ends and the intermediate Holliday junctions are resolved by resolvases [181].

If the DNA lesion is not easily repaired, the ataxia telangiectasia and Rad3-related protein (ATR) signaling route is activated by the interaction of RPA1 with the ATR-interacting protein (ATRIP). This is followed by RFC-mediated loading of 9-1-1 clamp and successive activation of topoisomerase II binding protein 1 (TOPBP1) [132].

PARP1 role in the recruitment of HR proteins has been discussed over the years and it has been highlighted the importance of PAR chains in the recruitment of breast cancer type 1 susceptibility protein (BRCA1) and breast cancer type 2 susceptibility protein (BRCA2) [170,182,183] (Table 2.3). The first is promoted by BRCA1-binding partner BARD1, while BRCA2 recruitment is related to its own tandem oligonucleotide/oligosaccharide (OB) - folds that help in the detection of ADP-ribose chains in the damage sites [170,182,183].

These specific interactions laid the foundations for the usage of PARP1 inhibitors in the clinical treatment of *BRCA1* or *BRCA2* mutated cancers [169]. In this line of treatment, the combined conditions (inhibitor + mutations) results in synthetic lethality, which will help to increase therapeutic efficacy [169]. By this approach the inhibition of PARP1 leads to the accumulation of SSBs, which are further processed into DSBs during replication. Because BRCA1/2-deficient cells have their DSBs repair capabilities reduced, the synthetic lethality approach with PARP1 inhibitors will culminate in cytotoxic effects and cell death [169].

Additionally, the role of PARP1 regarding the recruitment of MRE11, in HR, is a topic much debated, with evidence revealing that a complex regulation system is in play at the

replication forks [184]. Ying et al. [184] verified that MRE11 is recruited through PARP1 activity in a small portion of stalled replication forks, particularly not easily resected forks. In the case of easily resected forks, MRE11 recruitment was considered independent of PARP1 [184]. It was also demonstrated that PARP1 could act as a replication fork protectant against MRE11-mediated resection, with a distinctive stabilization role [184]. Furthermore, the authors uncovered that the resolution of unresected forks required PARP1 and DNA-dependent protein kinases catalytic subunit (DNA-PKcs), for the relocation of XRCC1 proteins [184]. In this way effective repair and replication fork restart is enable [184] (Table 2.3).

Studies have also revealed that PARP1 physically interacts and PARylates ATM, during DNA damage response [185,186] (Table 2.3). Additionally, PARP1-ATM interaction was considered important in the phosphorylation kinetics of downstream proteins (e.g. p53 and H2AX) [185–187]. Knockdown and inhibition of PARP1 was revealed to delay ATM activity [186].

2.4.3.5 Non-Homologous End Joining (NHEJ)

NHEJ is an error-prone mechanism that is active throughout the cell cycle, but it is the preferred mechanism in G1 phase when a DNA template is not available [169].

In classical NHEJ (c-NHEJ) the Ku heterodimer ring (Ku70/Ku8) binds to the DNA strand-break ends and recruits the DNA-dependent protein kinase (DNA-PK), XRCC4 and DNA ligase IV (LIG4). DNA-PKcs bind to DNA activates the protein and leads to a phosphorylation cascade onto ATM, p53 and itself. In the meantime, the Artemis DNA end-processing enzyme prepares DNA strands for ligation [132].

PARP1 acts in this sub-pathway (c-NHEJ) either by physical interaction with DNA-PKcs, or by further stimulating the protein kinase activity by PARylation [169]. Additionally, it was proved that PARP1 potentiates the efficiency of c-NHEJ repair by the recruitment of the chromodomain helicase DNA-binding protein 2 (CHD2) to DSB sites, to promote the assembly of the XRCC4-containing repair complex [188] (Table 2.3).

Besides c-NHEJ, several reports point a key function to PARP1 in alternative NHEJ (alt-NHEJ) [169,174,189]. alt-NHEJ is characterized by end resection and utilize sequence microhomology regions, which makes it an inherently mutagenic pathway and leads to the generation of insertions and deletions [169,174,189]. This process is dependent on PARP1, XRCC1, LIG3, MRE11, NBS1 and Flap endonuclease 1 (FEN1) [189]. Strand-end ligation is independent of LIG4 and Ku complex, while DSB processing is done by the MRN complex [169,174].

PARP1 is indicated to be involved in the promotion of alt-NHEJ [169,190,191]. This is done by competing for the access to DNA breaks with Ku proteins, and by favoring the

recruitment of the MRN complex (Table 2.3) [169,190,191]. Additionally, PARP1 is also suggested to be involved in the recruitment of DNA polymerase θ (Pol θ), that displays a terminal transferase-like activity [190,191]. In a recent study done by Luedeman et al. [192], the authors suggest that PARylation indirectly promotes Pol θ recruitment and repair, by increasing the frequency of end resection and leading to the redirection from c-NHEJ to Pol θ -mediated alt-NHEJ in the repair of these specific ends [192] (Table 2.3).

The PARP1-Pol θ mediated repair thus serves as an additional justification for the synthetic lethality effect of PARP1 inhibition and *BRCA1*-mutation therapy. It was also experimentally verified that BRCA1-deficient malignancies are extremely dependent on Pol θ – mediated damage repair [190].

Table 2.3 — PARP1 and PAR functions, regulation and protein partners in DNA repair pathways.

DNA strand break	DNA Repair Pathway	PARP1/PAR function	Repair Factors that interact with PARP1 or PAR	References
Single strand break (SSB)	Base excision repair (BER)	Bind and stabilize damage site Recruitment	XRCC1 LIG3 Polβ PNKP TDP1 (nick lesions)	[132,133,169,171]
	Nucleotide excision repair (NER)	Damage detection, recruitment, and activation	XPA XPC DDB2 ALC1	[169,174–177]
	Mismatch repair (MMR)	Interaction	MutSα EXO 1 RPA RFC PCNA	[179,180]
Double strand break (DSB)	Homologous repair (HR	Bind, stabilize and recruitment	BRCA1/2 MRE11 ATM	[170,182–186]
	Classical Non-homologous end joining (c-NHEJ)	Stimulate activity and recruitment	DNA-Pkcs CHD2	[169,184,188]

Alternative Non-homologous end joining (alt-NHEJ)	Recruitment	POL θ MRN complex	[190–192]

When DNA damage is minimal PARP1 role results in the activation of any of the repair pathways that were previously described. However, if DNA damage is too extensive to be repaired, PARP1 is rapidly cleaved by caspases [193]. The cleavage of PARP1 results in two specific fragments: a C-terminal fragment of approximately 89 kDa (comprising the catalytic domain) and a N-terminal fragment of around 24 kDa (comprising the DNA binding domains) [193]. The first fragment is known to be translocated from the nucleus to the cytosol, while the N-terminal is retained within the nucleus, irreversibly bound to DNA. The 24 kDa fragment, in its bound form, acts as a trans-dominant inhibitor of remaining active PARP1 and other repair enzymes [193]. The degradation mode of PARP1 and the intracellular localization of its fragments is believed to be a conservation energy (cellular ATP pools) requirement for apoptosis [193].

Curiously, PARP1 is also capable to mediate a different form of cellular death, which is named parthanatos [194,195]. Under pathophysiological conditions, the over-activation of PARP1 can lead to the accumulation of PAR polymers and subsequentially to the nuclear translocation of the apoptosis inducing factor (AIF) [194,195]. This cascade of events will then trigger this non-apoptotic programmed cell death. Parthanatos is reported to be widely involved in several pathological processes such as ischemic-reperfusion injuries, septic shock, neurodegenerative diseases (e.g. Parkinson and Alzheimer), cardiovascular diseases, diabetes and cancer [194,195].

2.5 PARP1 and Cancer

PARP1 has been implicated in several human pathologies, but cancer is still the disease where PARP1 has been shown to be implicated in numerous pathways. As we have shown so far, PARP1 is implicated in many of the biological functions and processes that are of essence for tumor development and growth.

This protein has been identified in the nucleus and cytoplasm of cancer cells and PARP1 expression studies have revealed that this protein is found upregulated in a multitude of

tumors [196]. The determination of the expression levels of PARP1 is important for the determination of therapeutic potential, effect and side-effect of clinical inhibitors [196].

A study of over 8000 surgical samples from cancer and healthy patients, carried out by Ossovskaya et al. [197], revealed that *PARP1* is overexpressed in several malignant tissues. Among them significant results were verified in patients with breast, uterine, lung, ovarian, skin cancers and non-Hodgkin's lymphoma. Of these, breast cancer attracted the most attention, since the authors verified that *PARP1* overexpression was detected in over 30 % of breast infiltrating ductal carcinoma (IDC) samples, when in normal tissues values were 2.9 % [197]. Additionally, the same study demonstrated that *PARP1* gene was up-regulated > 2-fold in approximately 70 % of primary breast adenocarcinomas, including triple-negative breast cancer, where gene upregulation was consistent with increased protein expression [197]. In other assessments, high levels of PARP1 expression were related to poor prognosis and decreased survival rates in breast cancer patients, for patients with worse clinical outcomes and in less aggressive clinical conditions [198].

High expression levels of PARP1 were also verified in lung carcinomas, however differences were retrieved when comparing small cell (SCLC) and non-small cell lung (NSCLC) carcinomas. mRNA and protein levels were higher in the first, than the last [199].

In Ewing's sarcoma, an aggressive malignancy that is characterized by the EWS-FLI1 or EWS-ERG genomic fusions, PARP1's expression was revealed to be maintained in a positive feedback loop by the EWS-FLI1 fusion genes [200]. The expression loop was also revealed to be required for EWS-FLI-mediated transcription. These findings led to the suggestion by the authors that EWS-FLI1:PARP1 intersection presented a therapeutic strategy to increase treatment efficacy of Ewing's sarcoma patients [200].

Zuo and colleagues verified that PARP1 mRNA levels in epithelial ovarian cancer patients (EOC) was higher in a platinum-resistant therapy group, than a platinum-sensitive group [201]. This was associated with a worse prognosis and the authors suggest that PARP1 may serve as potential biomarker to predict the resistance to platinum chemotherapy and the prognosis of EOC patients [201].

In a recent study, Puentes-Pardo et al. [202], attempted to analyze the expression of PARP1 in colorectal cancers (CRC) with different p53 status, to evaluate the influence on the cancer stem cells (CSC) phenotype. These are a subset of cancer cells that are also considered important for cancer initiation and metastasis [202]. The authors confirmed that *PARP1* gene was overexpressed in tumor tissues from cancer patients, when compared to healthy mucosa, and that it was correlated with the differentiation grade [202]. However, this association was

only upheld in tumors with wild-type p53. In patients with p53 mutation, PARP1 served as an independent prognostic survival factor [202]. The authors affirmed that PARP1 could be a clinical tool for personalized medicine, since patients with high PARP1 expression and wild-type p53 would benefit from PARP1 inhibitor therapy, while this could be adverse for patients harboring p53 mutations [202].

Comprehensive studies were also done in understanding the molecular role of PARP1 and association with key features of cancer initiation and progress.

Demény et al. [40,203], has done a two-part review about the involvement of all PARP family members in ten hallmarks of cancer: (Part.1) 1) uncontrolled proliferation, 2) evasion of growth suppressors, 3) cell death resistance, 4) genome instability, 5) reprogrammed energy metabolism, 6) escape from replicative senescence; (Part. 2) 7) angiogenesis, 8) invasion and metastasis, 9) evasion of immune response and 10) tumor-promoting inflammation. Within this review it was extensively debated how poly (ADP-ribose) polymerases are involved in the microevolution process and survival of tumors, and how PARP1 appears again as a player with vast contribution and interconnections in all ten hallmarks. The authors also highlight controversies and do an interesting introspection about open questions and future prospects related to the wide roles of PARPs in cancer biology [40,203].

Cancer survival can be regulated in several levels by PARP1 via DNA repair pathways [196]. For cancer survival, cells will activate PARP1 to repair mild damages and in this way maintain carcinogenic mutations that permit its tumor phenotype [196]. When in the presence of excessive DNA lesions, normal PARP1 activation will lead to insufficient repair and culminate in cellular apoptosis [196]. However, in the case of PARP1 overactivation, cancer cells will face further mutagenesis, metastasis, energy-depletion, necrosis, and autophagy, which in turn will promote increased inflammation (cancer hallmark) [196].

As can be perceived PARP1 is involved in multi-level biological controls and its activity can either enhance carcinogenic features or lead to cellular death.

Additionally, PARP1 can promote tumor development through its transcriptional regulation role. This is achieved by the interaction with transcriptional factors, transcription machinery and chromatin modulators [196]. PARP1 transcriptional regulation effect may be positive and negative. On one hand leading to the transcriptional activation of oncogenes (e.g. vascular endothelial growth factor receptor 1 (*VEGFR1*), hypoxia-inducible factor 1α (*HIF1 α*) and 2A (*HIF2A*), androgen receptor, melanocyte-lineage survival (*MITF*)), or have repressive effects on tumor suppressors (e.g. p53 and Adenomatous polyposis coli (*APC*)) [196,203]. PARP1 is also capable to influence chromatin remodeling by the activity and location of histones. This can

be done by interaction with the nucleosome leading to a suppression of transcription, or by dissociation of H1 promoting RNA polymerase II-mediated gene transcription [196].

When PARP1 is hyperactivated, it promotes a positive feedback cycle that leads to the upregulation of inflammatory signal factors, such as NF-κB [196,203]. The interaction of PARP1 with NF-κB upregulates pro-inflammatory cytokines like tumor necrosis factor α (TNF α) and interleukin 6 (IL6) [196,203]. These are involved in the initiation of tumor-promoting inflammation processes. Chronic inflammation conducts to a higher degree of cell malignancy, which in turn helps with immune surveillance evasion [196,203]. It was also demonstrated that the NF-κB signal factor has a major role in cancer progression, metastasis, and angiogenesis [196].

PARP1 is also capable to modulate the cell cycle of tumor cells, by regulating cellular mitosis and programmed cell death pathways [196,203]. Additionally, PARP1 can activate pro-angiogenic/metastasis factors (e.g. c-MYC, VEGF, platelet/endothelial cell adhesion molecule (PECAM1/CD31) and HIF), thus inducing angiogenesis and metastasis [196,203].

In Figure 2.5 it is depicted the multifactorial roles of PARP1 in tumorigenesis, giving a better image on its span in cancer biological processes.

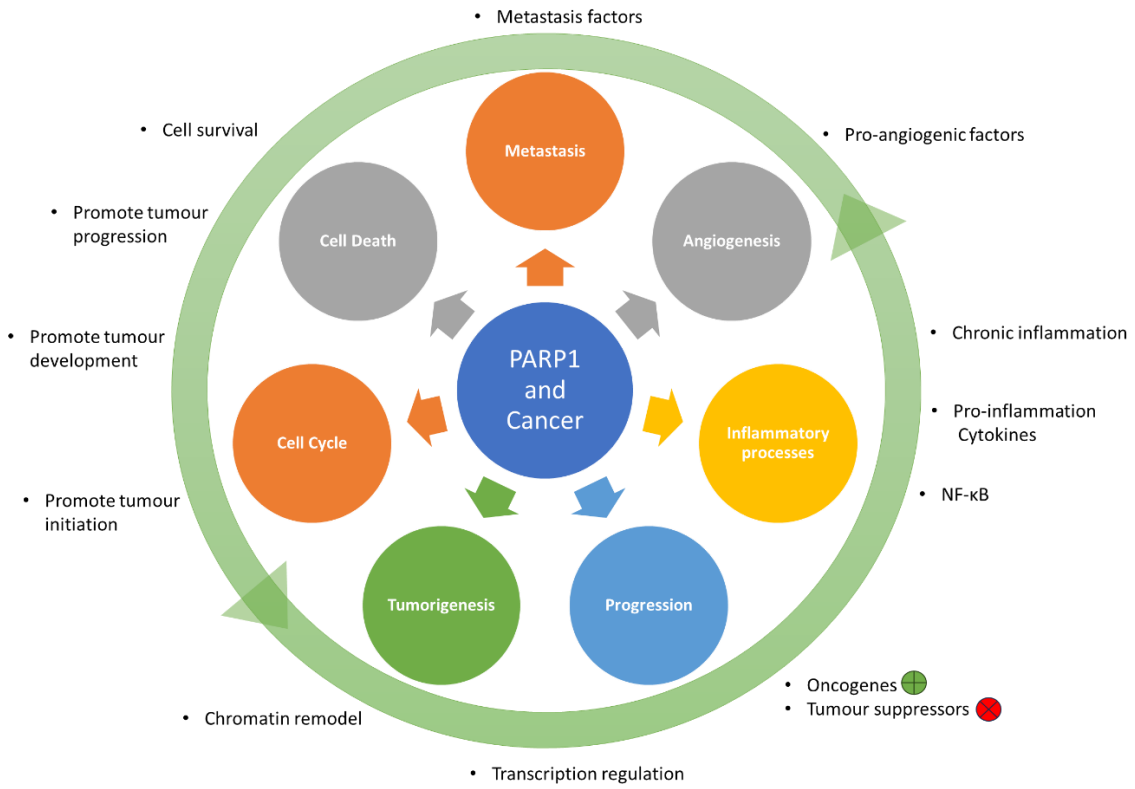

Figure 2.5 — Schematic summarizing the multifactorial roles of PARP1 in cancer. In the image it is depicted the way in which PARP1 is involved in tumorigenesis, tumor progression, inflammation processes, angiogenesis, metastasis, control of cell death and cell cycle. The multifaceted regulation done by PARP1 in numerous processes creates a "feed" cycle for cancer initiation, progression, malignancy, and survival. ⊕ means gene expression and ⊗ means gene silencing.

2.6 PARP1 the Desirable Therapeutic Target

PARP1 is one of the more interesting targets used in anti-cancer drug design. The abundant data proving its involvement in carcinogenesis reinforced the need for the development of better clinical inhibitors and treatments.

The therapeutic strategy behind the design of PARP1 inhibitors (PARPi) is based on the synthetic lethality theory, where cell survival is severely hindered by the simultaneous blockage of SSB repair and HR repair [204]. Since PARP1 was considered an ideal target in treating HR-deficient cancers, initial studies found that PARPis were effective in killing BRCA1/2-mutated tumors [204]. However, in more recent times it has been described that some non-mutated BRCA1/2 tumors are also sensitive to PARPi treatment [204].

Most PARP inhibitors were designed to mimic and compete with the cofactor NAD^+ for the protein catalytic domain of PARP1 [94,135,205,206]. These molecules are included in the monoaryl amides and bi-/tri-/tetracyclic lactam compound group [205], and their common pharmacophore features are the aromatic ring and carboxamide moiety [207]. The last interacts with CAT through three crucial hydrogen bonds with glycine-G863 and S904. Additionally, it was reported that the phenyl moiety of Y907 is involved in a π - π stacking interaction with the nicotinamide portion of NAD^+ [207].

In Malyuchenko's 2015 review [135] the rationality behind the design of PARPi and how their structure has evolved from first-generation compounds until the third-generation ones is extensively explained. This last category includes the FDA-approved inhibitors: Olaparib, Rucaparib, Niraparib and Talazoparib; and Veliparib, that is currently being tested in clinical trials [136,206,208–210]. Table 2.4 includes pertinent information regarding these inhibitors, namely their structure (with identification in red of nicotinamide pharmacophore), alternative designation, target protein and values regarding inhibitory potential.

Table 2.4 — Information regarding PARP1 clinical inhibitors. The nicotinamide pharmacophore that is common moiety among PARPi is highlighted in red.

Name	Alternative Name	Structure	Target	IC50 (nM)	K_I (nM)	References
Olaparib	AZD2281	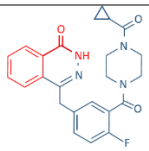	PARP1/2	5/1	0.97/0.34	[208,211]
Talazoparib	BMN673	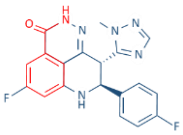	PARP1/2	1.2/0.9	0.012/0.18	
Rucaparib	AG-014699	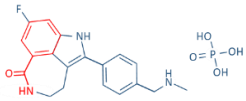	PARP1	1.4	0.09	
Niraparib	MK-4827	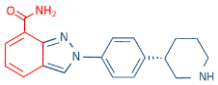	PARP1/2	3.2/4	1.2/--	
Veliparib	ABT-888	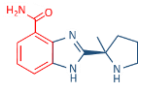	PARP1/2	5.2/2.9	0.96/9.9	

Note: IC50 – half maximal inhibitory concentration; K_I – inhibition/binding constant

PARPi's unique therapeutic potential confers great advantage in their usage in cancer treatment. They can either be used in synergistic lethal strategies, as a coadjutant to DNA damage agents (e.g. radiation or chemotherapeutics), or as mono-therapeutic agents (e.g. in tumors with specific genetic profiles) [94,204,212]. The use of PARPi, not only leads to the inhibition of PARP1's catalytic activity, but also to the prevention of its release from the damage sites. Moreover, it has been proved that chemical inhibition of PARP1 sensitizes cells to UVA, UVB and UVC treatment [174,204]. On the other hand, molecules such as Veliparib and Niraparib were also proved to be capable to bind cDNA, though intercalation in DNA grooves [213,214].

Over the years many X-ray crystal structures were determined for PARP1's CAT domain interaction with known inhibitors [74,95–97], as well as with some potential new molecules [98–114].

However, PARP therapeutic resistance has been reported in some cancers, which can be explained by the interplay effect of the c-MET membrane receptor [215]. Through the phosphorylation of PARP1's Y907 residue, the interaction CAT-inhibitor is prevented [215]. By blocking the c-MET-mediated phosphorylation of PARP1, the anti-tumor effect of PARPi is enhanced

[215]. Additionally, it was revealed that the cooperation between c-MET and epidermal growth factor receptor (EGFR) further enhances resistance to PARPi therapy in hepatocellular carcinoma [216].

Nevertheless, it was also verified that PARPi resistance could be circumvented by combination therapy. In NSCLC, it was established that tumor cells could be sensitized to PARPi and ionizing radiation through combination with DNA methyltransferase inhibitors [217].

Over the years a growing number of combination approaches with PARPi were assessed [40]. These include the combination with inhibitors of RTK, check-point kinase 1/2 (CHK1/2), ATR, Wee1, PI3K, HDAC, IGFR, Raf, MEK, or drugs that interfer with sex hormone synthesis [40].

Other drawbacks that have been associated with PARPi therapy, include 1) cytotoxic effects on normal cells, 2) high compound clearance rates in the organism and 3) drug interaction with plasma proteins [218,219]. Values as high as 83% binding with human plasma protein have been reported for Niraparib, after entering the blood through the digestive system [219]. One of the best approaches to circumvent these drawbacks Is by a combination therapy approach with nano-delivery systems, such as liposomes.

2.7 PARP1 Therapy Evolution - Combining ionizing radiation and Liposomal Nano-Delivery Systems

As we have discussed so far, PARPi combination therapy opens new horizons in cancer treatment. Until the present day PARPi clinical efficacy is far from what it is expected, and is associate with PARPi's oral administration, its relatively low accumulation in tumor mass, as well as to the complexity of the cellular microenvironment [220]. The use of nanotechnology helped to overcome most of these limitations and several nano-formulations were reported in the treatment of cancers [220,221]. Among these are included liposomes, polymeric micelles, hydrogels, nano-emulsions, nano-suspensions and nanoparticles (e.g. inorganic, polymeric and solid lipid nanoparticles) [220,221].

Multiple nano-systems have been developed for the delivery of PARP1 inhibitors, with most studies and systems focusing on Olaparib and Talazoparib. These are either used per se or in combination with other chemotherapeutic drugs [220–223]. The nano-systems described involve iron oxides, hydrogels, emulsions, polymer nanoparticles, implants and micelles, metal-organic frameworks, solid lipid nanoparticles, self-assembly nanoparticles, and liposomes [220–223]. A comprehensive review regarding these systems and their production methods

can be seen in [220] and [221], respectively. Besides Olaparib and Talazoparib, combination liposome systems were also reported for Rucaparib [220] and Veliparib [224], with the first being in clinical phase trials.

More recently, we have reported a new liposome system for the encapsulation and delivery of PARP1 inhibitors' Rucaparib, Niraparib and Veliparib [225]. In this study we have proved that 1,2-dipalmitoyl-sn-glycero-3-phospho-rac-(1'-glycerol) sodium salt (DPPG) liposomes are the best lipid system to achieve high drug encapsulation efficiency (> 40 %) and elevated particle stabilization [225]. Particle characterization revealed that DPPG-encapsulating PARPi presented zeta-potential values below -30 mV and increased population homogeneity. The main population of interest presented diameter values around 130 nm [225]. We were the first to report the specific application of DPPG lipids for PARPi liposome formulations and to uncover the preferable interaction/encapsulation mode of these inhibitors with the lipidic membrane.

Liposomes are considered efficient transport systems and present a similar structure to biological membranes, which makes them desirable for the delivery of clinical compounds through permeation [220]. Advantages related to the use of liposomes are excellent biocompatibility, biodegradability, low toxicity, lack of immune system activation and incorporation capability for both hydrophilic and hydrophobic molecules [226]. Several techniques can be used for their production, such as: thin-film hydration, detergent depletion, ethanol injection and reverse phase evaporation [227]. These usually require a post-processing step, either by extrusion or sonication to achieve the required size, structure, and population heterogeneity [227]. Furthermore, liposomes can act as a protective barrier for photosensitive molecules, protecting their molecular integrity and therapeutic activity [228]. Additionally, lipidic nano-formulations may serve as a biomimetic system for interaction studies, to reduce drug cytotoxicity and for co-loading systems to attain a higher degree of drug synergistic therapeutic effect [226]. Moreover, liposomes surface can be functionalized with other molecules (e.g. polymers, polyelectrolytes, antibodies, or even conjugation with other nano-systems) [229–232], thus increasing particle biocompatibility, stabilization, control drug release and confer target specificity [230–232]. In sum, liposomes are believed to be an adequate nano-delivery system to use in PARPi related cancer therapy, thus achieving a higher therapeutic efficacy and efficiency.

The use of nano-formulations permits to deliver clinical compounds though oral, injection, and transdermal administration, thus opening new possibilities for PARPi mono-therapy, their co-delivery with other drugs, or even to combine them with radiation and photodynamic therapy [220]. Nano-systems combined with radiotherapy were previously reported with

Olaparib and Talazoparib [220], while photodynamic therapy was reported in poly (lactic-co-glycolic acid) (PLGA) nanoparticles co-loading Veliparib and methylene blue [224].

Additionally, conventional PARPi therapy was proved to increase cell sensitization to UV irradiation [135] and positive feedback was reported when irradiation was combined with PARPi [94,204,212,233–235]. In this later condition, a synergistic lethal effect is generated, leading to cancer cell death [94,204,212,233–235]. Moreover, it was verified that even low-energy sources such as UVC light were capable of activating PARylation, due to intracellular DNA damage, and in turn PARP1 inhibition sensitized cells to UVC irradiation [236].

Some preclinical evidence came to reinforce the notion that PARPi provides tumor specific radio-sensitization in specific biological contexts, and currently some PARPi (e.g. Olaparib, Talazoparib, Rucaparib, Veliparib, Niraparib and Pamiparib) are in study in clinical trials while in combination with radiotherapy [235].

Taking into consideration all the data depicted, it is proved that the combination of PARPi + nano-system + irradiation therapeutic approaches (Figure 2.6) constitute an evolution and alternative to conventional cancer therapy.

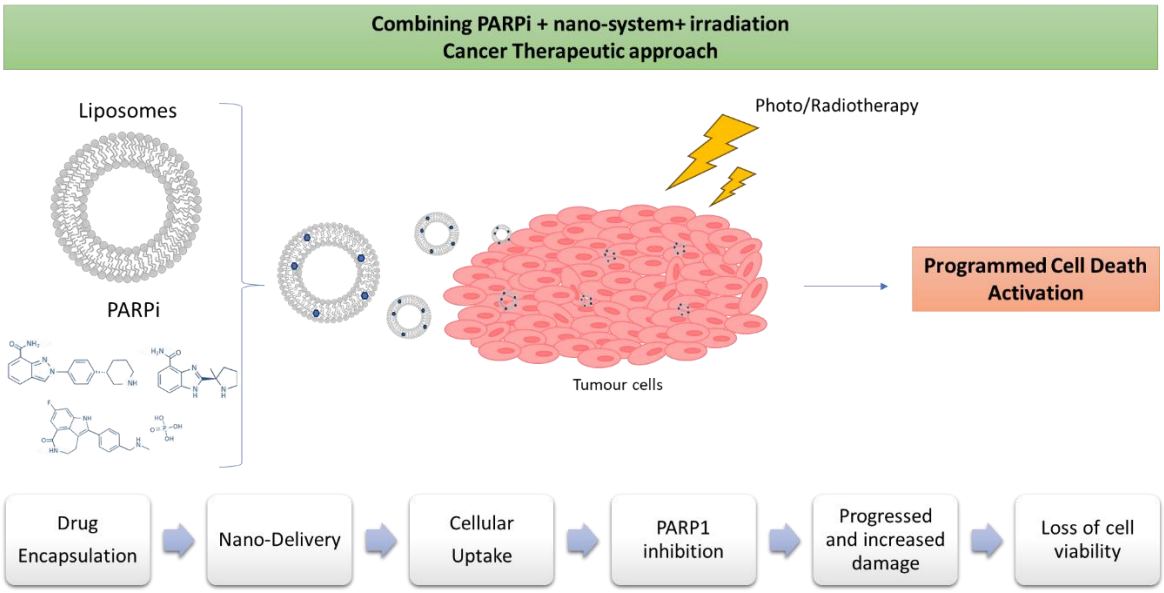

Figure 2.6 — Schematic representation of PARPi combination therapy with nano-system and irradiation in the treatment of tumor cells.

However, the development of nanomedicines is pointed to be faced with some challenges related to proper particle/formulation characterization, storage, manufacturing costs and consumer compliance [221]. Nevertheless, these issues could be overcome by the advancement of scientific methodologies and techniques used, as well as with the increase of the

fundamental knowledge related to molecular mechanisms and interactions [221]. In this way the strategies related to cancer treatment may evolve and possibly permit to stall, eradicate, and prevent cancer development and/or progression.

2.8 Conclusion and Future Perspectives

Poly (ADP-ribose) polymerase 1 (PARP1) is a 114 kDa multi-domain enzyme, that orchestrates vital biological processes such as inflammation, hypoxic response, transcriptional regulation, maintenance of chromosome stability, DNA repair, and cell death.

PARP1 presents multiple levels of intracellular regulation and any imbalance on its functions and biomolecular interactions may have profound consequences at the cellular level. Moreover, PARP1's function in intracellular signaling can be considered a double-edged-sword, since activated repair pathways may induce DNA damage in chronic inflammatory process.

Even though this protein has been implicated in several human pathologies, cancer is the disease where PARP1 has been shown to be involved at multiple stages. Thus, PARP1 has been considered a desirable target for cancer therapy. Several activity inhibitors were developed along the way and currently four are FDA-approved for clinical application. However, some drawbacks are associated to conventional PARPi treatment, such as therapeutic resistance, cytotoxic side-effects, and high clearance rates, among others. Consequently, combination therapy has emerged to circumvent PARPi therapy drawbacks and to increase the efficiency of PARPi-mediated therapy. The combination of nano-delivery systems and irradiation appears as a solution to span the applicability of PARPi, as well as conduct to the design of personalized treatments for cancer patients.

However, much is still needed to be done to better understand how these therapies may be formulated. Solutions are needed to solve problems related to proper particle/formulation characterization, storage, manufacturing costs and consumer compliance.

In the near future we believe that much will be uncovered regarding already known PARP1 biological functions and how this protein may be involved in the intersection of several intracellular pathways. These assessments will pass through the analysis of PARP1 interactors and regulators, as we have seen with HPF1. This will also lead to a better understanding of how to evolve in PARP1 targeted therapy. It will possibly pass through new chemotherapeutic combination approaches, such as with inhibitors of other proteins involved in the cell cycle, cell division, inflammatory processes, energy metabolism, among others. Every day new inhibitor

compounds are being designed and we believe that the next generation compounds may be targeting alternative PARP1 domains, besides CAT. Moreover, we hypothesize that the evolution of PARP1 cancer therapy will pass through the combination of PARPi + nano-systems + irradiation therapy. In this way nano-formulations, such as liposomes, may be designed to encapsulate PARPi with complementary chemotherapeutic compounds, and through liposome surface functionalization tumor target delivery may be achieved. Therefore, lower doses of irradiation therapy may be applied, thus reducing cytotoxic side-effects and increasing tumor elimination.

The next big steppingstone in PARP1 knowledge will be the determination of its complete structure by cryo-EM. Even though a putative molecular structure was determined with AI prediction software (Alphafold), several uncertainties are still to be verified. Through the structural determination of full-length PARP1, biological processes will be better understood, and newer and more specialized clinical compounds and therapies may be developed.

References

[1] N.E. Navin, J. Hicks, Tracing the tumor lineage, Mol. Oncol. 4 (2010) 267–283. https://doi.org/10.1016/j.molonc.2010.04.010.

[2] S. Bohunicky, B; Mousa, Biosensors: the new wave in cancer diagnosis, Nanotechnol. Sci. Appl. 4 (2010) 1–10. https://doi.org/10.2147/NSA.S13465.

[3] X. Meng, J. Zhong, S. Liu, M. Murray, A.M. Gonzalez-Angulo, A new hypothesis for the cancer mechanism, Cancer Metastasis Rev. 31 (2012) 247–268. https://doi.org/10.1007/s10555-011-9342-8.

[4] D. Hanahan, R.A. Weinberg, Hallmarks of cancer: The next generation, Cell. 144 (2011) 646–674. https://doi.org/10.1016/j.cell.2011.02.013.

[5] A.M. Sonnenschein, C; Soto, The aging of the 2000 and 2011 Hallarks of Cancer reviews: A critique, J. Biosci. 38 (2013) 651–663. https://doi.org/10.1007/s12038-013-9335-6.

[6] H.M. Shaw, M. Hall, Emerging treatment options for recurrent ovarian cancer: The potential role of olaparib, Onco. Targets. Ther. 6 (2013) 1197–1206. https://doi.org/10.2147/OTT.S30748.

[7] W. Zhang, D.C. van Gent, L. Incrocci, W.M. van Weerden, J. Nonnekens, Role of the DNA damage response in prostate cancer formation, progression and treatment, Prostate Cancer Prostatic Dis. 23 (2020) 24–37. https://doi.org/10.1038/s41391-019-0153-2.

[8] A.M. Buckley, N. Lynam-Lennon, H. O'Neill, J. O'Sullivan, Targeting hallmarks of cancer to enhance radiosensitivity in gastrointestinal cancers, Nat. Rev. Gastroenterol. Hepatol. 17 (2020) 298–313. https://doi.org/10.1038/s41575-019-0247-2.

[9] S. Vyas, M. Chesarone-Cataldo, T. Todorova, Y. Huang, P. Chang, A systematic analysis of the PARP protein family identifies new functions critical for cell physiology, Nat. Commun. 4 (2013) 1–13. https://doi.org/10.1038/ncomms3240.

[10] J.-C. Amé, C. Spenlehauer, G. de Murcia, The PARP superfamily, BioEssays. 26 (2004) 882–893. https://doi.org/10.1002/bies.20085.

[11] T. Jubin, A. Kadam, M. Jariwala, S. Bhatt, S. Sutariya, A.R. Gani, S. Gautam, R. Begum, The PARP family: insights into functional aspects of poly (ADP-ribose) polymerase-1 in cell growth and survival, Cell Prolif. 49 (2016) 421–437. https://doi.org/10.1111/cpr.12268.

[12] M.O. Hottiger, P.O. Hassa, B. Lüscher, H. Schüler, F. Koch-Nolte, Toward a unified nomenclature for mammalian ADP-ribosyltransferases, Trends Biochem. Sci. 35 (2010) 208–219. https://doi.org/10.1016/j.tibs.2009.12.003.

[13] G. Asher, H. Reinke, M. Altmeyer, M. Gutierrez-Arcelus, M.O. Hottiger, U. Schibler, Poly(ADP-Ribose) Polymerase 1 Participates in the Phase Entrainment of Circadian Clocks to Feeding, Cell. 142 (2010) 943–953. https://doi.org/10.1016/j.cell.2010.08.016.

[14] M. Mashimo, M. Kita, A. Nobeyama, A. Nomura, T. Fujii, PARP1 is activated by membrane damage and is involved in membrane repair through poly(ADP-ribosyl)ation, Genes to Cells. 27 (2022) 305–312. https://doi.org/10.1111/gtc.12926.

[15] F. Wang, M. Zhao, B. Chang, Y. Zhou, X. Wu, M. Ma, S. Liu, Y. Cao, M. Zheng, Y. Dang, J. Xu, L. Chen, T. Liu, F. Tang, Y. Ren, Z. Xu, Z. Mao, K. Huang, M. Luo, J. Li, H. Liu, B. Ge, Cytoplasmic PARP1 links the genome instability to the inhibition of antiviral immunity through PARylating cGAS, Mol. Cell. 82 (2022) 2032-2049.e7. https://doi.org/10.1016/j.molcel.2022.03.034.

[16] H. Fu, R. Liu, Z. Jia, R. Li, F. Zhu, W. Zhu, Y. Shao, Y. Jin, Y. Xue, J. Huang, K. Luo, X. Gao, H. Lu, Q. Zhou, Poly(ADP-ribosylation) of P-TEFb by PARP1 disrupts phase separation to

inhibit global transcription after DNA damage, Nat. Cell Biol. 24 (2022) 513–525. https://doi.org/10.1038/s41556-022-00872-5.

[17] S. Vyas, I. Matic, L. Uchima, J. Rood, R. Zaja, R.T. Hay, I. Ahel, P. Chang, Family-wide analysis of poly(ADP-ribose) polymerase activity, Nat. Commun. 5 (2014) 4426. https://doi.org/10.1038/ncomms5426.

[18] G.K. Herrmann, W.K. Russell, N.J. Garg, Y.W. Yin, Poly(ADP-ribose) polymerase 1 regulates mitochondrial DNA repair in an NAD-dependent manner, J. Biol. Chem. 296 (2021) 100309. https://doi.org/10.1016/J.JBC.2021.100309.

[19] T. Maruyama, K. Nara, H. Yoshikawa, N. Suzuki, Txk, a member of the non-receptor tyrosine kinase of the Tec family, forms a complex with poly(ADP-ribose) polymerase 1 and elongation factor 1 α and regulates interferon- γ gene transcription in Th1 cells, Clin. Exp. Immunol. 147 (2006) 164–175. https://doi.org/10.1111/j.1365-2249.2006.03249.x.

[20] J. Reinemund, K. Seidel, U.M. Steckelings, D. Zaade, S. Klare, F. Rompe, M. Katerbaum, J. Schacherl, Y. Li, M. Menk, J.H. Schefe, P. Goldin-Lang, C. Szabo, G. Olah, T. Unger, H. Funke-Kaiser, Poly(ADP-ribose) polymerase-1 (PARP-1) transcriptionally regulates angiotensin AT2 receptor (AT2R) and AT2R binding protein (ATBP) genes, Biochem. Pharmacol. 77 (2009) 1795–1805. https://doi.org/10.1016/j.bcp.2009.02.025.

[21] M.Y. Kim, S. Mauro, N. Gévry, J.T. Lis, W.L. Kraus, NAD+-Dependent Modulation of Chromatin Structure and Transcription by Nucleosome Binding Properties of PARP-1, Cell. 119 (2004) 803–814. https://doi.org/10.1016/j.cell.2004.11.002.

[22] B.A. Gibson, Y. Zhang, H. Jiang, K.M. Hussey, J.H. Shrimp, H. Lin, F. Schwede, Y. Yu, W.L. Kraus, Chemical genetic discovery of PARP targets reveals a role for PARP-1 in transcription elongation, Science (80-.). 353 (2016) 45–50. https://doi.org/10.1126/science.aaf7865.

[23] C. Kim, X.-D. Wang, Y. Yu, PARP1 inhibitors trigger innate immunity via PARP1 trapping-induced DNA damage response, Elife. 9 (2020). https://doi.org/10.7554/eLife.60637.

[24] S. Choudhuri, N.J. Garg, PARP1-cGAS-NF- κ B pathway of proinflammatory macrophage activation by extracellular vesicles released during Trypanosoma cruzi infection and Chagas disease, PLOS Pathog. 16 (2020) e1008474. https://doi.org/10.1371/journal.ppat.1008474.

[25] I. Talhaoui, N.A. Lebedeva, G. Zarkovic, C. Saint-Pierre, M.M. Kutuzov, M. V. Sukhanova, B.T. Matkarimov, D. Gasparutto, M.K. Saparbaev, O.I. Lavrik, A.A. Ishchenko, Poly(ADP-ribose) polymerases covalently modify strand break termini in DNA fragments in vitro, Nucleic Acids Res. (2016) gkw675. https://doi.org/10.1093/nar/gkw675.

[26] G. Zarkovic, E.A. Belousova, I. Talhaoui, C. Saint-Pierre, M.M. Kutuzov, B.T. Matkarimov, D. Biard, D. Gasparutto, O.I. Lavrik, A.A. Ishchenko, Characterization of DNA ADP-ribosyltransferase activities of PARP2 and PARP3: new insights into DNA ADP-ribosylation, Nucleic Acids Res. 46 (2018) 2417–2431. https://doi.org/10.1093/nar/gkx1318.

[27] I.A. Richard, J.T. Burgess, K.J. O'Byrne, E. Bolderson, Beyond PARP1: The Potential of Other Members of the Poly (ADP-Ribose) Polymerase Family in DNA Repair and Cancer Therapeutics, Front. Cell Dev. Biol. 9 (2022). https://doi.org/10.3389/fcell.2021.801200.

[28] M. Rouleau, D. McDonald, P. Gagné, M.-E. Ouellet, A. Droit, J.M. Hunter, S. Dutertre, C. Prigent, M.J. Hendzel, G.G. Poirier, PARP-3 associates with polycomb group bodies and with components of the DNA damage repair machinery, J. Cell. Biochem. 100 (2007) 385–401. https://doi.org/10.1002/jcb.21051.

[29] E.A. Belousova, A.A. Ishchenko, O.I. Lavrik, Dna is a New Target of Parp3, Sci. Rep. 8 (2018) 4176. https://doi.org/10.1038/s41598-018-22673-3.

[30] S. Smith, I. Giriat, A. Schmitt, T. de Lange, Tankyrase, a poly(ADP-ribose) polymerase at human telomeres., Science. 282 (1998) 1484–7. https://doi.org/10.1126/science.282.5393.1484.

[31] B.D. Cook, J.N. Dynek, W. Chang, G. Shostak, S. Smith, Role for the Related Poly(ADP-Ribose) Polymerases Tankyrase 1 and 2 at Human Telomeres, Mol. Cell. Biol. 22 (2002) 332–342. https://doi.org/10.1128/MCB.22.1.332-342.2002.

[32] J.I. Sbodio, H.F. Lodish, N.-W. Chi, Tankyrase-2 oligomerizes with tankyrase-1 and binds to both TRF1 (telomere-repeat-binding factor 1) and IRAP (insulin-responsive aminopeptidase), Biochem. J. 361 (2002) 451. https://doi.org/10.1042/0264-6021:3610451.

[33] S.-M.A. Huang, Y.M. Mishina, S. Liu, A. Cheung, F. Stegmeier, G.A. Michaud, O. Charlat, E. Wiellette, Y. Zhang, S. Wiessner, M. Hild, X. Shi, C.J. Wilson, C. Mickanin, V. Myer, A. Fazal, R. Tomlinson, F. Serluca, W. Shao, H. Cheng, M. Shultz, C. Rau, M. Schirle, J. Schlegl, S. Ghidelli, S. Fawell, C. Lu, D. Curtis, M.W. Kirschner, C. Lengauer, P.M. Finan, J.A. Tallarico, T. Bouwmeester, J.A. Porter, A. Bauer, F. Cong, Tankyrase inhibition stabilizes axin and

antagonizes Wnt signalling, Nature. 461 (2009) 614–620. https://doi.org/10.1038/nature08356.

[34] Y. Zhang, S. Liu, C. Mickanin, Y. Feng, O. Charlat, G.A. Michaud, M. Schirle, X. Shi, M. Hild, A. Bauer, V.E. Myer, P.M. Finan, J.A. Porter, S.-M.A. Huang, F. Cong, RNF146 is a poly(ADP-ribose)-directed E3 ligase that regulates axin degradation and Wnt signalling, Nat. Cell Biol. 13 (2011) 623–629. https://doi.org/10.1038/ncb2222.

[35] P.F. Cho-Park, H. Steller, Proteasome Regulation by ADP-Ribosylation, Cell. 153 (2013) 614–627. https://doi.org/10.1016/j.cell.2013.03.040.

[36] R.C.T. Aguiar, K. Takeyama, C. He, K. Kreinbrink, M.A. Shipp, B-aggressive Lymphoma Family Proteins Have Unique Domains That Modulate Transcription and Exhibit Poly(ADP-ribose) Polymerase Activity, J. Biol. Chem. 280 (2005) 33756–33765. https://doi.org/10.1074/jbc.M505408200.

[37] T. Karlberg, M. Klepsch, A.-G. Thorsell, C.D. Andersson, A. Linusson, H. Schüler, Structural Basis for Lack of ADP-ribosyltransferase Activity in Poly(ADP-ribose) Polymerase-13/Zinc Finger Antiviral Protein, J. Biol. Chem. 290 (2015) 7336–7344. https://doi.org/10.1074/jbc.M114.630160.

[38] W.L. Kraus, PARPs and ADP-Ribosylation: 50 Years … and Counting, Mol. Cell. 58 (2015) 902–910. https://doi.org/10.1016/j.molcel.2015.06.006.

[39] M.-F. Langelier, T. Eisemann, A.A. Riccio, J.M. Pascal, PARP family enzymes: regulation and catalysis of the poly(ADP-ribose) posttranslational modification, Curr. Opin. Struct. Biol. 53 (2018) 187–198. https://doi.org/10.1016/j.sbi.2018.11.002.

[40] M.A. Demény, L. Virág, The PARP Enzyme Family and the Hallmarks of Cancer Part 1. Cell Intrinsic Hallmarks, Cancers (Basel). 13 (2021) 2042. https://doi.org/10.3390/cancers13092042.

[41] C. V. Kuny, C.S. Sullivan, Virus–Host Interactions and the ARTD/PARP Family of Enzymes, PLOS Pathog. 12 (2016) e1005453. https://doi.org/10.1371/journal.ppat.1005453.

[42] A. Gomez, C. Bindesbøll, S. V. Satheesh, G. Grimaldi, D. Hutin, L. MacPherson, S. Ahmed, L. Tamblyn, T. Cho, H.I. Nebb, A. Moen, J.H. Anonsen, D.M. Grant, J. Matthews, Characterization of TCDD-inducible poly-ADP-ribose polymerase (TIPARP/ARTD14) catalytic activity, Biochem. J. 475 (2018) 3827–3846. https://doi.org/10.1042/BCJ20180347.

[43] I.A. Hendriks, S.C. Larsen, M.L. Nielsen, An Advanced Strategy for Comprehensive Profiling of ADP-ribosylation Sites Using Mass Spectrometry-based Proteomics*, Mol. Cell. Proteomics. 18 (2019) 1010–1026. https://doi.org/10.1074/mcp.TIR119.001315.

[44] S.C. Buch-Larsen, I.A. Hendriks, J.M. Lodge, M. Rykær, B. Furtwängler, E. Shishkova, M.S. Westphall, J.J. Coon, M.L. Nielsen, Mapping Physiological ADP-Ribosylation Using Activated Ion Electron Transfer Dissociation, Cell Rep. 32 (2020) 108176. https://doi.org/10.1016/j.celrep.2020.108176.

[45] M.J. Suskiewicz, L. Palazzo, R. Hughes, I. Ahel, Progress and outlook in studying the substrate specificities of PARPs and related enzymes, FEBS J. 288 (2021) 2131–2142. https://doi.org/10.1111/febs.15518.

[46] Y. Tang, Y.-L. Wang, L. Yang, J.-X. Xu, W. Xiong, M. Xiao, M. Li, Inhibition of arginine ADP-ribosyltransferase 1 reduces the expression of poly(ADP-ribose) polymerase-1 in colon carcinoma, Int. J. Mol. Med. 32 (2013) 130–136. https://doi.org/10.3892/ijmm.2013.1370.

[47] D.M. Leslie Pedrioli, M. Leutert, V. Bilan, K. Nowak, K. Gunasekera, E. Ferrari, R. Imhof, L. Malmström, M.O. Hottiger, Comprehensive ADP-ribosylome analysis identifies tyrosine as an ADP-ribose acceptor site, EMBO Rep. 19 (2018). https://doi.org/10.15252/embr.201745310.

[48] F. Yan, C. Huang, X. Wang, J. Tan, S. Cheng, M. Wan, Z. Wang, S. Wang, S. Luo, A. Li, X. Guo, M. Feng, X. Liu, Y. Zhu, Y. Zhou, Threonine ADP-Ribosylation of Ubiquitin by a Bacterial Effector Family Blocks Host Ubiquitination, Mol. Cell. 78 (2020) 641-652.e9. https://doi.org/10.1016/j.molcel.2020.03.016.

[49] J. O'Sullivan, M. Tedim Ferreira, J.-P. Gagné, A.K. Sharma, M.J. Hendzel, J.-Y. Masson, G.G. Poirier, Emerging roles of eraser enzymes in the dynamic control of protein ADP-ribosylation, Nat. Commun. 10 (2019) 1182. https://doi.org/10.1038/s41467-019-08859-x.

[50] M.O. Hottiger, SnapShot : ADP-Ribosylation Signaling SnapShot : ADP-Ribosylation Signaling, Mol. Cell. 58 (2015) 1134-1134.e1. https://doi.org/10.1016/j.molcel.2015.06.001.

[51] E. Barkauskaite, G. Jankevicius, A.G. Ladurner, I. Ahel, G. Timinszky, The recognition and removal of cellular poly(ADP-ribose) signals, FEBS J. 280 (2013) 3491–3507. https://doi.org/10.1111/febs.12358.

[52] F. Teloni, M. Altmeyer, Readers of poly(ADP-ribose): designed to be fit for purpose, Nucleic Acids Res. 44 (2016) 993–1006. https://doi.org/10.1093/nar/gkv1383.

[53] K. Crawford, J.J. Bonfiglio, A. Mikoč, I. Matic, I. Ahel, Specificity of reversible ADP-ribosylation and regulation of cellular processes, Crit. Rev. Biochem. Mol. Biol. 53 (2018) 64–82. https://doi.org/10.1080/10409238.2017.1394265.

[54] M.L. Meyer-Ficca, R.G. Meyer, D.L. Coyle, E.L. Jacobson, M.K. Jacobson, Human poly(ADP-ribose) glycohydrolase is expressed in alternative splice variants yielding isoforms that localize to different cell compartments, Exp. Cell Res. 297 (2004) 521–532. https://doi.org/10.1016/j.yexcr.2004.03.050.

[55] R.G. Meyer, M.L. Meyer-Ficca, C.J. Whatcott, E.L. Jacobson, M.K. Jacobson, Two small enzyme isoforms mediate mammalian mitochondrial poly(ADP-ribose) glycohydrolase (PARG) activity, Exp. Cell Res. 313 (2007) 2920–2936. https://doi.org/10.1016/j.yexcr.2007.03.043.

[56] G. Jankevicius, M. Hassler, B. Golia, V. Rybin, M. Zacharias, G. Timinszky, A.G. Ladurner, A family of macrodomain proteins reverses cellular mono-ADP-ribosylation, Nat. Struct. Mol. Biol. 20 (2013) 508–514. https://doi.org/10.1038/nsmb.2523.

[57] R. Žaja, G. Aydin, B.E. Lippok, R. Feederle, B. Lüscher, K.L.H. Feijs, Comparative analysis of MACROD1, MACROD2 and TARG1 expression, localisation and interactome, Sci. Rep. 10 (2020) 8286. https://doi.org/10.1038/s41598-020-64623-y.

[58] E. Prokhorova, T. Agnew, A.R. Wondisford, M. Tellier, N. Kaminski, D. Beijer, J. Holder, J. Groslambert, M.J. Suskiewicz, K. Zhu, J.M. Reber, S.C. Krassnig, L. Palazzo, S. Murphy, M.L. Nielsen, A. Mangerich, D. Ahel, J. Baets, R.J. O'Sullivan, I. Ahel, Unrestrained poly-ADP-ribosylation provides insights into chromatin regulation and human disease, Mol. Cell. 81 (2021) 2640-2655.e8. https://doi.org/10.1016/j.molcel.2021.04.028.

[59] M. Mashimo, J. Kato, J. Moss, Structure and function of the ARH family of ADP-ribosyl-acceptor hydrolases, DNA Repair (Amst). 23 (2014) 88–94. https://doi.org/10.1016/j.dnarep.2014.03.005.

[60] A.-L. Perraud, B. Shen, C.A. Dunn, K. Rippe, M.K. Smith, M.J. Bessman, B.L. Stoddard, A.M. Scharenberg, NUDT9, a Member of the Nudix Hydrolase Family, Is an Evolutionarily Conserved Mitochondrial ADP-ribose Pyrophosphatase, J. Biol. Chem. 278 (2003) 1794–1801. https://doi.org/10.1074/jbc.M205601200.

[61] B.A. Peculis, K. Reynolds, M. Cleland, Metal Determines Efficiency and Substrate Specificity of the Nuclear NUDIX Decapping Proteins X29 and H29K (Nudt16), J. Biol. Chem. 282 (2007) 24792–24805. https://doi.org/10.1074/jbc.M704179200.

[62] T. Iyama, N. Abolhassani, D. Tsuchimoto, M. Nonaka, Y. Nakabeppu, NUDT16 is a (deoxy)inosine diphosphatase, and its deficiency induces accumulation of single-strand breaks in nuclear DNA and growth arrest, Nucleic Acids Res. 38 (2010) 4834–4843. https://doi.org/10.1093/nar/gkq249.

[63] G. Lu, J. Zhang, Y. Li, Z. Li, N. Zhang, X. Xu, T. Wang, Z. Guan, G.F. Gao, J. Yan, hNUDT16: a universal decapping enzyme for small nucleolar RNA and cytoplasmic mRNA, Protein Cell. 2 (2011) 64–73. https://doi.org/10.1007/s13238-011-1009-2.

[64] S.I. Belli, J.W. Goding, Biochemical Characterization of Human PC-1, an Enzyme Possessing Alkaline Phosphodiesterase I and Nucleotide Pyrophosphatase Activities, Eur. J. Biochem. 226 (1994) 433–443. https://doi.org/10.1111/j.1432-1033.1994.tb20068.x.

[65] Y. Yano, Y. Hayashi, K. Sano, H. Nagano, M. Nakaji, Y. Seo, T. Ninomiya, S. Yoon, H. Yokozaki, M. Kasuga, Expression and localization of ecto-nucleotide pyrophosphatase/phosphodiesterase I-1 (E-NPP1/PC-1) and -3 (E-NPP3/CD203c/PD-I β /B10/gp130RB13-6) in inflammatory and neoplastic bile duct diseases, Cancer Lett. 207 (2004) 139–147. https://doi.org/10.1016/j.canlet.2003.11.002.

[66] L. Palazzo, C.M. Daniels, J.E. Nettleship, N. Rahman, R.L. McPherson, S. Ong, K. Kato, O. Nureki, A.K.L. Leung, I. Ahel, ENPP1 processes protein ADP-ribosylation in vitro, FEBS J. 283 (2016) 3371–3388. https://doi.org/10.1111/febs.13811.

[67] P. Chambon, J.D. Weill, P. Mandel, Nicotinamide mononucleotide activation of a new DNA-dependent polyadenylic acid synthesizing nuclear enzyme, Biochem. Biophys. Res. Commun. 11 (1963) 39–43. https://doi.org/10.1016/0006-291X(63)90024-X.

[68] P. Chambon, J.D. Weill, J. Doly, M.T. Strosser, P. Mandel, On the formation of a novel adenylic compound by enzymatic extracts of liver nuclei, Biochem. Biophys. Res. Commun. 25 (1966) 638–643. https://doi.org/10.1016/0006-291X(66)90502-X.

[69] L. van Beek, É. McClay, S. Patel, M. Schimpl, L. Spagnolo, T. Maia de Oliveira, Parp power: A structural perspective on parp1, parp2, and parp3 in dna damage repair and nucleosome remodelling, Int. J. Mol. Sci. 22 (2021) 1–23. https://doi.org/10.3390/ijms22105112.

[70] M.F. Langelier, L. Zandarashvili, P.M. Aguiar, B.E. Black, J.M. Pascal, NAD+ analog reveals PARP-1 substrate-blocking mechanism and allosteric communication from catalytic center to DNA-binding domains, Nat. Commun. 9 (2018). https://doi.org/10.1038/s41467-018-03234-8.

[71] J.D. Steffen, M.M. McCauley, J.M. Pascal, Fluorescent sensors of PARP-1 structural dynamics and allosteric regulation in response to DNA damage, Nucleic Acids Res. 44 (2016) 9771–9783. https://doi.org/10.1093/nar/gkw710.

[72] J.M. Dawicki-McKenna, M.F. Langelier, J.E. DeNizio, A.A. Riccio, C.D. Cao, K.R. Karch, M. McCauley, J.D. Steffen, B.E. Black, J.M. Pascal, PARP-1 Activation Requires Local Unfolding of an Autoinhibitory Domain, Mol. Cell. 60 (2015) 755–768. https://doi.org/10.1016/j.molcel.2015.10.013.

[73] M.F. Langelier, J.L. Planck, S. Roy, J.M. Pascal, Structural Basis for DNA Damage–Dependent Poly(ADP-ribosyl)ation by Human PARP-1, Science (80-.). 336 (2012) 728–732. https://doi.org/10.1126/science.1216338.

[74] J.M. Dawicki-Mckenna, M. Langelier, J.E. Denizio, A. Riccio, C.D. Cao, K.R. Karch, M. Mccauley, J.D. Steffen, E. Ben, J.M. Pascal, PARP-1 activation requires local unfolding of an autoinhibitory domain, Mol. Cell. 60 (2015) 755–768. https://doi.org/10.1016/j.molcel.2015.10.013.PARP-1.

[75] A.A. Riccio, G. Cingolani, J.M. Pascal, PARP-2 domain requirements for DNA damage-dependent activation and localization to sites of DNA damage, Nucleic Acids Res. 44 (2015) 1691–1702. https://doi.org/10.1093/nar/gkv1376.

[76] M.F. Langelier, A.A. Riccio, J.M. Pascal, PARP-2 and PARP-3 are selectively activated by 5′ phosphorylated DNA breaks through an allosteric regulatory mechanism shared with PARP-1, Nucleic Acids Res. 42 (2014) 7762–7775. https://doi.org/10.1093/nar/gku474.

[77] G.J. Grundy, L.M. Polo, Z. Zeng, S.L. Rulten, N.C. Hoch, P. Paomephan, Y. Xu, S.M. Sweet, A.W. Thorne, A.W. Oliver, S.J. Matthews, L.H. Pearl, K.W. Caldecott, PARP3 is a sensor of nicked nucleosomes and monoribosylates histone H2B(Glu2), Nat. Commun. 7 (2016) 12404. https://doi.org/10.1038/ncomms12404.

[78] E. Obaji, T. Haikarainen, L. Lehti, H. Artd, Structural basis for DNA break recognition by ARDT2/PARP2, Nucleic Acids Res. 46 (2018) 12154–12165. https://doi.org/10.1093/nar/gky927.

[79] E. Pion, G.M. Ullmann, J.C. Amé, D. Gérard, G. De Murcia, E. Bombarda, DNA-induced dimerization of poly(ADP-ribose) polymerase-1 triggers its activation, Biochemistry. 44 (2005) 14670–14681. https://doi.org/10.1021/bi050755o.

[80] S. Eustermann, H. Videler, J.C. Yang, P.T. Cole, D. Gruszka, D. Veprintsev, D. Neuhaus, The DNA-binding domain of human PARP-1 interacts with DNA single-strand breaks as a monomer through its second zinc finger, J. Mol. Biol. 407 (2011) 149–170. https://doi.org/10.1016/j.jmb.2011.01.034.

[81] A.D. Edwards, K.D. Raney, J.C. Marecki, A.K. Byrd, G-Quadruplex loops regulate PARP-1 enzymatic activation, 49 (2021) 416–431. https://doi.org/10.1093/nar/gkaa1172.

[82] S.J. Baptista, M.M.C. Silva, E. Moroni, M. Meli, G. Colombo, T.C.P. Dinis, J.A.R. Salvador, Novel PARP-1 Inhibitor scaffolds disclosed by a dynamic structure-based pharmacophore approach, PLoS One. 12 (2017) 1–20. https://doi.org/10.1371/journal.pone.0170846.

[83] M.-C. Caron, A.K. Sharma, J. O'Sullivan, L.R. Myler, M.T. Ferreira, A. Rodrigue, Y. Coulombe, C. Ethier, J.-P. Gagné, M.-F. Langelier, J.M. Pascal, I.J. Finkelstein, M.J. Hendzel, G.G. Poirier, J.-Y. Masson, Poly(ADP-ribose) polymerase-1 antagonizes DNA resection at double-strand breaks., Nat. Commun. 10 (2019) 2954. https://doi.org/10.1038/s41467-019-10741-9.

[84] M.J. Suskiewicz, D. Munnur, Ø. Strømland, J.-C. Yang, L.E. Easton, C. Chatrin, K. Zhu, D. Baretić, S. Goffinont, M. Schuller, W.-F. Wu, J.M. Elkins, D. Ahel, S. Sanyal, D. Neuhaus, I. Ahel, Updated protein domain annotation of the PARP protein family sheds new light on biological function, Nucleic Acids Res. (2023). https://doi.org/10.1093/nar/gkad514.

[85] J.D. Steffen, R.M. Tholey, M. Langelier, J.L. Planck, J. Schiewer, S. Lal, N.A. Bildzukewicz, C.J. Yeo, K.E. Knudsen, J.R. Brody, J.M. Pascal, Targeting PARP-1 allosteric regulation offers therapeutic potential against cancer, Cancer Res. 74 (2015) 31–37. https://doi.org/10.1158/0008-5472.CAN-13-1701.

[86] D. V. Ferraris, Evolution of Poly(ADP-ribose) Polymerase-1 (PARP-1) Inhibitors. From Concept to Clinic, J. Med. Chem. 53 (2010) 4561–4584. https://doi.org/10.1021/jm100012m.

[87] R.J. Henning, M. Bourgeois, R.D. Harbison, Poly(ADP-ribose) Polymerase (PARP) and PARP Inhibitors: Mechanisms of Action and Role in Cardiovascular Disorders, Cardiovasc. Toxicol. 18 (2018) 493–506. https://doi.org/10.1007/s12012-018-9462-2.

[88] C.M. Daniels, S.-E. Ong, A.K.L. Leung, The Promise of Proteomics for the Study of ADP-Ribosylation, Mol. Cell. 58 (2015) 911–924. https://doi.org/10.1016/j.molcel.2015.06.012.

[89] J.J. Bonfiglio, P. Fontana, Q. Zhang, T. Colby, I. Gibbs-Seymour, I. Atanassov, E. Bartlett, R. Zaja, I. Ahel, I. Matic, Serine ADP-Ribosylation Depends on HPF1, Mol. Cell. 65 (2017) 932-940.e6. https://doi.org/10.1016/j.molcel.2017.01.003.

[90] L. Palazzo, M.J. Suskiewicz, I. Ahel, Serine ADP-ribosylation in DNA-damage response regulation, Curr. Opin. Genet. Dev. 71 (2021) 106–113. https://doi.org/10.1016/j.gde.2021.07.005.

[91] N. Schultz, E. Lopez, N. Saleh-Gohari, T. Helleday, Poly(ADP-ribose) polymerase (PARP-1) has a controlling role in homologous recombination, Nucleic Acids Res. 31 (2003) 4959–4964. https://doi.org/10.1093/nar/gkg703.

[92] B.C. Woodhouse, I.I. Dianova, J.L. Parsons, G.L. Dianov, Poly (ADP-ribose) polymerase-1 modulates DNA repair capacity and prevents formation of DNA double strand breaks, DNA Repair (Amst). 7 (2008) 932–940. https://doi.org/10.1016/j.dnarep.2008.03.017.

[93] B.C. Woodhouse, G.L. Dianov, Poly ADP-ribose polymerase-1 : An international molecule of mystery, DNA Repair (Amst). 7 (2008) 1077–1086. https://doi.org/10.1016/j.dnarep.2008.03.009.

[94] B. Carney, S. Kossatz, T. Reiner, Molecular imaging of PARP, J. Nucl. Med. 58 (2017) 1025–1030. https://doi.org/10.2967/jnumed.117.189936.

[95] H. Thorsell, A; Ekblad, T; Karlberg, T; Low, M; Pinto, AF; Trésaugues, L; Moche, M; Cohen, MS; Schuler, Structural Basis for Potency and Promiscuity in Poly(ADP-ribose) Polymerase (PARP) and Tankyrase Inhibitors, J. Med. Chem. 60 (2017) 1262–1271. https://doi.org/10.1021/acs.jmedchem.6b00990.

[96] T.E.H. Ogden, J.-C. Yang, M. Schimpl, L.E. Easton, E. Underwood, P.B. Rawlins, M.M. McCauley, M.-F. Langelier, J.M. Pascal, K.J. Embrey, D. Neuhaus, Dynamics of the HD regulatory subdomain of PARP-1; substrate access and allostery in PARP activation and inhibition, Nucleic Acids Res. 49 (2021) 2266–2288. https://doi.org/10.1093/nar/gkab020.

[97] K. Ryan, B. Bolaños, M. Smith, P.B. Palde, P.D. Cuenca, T.L. VanArsdale, S. Niessen, L. Zhang, D. Behenna, M.A. Ornelas, K.T. Tran, S. Kaiser, L. Lum, A. Stewart, K.S. Gajiwala, Dissecting the molecular determinants of clinical PARP1 inhibitor selectivity for tankyrase, J. Biol. Chem. 296 (2021) 1–13. https://doi.org/10.1074/JBC.RA120.016573.

[98] L. Zandarashvili, M. Langelier, U.K. Velagapudi, A. Mark, J.D. Steffen, R. Billur, Z.M. Hannan, A.J. Wicks, B. Krastev, S.J. Pettitt, C.J. Lord, T.T. Talele, J.M. Pascal, B.E. Black, Structural basis for allosteric PARP-1 retention on DNA breaks, Science (80-.). 368 (2020) 1–24. https://doi.org/10.1126/science.aax6367.Structural.

[99] L. Fu, S. Wang, X. Wang, P. Wang, Y. Zheng, D. Yao, M. Guo, L. Zhang, L. Ouyang, Crystal structure-based discovery of a novel synthesized PARP1 inhibitor (OL-1) with apoptosis-inducing mechanisms in triple-negative breast cancer, Sci. Rep. 6 (2016) 1–14. https://doi.org/10.1038/s41598-016-0007-2.

[100] X. Chen, X. Huan, Q. Liu, Y. Wang, Q. He, C. Tan, Y. Chen, J. Ding, Y. Xu, Z. Miao, C. Yang, Design and synthesis of 2-(4,5,6,7-tetrahydrothienopyridin-2-yl)-benzoimidazole carboxamides as novel orally efficacious Poly(ADP-ribose)polymerase (PARP) inhibitors, Eur. J. Med. Chem. 145 (2018) 389–403. https://doi.org/10.1016/j.ejmech.2018.01.018.

[101] A. Ruf, G. De Murcia, G.E. Schulz, Inhibitor and NAD+ binding to poly(ADP-ribose) polymerase as derived from crystal structures and homology modeling, Biochemistry. 37 (1998) 3893–3900. https://doi.org/10.1021/bi972383s.

[102] T.D. Penning, G.D. Zhu, J. Gong, S. Thomas, V.B. Gandhi, X. Liu, Y. Shi, V. Klinghofer, E.F. Johnson, C.H. Park, E.H. Fry, C.K. Donawho, D.J. Frost, F.G. Buchanan, G.T. Bukofzer, L.E. Rodriguez, V. Bontcheva-Diaz, J.J. Bouska, D.J. Osterling, A.M. Olson, K.C. Marsh, Y. Luo, V.L. Giranda, Optimization of phenyl-substituted benzimidazole carboxamide poly(ADP-ribose) polymerase inhibitors: Identification of (S)-2-(2-fluoro-4- (pyrrolidin-2-yl)phenyl)-1 H -benzimidazole-4-carboxamide (A-966492), a highly potent and efficacious inhibitor, J. Med. Chem. 53 (2010) 3142–3153. https://doi.org/10.1021/jm901775y.

[103] K. Hattori, Y. Kido, H. Yamamoto, J. Ishida, K. Kamijo, K. Murano, M. Ohkubo, T. Kinoshita, A. Iwashita, K. Mihara, S. Yamazaki, N. Matsuoka, Y. Teramura, H. Miyake, Rational approaches to discovery of orally active and brain-penetrable quinazolinone inhibitors of poly(ADP-ribose)polymerase, J. Med. Chem. 47 (2004) 4151–4154. https://doi.org/10.1021/jm0499256.

[104] T. Kinoshita, I. Nakanishi, M. Warizaya, A. Iwashita, Y. Kido, K. Hattori, T. Fujii, Inhibitor-induced structural change of the active site of human poly(ADP-ribose) polymerase, FEBS Lett. 556 (2004) 43–46. https://doi.org/10.1016/S0014-5793(03)01362-0.

[105] A. Iwashita, K. Hattori, H. Yamamoto, J. Ishida, Y. Kido, K. Kamijo, K. Murano, H. Miyake, T. Kinoshita, M. Warizaya, M. Ohkubo, N. Matsuoka, S. Mutoh, Discovery of quinazolinone

and quinoxaline derivatives as potent and selective poly(ADP-ribose) polymerase-1/2 inhibitors, FEBS Lett. 579 (2005) 1389–1393. https://doi.org/10.1016/j.febslet.2005.01.036.

[106] A.R. Gangloff, J. Brown, R. De Jong, D.R. Dougan, C.E. Grimshaw, M. Hixon, A. Jennings, R. Kamran, A. Kiryanov, S. O'Connell, E. Taylor, P. Vu, Discovery of novel benzo[b][1,4]oxazin-3(4H)-ones as poly(ADP-ribose) polymerase inhibitors, Bioorganic Med. Chem. Lett. 23 (2013) 4501–4505. https://doi.org/10.1016/j.bmcl.2013.06.055.

[107] N. Ye, C.H. Chen, T. Chen, Z. Song, J.X. He, X.J. Huan, S.S. Song, Q. Liu, Y. Chen, J. Ding, Y. Xu, Z.H. Miao, A. Zhang, Design, synthesis, and biological evaluation of a series of benzo[de][1,7]naphthyridin-7(8 H)-ones bearing a functionalized longer chain appendage as novel PARP1 inhibitors, J. Med. Chem. 56 (2013) 2885–2903. https://doi.org/10.1021/jm301825t.

[108] S. Tomassi, J. Pfahler, N. Mautone, A. Rovere, C. Esposito, D. Passeri, R. Pellicciari, E. Novellino, M. Pannek, C. Steegborn, A. Paiardini, A. Mai, D. Rotili, From PARP1 to TNKS2 inhibition: A structure-based approach, ACS Med. Chem. Lett. 11 (2020) 862–868. https://doi.org/10.1021/acsmedchemlett.9b00654.

[109] G. Papeo, H. Posteri, D. Borghi, A.A. Busel, F. Caprera, E. Casale, M. Ciomei, A. Cirla, E. Corti, M. D'Anello, M. Fasolini, B. Forte, A. Galvani, A. Isacchi, A. Khvat, M.Y. Krasavin, R. Lupi, P. Orsini, R. Perego, E. Pesenti, D. Pezzetta, S. Rainoldi, F. Riccardi-Sirtori, A. Scolaro, F. Sola, F. Zuccotto, E.R. Felder, D. Donati, A. Montagnoli, Discovery of 2-[1-(4,4-Difluorocyclohexyl)piperidin-4-yl]-6-fluoro-3-oxo-2,3-dihydro-1H-isoindole-4-carboxamide (NMS-P118): A Potent, Orally Available, and Highly Selective PARP-1 Inhibitor for Cancer Therapy, J. Med. Chem. 58 (2015) 6875–6898. https://doi.org/10.1021/acs.jmedchem.5b00680.

[110] G. Papeo, P. Orsini, N.R. Avanzi, D. Borghi, E. Casale, M. Ciomei, A. Cirla, V. Desperati, D. Donati, E.R. Felder, A. Galvani, M. Guanci, A. Isacchi, H. Posteri, S. Rainoldi, F. Riccardi-Sirtori, A. Scolaro, A. Montagnoli, Discovery of Stereospecific PARP-1 Inhibitor Isoindolinone NMS-P515, ACS Med. Chem. Lett. 10 (2019) 534–538. https://doi.org/10.1021/acsmedchemlett.8b00569.

[111] H. Wang, B. Ren, Y. Liu, B. Jiang, Y. Guo, M. Wei, L. Luo, X. Kuang, M. Qiu, L. Lv, H. Xu, R. Qi, H. Yan, D. Xu, Z. Wang, C.-X. Huo, Y. Zhu, Y. Zhao, Y. Wu, Z. Qin, D. Su, T. Tang, F. Wang, X. Sun, Y. Feng, H. Peng, X. Wang, Y. Gao, Y. Liu, W. Gong, F. Yu, X. Liu, L. Wang, C. Zhou, Discovery of Pamiparib (BGB-290), a Potent and Selective Poly (ADP-ribose)

Polymerase (PARP) Inhibitor in Clinical Development, J. Med. Chem. 63 (2020) 15541–15563. https://doi.org/10.1021/acs.jmedchem.0c01346.

[112] M. Aoyagi-Scharber, A.S. Gardberg, B.K. Yip, B. Wang, Y. Shen, P.A. Fitzpatrick, Structural basis for the inhibition of poly(ADP-ribose) polymerases 1 and 2 by BMN 673, a potent inhibitor derived from dihydropyridophthalazinone, Acta Crystallogr. Sect. Struct. Biol. Commun. 70 (2014) 1143–1149. https://doi.org/10.1107/S2053230X14015088.

[113] A.E.G. Lindgren, T. Karlberg, A.G. Thorsell, M. Hesse, S. Spjut, T. Ekblad, C.D. Andersson, A.F. Pinto, J. Weigelt, M.O. Hottiger, A. Linusson, M. Elofsson, H. Schüler, PARP inhibitor with selectivity toward ADP-ribosyltransferase ARTD3/PARP3, ACS Chem. Biol. 8 (2013) 1698–1703. https://doi.org/10.1021/cb4002014.

[114] U.K. Velagapudi, M. Langelier, C. Delgado-martin, E. Morgan, S. Bakker, A. Ashworth, B.A. Patel, X. Shao, M. John, T.T. Talele, H. Sciences, U. States, H. Diller, F. Comprehensive, U. States, S. Francisco, U. States, Design and Synthesis of Poly(ADP-ribose) polymerase Inhibitors: Impact of Adenosine Pocket-Binding Motif Appendage to the 3-Oxo-2,3-dihydrobenzofuran-7-carboxamide on Potency and Selectivity, J. Med. Chem. 62 (2019) 5330–5357. https://doi.org/10.1021/acs.jmedchem.8b01709.Design.

[115] M.F. Langelier, J.L. Planck, S. Roy, J.M. Pascal, Crystal structures of poly(ADP-ribose) polymerase-1 (PARP-1) zinc fingers bound to DNA: Structural and functional insights into DNA-dependent PARP-1 activity, J. Biol. Chem. 286 (2011) 10690–10701. https://doi.org/10.1074/jbc.M110.202507.

[116] A.A.E. Ali, G. Timinszky, R. Arribas-bosacoma, M. Kozlowski, P.O. Hassa, M. Hassler, A.G. Ladurner, L.H. Pearl, A.W. Oliver, The zinc-finger domains of PARP1 cooperate to recognise DNA strand-breaks, Nat. Struct. Mol. Biol. 19 (2012) 685–692. https://doi.org/10.1038/nsmb.2335.The.

[117] M.R. Patel, A. Bhatt, J.D. Steffen, A. Chergui, J. Murai, Y. Pommier, J.M. Pascal, L.D. Trombetta, F.R. Fronczek, T.T. Talele, Discovery and Structure–Activity Relationship of Novel 2,3-Dihydrobenzofuran-7-carboxamide and 2,3-Dihydrobenzofuran-3(2 H)-one-7-carboxamide Derivatives as Poly(ADP-ribose)polymerase-1 Inhibitors, J. Med. Chem. 57 (2014) 5579–5601. https://doi.org/10.1021/jm5002502.

[118] S. Xie, O. Mortusewicz, H.T. Ma, P. Herr, R.R.Y. Poon, T. Helleday, C. Qian, Timeless Interacts with PARP-1 to Promote Homologous Recombination Repair, Mol. Cell. 60 (2015) 163–176. https://doi.org/10.1016/j.molcel.2015.07.031.

[119] F.H. Sun, P. Zhao, N. Zhang, L.L. Kong, C.C.L. Wong, C.H. Yun, HPF1 remodels the active site of PARP1 to enable the serine ADP-ribosylation of histones, Nat. Commun. 12 (2021) 1–10. https://doi.org/10.1038/s41467-021-21302-4.

[120] M.F. Langelier, K.M. Servent, E.E. Rogers, J.M. Pascal, A third zinc-binding domain of human poly(ADP-ribose) polymerase-1 coordinates DNA-dependent enzyme activation, J. Biol. Chem. 283 (2008) 4105–4114. https://doi.org/10.1074/jbc.M708558200.

[121] P.A. Loeffler, M.J. Cuneo, G.A. Mueller, E.F. Derose, S.A. Gabel, R.E. London, Structural studies of the PARP-1 BRCT domain, BMC Struct. Biol. 11 (2011) 37. https://doi.org/10.1186/1472-6807-11-37.

[122] T. Karlberg, M. Hammarstrom, P. Schutz, L. Svensson, H. Schuler, Crystal Structure of the Catalytic Domain of Human PARP2 in Complex with PARP Inhibitor ABT-888, Biochemistry. 49 (2010) 1056–1058. https://doi.org/10.1021/bi902079y.

[123] L. Lehtiö, A.-S. Jemth, R. Collins, O. Loseva, A. Johansson, N. Markova, M. Hammarström, A. Flores, L. Holmberg-Schiavone, J. Weigelt, T. Helleday, H. Schüler, T. Karlberg, Structural Basis for Inhibitor Specificity in Human Poly(ADP-ribose) Polymerase-3, J. Med. Chem. 52 (2009) 3108–3111. https://doi.org/10.1021/jm900052j.

[124] S. Eustermann, W.-F. Wu, M.-F. Langelier, J.-C. Yang, L.E. Easton, A.A. Riccio, J.M. Pascal, D. Neuhaus, Structural Basis of Detection and Signaling of DNA Single-Strand Breaks by Human PARP-1, Mol. Cell. 60 (2015) 742–754. https://doi.org/10.1016/j.molcel.2015.10.032.

[125] K. Kouyama, K. Mayanagi, S. Nakae, Y. Nishi, M. Miwa, T. Shirai, Single-particle analysis of full-length human poly(ADP-ribose) polymerase 1, Biophys. Physicobiology. 16 (2019) 59–67. https://doi.org/10.2142/biophysico.16.0_59.

[126] S. Bilokapic, M.J. Suskiewicz, I. Ahel, M. Halic, Bridging of DNA breaks activates PARP2–HPF1 to modify chromatin, Nature. 585 (2020) 609–613. https://doi.org/10.1038/s41586-020-2725-7.

[127] J. Jumper, R. Evans, A. Pritzel, T. Green, M. Figurnov, O. Ronneberger, K. Tunyasuvunakool, R. Bates, A. Žídek, A. Potapenko, A. Bridgland, C. Meyer, S.A.A. Kohl, A.J. Ballard, A. Cowie, B. Romera-Paredes, S. Nikolov, R. Jain, J. Adler, T. Back, S. Petersen, D. Reiman, E. Clancy, M. Zielinski, M. Steinegger, M. Pacholska, T. Berghammer, S. Bodenstein, D. Silver, O. Vinyals, A.W. Senior, K. Kavukcuoglu, P. Kohli, D. Hassabis, Highly accurate protein

structure prediction with AlphaFold, Nature. 596 (2021) 583–589. https://doi.org/10.1038/s41586-021-03819-2.

[128] M. Baek, F. DiMaio, I. Anishchenko, J. Dauparas, S. Ovchinnikov, G.R. Lee, J. Wang, Q. Cong, L.N. Kinch, R.D. Schaeffer, C. Millán, H. Park, C. Adams, C.R. Glassman, A. DeGiovanni, J.H. Pereira, A. V. Rodrigues, A.A. van Dijk, A.C. Ebrecht, D.J. Opperman, T. Sagmeister, C. Buhlheller, T. Pavkov-Keller, M.K. Rathinaswamy, U. Dalwadi, C.K. Yip, J.E. Burke, K.C. Garcia, N. V. Grishin, P.D. Adams, R.J. Read, D. Baker, Accurate prediction of protein structures and interactions using a three-track neural network, Science (80-.). 373 (2021) 871–876. https://doi.org/10.1126/science.abj8754.

[129] N. Bouatta, P. Sorger, M. AlQuraishi, Protein structure prediction by AlphaFold 2: are attention and symmetries all you need?, Acta Crystallogr. Sect. D Struct. Biol. 77 (2021) 982–991. https://doi.org/10.1107/S2059798321007531.

[130] M. Varadi, S. Anyango, M. Deshpande, S. Nair, C. Natassia, G. Yordanova, D. Yuan, O. Stroe, G. Wood, A. Laydon, A. Žídek, T. Green, K. Tunyasuvunakool, S. Petersen, J. Jumper, E. Clancy, R. Green, A. Vora, M. Lutfi, M. Figurnov, A. Cowie, N. Hobbs, P. Kohli, G. Kleywegt, E. Birney, D. Hassabis, S. Velankar, AlphaFold Protein Structure Database: massively expanding the structural coverage of protein-sequence space with high-accuracy models, Nucleic Acids Res. 50 (2022) D439–D444. https://doi.org/10.1093/nar/gkab1061.

[131] L.L.. Schrodinger, The Pymol Molecular Graphics System, version 2.0, (2017).

[132] H.L. Ko, E.C. Ren, Functional Aspects of PARP1 in DNA Repair and Transcription, Biomolecules. 2 (2012) 524–548. https://doi.org/10.3390/biom2040524.

[133] A. Swindall, J. Stanley, E. Yang, PARP-1: Friend or Foe of DNA Damage and Repair in Tumorigenesis?, Cancers (Basel). 5 (2013) 943–958. https://doi.org/10.3390/cancers5030943.

[134] D.W. Koh, A.M. Lawler, M.F. Poitras, M. Sasaki, S. Wattler, M.C. Nehls, T. Stöger, G.G. Poirier, V.L. Dawson, T.M. Dawson, Failure to degrade poly(ADP-ribose) causes increased sensitivity to cytotoxicity and early embryonic lethality, Proc. Natl. Acad. Sci. 101 (2004) 17699–17704. https://doi.org/10.1073/pnas.0406182101.

[135] N. V Malyuchenko, E.Y. Kotova, O.I. Kulaeva, M.P. Kirpichnikov, V.M. Studitskiy, PARP1 Inhibitors: antitumor drug design., Acta Naturae. 7 (2015) 27–37. http://www.ncbi.nlm.nih.gov/pubmed/26483957.

[136] J. Mateo, C.J. Lord, V. Serra, A. Tutt, J. Balmaña, M. Castroviejo-Bermejo, C. Cruz, A. Oaknin, S.B. Kaye, J.S. de Bono, A decade of clinical development of PARP inhibitors in perspective, Ann. Oncol. 30 (2019) 1437–1447. https://doi.org/10.1093/annonc/mdz192.

[137] P. Santofimia-Castaño, C. Huang, X. Liu, Y. Xia, S. Audebert, L. Camoin, L. Peng, G. Lomberk, R. Urrutia, P. Soubeyran, J.L. Neira, J. Iovanna, NUPR1 protects against hyperPARylation-dependent cell death, Commun. Biol. 5 (2022) 732. https://doi.org/10.1038/s42003-022-03705-1.

[138] H.-L. Ko, E.-C. Ren, Novel poly (ADP-ribose) polymerase 1 binding motif in hepatitis B virus core promoter impairs DNA damage repair, Hepatology. 54 (2011) 1190–1198. https://doi.org/10.1002/hep.24502.

[139] D.-S. Kim, C. V. Camacho, A. Nagari, V.S. Malladi, S. Challa, W.L. Kraus, Activation of PARP-1 by snoRNAs Controls Ribosome Biogenesis and Cell Growth via the RNA Helicase DDX21, Mol. Cell. 75 (2019) 1270-1285.e14. https://doi.org/10.1016/j.molcel.2019.06.020.

[140] C. Han, L.-Y. Sun, X.-Q. Luo, Q. Pan, Y.-M. Sun, Z.-C. Zeng, T.-Q. Chen, W. Huang, K. Fang, W.-T. Wang, Y.-Q. Chen, Chromatin-associated orphan snoRNA regulates DNA damage-mediated differentiation via a non-canonical complex, Cell Rep. 38 (2022) 110421. https://doi.org/10.1016/j.celrep.2022.110421.

[141] F. Berger, C. Lau, M. Ziegler, Regulation of poly(ADP-ribose) polymerase 1 activity by the phosphorylation state of the nuclear NAD biosynthetic enzyme NMN adenylyl transferase 1, Proc. Natl. Acad. Sci. 104 (2007) 3765–3770. https://doi.org/10.1073/pnas.0609211104.

[142] R. Midorikawa, Y. Takei, N. Hirokawa, KIF4 Motor Regulates Activity-Dependent Neuronal Survival by Suppressing PARP-1 Enzymatic Activity, Cell. 125 (2006) 371–383. https://doi.org/10.1016/j.cell.2006.02.039.

[143] K. Ouararhni, R. Hadj-Slimane, S. Ait-Si-Ali, P. Robin, F. Mietton, A. Harel-Bellan, S. Dimitrov, A. Hamiche, The histone variant mH2A1.1 interferes with transcription by down-regulating PARP-1 enzymatic activity, Genes Dev. 20 (2006) 3324–3336. https://doi.org/10.1101/gad.396106.

[144] A.B. Tufan, K. Lazarow, M. Kolesnichenko, A. Sporbert, J.P. von Kries, C. Scheidereit, TSG101 associates with PARP1 and is essential for PARylation and DNA damageinduced NF- κ B activation, EMBO J. 41 (2022). https://doi.org/10.15252/embj.2021110372.

[145] C. Zhang, B. Zhou, F. Gu, H. Liu, H. Wu, F. Yao, H. Zheng, H. Fu, W. Chong, S. Cai, M. Huang, X. Ma, Z. Guo, T. Li, W. Deng, M. Zheng, Q. Ji, Y. Zhao, Y. Ma, Q.-E. Wang, T.-S. Tang, C. Guo, Micropeptide PACMP inhibition elicits synthetic lethal effects by decreasing CtIP and poly(ADP-ribosyl)ation, Mol. Cell. 82 (2022) 1297-1312.e8. https://doi.org/10.1016/j.molcel.2022.01.020.

[146] H. Ma, G. Qi, F. Han, W. Lu, J. Peng, R. Li, S. Yan, C. Yuan, B. Kong, HMGB3 promotes PARP inhibitor resistance through interacting with PARP1 in ovarian cancer, Cell Death Dis. 13 (2022) 263. https://doi.org/10.1038/s41419-022-04670-7.

[147] F. Yang, J. Chen, B. Liu, G. Gao, M. Sebastian, C. Jeter, J. Shen, M.D. Person, M.T. Bedford, SPINDOC binds PARP1 to facilitate PARylation, Nat. Commun. 12 (2021) 6362. https://doi.org/10.1038/s41467-021-26588-y.

[148] R.J. Lake, R. Bilkis, H.-Y. Fan, Dynamic Interplay between Cockayne Syndrome Protein B and Poly(ADP-Ribose) Polymerase 1 during Oxidative DNA Damage Repair, Biomedicines. 10 (2022) 361. https://doi.org/10.3390/biomedicines10020361.

[149] F. Wang, S. Zhu, L.A. Fisher, L. Wang, N.J. Eurek, J.K. Wahl, L. Lan, A. Peng, Phosphatase 1 Nuclear Targeting Subunit Mediates Recruitment and Function of Poly (ADP-Ribose) Polymerase 1 in DNA Repair, Cancer Res. 79 (2019) 2526–2535. https://doi.org/10.1158/0008-5472.CAN-18-1673.

[150] S. Lee, N. Kim, S. Kim, I.B. Park, H. Kim, S. Kim, B. Kim, J.M. Hwang, I. Baek, A. Gartner, J.H. Park, K. Myung, Ewing sarcoma protein promotes dissociation of poly(ADP-ribose) polymerase 1 from chromatin, EMBO Rep. 21 (2020). https://doi.org/10.15252/embr.201948676.

[151] E. Bolderson, J.T. Burgess, J. Li, N.S. Gandhi, D. Boucher, L. V. Croft, S. Beard, J.J. Plowman, A. Suraweera, M.N. Adams, A. Naqi, S.-D. Zhang, D.A. Sinclair, K.J. O'Byrne, D.J. Richard, Barrier-to-autointegration factor 1 (Banf1) regulates poly [ADP-ribose] polymerase 1 (PARP1) activity following oxidative DNA damage, Nat. Commun. 10 (2019) 5501. https://doi.org/10.1038/s41467-019-13167-5.

[152] M.J. Suskiewicz, F. Zobel, T.E.H. Ogden, P. Fontana, A. Ariza, J.-C. Yang, K. Zhu, L. Bracken, W.J. Hawthorne, D. Ahel, D. Neuhaus, I. Ahel, HPF1 completes the PARP active site for DNA damage-induced ADP-ribosylation, Nature. 579 (2020) 598–602. https://doi.org/10.1038/s41586-020-2013-6.

[153] M.F. Langelier, R. Billur, A. Sverzhinsky, B.E. Black, J.M. Pascal, HPF1 dynamically controls the PARP1/2 balance between initiating and elongating ADP-ribose modifications, Nat. Commun. 12 (2021). https://doi.org/10.1038/s41467-021-27043-8.

[154] I. Gibbs-Seymour, P. Fontana, J.G.M. Rack, I. Ahel, HPF1/C4orf27 Is a PARP-1-Interacting Protein that Regulates PARP-1 ADP-Ribosylation Activity, Mol. Cell. 62 (2016) 432–442. https://doi.org/10.1016/j.molcel.2016.03.008.

[155] L. Piao, K. Fujioka, M. Nakakido, R. Hamamoto, Regulation of poly ADP-Ribose polymerase 1 functions by post-translational modifications, Front. Biosci. 23 (2018) 4578. https://doi.org/10.2741/4578.

[156] M. Altmeyer, S. Messner, P.O. Hassa, M. Fey, M.O. Hottiger, Molecular mechanism of poly(ADP-ribosyl)ation by PARP1 and identification of lysine residues as ADP-ribose acceptor sites, Nucleic Acids Res. 37 (2009) 3723–3738. https://doi.org/10.1093/nar/gkp229.

[157] T.M. Kauppinen, W.Y. Chan, S.W. Suh, A.K. Wiggins, E.J. Huang, R.A. Swanson, Direct phosphorylation and regulation of poly(ADP-ribose) polymerase-1 by extracellular signal-regulated kinases 1/2, Proc. Natl. Acad. Sci. 103 (2006) 7136–7141. https://doi.org/10.1073/pnas.0508606103.

[158] R.H.G. Wright, G. Castellano, J. Bonet, F. Le Dily, J. Font-Mateu, C. Ballaré, A.S. Nacht, D. Soronellas, B. Oliva, M. Beato, CDK2-dependent activation of PARP-1 is required for hormonal gene regulation in breast cancer cells, Genes Dev. 26 (2012) 1972–1983. https://doi.org/10.1101/gad.193193.112.

[159] B.-G. Ju, D. Solum, E.J. Song, K.-J. Lee, D.W. Rose, C.K. Glass, M.G. Rosenfeld, Activating the PARP-1 Sensor Component of the Groucho/ TLE1 Corepressor Complex Mediates a CaMKinase II δ -Dependent Neurogenic Gene Activation Pathway, Cell. 119 (2004) 815–829. https://doi.org/10.1016/j.cell.2004.11.017.

[160] I. Kassner, A. Andersson, M. Fey, M. Tomas, E. Ferrando-May, M.O. Hottiger, SET7/9-dependent methylation of ARTD1 at K508 stimulates poly-ADP-ribose formation after oxidative stress, Open Biol. 3 (2013) 120173. https://doi.org/10.1098/rsob.120173.

[161] L. Piao, D. Kang, T. Suzuki, A. Masuda, N. Dohmae, Y. Nakamura, R. Hamamoto, The Histone Methyltransferase SMYD2 Methylates PARP1 and Promotes Poly(ADP-ribosyl)ation Activity in Cancer Cells, Neoplasia. 16 (2014) 257-264.e2. https://doi.org/10.1016/j.neo.2014.03.002.

[162] P.O. Hassa, S.S. Haenni, C. Buerki, N.I. Meier, W.S. Lane, H. Owen, M. Gersbach, R. Imhof, M.O. Hottiger, Acetylation of Poly(ADP-ribose) Polymerase-1 by p300/CREB-binding Protein Regulates Coactivation of NF- κ B-dependent Transcription, J. Biol. Chem. 280 (2005) 40450–40464. https://doi.org/10.1074/jbc.M507553200.

[163] S.B. Rajamohan, V.B. Pillai, M. Gupta, N.R. Sundaresan, K.G. Birukov, S. Samant, M.O. Hottiger, M.P. Gupta, SIRT1 Promotes Cell Survival under Stress by Deacetylation-Dependent Deactivation of Poly(ADP-Ribose) Polymerase 1, Mol. Cell. Biol. 29 (2009) 4116–4129. https://doi.org/10.1128/MCB.00121-09.

[164] S. Messner, D. Schuermann, M. Altmeyer, I. Kassner, D. Schmidt, P. Schär, S. Müller, M.O. Rottiger, Sumoylation of poly(ADP-ribose) polymerase 1 inhibits its acetylation and restrains transcriptional coactivator function, FASEB J. 23 (2009) 3978–3989. https://doi.org/10.1096/fj.09-137695.

[165] N. Martin, K. Schwamborn, V. Schreiber, A. Werner, C. Guillier, X.-D. Zhang, O. Bischof, J.-S. Seeler, A. Dejean, PARP-1 transcriptional activity is regulated by sumoylation upon heat shock, EMBO J. 28 (2009) 3534–3548. https://doi.org/10.1038/emboj.2009.279.

[166] N. Zhang, Y. Zhang, B. Wu, S. You, Y. Sun, Role of WW domain E3 ubiquitin protein ligase 2 in modulating ubiquitination and Degradation of Septin4 in oxidative stress endothelial injury, Redox Biol. 30 (2020) 101419. https://doi.org/10.1016/j.redox.2019.101419.

[167] N. Zhang, Y. Zhang, H. Qian, S. Wu, L. Cao, Y. Sun, Selective targeting of ubiquitination and degradation of PARP1 by E3 ubiquitin ligase WWP2 regulates isoproterenol-induced cardiac remodeling, Cell Death Differ. 27 (2020) 2605–2619. https://doi.org/10.1038/s41418-020-0523-2.

[168] J. Groslambert, E. Prokhorova, I. Ahel, ADP-ribosylation of DNA and RNA, DNA Repair (Amst). 105 (2021) 103144. https://doi.org/10.1016/j.dnarep.2021.103144.

[169] A. Ray Chaudhuri, A. Nussenzweig, The multifaceted roles of PARP1 in DNA repair and chromatin remodelling, Nat. Rev. Mol. Cell Biol. 18 (2017) 610–621. https://doi.org/10.1038/nrm.2017.53.

[170] J.M. Pascal, The comings and goings of PARP-1 in response to DNA damage, DNA Repair (Amst). 71 (2018) 177–182. https://doi.org/10.1016/j.dnarep.2018.08.022.

[171] B.B. Das, S.N. Huang, J. Murai, I. Rehman, J.-C. Amé, S. Sengupta, S.K. Das, P. Majumdar, H. Zhang, D. Biard, H.K. Majumder, V. Schreiber, Y. Pommier, PARP1–TDP1 coupling for the repair of topoisomerase I–induced DNA damage, Nucleic Acids Res. 42 (2014) 4435–4449. https://doi.org/10.1093/nar/gku088.

[172] K.W. Caldecott, Single-strand break repair and genetic disease, Nat. Rev. Genet. 9 (2008) 619–631. https://doi.org/10.1038/nrg2380.

[173] P. Reynolds, S. Cooper, M. Lomax, P. O'Neill, Disruption of PARP1 function inhibits base excision repair of a sub-set of DNA lesions, Nucleic Acids Res. 43 (2015) 4028–4038. https://doi.org/10.1093/nar/gkv250.

[174] K. Martin-Hernandez, J.-M. Rodriguez-Vargas, V. Schreiber, F. Dantzer, Expanding functions of ADP-ribosylation in the maintenance of genome integrity, Semin. Cell Dev. Biol. 63 (2017) 92–101. https://doi.org/10.1016/j.semcdb.2016.09.009.

[175] A. Pines, M.G. Vrouwe, J.A. Marteijn, D. Typas, M.S. Luijsterburg, M. Cansoy, P. Hensbergen, A. Deelder, A. de Groot, S. Matsumoto, K. Sugasawa, N. Thoma, W. Vermeulen, H. Vrieling, L. Mullenders, PARP1 promotes nucleotide excision repair through DDB2 stabilization and recruitment of ALC1, J. Cell Biol. 199 (2012) 235–249. https://doi.org/10.1083/jcb.201112132.

[176] S.-K. Ooi, S. Sato, C. Tomomori-Sato, Y. Zhang, Z. Wen, C.A.S. Banks, M.P. Washburn, J.R. Unruh, L. Florens, R.C. Conaway, J.W. Conaway, Multiple roles for PARP1 in ALC1-dependent nucleosome remodeling, Proc. Natl. Acad. Sci. 118 (2021). https://doi.org/10.1073/pnas.2107277118.

[177] M. Robu, R.G. Shah, N. Petitclerc, J. Brind'Amour, F. Kandan-Kulangara, G.M. Shah, Role of poly(ADP-ribose) polymerase-1 in the removal of UV-induced DNA lesions by nucleotide excision repair, Proc. Natl. Acad. Sci. 110 (2013) 1658–1663. https://doi.org/10.1073/pnas.1209507110.

[178] O.D. Scharer, Nucleotide Excision Repair in Eukaryotes, Cold Spring Harb. Perspect. Biol. 5 (2013) a012609–a012609. https://doi.org/10.1101/cshperspect.a012609.

[179] Y. Liu, F.A. Kadyrov, P. Modrich, PARP-1 enhances the mismatch-dependence of 5′-directed excision in human mismatch repair in vitro, DNA Repair (Amst). 10 (2011) 1145–1153. https://doi.org/10.1016/j.dnarep.2011.08.012.

[180] J.-P. Gagné, M. Isabelle, K.S. Lo, S. Bourassa, M.J. Hendzel, V.L. Dawson, T.M. Dawson, G.G. Poirier, Proteome-wide identification of poly(ADP-ribose) binding proteins and poly(ADP-ribose)-associated protein complexes, Nucleic Acids Res. 36 (2008) 6959–6976. https://doi.org/10.1093/nar/gkn771.

[181] Y. Sun, T.J. McCorvie, L.A. Yates, X. Zhang, Structural basis of homologous recombination, Cell. Mol. Life Sci. 77 (2020) 3–18. https://doi.org/10.1007/s00018-019-03365-1.

[182] M. Li, X. Yu, Function of BRCA1 in the DNA Damage Response Is Mediated by ADP-Ribosylation, Cancer Cell. 23 (2013) 693–704. https://doi.org/10.1016/j.ccr.2013.03.025.

[183] F. Zhang, J. Shi, C. Bian, X. Yu, Poly(ADP-Ribose) Mediates the BRCA2-Dependent Early DNA Damage Response, Cell Rep. 13 (2015) 678–689. https://doi.org/10.1016/j.celrep.2015.09.040.

[184] S. Ying, Z. Chen, A.L. Medhurst, J.A. Neal, Z. Bao, O. Mortusewicz, J. McGouran, X. Song, H. Shen, F.C. Hamdy, B.M. Kessler, K. Meek, T. Helleday, DNA-PKcs and PARP1 Bind to Unresected Stalled DNA Replication Forks Where They Recruit XRCC1 to Mediate Repair, Cancer Res. 76 (2016) 1078–1088. https://doi.org/10.1158/0008-5472.CAN-15-0608.

[185] R. Aguilar-Quesada, J.A. Muñoz-Gámez, D. Martín-Oliva, A. Peralta, M.T. Valenzuela, R. Matínez-Romero, R. Quiles-Pérez, J.M. Murcia, G. de Murcia, M.R. de Almodóvar, F.J. Oliver, Interaction between ATM and PARP-1 in response to DNA damage and sensitization of ATM deficient cells through PARP inhibition, BMC Mol. Biol. 8 (2007) 29. https://doi.org/10.1186/1471-2199-8-29.

[186] J.-F. Haince, S. Kozlov, V.L. Dawson, T.M. Dawson, M.J. Hendzel, M.F. Lavin, G.G. Poirier, Ataxia Telangiectasia Mutated (ATM) Signaling Network Is Modulated by a Novel Poly(ADP-ribose)-dependent Pathway in the Early Response to DNA-damaging Agents, J. Biol. Chem. 282 (2007) 16441–16453. https://doi.org/10.1074/jbc.M608406200.

[187] S. Gajewski, A. Hartwig, PARP1 Is Required for ATM-Mediated p53 Activation and p53-Mediated Gene Expression after Ionizing Radiation, Chem. Res. Toxicol. 33 (2020) 1933–1940. https://doi.org/10.1021/acs.chemrestox.0c00130.

[188] M.S. Luijsterburg, I. de Krijger, W.W. Wiegant, R.G. Shah, G. Smeenk, A.J.L. de Groot, A. Pines, A.C.O. Vertegaal, J.J.L. Jacobs, G.M. Shah, H. van Attikum, PARP1 Links CHD2-Mediated Chromatin Expansion and H3.3 Deposition to DNA Repair by Non-homologous End-Joining, Mol. Cell. 61 (2016) 547–562. https://doi.org/10.1016/j.molcel.2016.01.019.

[189] S. Sharma, S.M. Javadekar, M. Pandey, M. Srivastava, R. Kumari, S.C. Raghavan, Homology and enzymatic requirements of microhomology-dependent alternative end joining, Cell Death Dis. 6 (2015) e1697–e1697. https://doi.org/10.1038/cddis.2015.58.

[190] R. Ceccaldi, J.C. Liu, R. Amunugama, I. Hajdu, B. Primack, M.I.R. Petalcorin, K.W. O'Connor, P.A. Konstantinopoulos, S.J. Elledge, S.J. Boulton, T. Yusufzai, A.D. D'Andrea, Homologous-recombination-deficient tumours are dependent on Pol θ-mediated repair, Nature. 518 (2015) 258–262. https://doi.org/10.1038/nature14184.

[191] P.A. Mateos-Gomez, F. Gong, N. Nair, K.M. Miller, E. Lazzerini-Denchi, A. Sfeir, Mammalian polymerase θ promotes alternative NHEJ and suppresses recombination, Nature. 518 (2015) 254–257. https://doi.org/10.1038/nature14157.

[192] M.E. Luedeman, S. Stroik, W. Feng, A.J. Luthman, G.P. Gupta, D.A. Ramsden, Poly(ADP) ribose polymerase promotes DNA polymerase theta-mediated end joining by activation of end resection, Nat. Commun. 13 (2022) 4547. https://doi.org/10.1038/s41467-022-32166-7.

[193] G.V. Chaitanya, J.S. Alexander, P.P. Babu, PARP-1 cleavage fragments: signatures of cell-death proteases in neurodegeneration, Cell Commun. Signal. 8 (2010) 31. https://doi.org/10.1186/1478-811X-8-31.

[194] Y. Zhou, L. Liu, S. Tao, Y. Yao, Y. Wang, Q. Wei, A. Shao, Y. Deng, Parthanatos and its associated components: Promising therapeutic targets for cancer, Pharmacol. Res. 163 (2021) 105299. https://doi.org/10.1016/j.phrs.2020.105299.

[195] P. Huang, G. Chen, W. Jin, K. Mao, H. Wan, Y. He, Molecular Mechanisms of Parthanatos and Its Role in Diverse Diseases, Int. J. Mol. Sci. 23 (2022) 7292. https://doi.org/10.3390/ijms23137292.

[196] L. Wang, C. Liang, F. Li, D. Guan, X. Wu, X. Fu, A. Lu, G. Zhang, PARP1 in Carcinomas and PARP1 Inhibitors as Antineoplastic Drugs, Int. J. Mol. Sci. 18 (2017) 2111. https://doi.org/10.3390/ijms18102111.

[197] V. Ossovskaya, I.C. Koo, E.P. Kaldjian, C. Alvares, B.M. Sherman, Upregulation of Poly (ADP-Ribose) Polymerase-1 (PARP1) in Triple-Negative Breast Cancer and Other Primary Human Tumor Types, Genes Cancer. 1 (2010) 812–821. https://doi.org/10.1177/1947601910383418.

[198] A. Mazzotta, G. Partipilo, S. De Summa, F. Giotta, G. Simone, A. Mangia, Nuclear PARP1 expression and its prognostic significance in breast cancer patients, Tumor Biol. 37 (2016) 6143–6153. https://doi.org/10.1007/s13277-015-4465-0.

[199] L.A. Byers, J. Wang, M.B. Nilsson, J. Fujimoto, P. Saintigny, J. Yordy, U. Giri, M. Peyton, Y.H. Fan, L. Diao, F. Masrorpour, L. Shen, W. Liu, B. Duchemann, P. Tumula, V. Bhardwaj, J. Welsh, S. Weber, B.S. Glisson, N. Kalhor, I.I. Wistuba, L. Girard, S.M. Lippman, G.B. Mills, K.R. Coombes, J.N. Weinstein, J.D. Minna, J. V. Heymach, Proteomic Profiling Identifies Dysregulated Pathways in Small Cell Lung Cancer and Novel Therapeutic Targets Including PARP1, Cancer Discov. 2 (2012) 798–811. https://doi.org/10.1158/2159-8290.CD-12-0112.

[200] J.C. Brenner, F.Y. Feng, S. Han, S. Patel, S. V. Goyal, L.M. Bou-Maroun, M. Liu, R. Lonigro, J.R. Prensner, S.A. Tomlins, A.M. Chinnaiyan, PARP-1 Inhibition as a Targeted Strategy to Treat Ewing's Sarcoma, Cancer Res. 72 (2012) 1608–1613. https://doi.org/10.1158/0008-5472.CAN-11-3648.

[201] W.-W. Zuo, C.-F. Zhao, Y. Li, H.-Y. Sun, G.-M. Ma, Y.-P. Liu, S. Kang, High Expression of PARP1 in Tumor and Stroma Cells Predicts Different Prognosis and Platinum Resistance in Patients With Advanced Epithelial Ovarian Cancer, Front. Oncol. 12 (2022). https://doi.org/10.3389/fonc.2022.931445.

[202] J.D. Puentes-Pardo, S. Moreno-SanJuan, J. Casado, J. Escudero-Feliu, D. López-Pérez, P. Sánchez-Uceta, P. González-Novoa, J. Gálvez, Á. Carazo, J. León, PARP-1 Expression Influences Cancer Stem Cell Phenotype in Colorectal Cancer Depending on p53, Int. J. Mol. Sci. 24 (2023) 4787. https://doi.org/10.3390/ijms24054787.

[203] M.A. Demény, L. Virág, The PARP Enzyme Family and the Hallmarks of Cancer Part 2: Hallmarks Related to Cancer Host Interactions, Cancers (Basel). 13 (2021) 2057. https://doi.org/10.3390/cancers13092057.

[204] M. Yi, B. Dong, S. Qin, Q. Chu, K. Wu, S. Luo, Advances and perspectives of PARP inhibitors, Exp. Hematol. Oncol. 8 (2019) 29. https://doi.org/10.1186/s40164-019-0154-9.

[205] E. Kotova, A.D. Pinnola, A. V. Tulin, Small-molecule collection and high-throughput colorimetric assay to identify PARP1 inhibitors., Methods Mol. Biol. 780 (2011) 491–516. https://doi.org/10.1007/978-1-61779-270-0_29.

[206] T. Zhu, J.-Y. Zheng, L.-L. Huang, Y.-H. Wang, D.-F. Yao, H.-B. Dai, Human PARP1 substrates and regulators of its catalytic activity: An updated overview, Front. Pharmacol. 14 (2023) 1137151. https://doi.org/10.3389/fphar.2023.1137151.

[207] G.F. Elmasry, E.E. Aly, F.M. Awadallah, S.M. El-Moghazy, Design and synthesis of novel PARP-1 inhibitors based on pyridopyridazinone scaffold, Bioorg. Chem. 87 (2019) 655–666. https://doi.org/10.1016/j.bioorg.2019.03.068.

[208] G. O'Sullivan Coyne, A. Chen, S. Kummar, Delivering on the promise: Poly ADP ribose polymerase inhibition as targeted anticancer therapy, Curr. Opin. Oncol. 27 (2015) 475–481. https://doi.org/10.1097/CCO.0000000000000238.

[209] C.J. Lord, A. Ashworth, PARP Inhibitors: The First Synthetic Lethal Targeted Therapy Europe PMC Funders Group, Science (80-.). 355 (2017) 1152–1158. https://doi.org/10.1126/science.aam7344.PARP.

[210] K.E. McCann, S.A. Hurvitz, Advances in the use of PARP inhibitor therapy for breast cancer, Drugs Context. 7 (2018) 1–30. https://doi.org/10.7573/dic.212540.

[211] J. Rudolph, G. Roberts, K. Luger, Histone Parylation factor 1 contributes to the inhibition of PARP1 by cancer drugs, Nat. Commun. 12 (2021) 736. https://doi.org/10.1038/s41467-021-20998-8.

[212] S. Boussios, P. Karihtala, M. Moschetta, A. Karathanasi, A. Sadauskaite, E. Rassy, N. Pavlidis, Combined Strategies with Poly (ADP-Ribose) Polymerase (PARP) Inhibitors for the Treatment of Ovarian Cancer: A Literature Review, Diagnostics. 9 (2019) 87. https://doi.org/10.3390/diagnostics9030087.

[213] H. Yang, P. Tang, B. Tang, Y. Huang, X. Xiong, H. Li, Novel poly(ADP-ribose) polymerase inhibitor veliparib: biophysical studies on its binding to calf thymus DNA, RSC Adv. 7 (2017) 10242–10251. https://doi.org/10.1039/C6RA28213J.

[214] H. Yang, Q. Zeng, Z. He, D. Wu, H. Li, Determination of the DNA binding properties of a novel PARP inhibitor MK-4827 with calf-thymus DNA by molecular simulations and

detailed spectroscopic investigations, New J. Chem. 43 (2019) 6702–6711. https://doi.org/10.1039/C9NJ00667B.

[215] Y. Du, H. Yamaguchi, Y. Wei, J.L. Hsu, H.-L. Wang, Y.-H. Hsu, W.-C. Lin, W.-H. Yu, P.G. Leonard, G.R. Lee, M.-K. Chen, K. Nakai, M.-C. Hsu, C.-T. Chen, Y. Sun, Y. Wu, W.-C. Chang, W.-C. Huang, C.-L. Liu, Y.-C. Chang, C.-H. Chen, M. Park, P. Jones, G.N. Hortobagyi, M.-C. Hung, Blocking c-Met–mediated PARP1 phosphorylation enhances anti-tumor effects of PARP inhibitors, Nat. Med. 22 (2016) 194–201. https://doi.org/10.1038/nm.4032.

[216] Q. Dong, Y. Du, H. Li, C. Liu, Y. Wei, M.-K. Chen, X. Zhao, Y.-Y. Chu, Y. Qiu, L. Qin, H. Yamaguchi, M.-C. Hung, EGFR and c-MET Cooperate to Enhance Resistance to PARP Inhibitors in Hepatocellular Carcinoma, Cancer Res. 79 (2019) 819–829. https://doi.org/10.1158/0008-5472.CAN-18-1273.

[217] R. Abbotts, M.J. Topper, C. Biondi, D. Fontaine, R. Goswami, L. Stojanovic, E.Y. Choi, L. McLaughlin, A.A. Kogan, L. Xia, R. Lapidus, J. Mahmood, S.B. Baylin, F. V. Rassool, DNA methyltransferase inhibitors induce a BRCAness phenotype that sensitizes NSCLC to PARP inhibitor and ionizing radiation, Proc. Natl. Acad. Sci. 116 (2019) 22609–22618. https://doi.org/10.1073/pnas.1903765116.

[218] C.E. Knezevic, G. Wright, L.L. Remsing Rix, W. Kim, B.M. Kuenzi, Y. Luo, J.M. Watters, J.M. Koomen, E.B. Haura, A.N. Monteiro, C. Radu, H.R. Lawrence, U. Rix, Proteome-wide Profiling of Clinical PARP Inhibitors Reveals Compound-Specific Secondary Targets, Cell Chem. Biol. 23 (2016) 1490–1503. https://doi.org/10.1016/j.chembiol.2016.10.011.

[219] N. Gan, Q. Sun, P. Tang, D. Wu, T. Xie, Y. Zhang, H. Li, Determination of interactions between human serum albumin and niraparib through multi-spectroscopic and computational methods, Spectrochim. Acta - Part A Mol. Biomol. Spectrosc. 206 (2019) 126–134. https://doi.org/10.1016/j.saa.2018.07.100.

[220] L. Cai, X. Xu, W. Chen, The Current State of the Art in PARP Inhibitor-Based Delivery Nanosystems, Pharmaceutics. 14 (2022) 1647. https://doi.org/10.3390/pharmaceutics14081647.

[221] B. Singh, S. Yang, A. Krishna, S. Sridhar, Nanoparticle Formulations of Poly (ADP-ribose) Polymerase Inhibitors for Cancer Therapy, Front. Chem. 8 (2020). https://doi.org/10.3389/fchem.2020.594619.

[222] J. Li, Q. Sun, C. Lu, H. Xiao, Z. Guo, D. Duan, Z. Zhang, T. Liu, Z. Liu, Boron encapsulated in a liposome can be used for combinational neutron capture therapy, Nat. Commun. 13 (2022) 2143. https://doi.org/10.1038/s41467-022-29780-w.

[223] J.A. Perez-Fidalgo, A. Cortés, E. Guerra, Y. García, M. Iglesias, U. Bohn Sarmiento, E. Calvo García, L. Manso Sánchez, A. Santaballa, A. Oaknin, A. Redondo, M.J. Rubio, A. González-Martín, Olaparib in combination with pegylated liposomal doxorubicin for platinum-resistant ovarian cancer regardless of BRCA status: a GEICO phase II trial (ROLANDO study), ESMO Open. 6 (2021) 100212. https://doi.org/10.1016/j.esmoop.2021.100212.

[224] J.A. Magalhães, D.C. Arruda, M.S. Baptista, D.B. Tada, Co-Encapsulation of Methylene Blue and PARP-Inhibitor into Poly(Lactic-Co-Glycolic Acid) Nanoparticles for Enhanced PDT of Cancer, Nanomaterials. 11 (2021) 1514. https://doi.org/10.3390/nano11061514.

[225] C.J.F. Conceição, E. Moe, P.A. Ribeiro, M. Raposo, Liposome Formulations for the Strategic Delivery of PARP1 Inhibitors: Development and Optimization, Nanomaterials. 13 (2023) 1613. https://doi.org/10.3390/nano13101613.

[226] Y. Cheng, P. Zhao, S. Wu, T. Yang, Y. Chen, X. Zhang, C. He, C. Zheng, K. Li, X. Ma, G. Xiang, Cisplatin and curcumin co-loaded nano-liposomes for the treatment of hepatocellular carcinoma, Int. J. Pharm. 545 (2018) 261–273. https://doi.org/10.1016/j.ijpharm.2018.05.007.

[227] C. Has, S.M. Phapal, P. Sunthar, Rapid single-step formation of liposomes by flow assisted stationary phase interdiffusion, Chem. Phys. Lipids. 212 (2018) 144–151. https://doi.org/10.1016/j.chemphyslip.2018.01.007.

[228] G. Ioele, M. De Luca, A. Garofalo, G. Ragno, Photosensitive drugs: a review on their photoprotection by liposomes and cyclodextrins, Drug Deliv. 24 (2017) 33–44. https://doi.org/10.1080/10717544.2017.1386733.

[229] N. Dan, Core–shell drug carriers: liposomes, polymersomes, and niosomes, in: E. Andronescu, A.M. Grumezescu (Eds.), Nanostructures Drug Deliv., Elsevier, Cambridge, USA, 2017: pp. 63–105. https://doi.org/10.1016/B978-0-323-46143-6.00002-6.

[230] F. Pires, J.F. Santos, D. Bitoque, G. Araujo, A. Marletta, V.A. Nunes, P.A. Ribeiro, J.C. Silva, M. Raposo, Polycaprolactone / Gelatin Nano fi ber Membranes Containing EGCG- Loaded Liposomes and Their Potential Use for Skin Regeneration, ACS Appl. Bio Mater. 2 (2019) 4790–4800. https://doi.org/10.1021/acsabm.9b00524.

[231] M. Ruano, A. Mateos-Maroto, F. Ortega, H. Ritacco, J.E.F. Rubio, E. Guzmán, R.G. Rubio, Fabrication of Robust Capsules by Sequential Assembly of Polyelectrolytes onto Charged Liposomes, Langmuir. 37 (2021) 6189–6200. https://doi.org/10.1021/acs.langmuir.1c00341.

[232] S. Hama, M. Sakai, S. Itakura, E. Majima, K. Kogure, Rapid modification of antibodies on the surface of liposomes composed of high-affinity protein A-conjugated phospholipid for selective drug delivery, Biochem. Biophys. Reports. 27 (2021). https://doi.org/https://doi.org/10.1016/j.bbrep.2021.101067.

[233] T. Hirai, S. Saito, H. Fujimori, K. Matsushita, T. Nishio, R. Okayasu, M. Masutani, Radiosensitization by PARP inhibition to proton beam irradiation in cancer cells, Biochem. Biophys. Res. Commun. 478 (2016) 234–240. https://doi.org/10.1016/j.bbrc.2016.07.062.

[234] S.A. Jannetti, B.M. Zeglis, M.R. Zalutsky, T. Reiner, Poly(ADP-Ribose)Polymerase (PARP) Inhibitors and Radiation Therapy, Front. Pharmacol. 11 (2020) 170. https://doi.org/10.3389/fphar.2020.00170.

[235] S.J. Derby, A.J. Chalmers, R.D. Carruthers, Radiotherapy-Poly(ADP-ribose) Polymerase Inhibitor Combinations: Progress to Date, Semin. Radiat. Oncol. 32 (2022) 15–28. https://doi.org/10.1016/j.semradonc.2021.09.005.

[236] J.M.F. Fischer, O. Popp, D. Gebhard, S. Veith, A. Fischbach, M. Scheffner, E. Ferrando-may, S. Beneke, A. Leitenstorfer, Poly (ADP-ribose) -mediated interplay of XPA and PARP1 leads to reciprocal regulation of protein function, 281 (2014) 3625–3641. https://doi.org/10.1111/febs.12885.

3

EXPERIMENTAL CONCEPTS & METHODOLOGY

In this chapter it will be given an overall overview and introduction to the central methodologies that were employed in this work. These comprise the production of human PARP1 and the production of liposomes for the encapsulation of PARP1 inhibitors. Additionally, the spectroscopic techniques that were used for the characterization of all biomolecules will be briefly explained. Detailed information regarding procedure description and conditions will not be mentioned here, to avoid unnecessary repetition, but can be found in the Materials and Methods sub-sections in the main chapters.

3.1 Production of recombinant human PARP1

3.1.1 Gene cloning

DNA gene cloning is a technology that greatly contributed to the growth of scientific knowledge in the field of molecular and cellular biology. This systematic methodology is based on the insertion/ligation of a DNA fragment into a receptor plasmid, thus resulting in a recombinant DNA molecule [1]. Afterwards the recombinant plasmid is incorporated (transformation) and propagated on competent host cells, thus helping in the maintenance and amplification of DNA fragments [1].

In the present work, the Gateway recombinant cloning system was used for human PARP1 gene cloning. The Gateway system is an extremely efficient and robust procedure that can be used to clone in parallel several DNA fragments [2]. The process is based on the bacteriophage λ integration and excision reactions in the *Escherichia coli* genome [2]. Fragment integration is done through "att" recombination sites (25-242bp), that are more reliable than the conventional restriction sites. With the Gateway system the same recombinant enzyme can

be used to clone different fragments of variable sizes, thus generating numerous constructs in just a few days [2]. This system also presents a large selection of integration plasmids, thus making possible numerous combinations of Entry and Destination vectors [2]. One of the major disadvantages of this system is that once the fragment is inserted into the cloning vectors, reversal to traditional methods and other recombinant systems is very difficult [2].

The cloning process through the Gateway system involves two different enzyme mixtures and recombination reactions, BP and LR [2]. The use of the BP clonase facilitates the recombination of attB and attP sites to generate attL and attR sites. While the LR clonase promotes the reversal of the BP reaction [2]. The recombination events that occur are specific and precise, without any gain or loss of nucleotides. For each DNA fragment, a "Entry clone" must first be generated (BP reaction) using a Donor vector, which afterwards can be transferred into various "Destination vectors" (LR reaction) [2]. Each vector comes with a "Gateway cassette" that comprises different antibiotic-resistance genes (e.g. chloramphenicol or ampicillin) and a toxic ccdB gene. In this way the selection of positive cells containing the recombinant plasmid may be done [2]. Moreover, the Gateway system has the possibility to do "multisite" LR reaction, which facilitates the incorporation of DNA fragments from multiple Entry clones, into one single Destination vector. In this way the generation of complex constructs may be achieved [2].

More details regarding the primers and the conditions used for the isolation and cloning of the human PARP1 gene can be found in Chapter 4.

3.1.2 Recombinant protein expression and purification

3.1.2.1 PARP1 expression in bacteria

Recombinant protein expression involves the transfer of a recombinant vector into a host cell, that is then cultured and induced to express the desired protein. The selection of host cell is of significance since it will influence the protein production process [3]. This will define the molecular tools, apparatus and reagents that are needed for the process. Several host systems are available to express recombinant proteins, such as bacteria, yeast, filamentous fungi, unicellular algae, and insect cells [3].

In this work several *E. coli* strains were tested for the expression of human PARP1 and details regarding this matter can be found in Chapter 4.

The *E. coli* host system is one of the most know and extensively used in recombinant protein production. This is due to the many advantages associated to this organism, namely

its fast growth kinetics and consequently easily attained high cell densities [4]. Growth media is simple to prepare and uses mostly inexpensive reagents [4]. Moreover, cell transformation with foreign DNA is very fast and follows a standard protocol. However, some of its challenges may be related to possible low cell production, recombinant protein toxicity, codon bias, among others [4].

3.1.2.2 PARP1 protein purification

The first steps of protein purification involve the need to remove the expressed protein from the cell extract. The extraction methods vary depending on the presence of protein in the soluble or insoluble fractions of the cell extract. Soluble proteins may be isolated using mild extraction techniques, while proteins associated with membranes or in inclusion bodies need harsher procedures. Even though, the main purpose of recombinant expression is to obtain high yields of soluble protein, sometimes this is not achievable in some hosts (due to their metabolism) and stress situations [5]. In these cases, usually the protein of interest accumulates in insoluble aggregates, that are known as inclusion bodies. Multiple literature has described different methods to solve this problem and redirect proteins into the cytoplasmatic fractions [5]. These involve the refold of the protein from the inclusion bodies or the modification of the expression strategy [5].

In general terms, protein extraction and isolation from cells and cell debris include: 1) a initial step of breaking cell walls and membranes (either by resorting to detergents, cycles of freeze and thaw or sonication processes) and afterwards 2) the clarification of the extract (by centrifugation and /or filtration) [6].

However, if the protein is present in the periplasmic space or the culture medium, the recovery process is simplified and resorts to softer methods [6]. In the first case, protein extraction can be done by a simple osmotic shock or outer membrane disruption with lysozyme. In the second condition, a centrifugation step will suffice [6]. Nevertheless, high levels of protein secretion into the periplasmatic space can result in the formation of similar aggregates to the inclusion bodies. The aggregates can be extracted from the pellet fraction with a low-speed centrifugation, after cell disruption [6].

Regarding the purification of soluble proteins, several techniques can be employed, such as affinity approaches, ion exchange chromatography and gel filtration/size exclusion [6]. In the present work we have used two different affinity approaches, namely histrap and heparin columns, and a size exclusion chromatography (SEC) was also performed in the purification of

PARP1 recombinant proteins (seen in Figure 3.1). Information regarding the complete purification process and final conditions can be found in Chapter 4 and 5.

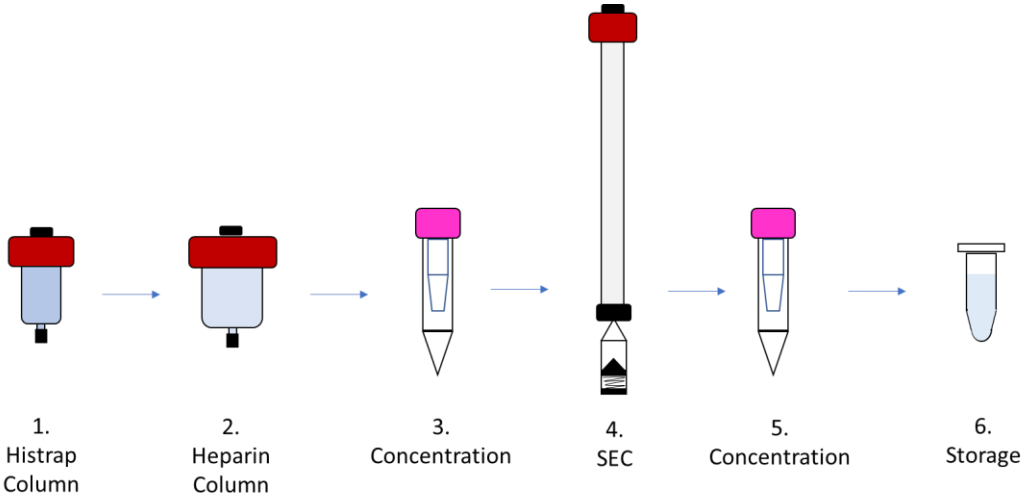

Figure 3.1 — Schematic showing the general workflow involving the use of Histrap, Heparin and Size-exclusion (SEC) columns in the purification of His-tag proteins. The first step consists of a Histrap purification followed by a heparin column purification (second step). Afterwards, the third step involves the concentration of the protein sample prior to the SEC purification step (fourth step). Before storage, the purified protein sample is subjected to a new concentration process (steps five and six).

The use of affinity methods comes as a very useful approach when high yields of protein is required or when rapid purification is needed [6]. This methodology can be used with Hist-tag proteins, thus simplifying the purification process, and helping in achieving a high purity level [6]. The His-tag motif comprises six or more consecutive histidine residues, which can be added either to the N- or C-terminal regions of the protein. The tag residues help in the purification process, through their instant coordination with specific transition metal ions (e.g. Ni^{2+} or Co^{2+}) [7]. These ions are immobilized onto the resin of purification columns by linkages such as Ni(II)-nitrilotriacetic acid (Ni-NTA) or Co^{2+}-carboxymethyl-aspartate [7]. Advantages associated to the use of immobilized-metal affinity columns (IMAC), such as the Histrap column, are their high binding capacity (5-40 mg of protein/ml of media), low-cost production and easy cleaning process [7].

The Heparin column is considered an affinity chromatography column, that may be used to purify tag-free proteins and viral particles [8,9]. The affinity property is based on the presence of intrinsic heparin-binding domains in target proteins [8,9]. The heparin molecule is a highly negatively charged glycosaminoglycan, that due to its high amount of anionic sulphate groups has also the capability to function as a cation exchanger [8,9]. In this way the heparin column may be used to remove "free" DNA molecules and promote chromatographic

separation of DNA bound proteins [8]. Through this adsorption technique, a wide range of biomolecules (e.g. serine protease inhibitors, growth factors, extracellular matrix proteins, DNA modification enzymes and hormone receptors) can be specifically adsorbed onto immobilized heparins, leading to their enrichment by an indirect concentration effect [10].

Size exclusion-chromatography (SEC), or gel filtration, is a purification technique that separates proteins by molecular size. However, this is not entirely true for non-globular proteins, with protein folding/structure influencing the retention volumes [11]. The column matrix usually consists in spherical gel beads that contain pores of specific size distribution, and protein separation is dependent on whether it is included or excluded from the pores [11]. In sum, molecules within the size range of the column are eluted in order of decreasing molecular weight and molecules with sizes above the gel pores are excluded and eluted in the void volume [11]. Moreover, SEC columns can be used either to fractionate biomolecules or to perform sample desalting/buffer exchange [11]. Resins used within SEC columns include agar, agarose, polyacrylamide, polyvivylethylcarbiol and polyvinylpyrrolidone gels [11].

Additionally, size-exclusion chromatography may serve to estimate the molecular weight of unknown molecules. This can be achieved by the elaboration of a calibration curve using standard proteins of known molecular weight [11]. The calibration curve is defined by plotting gel-phase distribution coefficient (Kav) vs. the molecular weight (Mw) of each standard. More information regarding standard proteins and formulae that were used in this work can be found in the Material and Methods subsection of Chapter 5.

3.2 PARP1 qualitative evaluation

Multiple spectroscopic techniques were used to analyze protein stability, particle size and secondary structure. These assessments were needed to guarantee the utmost stabilization of the protein, so that it could sustain the purification process and present the best fit for the biochemical and biophysical analysis with inhibitors. Additionally, PARP1's DNA binding capability and enzymatic activity were confirmed by means of electrophoretic mobility shift assay (EMSA) and activity assay (auto-modification activity assay), respectively. More information regarding these procedures is extensively explained and debated in Chapters 4 and 5.

3.2.1 Nano-DSF and Thermal Shift Assays - stability assessment

Protein stability was assessed using the nano-differential scanning fluorimetry (Nano-DSF) and thermal shift/Thermofluor assays (TSF). The first technique resorts to the

measurement of intrinsic tryptophan fluorescence emitted at 350 nm and 330 nm. The protein sample is exposed to an UV excitation at 280 nm. Emissions at 350 nm are related to hydrophilic exposed residues and 330 nm to more enclose hydrophobic residues [12]. This technique provides biophysical information regarding the melting (Tm) and onset (T_{onset}) temperatures, that are extrapolated from the denaturation process [12]. In sum, the protein is subjected to a range of increasing temperatures and because protein unfolding leads to a change in the microenvironment polarity around the tryptophan residues, a red-shift on fluorescence emission is traditionally observed [12]. In this way, results retrieved are presented as a ratio of fluorescence intensity (350 nm/330 nm) in function to temperature [12].

In the case of TSF, the thermal denaturation of proteins is done with the help of a fluorescent dye, such as SYPRO orange. These assessments are performed in a real-time polymerase chain reaction (PCR) instrument, that applies a ramp of temperatures and records the intensity of fluorescence emission from SYPRO orange. This dye binds non-specifically to the hydrophobic residues and when the protein unfolds they are exposed, which leads to dye binding and increased fluorescence emission [13].

One of the biggest advantages of Nano-DSF is the possibility to analyse low amounts of protein (0.5-1 μg), which is of great assistance when working with low yields [14]. Also this technique can be helpful in circumventing Thermofluor dye incompatibility with some stabilization additives and buffer formulations [15]. Nevertheless, in the opinion of this author, these techniques should be used as a complement to each other, when working with proteins that are similar to PARP1's tryptophan content, distribution and folding.

These techniques were used to assess the stability of PARP1 in the presence of multiple buffers, buffer components, additives, and binding partners. Detailed information regarding the molecules tested, concentrations used, and experimental conditions can be found in Chapters 4 and 5, in the Material and Methods.

3.2.2 Dynamic Light Scattering (DLS) - size distribution characterization

Protein size assessments was done by dynamic light scattering with the Zetasizer Nano ZS (Malvern Instruments, 633nm He-Ne laser, θ = 173°) (Malvern Panalytical, UK). Further information concerning experimental and measurement conditions can be found in Chapter 5.

This characterization technique measures the Brownian motion of macromolecules in solution and relates this motion with the size of the particle [16]. It is considered a popular technique for biophysical characterization of the hydrodynamic behaviour of proteins, nucleic acids, biomolecules, and polymers [16]. DLS measurements are related to the intensity of the

scattering event, which occurs when the incident monochromatic light encounters the solution [16]. In this way, DLS provides information regarding particle size, shape, and aggregation [16]. Additionally, the motion of the assessed macromolecules is strongly dependent on their size, temperature, and solvent viscosity [16].

In this way the dynamic information of the particles is derived from the autocorrelation curve generated from the intensity trace in the following equation [16]:

$$g_{2(\tau)}=\frac{\langle I(t)I(t+\tau)\rangle}{\langle I(t)\rangle^2} \tag{3.1}$$

where $g_{2(\tau)}$ is the autocorrelation function, τ is the delay time and I is the intensity. The brackets represent the averaging of properties over the experiment and t the time.

This equation can further be rewritten combining particle motion with measurement fluctuations generating the following [16]:

$$g_{2(\tau)=1+\beta e^{-2D_\tau q^2 \tau}} \tag{3.2}$$

where D_τ is the diffusion behaviour of macromolecules, β is the coherence factor and q is the Bragg wave vector.

The diffusion behaviour of a macromolecule (D_τ) is extremely important for the determination of other parameters, such as the hydrodynamic radius. This parameter can be obtained by using the Stokes-Einstein equation [16]:

$$D_\tau = \frac{\kappa_B T}{6\pi\eta R_h} \tag{3.3}$$

where κ_B is the Boltzmann coefficient ($\kappa_B = 1.380 \times 10^{-23} kg.m^2.s^{-2}.K^{-1}$), T is the absolute temperature and η is the medium viscosity.

3.2.3 Circular Dichroism (CD) - secondary structure assessment

Circular dichroism (CD) is an absorption spectroscopic technique that measures the differential absorption of right and left circularly polarized light. This method can provide information regarding secondary and tertiary structure of multiple biological molecules, such as proteins, peptides, and nucleic acids [17]. Secondary structure of proteins can be analysed based on the electronic transition in the far UV region (170-240 nm) and the tertiary structure can be monitored in the near UV region (260-300 nm) [17]. The far-near UV range is the wavelength region where the amide and carbonyl groups of the polypeptide backbone absorbs [17]. The data provided by this method if often considered complementary to other biophysical characterization techniques (e.g. crystallography, cyo-EM, NMR, FTIR, among others) [17]. One

of the biggest advantages of this method, in comparison to others, is the small amount of sample that is needed for each measurement [17]. With CD, quick assessments may be done in terms of proper folding of a protein, but also ligand interaction can be monitored, and protein stability may be inferred [17]. In this way, CD spectroscopy is considered a reliable method to use in the biochemistry, structural biology, and pharmaceutical fields [17].

In this work CD spectroscopy was used to characterize the secondary structure of native recombinant human PARP1 protein. Also, ligand effect and stabilization assessments were done in the presence of three specific PARP1 inhibitors. Information regarding experimental conditions can be found in Chapter 5.

3.3 Liposome Nano-systems

3.3.1 Preparation of liposomes and drug encapsulation

Liposomes have been used and studied as efficient transport system, and to target deliver therapy agents. This ability is mostly due to its excellent biocompatibility, biodegradability, lack of immune system activation, low toxicity, and incorporation capability for both hydrophilic and hydrophobic compounds [18]. Liposomes can be prepared by multiple techniques, such as the thin film hydration method, detergent depletion, ethanol injection and reverse phase evaporation, which usually requires a post-processing step. This additional step includes extrusion or sonication processes, that will help to achieve the desired particle size, structure, and population heterogeneity [19]. Furthermore, liposomes can act as a protective barrier for photosensitive molecules [20] and be used as a biomimetic system for interaction studies [18].

In this work, liposome production was done following the thin-dry film method developed by Alec Bangham and colleagues (illustration in Figure 3.2). Liposomes were prepared by dissolving the phospholipid in a chloroform/methanol mixture. The solvent is then evaporated by means of a gentle nitrogen air stream, to form a homogeneous thin film in the glass tube wall, and residual solvent elements are removed by an overnight step in a vacuum desiccator. Afterwards, the dry film is hydrated with an aqueous solution for 2 hours, at a temperature above the phase transition temperature of the lipid. In this way multilamellar vesicles are formed and an additional sonication step is needed to reduce particle size and increase sample homogeneity. The sonication process will lead to the production of small to large unilamellar vesicles. Briefly, the tip sonicator is immersed in the hydrated sample and several cycles of sonication are applied. Caution must be taken to prevent sample overheating and it is expected

that metal particles may be shed from the probe tip. These particles can be removed by filtration and/or decantation.

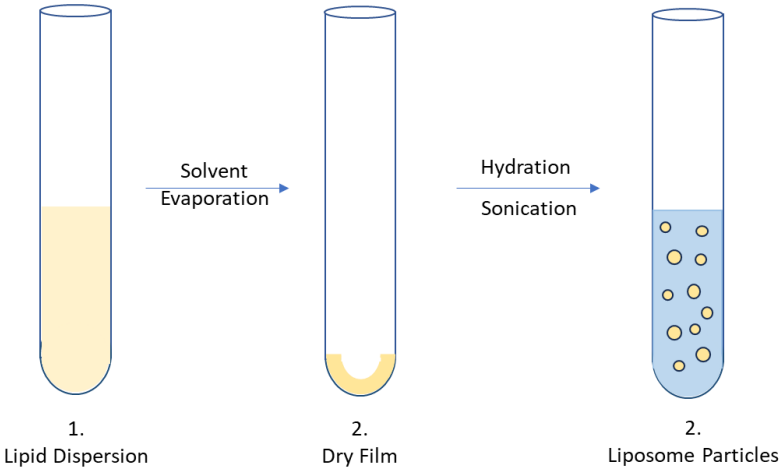

Figure 3.2 — Preparation of liposomes following the dry film method. Lipid dispersion is prepared by dissolution of dry lipid in an organic solvent (step one), that afterwards is evaporated to produce a thin dry film of lipids (second step). The film is then hydrated and subjected to several cycles of sonication to produce small to large unilamellar vesicles (third step).

The lipids tested in this work were 1,2-Dipalmitoyl-sn-glycero-3-phospho-rac-(1'-glycerol) sodium salt (DPPG) (MW 744.96 g/mol) and 1,2-dipalmitoyl-sn-glycero-3-phosphocoline (DPPC) (MW 734.05 g/mol). Relevant information regarding their structure, formal charge, phase transition temperatures (Tc), length of the acyl chain and chain saturation is displayed in Table 3.1. The gel-to-liquid transition temperature of each lipid is governed by the polar "head" group, the length and saturation of the acyl chain, but also by the purification procedure of the lipid [21,22].

Table 3.1 — Information regarding DPPG and DPPC structure, charge, phase transition temperature (Tc), length and saturation of the acyl chain, taking into account [21,22].

Name	Lipid Structure	Charge	Tc (°C)	Length and saturation of acyl chain
DPPG	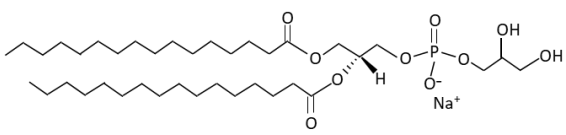	Anionic	41	16:0

DPPC	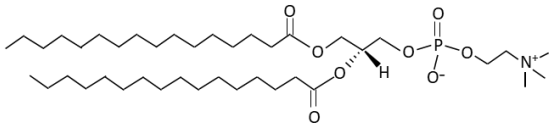	Zwitterionic	41	16:0

In this work, the particle size intended for the liposome formulations that were produced using DPPC and DPPG was around the 100 to 200 nm in diameter. Further information on the production method, conditions and PARPi encapsulation procedure can be found in Chapter 6.

3.3.2 Spectroscopic characterization

A mandatory step in liposome production is the biophysical characterization of the obtained formulations. This is a mean to guarantee proper pharmacokinetic behaviour. Liposome characterization involves the use of several spectroscopic techniques to determine particle size distribution, physical integrity, drug encapsulation, drug-liposome interactions, release rates and mechanisms that govern drug release. This was done by using UV-visible spectroscopy, Fourier transform infrared spectroscopy and DLS.

3.3.2.1 Ultraviolet (UV) - visible spectroscopy

The Ultraviolet- visible spectroscopy is a technique that permits to determine the concentration of a given sample. This is done due to the energy that is absorbed by the molecule at a given wavelength. When the sample absorbs the electromagnetic radiation provided by the irradiation source, the electrons around the atoms change their distribution and migrate from low to high levels of energy, thus promoting electronic transitions. Molecules that absorb in the UV-vis range usually contain π-electrons or non-boding electrons that are excitable to anti-bonding molecular orbitals [23].

The energy that is absorbed can be extrapolated from the Planck-Einstein equation:

$$\Delta E = h_p v = \frac{h_p c_L}{\lambda} \tag{3.4}$$

where h_p is the is the Planck constant (6.62607004 × 10^{-34} m^2 kg/s), v is the frequency, c_L refers to the speed of light in vacuum and λ the wavelength.

The quantification of a molecule can be extrapolated from the Beer-Lambert law, where the absorbance of a molecule in a specific wavelength is proportional to its concentration [23]. This is best perceived in the following equation:

$$A = \mathrm{Log}_{10}\left(\frac{I_0}{I}\right) = \varepsilon c l \tag{3.5}$$

where A is the measured absorbance, I_0 is the intensity of the incident light beam, I is the intensity of the transmitted light, ε is the molar absorptivity or extinction coefficient, c is the concentration and l is the path length through the sample.

In this work, the UV-vis spectroscopy was used to verify and calculate the encapsulation efficiencies of PARPi in the different liposome formulations. Furthermore, this technique was used to determine PARPi drug release rates and infer on the release mechanisms that were in rule (for more details refer to Chapter 6). Also, UV-vis served as a mean to analyse the degradation process of Veliparib (either encapsulated or not encapsulated) when subjected to UVC irradiation (refer to Chapter 7).

3.3.2.2 DLS - size and zeta-potential characterization

Liposome formulations were characterized using DLS. Size distribution and zeta-potential values were determined for simple liposome formulations and liposome-encapsulating PARPi. Information regarding the conditions and set-up that were used can be found in the Material and Methods sub-section of Chapter 6.

3.3.2.3 Fourier transform infrared spectroscopy (FTIR) - the study of lipid-drug interaction

Infrared spectroscopy is an absorption technique that can be used for qualitative and quantitative analysis. Contrary to UV-vis, that uses larger energy absorbances, infrared spectroscopy relies on the smaller energy absorbances involved in the vibration and rotation states [24]. Molecules that absorb infrared radiation undergo a net change in their dipole moment, which translates in a vibrational transition [24]. These can be classified as stretching or bending alterations, that result from changes in the distance between the bond of two atoms or a change in the angle between two bonds, respectively [24]. The different types of vibration and rotation modes present specific absorption bands at different frequencies, which results in a unique and specific spectrum for each molecule [24].

In this way, FTIR was employed for the spectroscopic characterization of PARPi, liposomes and liposomes encapsulating PARPi (refer to Chapter 6). Furthermore, this technique was used to determine the encapsulation and interaction mode of PARPi with DPPG membranes. Finally, the effects of UVC irradiation on Veliparib and DPPG + Veliparib samples were determined by infrared spectroscopy, and a putative degradation profile of Veliparib was

described (see results from Chapter 7). This analysis was complemented with the data provided from UV-vis spectroscopy analysis.

Information regarding the experimental set-up and conditions can be found in the material and methods subsections of Chapter 6 and 7.

3.4 Irradiation Assays - UVC Irradiation

UV irradiation assessments were done by placing aqueous solutions of Veliparib, DPPG and DPPG+Veliparib in closed quartz cuvettes. The samples were then irradiated with a 254 nm UVC germicide lamp (Philips TUV PL-S 5 W/2 P 1CT) at a radiance of 28.9 W/m^2. Afterwards, the UV damage produced over specific time-points was analyzed through UV-Visible and FTIR spectra. More information concerning these experiments can be found in Chapter 7.

3.5 Statistical Analysis

Principal Component analysis (PCA) was performed with the UV-vis spectra of irradiated and non-irradiated samples over time. This was done as a mean to analyse the independency of the degradation process between samples and to unravel where major differences could be found in the degradation process. Also, T-test statistical analysis was done to determine the statistical significance regarding the variation of PARP1's melting temperature in the stabilization assessments. Values below 0.05 were considered to have statistical significance ($p < 0.05$).

References

[1] J.S. Miles, C.R. Wolf, Principles of DNA cloning., BMJ. 299 (1989) 1019–1022. https://doi.org/10.1136/bmj.299.6706.1019.

[2] J.S. Reece-Hoyes, A.J.M. Walhout, Gateway Recombinational Cloning, Cold Spring Harb. Protoc. 2018 (2018) pdb.top094912. https://doi.org/10.1101/pdb.top094912.

[3] C. Langlais, B. Korn, Recombinant Protein Expression in Bacteria, in: Encycl. Ref. Genomics Proteomics Mol. Med., Springer Berlin Heidelberg, Heidelberg, Berlin, 2005: pp. 1609–1616. https://doi.org/10.1007/3-540-29623-9_4800.

[4] G.L. Rosano, E.A. Ceccarelli, Recombinant protein expression in Escherichia coli: advances and challenges, Front. Microbiol. 5 (2014) 172. https://doi.org/10.3389/fmicb.2014.00172.

[5] H.P. Sørensen, K.K. Mortensen, Soluble expression of recombinant proteins in the cytoplasm of Escherichia coli., Microb. Cell Fact. 4 (2005) 1. https://doi.org/10.1186/1475-2859-4-1.

[6] P.T. Wingfield, Overview of the Purification of Recombinant Proteins, Curr. Protoc. Protein Sci. 80 (2015). https://doi.org/10.1002/0471140864.ps0601s80.

[7] A. Malhotra, Tagging for Protein Expression, Academic Press, 2009. https://doi.org/10.1016/S0076-6879(09)63016-0.

[8] B. Barnes, T. Caws, S. Thomas, A.P. Shephard, R. Corteling, P. Hole, D.G. Bracewell, Investigating heparin affinity chromatography for extracellular vesicle purification and fractionation, J. Chromatogr. A. 1670 (2022) 462987. https://doi.org/10.1016/j.chroma.2022.462987.

[9] S.N. Bolten, U. Rinas, T. Scheper, Heparin: role in protein purification and substitution with animal-component free material, Appl. Microbiol. Biotechnol. 102 (2018) 8647–8660. https://doi.org/10.1007/s00253-018-9263-3.

[10] S. Xiong, L. Zhang, Q.-Y. He, Fractionation of Proteins by Heparin Chromatography, in: A. Posh (Ed.), 2D PAGE Sample Prep. Fractionation. Methods Mol. Biol., Humana Press, Munich, 2008: pp. 213–221. https://doi.org/10.1007/978-1-60327-064-9_18.

[11] P. Hong, S. Koza, E.S.P. Bouvier, Size-Exclusion Chromatography for the Analysis of Protein Biotherapeutics and their Aggregates, J. Liq. Chromatogr. Relat. Technol. 35 (2012) 2923–2950. https://doi.org/10.1080/10826076.2012.743724.

[12] S.H. Kim, H.J. Yoo, E.J. Park, D.H. Na, Nano Differential Scanning Fluorimetry-Based Thermal Stability Screening and Optimal Buffer Selection for Immunoglobulin G, Pharmaceuticals. 15 (2021) 29. https://doi.org/10.3390/ph15010029.

[13] K. Huynh, C.L. Partch, Analysis of Protein Stability and Ligand Interactions by Thermal Shift Assay, Curr. Protoc. Protein Sci. 79 (2015). https://doi.org/10.1002/0471140864.ps2809s79.

[14] V. Kotov, G. Mlynek, O. Vesper, M. Pletzer, J. Wald, C.M. Teixeira-Duarte, H. Celia, M. Garcia-Alai, S. Nussberger, S.K. Buchanan, J.H. Morais-Cabral, C. Loew, K. Djinovic-Carugo,

T.C. Marlovits, In-depth interrogation of protein thermal unfolding data with MoltenProt, Protein Sci. 30 (2021) 201–217. https://doi.org/10.1002/pro.3986.

[15] T. Kroeger, B. Frieg, T. Zhang, F.K. Hansen, A. Marmann, P. Proksch, L. Nagel-steger, G. Groth, S.H.J. Smits, H. Gohlke, EDTA aggregates induce SYPRO orange-based fluorescence in thermal shift assay, (2017) 1–21.

[16] J. Stetefeld, S.A. McKenna, T.R. Patel, Dynamic light scattering: a practical guide and applications in biomedical sciences, Biophys. Rev. 8 (2016) 409–427. https://doi.org/10.1007/s12551-016-0218-6.

[17] A.J. Miles, R.W. Janes, B.A. Wallace, Tools and methods for circular dichroism spectroscopy of proteins: a tutorial review, Chem. Soc. Rev. 50 (2021) 8400–8413. https://doi.org/10.1039/D0CS00558D.

[18] Y. Cheng, P. Zhao, S. Wu, T. Yang, Y. Chen, X. Zhang, C. He, C. Zheng, K. Li, X. Ma, G. Xiang, Cisplatin and curcumin co-loaded nano-liposomes for the treatment of hepatocellular carcinoma, Int. J. Pharm. 545 (2018) 261–273. https://doi.org/10.1016/j.ijpharm.2018.05.007.

[19] C. Has, S.M. Phapal, P. Sunthar, Rapid single-step formation of liposomes by flow assisted stationary phase interdiffusion, Chem. Phys. Lipids. 212 (2018) 144–151. https://doi.org/10.1016/j.chemphyslip.2018.01.007.

[20] G. Ioele, M. De Luca, A. Garofalo, G. Ragno, Photosensitive drugs: a review on their photoprotection by liposomes and cyclodextrins, Drug Deliv. 24 (2017) 33–44. https://doi.org/10.1080/10717544.2017.1386733.

[21] J. Li, X. Wang, T. Zhang, C. Wang, Z. Huang, X. Luo, Y. Deng, A review on phospholipids and their main applications in drug delivery systems, Asian J. Pharm. Sci. 10 (2015) 81–98. https://doi.org/10.1016/j.ajps.2014.09.004.

[22] W. Chen, F. Duša, J. Witos, S.-K. Ruokonen, S.K. Wiedmer, Determination of the Main Phase Transition Temperature of Phospholipids by Nanoplasmonic Sensing, Sci. Rep. 8 (2018) 14815. https://doi.org/10.1038/s41598-018-33107-5.

[23] H. Wang, P.K. Chu, Surface Characterization of Biomaterials, in: A. Bandyopadhyay, S. Bose (Eds.), Charact. Biomater., Elsevier, 2013: pp. 105–174. https://doi.org/10.1016/B978-0-12-415800-9.00004-8.

[24] A. Subramanian, V. Prabhakar, L. Rodriguez-Saona, Analytical Methods: Infrared Spectroscopy in Dairy Analysis, in: Ref. Modul. Food Sci., Elsevier, Washington, DC, 2016. https://doi.org/10.1016/B978-0-08-100596-5.00602-8.

4

PRODUCTION OF HUMAN PARP1: PROTOCOL DEVELOPMENT AND OPTIMIZATION

Advances in the expression and purification of human PARP1: a user-friendly protocol[2]

Abstract

The PARP1 (Poly (ADP-ribose) polymerase 1) enzyme is essential for single and double-strand break repair in humans. Alterations affecting PARP1 activity have severe consequences for human health and are associated with pathologies like cancer, and metabolic and neurodegenerative disorders. Here, we have developed a fast and easy procedure for the expression and purification of full-length and WGR-CAT PARP1. A two and three-step purification protocols were established for the first and second construct, respectively. Biologically active full-length protein was purified to an apparent purity > 95 %, with only two purification steps. A thermostability analysis revealed that full-length PARP1 possessed improved stability in 50 mM Tris-HCl pH 8.0 (Tm = 44.2 ± 0.3 ºC), thus this buffer was used throughout the whole purification procedure. WGR-CAT presented a two-domain stabilization in the same conditions. The full-length protein was shown to bind to DNA and has no inhibitor molecules bound to the active site. Finally, the yield of the purified full-length PARP1 protein is sufficient for both biochemical, biophysical and structural analysis. The overall expression and purification protocol of full-length PARP1 is fast and easy to follow, and results in a highly pure protein (> 95 %)

[2] Parts of this chapter is based on the following publication:

Conceição, C.J.F., Salgueiro, B. A., Ribeiro, P. A., Raposo, M. and Moe, E.. Advances in the expression and purification of human PARP1: a user-friendly protocol. Protein Expression and Purification, 2023, 211: 106336, DOI: 10.1016/j.pep.2023.106336.

which is biologically active. The new protocol is more effective and produces similar protein quantities in less time.

4.1 Introduction

Poly (ADP-ribose) polymerase 1 (PARP1) belongs to a large protein family with 17 members. The protein can be found in several cellular compartments and is involved in various cellular processes [1]. PARP1 is categorized as a nuclear PARP along with two other members of the family, PARP2 and PARP3 [2]. These three proteins are associated with poly (ADP-ribosyl) (PAR) post-translational modifications, with PARP1 being the major executer [3]. PARP1 is composed of a single chain of 1014 amino acids and contains 6 major domains. Homology with other family members is only observed in the C-terminal domain, where the catalytic domain (CAT) is present [4]. In structural terms, the protein consists of three zinc finger domains (Zn1, Zn2 and Zn3), a BRCT domain (BRCA-1 C-terminus fold), the WGR (Tryptophan-Glycine-Arginine) domain and the CAT domain (comprises the α-helical subdomain (HD) and the ADP-ribosyltransferase fold (ART)) [5,6]. The multiple-domain structure is pivotal for PARP1's numerous biological functions. The protein is primarily associated with DNA damage repair pathways (e.g. BER, NER, among others), but is also involved in events such as transcription, cell cycle regulation and death [4,5].

The role of PARP1 is to detect, bind, and stabilize DNA breaks. DNA repair is then initiated by the addition of poly (ADP-ribose) (PAR) chains to its own BRCT domain, termed PARylation, leading to the recruitment of effector proteins and the release of PARP1 from the damaged site [2,6]. The PARylation process is tightly regulated and proves to be of high importance, if not essential, since PARP1 is capable to both auto- and hetero modify several targets [7]. Deregulation of PARP1 enzymatic activity is often associated with several pathologies, such as inflammatory processes, metabolic disorders, neurodegenerative diseases, ageing and cancer [8–10].

Despite years of extensive studies of PARP1, there are still a lot of questions that remain to be answered regarding its biochemical and biophysical properties, inhibition and structure. However, it is a challenge to obtain high yields of pure biologically active PARP1 enzyme for studies at a molecular level. In this work, we have developed a fast and efficient method for expression and purification of recombinant PARP1, compared to other published work [5,11–14]. Our focus was on full-length human PARP1 and a construct consisting of the WGR-CAT domain. The protocol is easy to reproduce and results in pure, stable, and biologically active

recombinant protein in amounts sufficient for characterization, structural and radiation experiments.

4.2 Materials and Methods

4.2.1 Gene cloning

The gene encoding for full-length human PARP1 and the WGR-CAT truncated version were amplified from the plasmid pCMV-PARP1-3xFlag-WT which was a gift from Thomas Muir (Addgene plasmid # 111575; http://n2t.net/addgene:111575; RRID: Addgene_111575) [15]. The two set of primers used for gene amplification and cloning are shown in Table 4.1. Nucleotides encoding an N-terminal 6x-Histag sequence and a TEV cleavage site were included in the amplified PARP1 gene via the primer FDRall. 50 µL reactions contained 1x Phusion Buffer HF, 0.2 mM dNTPs, 10 µM forward and reverse primer, 3% dimethyl sulfoxide and 0.5 U Phusion DNA Polymerase (ThermoFisher, Waltham, MA, USA). PCR reactions included a 98 °C initial denaturation step (5 min); 30 cycles of denaturation (98 °C for 30 seconds), annealing (55 °C for 1 min) and extension (72 °C for 2 min). A final extension was performed at 72 °C for 7 min. PARP1 amplicons were inserted in the pDest14 expression vector following the Gateway Cloning system (ThermoFisher) recommendations. Vectors selected for the cloning processes were entry vector pDONR221 and destination vector pDest14. The correct clones were verified by sequencing using the Eurofins Genomics services.

Table 4.1 — Primer sequences used for the amplification and cloning of the PARP1 gene encoding full-length PARP1 and WGR-CAT PARP1.

Name	Nucleotide Sequence
FPPARP1	5′-CATCACCATCACCATCACGAAAACCTGTATTTCCAGGGAGCAATGGCGGAG-TCTTCGGATAAG-3′
FPPARP1 WGRCAT	5′-CATCACCATCACCATCACGAAAACCTGTATTTCCAGGGAGCAGCAGCTGTG-GATCCTGATTCT-3′
RPPARP1	5′-GGGGACCACTTTGTACAAGAAAGCTGGGTCTCACCACAGGGAGGTCTTAAA-3′
FDRall	5′ - GGGGACAAGTTTGTACAAAAAAGCAGGCTTCGAAGGAGATAGAACCATGCATCAC-CATCACCATCAC- 3′

4.2.2 Protein Expression - Small to large scale

Initial small-scale expression tests (10 ml) were performed with seven different *Escherichia coli* expression strains. Rosetta™, Rosetta™ 2, Rosetta-gami ™ 2, Rosetta™ pLysS 2, Tuner (DE3), pLysS star (DE3) and Lemo 21 (DE3) were transformed with pDest14 containing the genes encoding full-length PARP1 and the WGR-CAT domain. Different growth media (LB Broth (LB), Power Broth (PB) and Auto-induction), growth temperatures (37 °C and 18 °C) and incubation time (2 hours, 3 hours and overnight) were tested. Induction of protein expression was performed by addition of 1 mM isopropyl β-D-1- thiogalactopyranoside (IPTG). Culture media was supplemented with Ampicilin (200 μg/ml) and Chloramphenicol (34 μg/ml). Cells were harvested by centrifugation and lysed using 200 µL lysis buffer (50 mM Tris-HCl pH 7.5, 150 mM NaCl, 5 mM $MgCl_2$, 0.1 mg/ml lysozyme, 1 μg/ml DNase) and subjected to three cycles of freeze and thaw in liquid nitrogen. Centrifugation (15000 xg, 10 min, 4 °C) was performed to recover cytoplasmatic fractions (soluble fraction) and the pellet (insoluble fraction). The pellet was resuspended in 50 µL 1 % SDS and heated (95 °C, 5 min). Fractions were analysed on 10 % and 12.5% Tris-glycine-SDS-PAGE gel, stained with Blue-Safe (NZYTech, Lisbon, Portugal). Protein expression of PARP1 was confirmed by Western blot (Wet-System BioRad, Hercules, CA, USA) (protocol depicted in next subsection). The expected molecular mass of full length and WGR-CAT PARP1 is 114 kDa and 54 kDa, respectively. After determination of the best strain for PARP1 expression, a scale-up was performed in 1 L LB media.

The WGR-CAT domain was expressed in Rosetta2 cells. Colonies selected on LB agar plate, with previously referred antibiotics, were used to inoculate 25mL PB medium. A pre-inoculum was grown overnight at 37 °C and 150 rpm. 10 mL of this pre-culture was then used to inoculate 1 L PB medium (with antibiotics) and grown to an optical density at 600 nm (OD600) equal to 0.65. Expression was induced by adding 1 mM IPTG. Cells were harvested after 3 hours of induction at 37 °C and stored at -20 °C.

Recombinant full-length PARP1 expression was performed using an adapted protocol from Langelier et al., [16]. 25 ml of LB broth supplemented with Ampicillin (200 μg/ml), Chloramphenicol (34 μg/ml) and 1 % glucose was inoculated with Rosetta 2 (DE3) E. coli colonies, transformed with the pDest14 vector containing the gene encoding full-length PARP1. The culture was grown overnight at 37 °C and 150 rpm. 10 ml of the overnight culture was used to inoculate 1 L LB medium with 200 μg/ml Ampicillin, 34 μg/ml Chloramphenicol and grown to an OD600 = 0.65 at 37 °C at 120 rpm. At this point the culture medium was cooled down in a

cold chamber for 30 min and supplemented with 0.1 mM $ZnSO_4$ solution (100 mM stock). Expression was induced by addition of 0.2 mM of IPTG and the culture was grown overnight at 18 °C at 120 rpm. Cells were harvested by centrifugation for 30 minutes at 8000 rpm (Avanti™ J-26 XPI High Performance Centrifuge, with Beckman Coulter JA-10 fixed-angle rotor), 4 °C and stored at -20 °C.

4.2.3 Protein Purification

Cells were resuspended in 20 ml of lysis buffer (50 mM Tris pH 8.0, 150 mM NaCl, 5 mM $MgCl_2$, 0.1 mg/ml lysozyme, 1 μg/ml DNase and 1 tablet protease inhibitor cocktail III (Merck Millipore, Darmstadt, Germany). Resuspended cells were lysed by repeated freeze-thaw cycles using liquid nitrogen. The cell extract was centrifuged at 17000 rpm (Avanti™ J-26 XPI with Beckman Coulter JA-25.50 fixed-angle rotor) for 30 min at 4 °C. The supernatant was injected into a pre-equilibrated 1 mL Histrap HP™ column (GE Healthcare, Chicago, IL, USA) in buffer A (50 mM Tris-HCl pH 8.0, 150 mM NaCl, 0.5 mM TCEP, protease inhibitor cocktail III). The purification steps utilized an AKTA FPLC and Explorer systems (GE Healthcare) implementing both isocratic and gradient methods and employing a flow rate of 1 mL/min. A 5 % buffer B (50 mM Tris-HCl pH 8.0, 150 mM NaCl, 0.5 mM TCEP, protease inhibitor cocktail III, 500 mM Imizadole) step was included to remove low affinity contaminants and a gradient of 5-100 % buffer B was employed to elute the target protein. Eluted fractions were assessed by 10 and 12.5 % SDS-PAGE and fractions of interest were pooled. Buffer exchange was performed using a Cytiva HiPrep™ 26/10 Desalting column (Fisher Scientific) and Heparin Buffer A (50 mM Tris-HCl pH 8.0, 75 mM NaCl, 0.1 mM TCEP, 1mM EDTA), with a flowrate of 3 ml/min. Desalted fractions were loaded onto a 5 ml HiTrap Heparin HP™ column (GE Healthcare) for removal of bound DNA. The protein was eluted over a 0-100 % buffer B gradient (50 mM Tris-HCl pH 8.0, 1 M NaCl, 0.1 mM TCEP, 1 mM EDTA) and flowrate of 2 mL/min. Protein fractions eluted were analysed by SDS-PAGE, pooled, and concentrated to approximately 1 mg/ml in a Amicon® Ultra-4 (10 kDa MWCO) (Merck), and flash frozen in liquid nitrogen and stored at -80 °C. Protein concentration determination was performed using the Bradford method.

Full-length and WGR-CAT PARP1 aliquots of 250 µL were injected and analyzed in a Superdex 200 10/300GL (GE Healthcare) and Superdex 75 10/300GL (GE Healthcare) in an AKTA Explorer/FPLC system (GE Healthcare), respectively. The elution buffer used was 50 mM Tris-HCl pH 8.0 and 150 mM NaCl.

4.2.4 $Zinc^{2+}$ Ion Quantification – Zincon (2-carboxy-2′-hydroxy-5′-sulfo-formazylbenzene) Assay

1.6 mM Zincon monosodium salt (Thermo Scientific) solution was dissolved in 1 ml 1 M NaOH and diluted in Milli-Q water until the designated final concentration. A stock solution of 51.28 mM borate pH 9.0, 8.2 M urea was prepared for assay incubation and a 40-fold concentrated work solution of $ZnSO_4.7H_2O$ (Merck) [17] was used for construction of a standard metal ion curve. The zinc work solution was prepared from a 100 mM stock. Final concentrations of 0 to 40 µM metal ion and 1 µM of recombinant PARP1 were used in the assay. An initial 10 min incubation of the protein in 50 mM borate pH 9.0, 8 M urea at room temperature was carried out to release zinc ions from the protein's metal cores. The Zincon reagent was used at a final concentration of 40 µM, and the chelation reaction was left to incubate at room temperature for 5 min. Absorbance at 628 nm was recorded in the Spark® multimode microplate reader (Tecan), with a Nunc™ 96-well polystyrene plate (Thermo Scientific). At least three replicas were done and mean values with standard deviation values are presented.

4.2.5 PARP1 Auto-modification Activity Assay

PARP1 auto-modification activity reactions were conducted following the protocol described by Langelier [16]. Activity reactions were all prepared on ice and incubated at room temperature for 10 min. Reaction solutions used 1 µM protein, 1 µM blunt non-labelled DNA template (Seq.Fw: 5′-AGTACGGTCATCGCG-3′ and Seq.Rv: 5′-CGCGATGACCGTACT-3′), 5 mM beta - nicotinamide adenine dinucleotide (β-NAD+) and incubation buffer (20 mM Tris-HCl pH 7.5, 50 mM NaCl, 5 mM $MgCl_2$). Auto-modification reactions were stopped by adding SDS-loading buffer (15.6 mM Tris, 100 mM EDTA, 2.5% glycerol, 0.2 M β-mercaptoethanol, 0.26% SDS, 0.001% bromophenol blue). Reactions were analysed in 10 % SDS-PAGE gel, stained with BlueSafe (NZYTech) and images were acquired using the Gel Doc EZ System (BIORAD).

4.2.6 Wet-system Western-Blot

Protein samples were loaded onto 10 or 12.5% SDS-PAGE gels (1.0 mm, 15-well gel) and run at 180 V. Gels were wet transferred in 0.45 µm nitrocellulose filter paper sandwiches 7 x 8.5 cm (BioRAD) previously prepared in 1x Transfer Buffer (25 mM Tris-base 192 mM glycine 0.05 % SDS 20 % methanol). Membranes were blocked for 1h at room temperature in 5 % powder skim milk solution (1x TBST), and thereafter incubated in primary (Mouse monoclonal

Anti-6x Histag antibody, Catalog No: SAB1305538) and secondary (Goat Anti-Mouse IgG antibody, alkaline phosphatase-conjugated, Catalog No: AP124A) antibody (Sigma-Aldrich, St. Louis, MO, USA) (diluted 1:6000 in 5 % skim milk) for 1 h at room temperature with gentle shaking. Washes were performed after each antibody incubation with 1x TBST with gentle shaking. Detection was performed with membrane incubation in BCIP®/NBT Liquid Substrate System (Sigma-Aldrich).

4.2.7 Protein Mass Spectrometry Analysis

Peptide mapping was performed by the UniMS (ITQB/iBET, Oeiras, Portugal) using a nanoLC-MS and Sciex TripleTOF 6600 mass spectrometer. Mass spectra data was processed with Protein Pilot Software v. 5.0 (Sciex) for protein identification, and search was done against the SwissProt protein sequences for *E. coli* and human PARP1 sequence (P09874 – PARP1_HUMAN). A confidence cut-off at least of 95% and percentage of amino acids in protein sequence identified with set cut-off were used for data analysis and peptide identification.

4.2.8 Nano Differential Scanning Fluorimetry (Nano-DSF)

Real-time monitoring of Intrinsic Tryptophan Fluorescence (ITF) at 330 nm and 350 nm was performed in a Prometheus NT.48 (NanoTemper Technologies, München, Germany) with an excitation wavelength of 280 nm. High-sensitivity capillaries were filled with 10 µl full-length and WGR-CAT PARP1 at a final concentration of 0.2 mg/ml. A buffer screen comprising 50mM Tris-HCl, 50 mM Tricine, 20 mM HEPES and 50 mM Gly-Gly at pH ranging from 7.0 to 8.0 were assessed. A temperature ramp from 20 to 90 °C at a rate of 1 °C/min, was employed. Emission intensity ratio (Em_{350nm}/Em_{330nm}), was plotted as a function of temperature and first derivatives were calculated using the manufacturer's software (PR.ThermControl, version 2.1.2). Three independent measurements were carried out and mean values are presented.

4.3 Results and Discussion

4.3.1 Protein expression tests

Upon achieving positive clones, small scale test expression experiments of full-length and WGR-CAT PARP1 were carried out. Several *E. coli* strains, growth medium (Luria Broth (LB), Power Broth (PB) and auto-induction) and culture conditions (37 °C 2h-3h and 18 °C overnight)

were selected and tested. The E. coli strains listed in Table 4.2 were selected based on their unique features and suitability for expression of recombinant human proteins.

Table 4.2 — Cell lines tested for expression of full-length PARP1and WGR-CAT, with X indicating no expression, v indicating expression and – indicating strain not tested.

Strains	Medium	PARP1 construct			
		Full-length		WGR-CAT	
		18 ºC	37 ºC	18 ºC	37 ºC
Rosetta™	LB	-	X	-	X
	PB	-	X	-	X
	Auto induction	-	-	-	-
Rosetta™ 2	LB	✓ *	X	-	X
	PB	-	X	-	✓
	Auto induction	X	-	-	-
Rosetta-gami™ 2	LB	-	X	-	X
	PB	-	X	-	X
	Auto induction	-	-	-	-
Rosetta™ pLysS 2	LB	-	X	-	X
	PB	-	X	-	X
	Auto induction	-	-	-	-
Tuner (DE3)	LB	-	X	-	-
	PB	-	X	-	-
	Auto induction	X	-	-	-
pLysS * (DE3)	LB	-	X	-	-
	PB	-	X	-	-
	Auto induction	X	-	-	-
Lemo 21	LB	-	X	-	-
	PB	-	X	-	-
	Auto induction	-	-	-	-

*in specific growth conditions (see subsection 3.2.2, third paragraph)

WGR-CAT expression was only achieved with Rosetta 2 in PB medium and a 3-hour incubation time after induction at 37 ºC (Figure 4.1). Other bacterial strains were tested for expression of WGR-CAT (Table 4.2), using LB and PB medium, however the cells never reached

the desired OD_{600} = 0.65 for induction and cell death was observed. WGR-CAT expression in Rosetta 2 was detected both in the soluble and insoluble fractions of bacterial lysates (Figure 4.1).

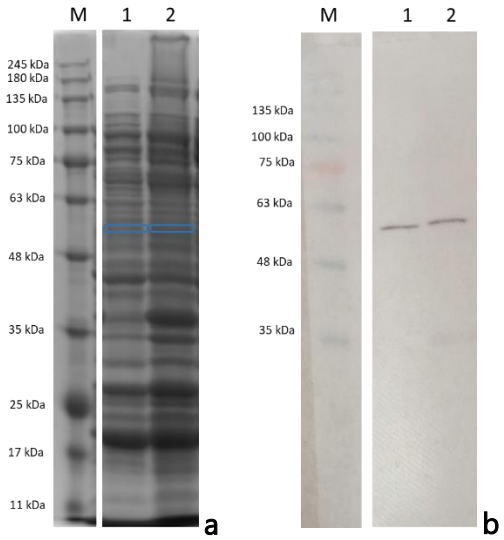

Figure 4.1 — WGR-CAT domain (54 kDa) expression confirmation in Rosetta 2 using PB medium and protein expression incubation for 3h at 37 ºC. a) SDS-PAGE gel (12.5%) results; b) Western blot results. M – NZYColour Protein Marker II (NZYTech); 1 – Rosetta 2 PB (soluble fraction); 2 – Rosetta 2 PB (insoluble infraction).

The expression tests of full-length PARP1 encompassed a total of 21 conditions (Figure 4.2 and Figure A.1-4). Among those, Rosetta in LB and PB media presented substantial growth problems, not even achieving the desired OD600 for expression induction. Also, an attempt to verify if full-length PARP1 could be expressed in a short time interval (2h) in Rosetta 2 (selected due to the expression of WGR-CAT seen in Figure 4.1 with LB medium at 37 ºC proved to be ineffective (Figure A.4). Protein expression was induced by the addition of 1 mM IPTG at an optical density (OD_{600}) of 0.65 in all conditions, except for the auto-induction medium.

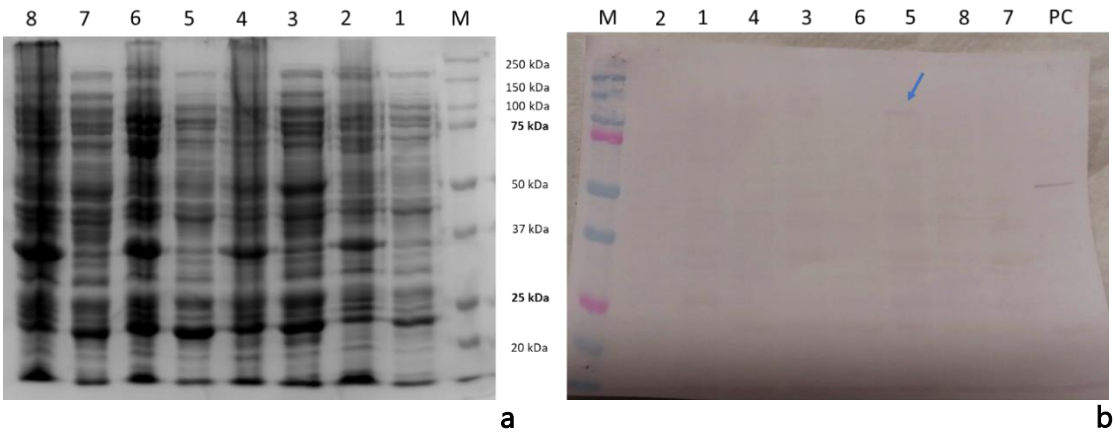

Figure 4.2 — Full-length PARP1 (114 kDa) expression tests in different cell lines and media conditions. a) SDS-PAGE gel (10%) of soluble and insoluble fractions of PARP1 full-length protein; b) Western blot results with identification of full-length PARP1 expression in well 5. M – Precision Plus Protein™ Dual colour standard (BioRad); 1- Tuner Auto-induction medium (soluble fraction); 2 - Tuner Auto-induction medium (insoluble fraction); 3 – pLysS* Auto-induction medium (soluble fraction); 4 – pLysS* Auto-induction medium (insoluble fraction); 5 – Rosetta 2 LB (soluble fraction) (adapted Langelier protocol); 6 - Rosetta 2 LB (insoluble fraction) (adapted Langelier protocol); 7 – pLysS* LB (soluble fraction); 8 – pLysS* LB (insoluble fraction); PC- positive control (PARP1 WGR-CAT construct)

Due to the difficulty of obtaining full-length PARP1 protein expression a protocol from Langlier et al. [16] was tested following the methodology described in subsection 4.2.2. This protocol includes the use of a pre-inoculum supplementation with 1% glucose (*v/v*) and addition of 0.1 mM $ZnSO_4$ to the main culture. Protein expression was verified, as seen in Figure 4.2, with expression induction being initiated at a lower OD_{600} (0.65) than Langelier et al., [16].

Difficulties in the expression of PARP1 may be related to the toxicity due to its enzymatic activity [6], but also to the complex structure and folding capability of the protein. It is likely that the addition of zinc into the growth media, allowed for a stabilization of the zinc-finger domain, and thus the overall stability of the protein structure [16]. It's important to emphasize that contrary to the Langelier et al., [16] expression protocol, our adapted procedure does not resort to the use of any type of PARP1 inhibitor (benzamide), thus leaving our recombinant protein close to its biologically active state. Furthermore, it is important to note that the ability of Rosetta 2 to express both proteins may be linked to its utility in the expression of human recombinant proteins, having present a chloramphenicol-resistant plasmid that encodes tRNA genes for seven rare codons in *E. coli* (AGA, AGG, AUA, CUA, GGA, CCC and CGG) [18].

4.3.2 Full-length and WGR-CAT PARP1 Purification

After the determination of optimal expression conditions, a large-scale expression was performed in a 1 L culture, followed by protein purification. The purification protocol involved the use of a 1 ml Histrap and a 5 ml Heparin column. From the Histrap column, both full-length PARP1 and WGR-CAT proteins were eluted at ~20% buffer B, and the use of a 5% buffer B step before the gradient removed a large part of contaminating *E. coli* proteins, as shown in the chromatogram profiles of Figure 4.3a and b. From the analysis of the 254 nm chromatogram profiles, full-length PARP1 appears to be bound to DNA, while this does not seem to be the case for WGR-CAT (Figure 4.3a and b). Because of this and the knowledge that the Zinc fingers

(Zn1-3) [6,19] and WGR domain are capable of binding nucleic acids [20], we decided to proceed with a Heparin purification step.

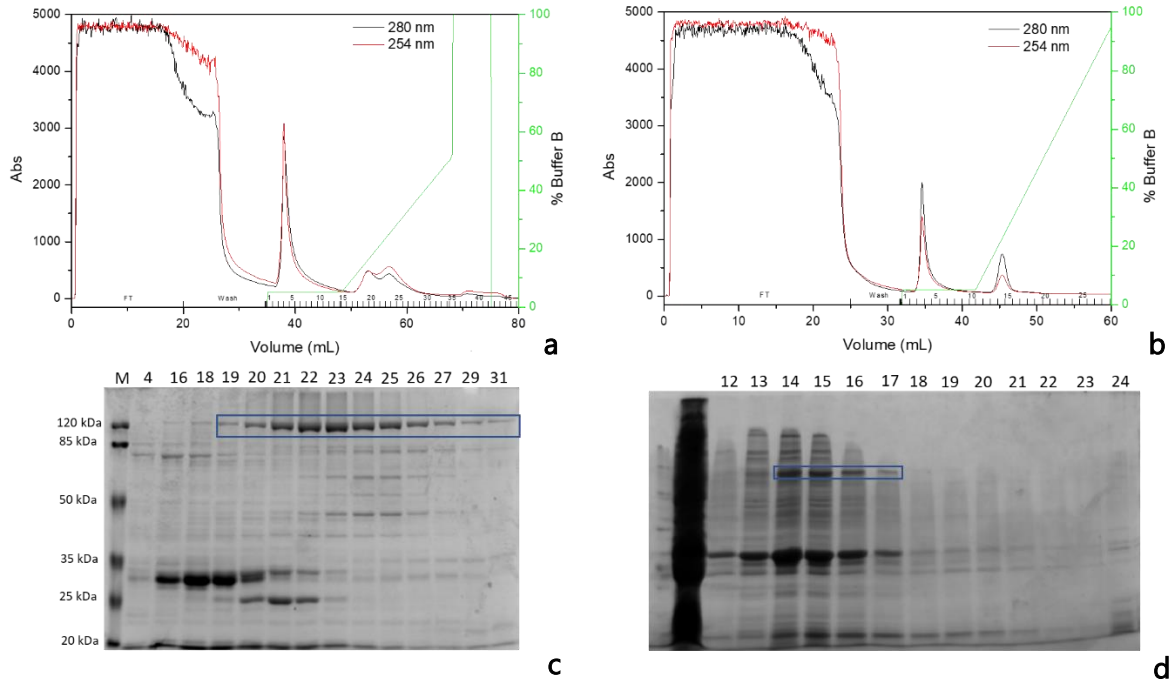

Figure 4.3 — Histrap purification of full-length PARP1 (a and c) and WGR-CAT truncated version (b and d). a and b) Chromato-gram of HisTrap purification. A large amount of contaminating proteins from E. coli were removed with a 5% buffer B step and the protein of interest was eluted in approximately 20% buffer B. c and d) SDS-PAGE analysis of Histrap purification. Fractions that were analysed are identified with their respective fraction number and fractions pooled are selected in a blue frame. M - Precision Plus Protein™ Dual color standard (BioRad)).

Prior to the Heparin purification, a sample desalting (HiPrep™ 26/10 Desalting) was conducted to remove imidazole and reduce the salt concentration. Desalted fractions were injected into the 5 ml Heparin column, and a gradient from 0 to 100 % buffer B (50 mM Tris-HCl pH 8.0, 1 M NaCl, 0.1 mM TCEP, 1 mM EDTA) was employed to purify full-length and WGR-CAT PARP1. Even though the WGR-CAT Histrap purification chromatogram did not show high absorbance at 254nm (Figure 4.3b), we verified an elevated absorbance at 280 nm in the flow-through of the Heparin chromatogram (not shown), which could be an indication that nucleic acids are present in the protein sample after Histrap. In Figure 4.4 it can be observed that we were able to remove several contaminants, and that our protein targets present different binding affinities to the column. Full-length PARP1 presents low to medium affinity to the Heparin resin, with the elution occurring at approximately 45-50 % buffer B (Figure 4.4a), while WGR-CAT is eluted at approximately 60-75% buffer B (Figure 4.4c). It should be noticed that the low to medium affinity to the column verified with the full-length protein may be an indication of the native affinity of PARP1's WGR and Zn domains to nucleic acids. Also, a variation in binding

affinity to the column may be explained by differences in protein folding between the truncated and full-length PARP1. The WGR domain is a domain that is conserved among the three nuclear human PARPs (1-3), where it has a central role in DNA dependent regulation of PARP 2 and 3 repair activity [21]. While PARP1's DNA dependent activity solely rely on the Zn1 and 3 domains, PARP2 recruitment to DNA breaks is orchestrated by the WGR and CAT domain [22].

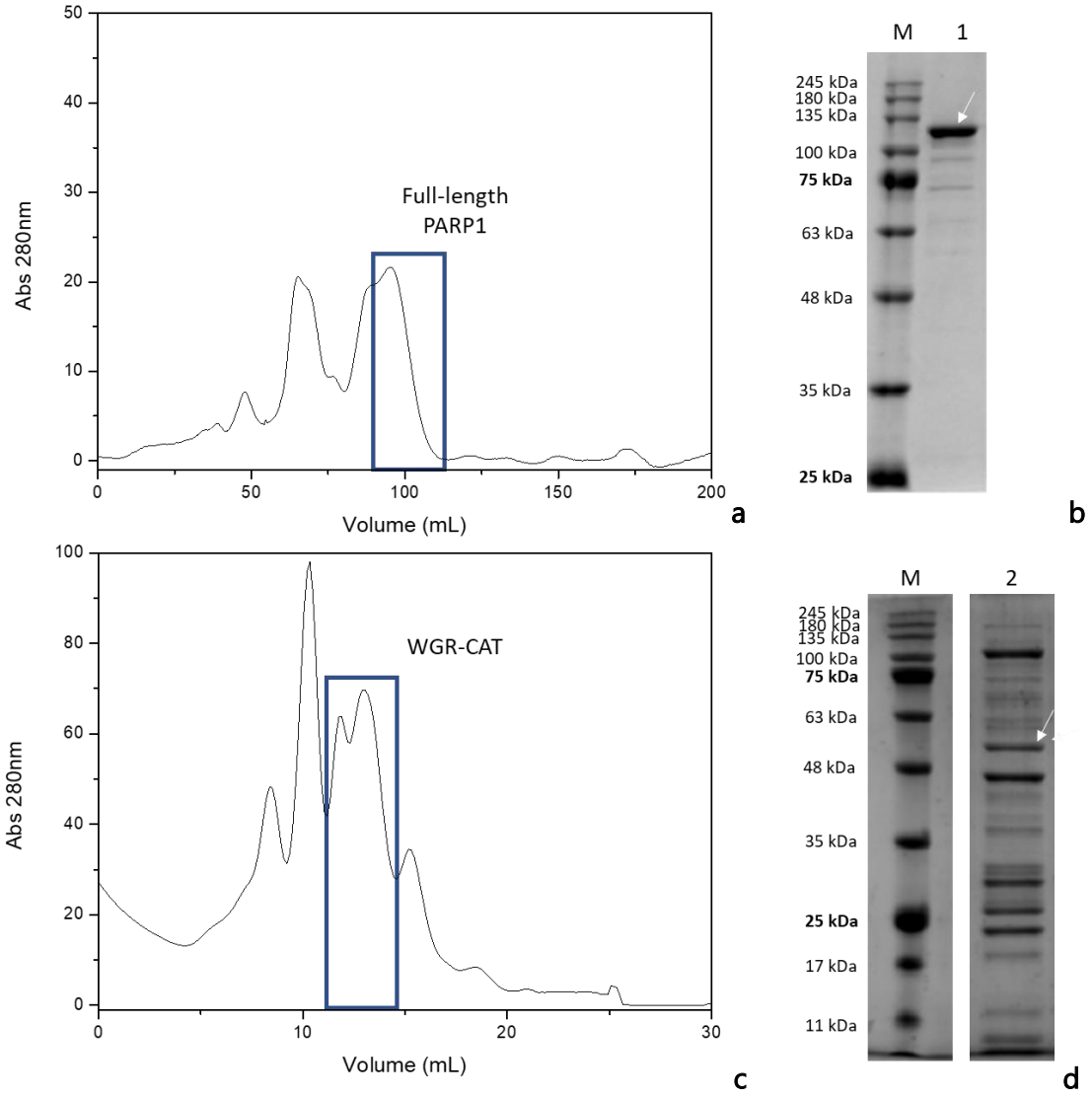

Figure 4.4 — Heparin purification of full-length and WGR-CAT PARP1 for DNA removal. a) Chromatogram for Heparin purifica-tion. A gradient of 0-100 % buffer B was used, and the protein was eluted at 45-50 % buffer B. The fractions se-lected and pooled for analysis on SDS-PAGE gel are identified in the dark blue frame; b) SDS-PAGE gel analysis of full-length PARP1 Heparin purification; c) Chromatogram for Heparin purification. A gradient of 0-100 % buffer B was used, and the protein was eluted at 60-75 % buffer B. The fractions selected and pooled for analysis on SDS-PAGE gel are identified in the dark blue frame; d) SDS-PAGE gel analysis of WGR-CAT Heparin purification, M – NZYColour Protein Marker II (NZYTech); 1- Pooled fractions of full-length PARP1; 2 – WGR-CAT PARP1.

Upon finalization of the Heparin purification, selected protein fractions were analysed in a polyacrylamide gel, results shown in Figure 4.4b and d. This assessment revealed that full-length PARP1 presented a high degree of purity (> 95 %). Protein yield after Heparin purification was 3.5 ± 0.3 mg. WGR-CAT sample still presented a high amount of contaminants, thus requiring additional purification. Because of this, it was decided to do a size exclusion chromatography to further purify WGR-CAT and confirm full-length PARP1 purity.

4.3.3 Protein Purity Evaluation and Yield

In order to further analyze the purity of PARP1, aliquots of Heparin purified samples were analyzed by gel filtration using a Superdex 200 10/300GL column (24 ml column) (full-length PARP1) and a Superdex 75 10/300GL column (24 ml column) (WGR-CAT). In Figure 4.5a and c it can be observed that full-length PARP1 is eluted from the column at 12 ml volume and appears in the chromatogram as a single isolated peak. As for the WGR-CAT chromatogram, Figure 4.5b, a multi peak pattern is observed, with the protein of interest being eluted at 13 mL volume (peak 3), which was confirmed by SDS-PAGE gel analysis (Figure 4.5d). This result reinforces the need for an additional purification step to the WGR-CAT purification protocol. Thus, we can state that a two-step purification is sufficient for full-length PARP1 purification, while WGR-CAT purification needs an additional third step.

Even though pure full-length PARP1 is achieved after heparin purification and can be used in biophysical and biochemical characterization studies, we would like to emphasize that in the case of protein structural analysis (e.g. crystallography or cryo-EM) it is advised to proceed with a SEC step to ensure that any type of aggregates or trace elements from purification/storage buffer are removed.

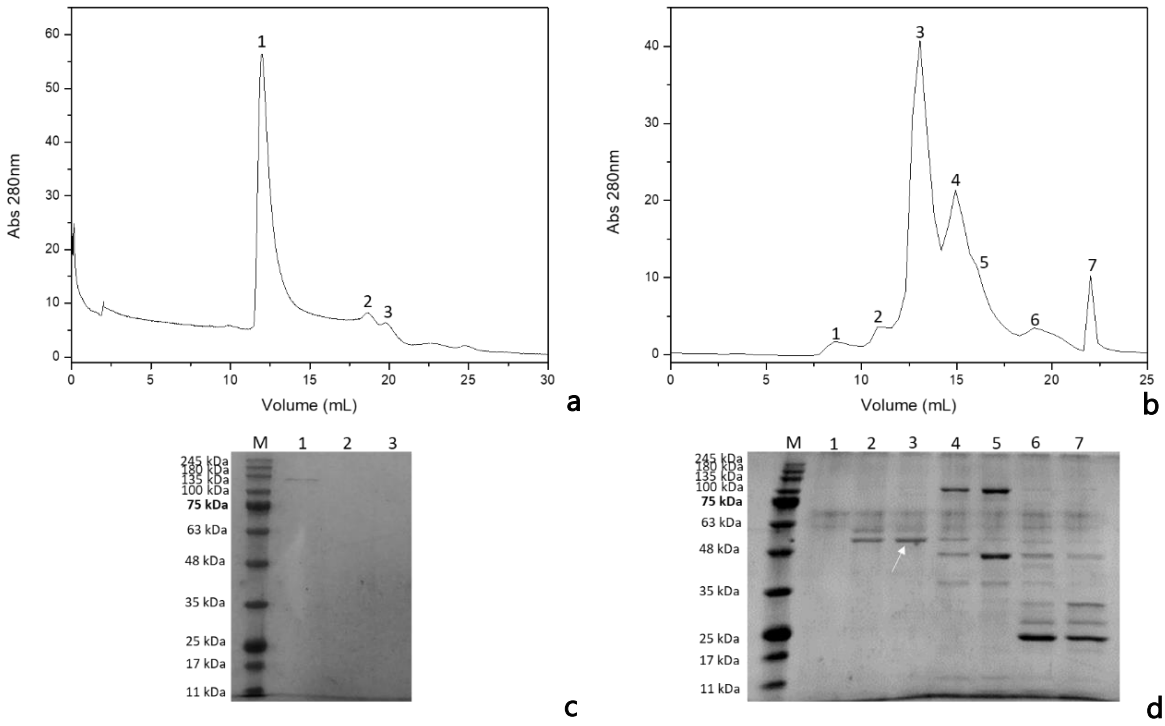

Figure 4.5 — Size exclusion chromatography analysis of PARP1. a) Superdex 200 10/300GL (24 ml column) analysis of full-length PARP1 with the presence of protein peak of interest at 12 ml elution volume. Peak 2 and 3 appear to be some small trace elements besides protein, that we hypothesise to be some RNA traces. b) Superdex 75 10/300GL (24 ml column) analysis of WGR-CAT protein with presence of several protein peaks with protein of interest being eluted at 13mL (WGR-CAT band identified with white arrow). c) Full-length PARP1peak fractions analysed by SDS-PAGE: M - NZYColour Protein Marker II (NZYTech); 1 – fraction eluted at 12 ml; 2 – fraction eluted at 18.6 and 3-fraction eluted at 19.8 ml.; d) WGR-CAT peak fractions: M - NZYColour Protein Marker II (NZYTech); 1 – fraction eluted 8.6 ml; 2 – fraction eluted 10.9 ml; 3 – fraction eluted 13 ml; 4 – fraction eluted 14.9 mL; 5 – fraction eluted 16 ml; 6 – fraction eluted 19.1 ml; 7 – fraction eluted 22 ml.

The use of a two-step purification procedure for full-length PARP1 opens new possibilities in decreasing protein loss, which usually is associated with a multi-step purification process, as well as reducing protein stability problems due to exposure to environmental temperature variations. Even though the WGR-CAT needed an additional purification step, this truncated version revealed to be stable and able to sustain the complete process.

An evaluation of the protein yield along the expression and purification process (Table 4.3) shows great differences in values. We verified that after expression, the cell mass was approximately 4 g/l and that after the first purification step (Histrap) the protein mass was of 4.1 ± 0.3 mg and 4.00 ± 0.20 mg for full-length and WGR-CAT, respectively. The difference in protein yields can be explained by the substantial amount of contaminant proteins present, as seen in Figure 4.3c and d. The protein yield significantly changed in the final purification step,

with full-length PARP1 presenting a total mass of 3.5 ± 0.3 mg and WGR-CAT 0.03 ± 0.01 mg. The change between full-length/WGR-CAT yields and the great decrease in WGR-CAT mass is mainly due the additional SEC purification step, but it could also be related to sample nature (presence of contaminants). The WGR-CAT band profile seen in the Histrap (Figure 4.4d) and Heparin (Figure 4.5d) SDS-PAGE gels, consistently presents a higher level of contaminants during the purification process (lower protein: contaminant ratio), than full-length PARP1. Furthermore, the concentration procedure showed to have a great impact on the complete process, as can be observed from Table 4.3. The final yield, after protein concentration was only 0.24 ± 0.02 mg and 0.03 ± 0.01 mg for full-length and WGR-CAT PARP1, respectively, and translates into a reduction of protein mass of around 90%. Before concentration, protein loss was only 14.6 % for full-length PARP1 and around 90 % for WGR-CAT.

It´s important to emphasize that the major loss seen in full-length PARP1 purification is due to the concentration process. We have indications that this was caused by the proteins interaction with the membrane from the Amicon system. Upon experimenting with different centrifugation systems (Amicon, DiaFlow and Vivapore) and different membrane materials (cellulose and PES), we verified that the protein loss was similar or even greater (results not shown) than the values here depicted, using the Amicon® Ultra-4 (10 kDa MWCO) system.

To our knowledge, the problems with a massive loss of full-length PARP1 during the concentration step has not been reported previously in the literature. However here we observed this phenomenon and suggest that care should be taken at this critical step, while attempting to obtain pure full-length recombinant PARP1 protein. The resort to non-ionic detergents, such as NP40, is a common alternative in purification procedures and can be taken into consideration if a further increase in protein yield values is needed. Detergents are used to reduce protein-protein association and protein loss due to adsorption to surfaces [23]. However, because of detergents interference with or loss of sensitivity to protein characterization techniques (e.g. MS), protein quantification methods (e.g. Bradford method) and biochemical assays (e.g. protein-protein/lipid interaction assays), we did not include it in our purification protocol [23,24].

Table 4.3 — Full-length and WGR-CAT PARP1 large-scale expression and purification yields.

Protein Expression (1L)	Cell Mass (g)	Histrap Protein Yield (mg)	Heparin/SEC Protein Yield (mg)	Final Yield (mg)
Full-length PARP1	4.8 ± 0.3	4.1 ± 0.3	3.5 ± 0.3	0.24 ± 0.02
PARP1 WGR-CAT	4.00 ± 0.20	6.32 ± 0.42	0.30 ± 0.14	0.03 ± 0.01

*mean ± SD values

Although we identified the concentration step as one of the major critical points in PARP1's purification process, the quantification procedure also proved to be complicated. Quantification using the Nanodrop (absorbance at 280 nm – A_{280nm}) proved to be inefficient. We consider this problem to be related to PARP1's intrinsic low aromatic residue composition (1.3 % tryptophan, 3.2 % tyrosine and 3.0 % phenylalanine), but also to the protein folding. Depending on the three-dimensional structure of a protein in solution, residues can be more or less exposed to the surrounding environment, and this will affect the UV light absorption of the aromatic rings in the 280, 275 and 258 nm wavelengths [25]. Due to this problem, we resorted to the Bradford method. This method revealed to be a reliable alternative. Nevertheless, several limitations are associated with this quantification procedure, such as dye interaction or incompatibility to some buffers/additives and problems related to proper protein standard selection [24]. In the present case, we selected bovine serum albumin (BSA) as our standard for protein quantification curves.

In summary, a fast and easy PARP1 purification protocol was developed, requiring a minimum number of steps to obtain pure protein. The full-length PARP1 protocol required a 2-step purification, and the protein mass loss was reduced to a minimum. In the literature most laboratories refer to the Langelier's 3-step protocol (Histrap, Heparin and SEC) [5,11–14]. A direct comparison of our yield to the Langelier protocol is difficult since the latter does not give any exact number which we can compare with [11]. However, they claim that the yield is sufficient for structural and biophysical studies, which is also true for the outcome of our purification, it should thus be similar. However, in our case we report the yield from expression in one liter culture, while Langlier et al. has used 6 liters. Regarding the purity, a comparison of our protein in the SDS-PAGE gel in Figure 4.3b in this work and Figure 1 in Langlier et al., 2011

[11] demonstrate that there are some contaminants in the same size range for both samples. The purity is thus similar for the two samples.

Thus, following our 2-step protocol, the yield and the purity of PARP1 is comparable to previously published protocols, however the SEC purification and an additional protein concentration step can be dismissed, which thus simplifies he purification procedure, and in our case reduced the loss of protein during an additional purification and protein concentration step. Additionally, we are using a Tris-HCl buffer pH 8.0 for all the purification steps, which has not been reported before. This removes the need for an eventual buffer exchange and contributes to a further simplification of the protocol.

Regarding the WGR-CAT domain, few protocols are described which generally follow a 2 to 3 step procedure [5,11,20]. Even though our protocol follows the same tendency, we consider that some optimizations to the heparin gradient could lead to a reduction to a 2-step procedure, as with full-length PARP1.

4.3.4 Western blot and PARP1 MS analysis for target confirmation

A qualitative analysis of the full-length and WGR-CAT PARP1 samples was performed by SDS-PAGE (Figure 4.6a) and WB (to confirm protein target) (Figure 4.6b), followed by MS analysis. In Figure 4.6a it is observed that both recombinant PARP1 constructs were purified, with a low amount of contaminant proteins, and that a relatively high purity value (> 95 %) was attained. Full-length PARP1 presented the highest degree of purity, when compared to WGR-CAT. However, trace amounts of contaminants between 75 to 100 kDa region are still observed in the first (Figure 4.6a, 1st well), while WGR-CAT contaminants are observed above the protein band region (> 54 kDa) (Figure 4.6a, 2nd well).

Western blot assessments, by detection of the 6x Histag tail motifs, unequivocally identified the proteins by band detection in the expected molecular mass region of full-length PARP1 (114 kDa) and WGR-CAT (54 kDa) (Figure 4.6b). It is also important to emphasize that no contaminant was detected by this technique, which is a good indication of the integrity state of the protein of interest.

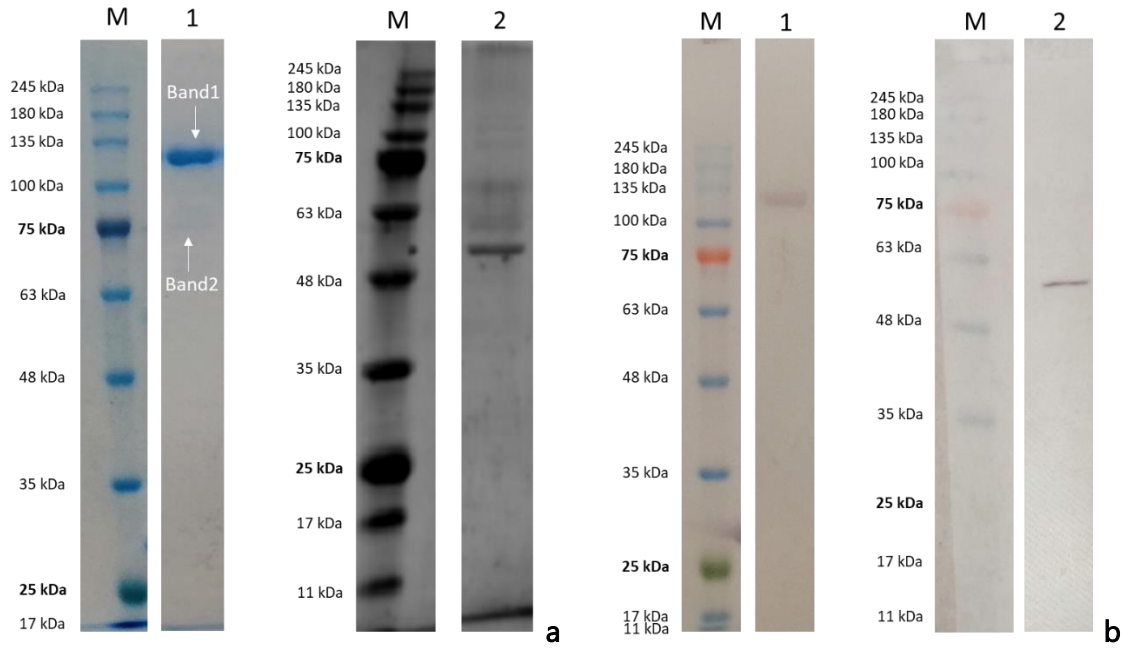

Figure 4.6 — Purified recombinant human PARP1 protein analysis by SDS-PAGE gel (a) and western blot (b). M- NZYColour Protein Marker II (NZYTech); 1 – Full-length PARP1 (identification of Band1 and 2 analysed by Mass-spectrometry); 2 – WGR-CAT PARP1

To ensure the identity of the expressed and purified full-length PARP1 protein, the 114 kDa band (identified as Band1) and the 75 kDa contaminant band (identified as Band2) (Figure 4.6a 1st well) were analysed by mass spectrometry (MS). Results retrieved from nanoLC-MS (Figure A.5 and Table A.1) presented unequivocal identification of Band1 as human Full-length PARP1 (Table A.1) and Band2 as the *E. coli* protein maltodextrin phosphorylase (P00490 – PHSM_ECOLI) (Table A.2), an enzymatic protein involved in *E. coli* carbohydrate metabolism [26,27]. For both identifications high degree of confidence was considered (> 95 %).

4.3.5 Protein qualitative confirmation/evaluation (Zincon and activity assays)

Additional full-length PARP1 quality assessments were performed to ensure proper enzymatic activity and were focused on: 1) the determination of protein's zinc content and 2) PARP1's auto-modification activity. These assays make sense since PARP1's DNA dependent enzymatic activity solely relies on the zinc fingers (Z1-3), BRCT (BRCA-1 C-terminus fold) and CAT (catalytic) domains. From the three, the Zn1-3 domain intervenes in the binding to DNA break loci, the CAT domain catalyses NAD^+ molecules to build poly(ADP- ribose) (PARP) chains

(on itself or other protein targets) and the BRCT is pointed as the auto-modification domain, where PAR chains addition leads to PARP1 release from the break site [2,5,6,28].

Zinc fingers (ZF) are one of the most abundant motifs in proteins and are involved in the coordination of zinc atoms by specific amino acid residues (cysteines (C) and histidines (H), but also in specific cases by aspartate (D) and glutamate (E)) [29]. One of the more conserved orientations in eukaryotes is the CCHH, a classical ββα-fold, but other non-classical forms have also been identified, where C and H combinations differ [29,30]. These motifs are of key importance in molecular functions that require protein-DNA/RNA, protein-protein and protein-PAR interactions [30]. PARP1's three ZF domains are oriented by two CCHC and one CCCC in the Zn1, Zn2 and Zn3, respectively. Zn1-2 participate in DNA binding and Zn3 is responsible for interdomain interactions [31,32].

The Zn^{2+} quantification was performed using the chelating agent Zincon (2-carboxy-2'-hydroxy-5'-sulfoformazylbenzene) and a zinc ion standard curve was prepared (Figure A.6). Results revealed that the purified full-length protein presented a 1.1 ± 0.2 μM concentration of Zn^{2+}, which translates in a 1:1 protein:ion ratio. This value was inferior to what was expected of a three ZF domain protein (1:3) and could be justified by: 1) the technique's indirect detection mode, 2) the dependency on the effectiveness of the Zincon chelator reagent, and 3) an inefficient protein denaturation with urea. This last problem could be solved by increasing denaturant concentration and/or addition of guanidine hydrochloride (GdnHCl) [17], that will help to increase the availability of metalloprotein ions to chelation agents [17,33]. In addition, Bossak and colleagues [31] have previously presented evidence that point to an incomplete allocation of Zn^{2+} to PARP1 ZFs, which may explain part of the discrepancy between expected and observed zinc concentration. The authors verified that Zn^{2+} dissociation constants for Zn1 and Zn2 significantly differed, with values of 26 ± 4 nM and 4 ± 1 pM respectively. Zn1 low affinity to Zn^{2+} was suggested as an indication of Zn1 domain in a "metal-free" state, in the biological environment [31]. The incomplete Zn^{2+} allocation could partially explain the 1:1 protein/metal ion ratio detected by us, but also incomplete metal ion removal from PARP1's metal coordination core and subsequent reduced chelator interaction can justify the results obtained.

Additionally, we cannot rule out the chelator effect of the EDTA present in the purification buffer that could have some impact in the metal ion content of the protein. However, by the Zincon assay we were able to verify that the EDTA chelation effect wasn't complete, since zinc ions were detected. This event could be due to the protein folding state and/or to protein-protein interactions, that could prevent complete metal ion depletion or slow-down metal ion

dissociation, stabilizing the metal cores. This was previously reported with Ca^{2+}-binding proteins [34].

An auto-modification activity assay, following Langelier's protocol [16], was employed to confirm PARP1's DNA binding capability and DNA dependent enzymatic activity. PARP1 is incubated in a 1:1 ratio with a DNA template and upon addition of the NAD^+ cofactor the formation of PAR chains (PARylation) onto itself is triggered. The post-translational modification serves as a mean for PARP1's release from DNA molecule and recruitment of repair effectors [28]. PARylation contributes to PARP1's size/weight increase, which can be visualized in an SDS-PAGE gel by a shift in the protein band to higher weight values. In Figure 4.7, a shift is observed on PARP1's band localization to a higher molecular mass region, when compared to the negative control (CN). It is verified that the protein activity is triggered within seconds, and that the intensity of the unmodified protein band (114 kDa) decreases with time, while the intensity of the modified protein band is sharpened. A smear pattern is observed in the concentration gel portion at the 10-minute reaction time point, which serves as indication that further protein size increase occurs.

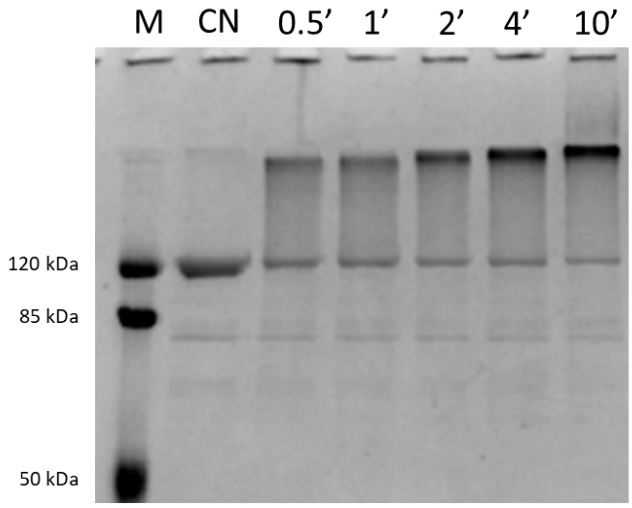

Figure 4.7 — Full-length PARP1 auto-modification activity assay with analysis of different reaction time points. M- Protein mark-er III (VWR); CN – negative control; X' – reaction time (minutes).

Full-length PARP1's qualitative analysis revealed that the purified protein is fully active and that interaction with DNA occurs even at a low Zn^{2+}: protein ratio. Differences between expected and observed Zn^{2+}: protein ratio may be related to incomplete metal ion allocation, incomplete metal ion removal from PARP1's metal coordination core in the Zincon assay and

partial EDTA chelation effect. However, the detected Zn^{2+} content proved to be sufficient for DNA binding and subsequently to trigger PARP1's DNA dependent auto-modification activity.

4.3.6 Buffer thermostability assessment

Thermostability analysis of both PARP1 constructs was performed by means of intrinsic fluorescence emission spectrometry (Nano-DSF). Four different buffers (Tris-HCl, HEPES, Tricine and Gly-Gly) at three different pH (7.0, 7.5 and 8.0) conditions were assessed (Figure A.7). Results indicated that full-length stabilization was attained in all buffers, by the observation of a single peak denaturation profile (Figure 4.8a and Figure A.7 a-c). The highest melting temperature (Tm) was verified at pH 8.0, with values ranging from 43 to 44 degrees (Table 4.4). An overall increase in Tm is verified with the increase in the ionic strength of the buffer. Tris-HCl (50 mM) at pH 8.0 presented the highest Tm value (44.2 ± 0.3 °C), when compared to remaining buffers. Tm differences between Tris-HCl and other buffers, at pH 8.0, present statistical significance ($p < 0.05$), except with Tricine (Table A.3). Tm variation in Tricine vs. Gly-Gly and HEPES vs. Tricine/Gly-Gly at pH 8.0, did not present statistical significance ($p \geq 0.05$). In terms of biological significance (≥ 3 °C) this is only verified in Tris-HCl buffer when pH 7.0 and pH 7.5/8.0 are compared, which in turn also presents statistical significance ($p < 0.05$).

The WGR-CAT thermostability analysis retrieved a differential degradation process, than full-length PARP1, with indication of a two-stage degradation process (seen in Figure 4.8b and Figure A.7d-f) and determination of two Tm values (Table 4.5). The differential stabilization was detected in all buffers and pH conditions that were tested, with Tm values for Tm1 being ~48-50 °C and Tm2 ~69 -74 °C (Table 4.5). 50mM Gly-Gly buffer condition displayed the best Tm1 and Tm2 values. Also, 50mM Gly-Gly pH 7.0 and 7.5 appeared to be most suitable. Between the two, pH 7.5 appears to be the best choice if we consider T-onset values (temperature at which the denaturation process begins) (Table A.4). Retrieved initial denaturation temperatures were of 41.4 ± 5.4 °C and 45.2 ± 0.4 °C for pH 7.0 and 7.5, respectively. Tm (1 and 2) variations at pH 7.5 conditions present statistical significance ($p < 0.05$) in Gly-Gly vs. Tris-HCl/Hepes, except Tris-HCl vs Hepes at Tm2. Statistical significance is also observed in Tm1 and 2 variations with 50mM Gly-Gly pH 7.0 vs 8.0, and Tm2 variations with 50mM Gly-Gly pH 7.0 vs 8.0 (Table A.3). However, all conditions do not appear to present biological significance (≥ 3 ºC).

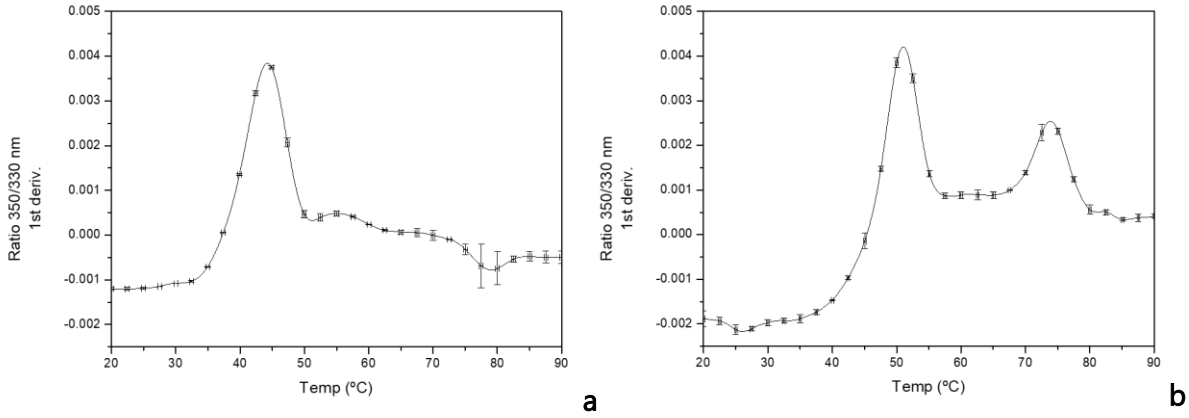

Figure 4.8 — Full-length and WGR-CAT PARP1 buffer stabilization assessment by Nano-DSF. a) Full-length PARP1 stabilization curve (1st derivative 350/330 nm ratio) with buffer 50 mM Tris-HCl pH 8.0.; b) PARP1 WGR-CAT stabilization curve (1st derivative 350/330 nm ratio) with buffer 50 mM Gly-Gly pH 7.5.

Table 4.4 — Full-length PARP1 determined melting temperatures for assessed buffers and pH values.

	Full-length PARP1*			
	50 mM Tris-HCl	20 mM HEPES	50 mM Tricine	50 mM Gly-Gly
pH 7.0	39.3 ± 0.2	39.3 ± 0.1	N/A	39.8 ± 0.1
pH 7.5	43.0 ± 0.3	41.9 ± 0.1	N/A	42.0 ± 0.2
pH 8.0	44.2 ± 0.3	43.7 ± 0.2	44.2 ± 0.5	43.3 ± 0.4

*mean ±SD value

Table 4.5 — WGR-CAT domains determined melting temperature values for different buffers and pH conditions.

		PARP1 WGR-CAT*			
		50 mM Tris-HCl	20 mM HEPES	50 mM Tricine	50 mM Gly-Gly
pH 7	Tm1	50.5 ± 0.1	50.6 ± 0.1	N/A	51.1 ± 0.1
	Tm2	73.2 ± 0.2	72.9 ± 0.2	N/A	73.9 ± 0.2

pH 7.5	Tm1	48.5 ± 0.3**	50.4 ± 0.1	N/A	51.1 ± 0.1
	Tm2	72.5 ± 0.5	72.0 ± 0.1	N/A	73.8 ± 0.2
pH 8	Tm1	50.3 ± 0.1	50.0 ± 0.1	50.0 ± 0.1	50.7 ± 0.1
	Tm2	71.0 ± 0.6	70.4 ± 0.2	69.9 ± 0.2	73.1 ± 0.3

*mean ± SD value; ** negative 350/330 nm ratio value

In sum, protein stabilization was achieved for full-length PARP1, however further work needs to be done regarding WGR-CAT construct stabilization. Additional work can also be carried out in further improving full-length PARP1protein thermostability. This may be devised and supported by the buffer and pH conditions that rendered the best results (50 mM Tris-HCl pH 8.0) in this work. Salt and additives are good options for these further assessments. Specific stabilization conditions can be expected, and "tailor-made" buffers are required for optimal stabilization.

4.4 Conclusion

A user-friendly optimized protocol for expression, and purification of full-length PARP1 was developed and analyzed. However, some additional optimizations are needed for WGR-CAT construct purification protocol. Purification with high purity yields was achieved by means of a two- and three step protocols, for full-length and WGR-CAT, respectively. However, elevated levels of protein loss were observed along the complete process, with the concentration procedure being the major limiting factor.

The purification protocol of full-length PARP1 was optimized with as few steps as possible, making the complete purification process simpler. With this protocol there is only a need for two main purification steps (Histrap and Heparin) (Figure 4.9). The SEC purification, that is associated with great protein loss, was abolished. Moreover, our protocol was optimized to reduce the number of protein concentration cycles (Figure 4.9), thus decreasing the protein loss. The present work demonstrates that it is possible to purify full-length PARP1 to an apparent purity of > 95% following a 2-step protocol. The SEC purification can be dismissed, and concentration cycles decreased to a minimum. Thus, making the reported protocol a fast and easy stepwise procedure to obtain pure and biologically active full-length protein. The protein sample obtained is close to its biological active human state and is thus suitable for biochemical and biophysical characterization studies. However, in case of structural studies (e.g.

crystallography and cryo-EM) we advise that a SEC purification should be done to ensure removal of possible aggregates and/or buffer trace elements, but it should be kept in mind that the protein yield will be lower. As for WGR-CAT, even though our protocol follows the same tendency as previously developed protocols, we consider that with some optimizations of the gradient in the heparin purification step, a reduction to a 2-step protocol is achievable.

Figure 4.9 — Purification workflow. A schematic comparison of the 3-step (Langelier et al. [16]) and 2-step (Author's present work) PARP1 purification protocols.

Additionally, a positive identification and confirmation of PARP1 purification was conducted by MS and WB.

A qualitative analysis performed on full-length PARP1 samples demonstrated its DNA-binding aptitude and enzymatic capability. Even though the Zn2+ content revealed a possible incomplete metal bound state for the zinc finger domains, previously reported evidence corroborates a possible Zn1 domain "metal free-state".

Thermostability assessments by Nano-DSF allowed to determine the best buffer and pH conditions for protein purification and storage. WGR-CAT results indicated that all buffers and pH conditions conducted to a differential two-domain stabilization event, with reported melting values around the 48 – 50 °C and 69 – 74 °C ranges. Best Tm results were determined for 50 mM Gly-Gly pH 7.5, however further tests need to be done to attain proper protein stabilization. On the other hand, Full-length PARP1 stabilization was achieved with 50 mM Tris-HCl pH 8.0, with an observation of a single unfolding peak and determination of Tm = 44.2 ± 0.3 °C.

4.5 Funding Statement

This research was funded by the Portuguese National Funding Agency (FCT-MCTES), Radiation Biology and Biophysics Doctoral Training Programme (RaBBiT, PD/00193/2012), the Applied Molecular Biosciences Unit—UCIBIO (UIDB/04378/2020), the CEFITEC Unit (UIDB/00068/2020), UIDB/04559/2020 (LIBPhys) and UIDP/04559/2020 (LIBPhys), the scholarships grant number PD/BD/142765/2018 and COVID/BD/152660/2022, to C.J.F.C. from the

RaBBiT Doctoral Training Programme, and the project LISBOA-01-0145-FEDER-007660 (Microbiologia Molecular, Estrutural e Celular) funded by FEDER funds through COMPETE2020. B.S. acknowledge the funding from (DOCTOrates 4 covid-19 2020.08066.BD) PhD Programme in Molecular Biosciences.

4.6 Acknowledgements

The Authors acknowledge Sandra Santos, Filipe Rollo, Andreia Fernandes and Catarina Paiva for technical assistance. The Merck Unit at ITQB/iBET for NanoDSF and Tecan equipment availability and usage. The Mass Spectrometry Unit (UniMS), ITQB/iBET, Oeiras, Portugal for providing the MS data.

References

[1] S. Vyas, M. Chesarone-Cataldo, T. Todorova, Y. Huang, P. Chang, A systematic analysis of the PARP protein family identifies new functions critical for cell physiology, Nat. Commun. 4 (2013) 1–13. https://doi.org/10.1038/ncomms3240.

[2] L. van Beek, É. McClay, S. Patel, M. Schimpl, L. Spagnolo, T. Maia de Oliveira, Parp power: A structural perspective on parp1, parp2, and parp3 in dna damage repair and nucleosome remodelling, Int. J. Mol. Sci. 22 (2021) 1–23. https://doi.org/10.3390/ijms22105112.

[3] S.J. Baptista, M.M.C. Silva, E. Moroni, M. Meli, G. Colombo, T.C.P. Dinis, J.A.R. Salvador, Novel PARP-1 Inhibitor scaffolds disclosed by a dynamic structure-based pharmacophore approach, PLoS One. 12 (2017) 1–20. https://doi.org/10.1371/journal.pone.0170846.

[4] F.G. Sousa, R. Matuo, D.G. Soares, A.E. Escargueil, J.A.P. Henriques, A.K. Larsen, J. Saffi, PARPs and the DNA damage response, Carcinogenesis. 33 (2012) 1433–1440. https://doi.org/10.1093/carcin/bgs132.

[5] J.D. Steffen, R.M. Tholey, M. Langelier, J.L. Planck, J. Schiewer, S. Lal, N.A. Bildzukewicz, C.J. Yeo, K.E. Knudsen, J.R. Brody, J.M. Pascal, Targeting PARP-1 allosteric regulation offers therapeutic potential against cancer, Cancer Res. 74 (2015) 31–37. https://doi.org/10.1158/0008-5472.CAN-13-1701.

[6] J.M. Dawicki-McKenna, M.F. Langelier, J.E. DeNizio, A.A. Riccio, C.D. Cao, K.R. Karch, M. McCauley, J.D. Steffen, B.E. Black, J.M. Pascal, PARP-1 Activation Requires Local Unfolding of an Autoinhibitory Domain, Mol. Cell. 60 (2015) 755–768. https://doi.org/10.1016/j.molcel.2015.10.013.

[7] E.E. Alemasova, O.I. Lavrik, Poly(ADP-ribosyl)ation by PARP1: Reaction mechanism and regulatory proteins, Nucleic Acids Res. 47 (2019) 3811–3827. https://doi.org/10.1093/nar/gkz120.

[8] Ke, Wang, Zhang, Zhong, Wang, Zeng, Ba, The Role of PARPs in Inflammation—and Metabolic—Related Diseases: Molecular Mechanisms and Beyond, Cells. 8 (2019) 1047. https://doi.org/10.3390/cells8091047.

[9] N. V. Maluchenko, A. V. Feofanov, V.M. Studitsky, PARP-1-Associated Pathological Processes: Inhibition by Natural Polyphenols, Int. J. Mol. Sci. 22 (2021) 11441. https://doi.org/10.3390/ijms222111441.

[10] K. Mao, G. Zhang, The role of PARP1 in neurodegenerative diseases and aging, FEBS J. 289 (2022) 2013–2024. https://doi.org/10.1111/febs.15716.

[11] J.M. Langelier, MF; Planck, JL.; Servent, Kristin M.; Pascal, Purification of Human PARP-1 and PARP-1 Domains from Escherichia coli for Structural and Biochemical Analysis, in: A. V. Tulin (Ed.), Poly Polym. Methods Protoc., Humana Press, Totowa, NJ, 2011: pp. 93–115. https://doi.org/10.1007/978-1-61779-270-0.

[12] J. Rudolph, U.M. Muthurajan, M. Palacio, J. Mahadevan, G. Roberts, A.H. Erbse, P.N. Dyer, K. Luger, The BRCT domain of PARP1 binds intact DNA and mediates intrastrand transfer, Mol. Cell. 81 (2021) 4994-5006.e5. https://doi.org/10.1016/j.molcel.2021.11.014.

[13] M.F. Langelier, R. Billur, A. Sverzhinsky, B.E. Black, J.M. Pascal, HPF1 dynamically controls the PARP1/2 balance between initiating and elongating ADP-ribose modifications, Nat. Commun. 12 (2021). https://doi.org/10.1038/s41467-021-27043-8.

[14] N.J. Clark, M. Kramer, U.M. Muthurajan, K. Luger, Alternative modes of binding of poly(ADP-ribose) polymerase 1 to free DNA and nucleosomes, J. Biol. Chem. 287 (2012) 32430–32439. https://doi.org/10.1074/jbc.M112.397067.

[15] G. Liszczak, K.L. Diehl, G.P. Dann, T.W. Muir, Acetylation blocks DNA damage–induced chromatin ADP-ribosylation, Nat. Chem. Biol. 14 (2018) 837–840. https://doi.org/10.1038/s41589-018-0097-1.

[16] M.F. Langelier, J.D. Steffen, A.A. Riccio, M. McCauley, J.M. Pascal, Purification of DNA Damage-Dependent PARPs from E. coli for Structural and Biochemical Analysis, Methods Mol Biol. 1608 (2017) 431–444. https://doi.org/10.1007/978-1-4939-6993-7_27.

[17] C.E. Säbel, J.M. Neureuther, S. Siemann, A spectrophotometric method for the determination of zinc, copper, and cobalt ions in metalloproteins using Zincon, Anal. Biochem. 397 (2010) 218–226. https://doi.org/10.1016/j.ab.2009.10.037.

[18] J.L. Kopanic, M. Al-Mugotir, S. Zach, S. Das, R. Grosely, P.L. Sorgen, An Escherichia coli strain for expression of the connexin45 carboxyl terminus attached to the 4th transmembrane domain, Front. Pharmacol. 4 (2013). https://doi.org/10.3389/fphar.2013.00106.

[19] J.D. Steffen, M.M. McCauley, J.M. Pascal, Fluorescent sensors of PARP-1 structural dynamics and allosteric regulation in response to DNA damage, Nucleic Acids Res. 44 (2016) 9771–9783. https://doi.org/10.1093/nar/gkw710.

[20] M.F. Langelier, J.L. Planck, S. Roy, J.M. Pascal, Structural Basis for DNA Damage–Dependent Poly(ADP-ribosyl)ation by Human PARP-1, Science (80-.). 336 (2012) 728–732. https://doi.org/10.1126/science.1216338.

[21] M.F. Langelier, A.A. Riccio, J.M. Pascal, PARP-2 and PARP-3 are selectively activated by 5′ phosphorylated DNA breaks through an allosteric regulatory mechanism shared with PARP-1, Nucleic Acids Res. 42 (2014) 7762–7775. https://doi.org/10.1093/nar/gku474.

[22] A.A. Riccio, G. Cingolani, J.M. Pascal, PARP-2 domain requirements for DNA damage-dependent activation and localization to sites of DNA damage, Nucleic Acids Res. 44 (2015) 1691–1702. https://doi.org/10.1093/nar/gkv1376.

[23] Y.-G. Yeung, E. Nieves, R.H. Angeletti, E.R. Stanley, Removal of detergents from protein digests for mass spectrometry analysis, Anal. Biochem. 382 (2008) 135–137. https://doi.org/10.1016/j.ab.2008.07.034.

[24] M.I. Knight, P.J. Chambers, Problems associated with determining protein concentration: A comparison of techniques for protein estimations, Appl. Biochem. Biotechnol. - Part B Mol. Biotechnol. 23 (2003) 19–28. https://doi.org/10.1385/MB:23:1:19.

[25] A.B. Biter, J. Pollet, W.-H. Chen, U. Strych, P.J. Hotez, M.E. Bottazzi, A method to probe protein structure from UV absorbance spectra, Anal. Biochem. 587 (2019) 113450. https://doi.org/10.1016/j.ab.2019.113450.

[26] R. Dippel, W. Boos, The maltodextrin system of Escherichia coli: metabolism and transport., J. Bacteriol. 187 (2005) 8322–31. https://doi.org/10.1128/JB.187.24.8322-8331.2005.

[27] H. Nakai, M.J. Baumann, B.O. Petersen, Y. Westphal, H. Schols, A. Dilokpimol, M.A. Hachem, S.J. Lahtinen, J.Ø. Duus, B. Svensson, The maltodextrin transport system and metabolism in Lactobacillus acidophilus NCFM and production of novel α-glucosides through reverse phosphorolysis by maltose phosphorylase, FEBS J. 276 (2009) 7353–7365. https://doi.org/10.1111/j.1742-4658.2009.07445.x.

[28] P.A. Loeffler, M.J. Cuneo, G.A. Mueller, E.F. Derose, S.A. Gabel, R.E. London, Structural studies of the PARP-1 BRCT domain, BMC Struct. Biol. 11 (2011) 37. https://doi.org/10.1186/1472-6807-11-37.

[29] K. Kluska, J. Adamczyk, A. Kręzel, Metal binding properties of zinc fingers with a naturally altered metal binding site, Metallomics. 10 (2018) 248–263. https://doi.org/10.1039/c7mt00256d.

[30] M. Cassandri, A. Smirnov, F. Novelli, C. Pitolli, M. Agostini, M. Malewicz, G. Melino, G. Raschellà, Zinc-finger proteins in health and disease, Cell Death Discov. 3 (2017). https://doi.org/10.1038/cddiscovery.2017.71.

[31] K. Bossak, W. Goch, K. Piatek, T. Fraczyk, J. Poznański, A. Bonna, C. Keil, A. Hartwig, W. Bal, Unusual Zn(II) Affinities of Zinc Fingers of Poly(ADP-ribose) Polymerase 1 (PARP-1) Nuclear Protein, Chem. Res. Toxicol. 28 (2016) 191–201. https://doi.org/10.1021/tx500320f.

[32] M.N. Wenzel, S.M. Meier-Menches, T.L. Williams, E. Rämisch, G. Barone, A. Casini, Selective targeting of PARP-1 zinc finger recognition domains with Au(III) organometallics, Chem. Commun. 54 (2018) 611–614. https://doi.org/10.1039/c7cc08406d.

[33] S. Siemann, D. Brewer, A.J. Clarke, G.I. Dmitrienko, G. Lajoie, T. Viswanatha, IMP-1 metallo-β-lactamase: effect of chelators and assessment of metal requirement by electrospray mass spectrometry, Biochim. Biophys. Acta - Gen. Subj. 1571 (2002) 190–200. https://doi.org/10.1016/S0304-4165(02)00258-1.

[34] J.K. Nyborg, O.B. Peersen, That zincing feeling: the effects of EDTA on the behaviour of zinc-binding transcriptional regulators, Biochem. J. 381 (2004). https://doi.org/10.1042/BJ20041096.

5

UNDERSTANDING THE INTRINSIC NATURE OF PARP1: STABILITY AND OLIGOMERIZATION

Assessing PARP1 stability and oligomerization status[3]

Abstract

Poly (ADP-ribose) polymerase 1 (PARP1) is an abundant nuclear enzyme, that has been associated with several pathologies. PARP1 still presents a challenge to tackle regarding structural determination, due to its flexible multi-domain nature. Thus, there is a need to further investigate the nature of its activity, stability, and oligomerization. Here we have studied how protein concentration procedure can impact PARP1s oligomeric state and uncovered the formation of a dimeric form not bound to DNA. We have also determined the effect of additives on the protein stabilization, enzymatic activity, and DNA binding affinities, and reveal how they can be used in combination to attain a higher degree of structural stability. Increased protein stability was achieved by adding divalent cations such as Mg^{2+} and Ca^{2+} to the protein in complex with oligonucleotides with double strand breaks (Tm ≥ 50 °C). Circular dichroism experiments revealed that PARP1 inhibitors have a significant impact on the secondary structure of PARP1, leading to an apparent shift of regular α-helixes to 3_{10} – or π - helixes, that translates in an overall enriched β-sheet CD spectrum. Thermostability assessments also revealed a multi-step denaturation process and optimum Tm values for PARP1 in complex with Rucaparib (Tm

[3] This chapter is based on a manuscript that is in preparation for submission for publication:

Conceição, C.J.F., Salgueiro, B. A., Ribeiro, P. A., Raposo, M. and Moe, E.. Assessing PARP1 stability and oligomerization.

as high as 60 °C). The order of protein stabilization is as follow: Rucaparib > Niraparib > Veliparib.

5.1 Introduction

Poly (ADP-ribose) polymerase 1 (PARP1) is an abundant nuclear enzyme, with primary activity in DNA repair, such as Base Excision Repair (BER). Its repair capability includes binding of chromatin ends in DNA strand breaks (DSB), stabilization of the site and recruitment of repair and chromatin remodeling effectors [1,2]. The enzymatic activity is triggered by alteration in protein folding and translates in the addition of poly ADP-ribose polymer chains on specific targets such as DNA, proteins or PARP1 itself [3,4]. By an overall change in the targets' net surface charge, the following repair stages are prompted [5]. Human PARP1 orchestrates several vital processes that are not only related to DNA repair, but also transcription, epigenetics, cell fate determination, among others [1]. The vast cellular activities of PARP1 are linked to its flexible multi-domain structure, which consist of six domains: (1-3) three zinc fingers (Zn1, Zn2 and Zn3), (4) BRCA-1 C-terminus fold (BRCT), (5) WGR domain and (6) catalytic (CAT) domain (with two subdomains: HD and ART) [1,2,5].

PARP1 is viewed as a desirable therapeutic target in cancer, and strategies employed involve the use of PARP inhibitors (PARPi) with traditional therapies. This led to a synergistic lethal effect in tumor cells and an increase in treatment efficacy [6,7]. PARPi such as Olaparib, Veliparib, Rucaparib, Niraparib and Talazoparib were developed for this purpose [7–9] and by its interaction with PARP1's β-NAD^+ cofactor binding site, in the ART domain, DSB repair is stalled [6,8]. Moreover, it has been reported that solely PARP1 is responsible for close to 90 % of all cellular PAR modification activity [10], which is a strong indication of the importance that PARP1 plays in cellular pathways and homeostasis.

Due to PARP1s vast cellular roles, this protein has been associated with pathologies like neurodegenerative diseases, brain injuries, inflammatory-based diseases, metabolic disorders, among others [11]. Even though PARP1 is well studied, it still presents a challenge to tackle with regards to structural determination. Due to its flexible multi-domain nature and the presence of several linkers, only X-ray crystal structures of truncated or engineered versions of this protein have been published [2,12]. Most of the structures are of the CAT domain with known [3,12–14] and potential novel inhibitors [15–31]. With the rise of the cryo-EM technology, the full-length structure of PARP2 associated with the histone PARylation factor 1 (HPF1) has been determined [32] and a low-resolution (28 Å) full-length PARP1 was reported [33]. These reports

emphasize the need to uncover the nature and regulation of PARP1 activity, which is intrinsically associated to its structure, environment, and interactors.

Here, we have performed experiments which aimed to clarify the dynamic structural nature, oligomerization, and stabilization of full-length PARP1's alone and upon interaction with different molecules and binding partners. Our results showed that purified PARP1 self-associates and forms a dimer following centrifugal concentration. We were also able to separate auto-modified PARP1, DNA bound PARP1, free and non-modified PARP1 during the purification procedure. Increased protein stabilization of PARP1 was achieved in presence of divalent cations such as Mg^{2+} and Ca^{2+}, and with oligonucleotides containing double strand breaks. Finally, the inhibitors Veliparib, Rucaparib and Niraparib appear to partially stabilize the full-length protein and induce fundamental structural rearrangements of PARP1.

5.2 Materials and Methods

5.2.1 Human PARP1 gene cloning, protein expression and purification

The human PARP1 gene was cloned, and the full-length protein was expressed and purified as previously described [34]. Purified protein was concentrated to approximately 1mg/mL using an Amicon® Ultra-4 (10 kDa MWCO) (Merck Millipore, Darmstadt, Germany), flash frozen in liquid nitrogen and stored at -80 °C. The protein storage buffer composition is 50 mM Tris-HCl pH 8.0, 400-500 mM NaCl, 0.1 mM TCEP and 1mM EDTA.

5.2.2 Nano Differential Scanning Fluorimetry (Nano-DSF)

Real-time monitoring of intrinsic tryptophan fluorescence (ITF) at 330 nm and 350 nm was performed in a Prometheus NT.48 (NanoTemper Technologies, München, Germany) with an excitation wavelength of 280 nm. High-sensitivity capillaries were filled with 10 µl PARP1 samples at a final concentration of 0.2 mg/ml in 50 mM Tris-HCl pH 8.0. Several buffer components were assessed: salt (NaCl and KCl), salt concentrations (100, 150, 300 and 500 mM), detergents (Zwittergent 3-10, Mega 8 and n-octyl-β-D glucoside), reducing agent (0.1 mM TCEP), chelating agent (1 mM EDTA), amino acids (1 mM) and divalent cations (0 - 5 mM). PARP 1 inhibitors (Rucaparib, Niraparib and Veliparib) at 1.76 µM and DNA templates blunt, 5'- (1.76 µM) and 3'-overhang (0.88 µM and 1.76 µM) stabilization effect was also assessed. A temperature ramp from 20 to 90 °C at a rate of 1 °C/min, was employed. The emission intensity ratio (Em_{350nm}/Em_{330nm}), was plotted as a function of the temperature and the first derivatives were

calculated by the manufacturer's software (PR.ThermControl, version 2.1.2). Three independent measurements were carried out and mean values are presented.

5.2.3 Thermal Shift Assay (TSF) - Thermofluor

SYPRO orange (Invitrogen) thermal shift assays were performed in 20 µl protein mix, containing 2.5 µg of protein and 10× dye. A 20 °C to 90 °C temperature ramp, with 1 °C/min increase was employed in all tested conditions. Fluorescence measurements were done in an iQ5 Real Time PCR Detection System (Bio-Rad Laboratories, Hercules, CA, USA) with a charge-coupled device (CCD) camera. Measurements were done with excitation at 490 nm and recording emission at 575 nm. Results were presented as the first derivative [d(RFU)/dT] from the Relative Fluorescence Units (RFU) plotted over temperature (T). Value resultant from First derivative maximal negative peak was deemed as protein melting temperature (Tm). Conditions assessed were buffer composition (50 mM Tris-HCl pH 8.0, 150/500 mM NaCl, 0.1 mM TCEP 1 mM EDTA), presence of calcium and magnesium cations (1 mM), DNA templates blunt, 3'- and 5'-overhang (1.16 µM) and PARP1 inhibitors (1.16 µM). Three independent measurements were carried out and mean values are depicted.

5.2.4 Analytic Size Exclusion Chromatography

Protein oligomeric state was analyzed by size exclusion chromatography using a Superdex S200 10/300 GL (Cytiva, Sigma-Aldrich, St. Louis, MO, USA) in an AKTA Explorer system (GE Healthcare, Chicago, IL, USA). 250 µL aliquots of protein at 1 mg/mL were loaded into a pre-equilibrated column with 50 mM Tris-HCl pH 8.0 and 150 mM NaCl. To determine protein molecular weight, a calibration curve with protein standards was determine by plotting K_{av} values with molecular weight values (Figure B.1). K_{av} values were determined following the equation:

$$K_{av} = \frac{V_e - V_o}{V_{total} - V_o} \tag{5.1}$$

where where V_e is the elution volume, V_o is the void volume and V_{total} is the SEC column total volume.

This step was performed following Cytiva guidelines and standards used were: Blue Dextran (1 mg/mL), Thyroglobulin (3 mg/ml), Ferritin (0.3 mg/mL), Aldolase (3 mg/mL), Conalbumin (3 mg/mL), and Ovalbumin (3 mg/mL).

5.2.5 Electrophoretic Mobility Shift Assay (EMSA)

To assess binding affinities between full-length PARP1 and DNA, several nucleic acid templates representing undamaged (blunt ends template DNA) and different type of damages (double strand break DNA with 5' and 3' overhang strands (DSB), nicked DNA (SSB), abasic site (Ab) and Ab in combination with DSB) were used (Table B.1). Non-labelled and FAM labelled oligos were used and annealed in a 25 mM Hepes pH 7.5, 50 mM NaCl to a final concentration of 10 μM and 0.5 μM, respectively. Non-labelled DNA templates were used in a 1 μM final concentration, mixed with protein at increasing concentrations (1, 1.5, 2, 3 and 4 μM) in 50 mM Tris-HCl pH 8.0, 150 mM NaCl, 25 % glycerol, 1 mM $MgCl_2$. Samples were separated in a 1 % agarose gel with TBE 0.5× running buffer at 80 V at 4 °C. Fluorescent labelled DNA templates at 0.1 μM final concentration were incubated for 20 min with increasing protein concentrations (0, 0.1, 0.3, 0.5, 1, 1.5 and 2 μM) in 50 mM Tris-HCl pH 8.0, 150 mM NaCl, 25 % glycerol, 5 mM divalent cation. Samples were separated in a 4 % native acrylamide/bis-acrilamide (37.5:1) (BIORad) gel in TBE 0.5x buffer. Electrophoretic runs were performed at 60 V at 4 ºC. Bands were visualized on Gel Doc EZ System (BIORAD) with an excitation source of Trans UVB (302 nm) and blue tray (430-460 nm).

5.2.6 PARP1 auto-modification activity assay

PARP1 auto-modification activity reactions were performed following the activity assay described by Langelier [35]. Activity reactions were prepared on ice and incubated at room temperature for 10 min. Reaction solutions consisted of 1 μM protein, 1 μM DNA template (blunt or 3'-overhang non-labelled DSB), 5 mM beta - nicotinamide adenine dinucleotide (β-NAD^+) and incubation buffer (20 mM Tris-HCl pH 7.5, 50 mM NaCl, 5 mM $MgCl_2$). In some assays the ion content was varied (0-5 mM), to assess ion effect on PARP1's activity. Ion solutions used were calcium chloride ($CaCl_2$), magnesium chloride ($MgCl_2$), manganese sulphate ($MnSO_4$), zinc sulphate ($ZnSO_4$), and nickel chloride ($NiCl_2$). Auto-modification reactions were stopped by the addition of SDS-loading buffer (15.6 mM Tris, 100 mM EDTA, 2.5 % glycerol, 0.2 M β-mercaptoethanol, 0.26 % SDS, 0.001 % bromophenol blue). Reaction mixtures were separated in a 10 % SDS-PAGE gel, stained with BlueSafe (NZYtech, Lisbon, Portugal). Gel images were acquired using the Gel Doc EZ System (BIORAD). Stained protein that was present in a region above the 114 kDa was assumed to be auto-modified.

5.2.7 Dynamic Light Scattering

Protein size and polydispersity index were determined by dynamic light scattering measurements in the Zetasizer Nano ZS (Malvern Instruments, 633nm He-Ne laser, θ = 173º) (Malvern Panalytical, Malvern, UK). Measurements were done using a 0.3 mm quartz cuvette (ZEN 2112) for low volume samples. Protein analysed was at 1 mg/mL concentration. At least three measurements per sample were done, with 1 minute waiting time and 30 seconds equilibration time. Sample refractive index input was 1.45 and dispersant was defined as 1.34. Intensity particle size distributions were recorded with Zetasizer software v.7.11. Mean and deviation standard values are presented. Three independent measurements were carried out.

5.2.8 Circular Dichroism

Circular dichroism (CD) spectra were acquired with a Jasco-815 CD spectrometer (Jasco Global, Japan) equipped with a Peltier temperature controller, in a one-position sample holder and a 0.01 cm quartz cuvette. A scanning speed of 50 nm/min and 4 sec response time were used. Scans were performed in the range of 260 to 200 nm, with a bandwidth of 2 nm and data pitch of 0.5 nm. A temperature ramp from 20 to 100 °C with 5 °C intervals was performed, and full spectra measurements were acquired at each point after 1 min stabilization. Each spectrum was obtained from 3 scans. Protein sample analysed was of 1 mg/mL concentration in 50 mM Tris-HCl pH 8.0, 453 mM NaCl, 0.1 mM TCEP, 1 mM EDTA. Niraparib, Rucaparib and Veliparib were used in a 1:1 ratio to protein concentration (8.7 μM). Melting temperatures were calculated using OriginPro 8.5 sigmoidal fit graphic tools. All spectra were normalized against buffer spectra. BeStSel (Beta Structure Selection) software multi-spectra analyser [36,37] was used for secondary structure identification and contribution determination.

5.3 Results and Discussion

5.3.1 Evaluation of PARP1 biological nature and form in the purification process

Recombinant PARP1 was purified following our previously described 2-step protocol [34], however a stepwise purification mode was employed in the second purification step (Heparin column) to further analyse the pool of PARP1 forms that it is possible to encounter after expression, cell lysis and HisTrap purification.

Four separate peaks were observed and assigned as PARP1 (Figure 5.1a and b), with the different "forms" being eluted at increasing salt concentration. After purification and protein concentration, pure PARP1 was obtained and visualized in an SDS-PAGE, demonstrating a band at 114 kDa, with an apparent purity > 95% (Fig 5.1b, fourth well).

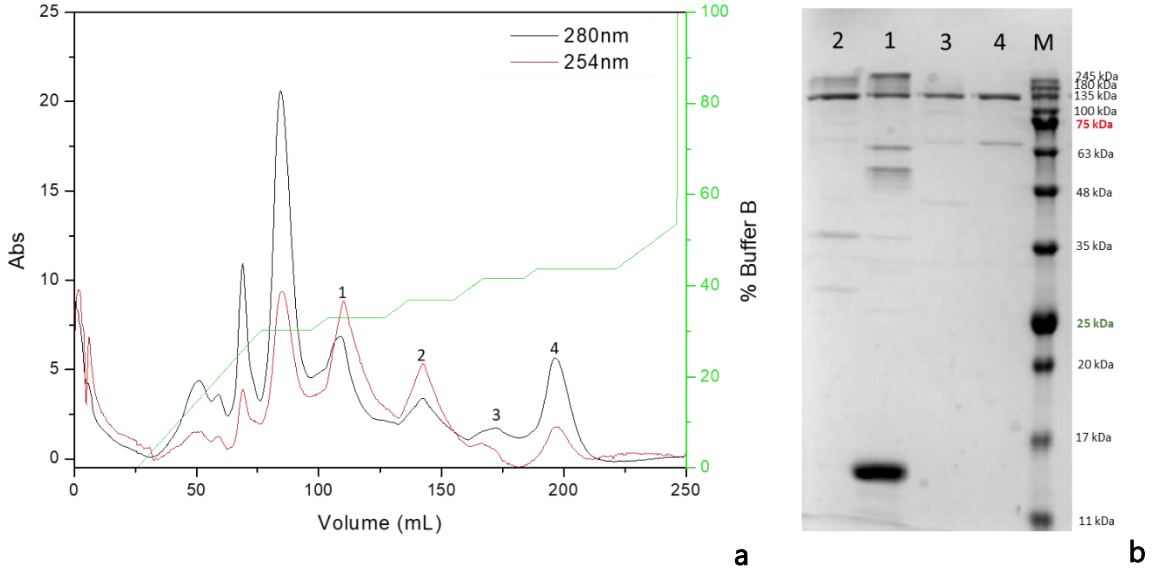

Figure 5.1 — PARP1 Heparin purification. a) Heparin Chromatogram with evaluation of protein UV absorption at 280nm and DNA at 254nm, with indication of four elution peaks representing different "forms" of PARP1 which appeared during the purification process; b) 12.5% SDS-PAGE Gel analysis of the identified PARP1 eluted peaks: M- Molecular weight marker (NZY Colour Protein Molecular II); 1 – peak 1; 2 – peak2; 3- peak 3 and 4- elution peak 4.

SDS-PAGE results indicate that peak 1-3 consist of native PARP1 and PARP1 with increased molecular mass (> 114kDa), while peak 4 seems to comprise pure PARP1 (Figure 5.1b). The shift in mass of the protein in peak 1 and 2 could be related to PARP1 bound to DNA, since the 254 nm UV absorption appears higher than the 280 nm (Figure 5.1a). However, it can also be a result of PARP1 auto-modification since poly (ADP)-ribose (PAR) chains absorb light in the 258 nm [38]. With regards to peak 3, the protein eluted appears to be PARP1 in its auto-PARylated state, as previously described by Langelier et al. (2017) [35].

Analytical size exclusion chromatography (SEC) results confirmed that peak 1 and 2 are mainly DNA bound and PARylated PARP1, since a high absorbance peak was observed at 254 nm, and elution volumes at 9.65 ml (Figure 5.2a) and 11.92 ml (Figure 5.2b), for peak 1 and 2 respectively. In sample 3 (Figure 5.2c) the elution volume was 12.28 ml and a low absorbance peak at 254 nm confirms the hypothesis that the protein sample is free of DNA. However, we cannot discard protein PARylation. This is confirmed when comparing the elution volume of sample 4 (12.7 ml) (Figure 5.2c) to sample 3 (12.28 ml). The results suggest that the mass of PARP1 in sample 3 is higher than in sample 4. The chromatogram profile of sample/peak 4

(Figure 5.2d) is quite distinct from the remaining samples, and due to the low absorbance at 254 nm we suggest that PARP1 is in a "free" form, not bound to DNA nor PARylated. Additionally, the retention volume of PARP1 in sample 4 indicate that the protein has a smaller molecular mass than the remaining PARP1 forms and translates in a molecular value of 261 kDa (refer to Calibration Curve in Figure B.1). This value is quite distinct from the expected PARP1 monomer size (114 kDa) and points to a possible dimeric form of sample 4 PARP1. The second peak eluted at 14.1 ml (equivalent to 146 kDa) in the chromatogram of sample 4 (Figure 5.2d) is confirmed to be PARP1 (Figure B.2), which is a clear indication that besides the dimeric form, PARP1 is also present in an extended monomeric form in sample 4 from the heparin purification step after protein concentration.

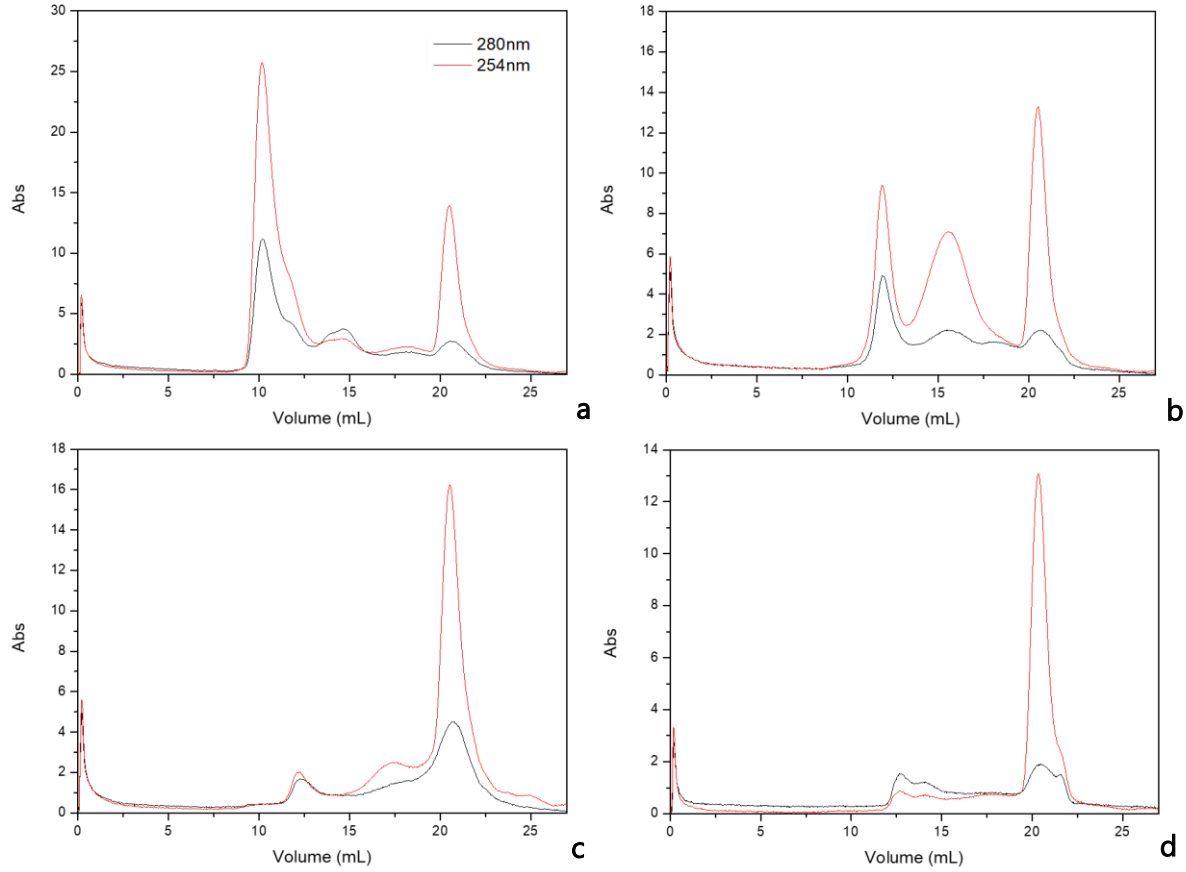

Figure 5.2 — Analytic Size Exclusion Chromatograms from the four PARP1 samples/peaks purified by Heparin affinity chromatography. a) Chromatogram from peak1; b) Chromatogram from peak 2; c) Chromatogram from peak 3 and d) Chromatogram from peak 4.

The low absorbances at 280 nm of PARP1 samples can be explained by the low amount of aromatic residues in this protein (7.5 % of total amino acid residues). This feature represents

some challenges when it comes to protein concentration measurements, which has been reported previously by us [34] and Knight et al. [39].

These results point out to the interesting biological features of PARP1. While conducting the purification, we were able to separate different forms of the protein. We can detect a strong interaction with DNA, possible post-translational modifications and/or interaction with other native proteins (the contaminants that we are not able to remove completely), and finally the free and unmodified form of PARP1.

5.3.2 The PARP1 Oligomeric states

In previous studies it has been suggested that recombinant PARP1 presents two main biological forms: monomer and dimer [33,40,41], that both are able to bind to DNA and are enzymatically active [33,40–42]. To provide more information about this phenomenon, we conducted an oligomeric state analysis of three independent PARP1 purifications (Figure 5.3). In two of the purifications all forms of PARP1 were pooled (Figure 5.1 peak 1-4). One of these pools was concentrated in the Amicon® Ultra-4 (10 kDa MWCO) (Figure 5.3b) and the other was purified using a 1ml Heparin column (Figure 5.3a). The latter served as a batch control sample that is not concentrated. The third independent sample was of the "free" form of PARP1 (Figure 5.1 peak 4), that was also concentrated. The control sample had a concentration of 0.3 mg/ml and the Amicon concentrated samples 1mg/ml.

Results from the SEC analysis of these batches show that PARP1 in the control sample appears in two main oligomeric forms (Figure 5.3a): one bound to DNA (10.6 ml) and one "free" form (13.95 ml) (Figure B.3). Molecular weight estimation using the SEC calibration curve in Figure B.1 indicates that the "free" form has a molecular mass of 158 kDa and the DNA bound form 434 kDa. Taking into consideration PARP1's reported 114 kDa molecular mass [43], the estimated 158 kDa of the "free" form can be an indication that the protein is in the form of an extended/elongated monomer. This proposal is in line with previous suggestions that state that PARP1 in its "free" form has a non-globular extended structure, with an overall "bead-on-a-string" shape [1], and that upon binding to DNA, protein dimerization occurs [33,40,41].

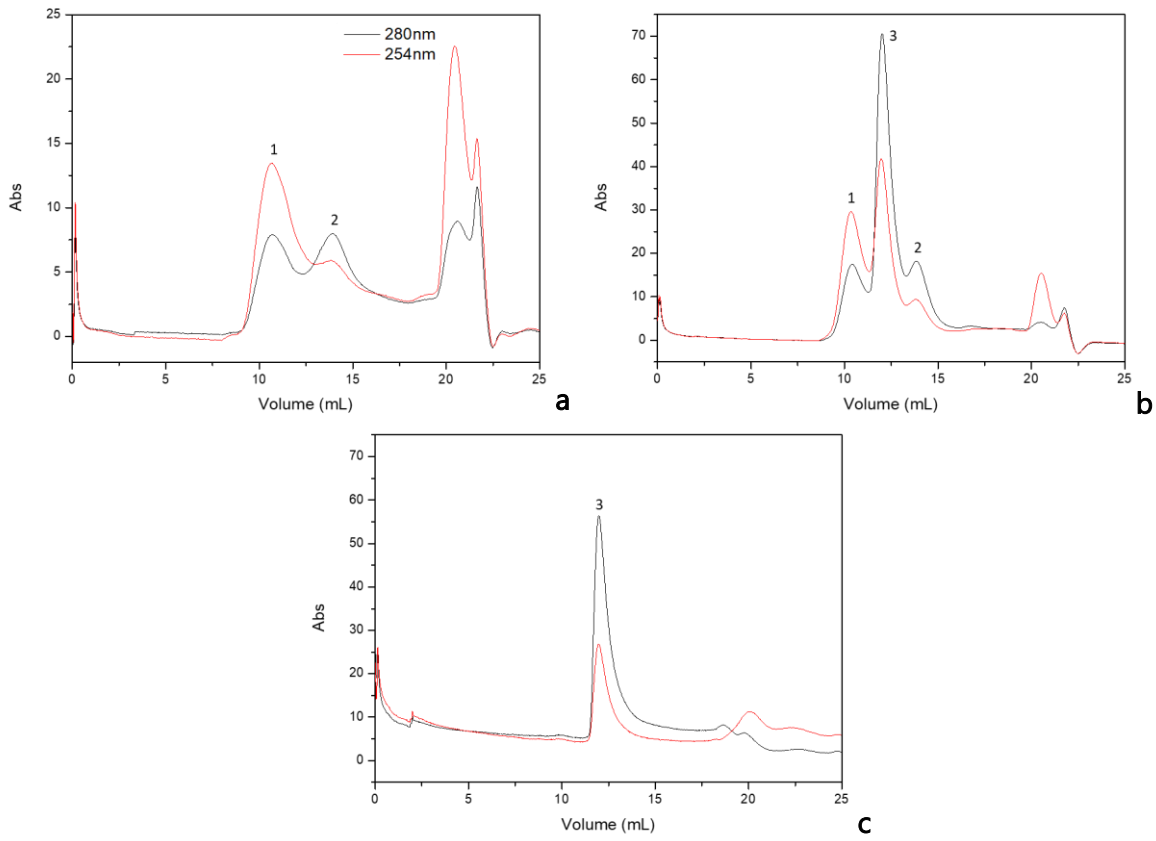

Figure 5.3 — Analytic Size Exclusion Chromatography analysis for concentration effect on PARP1 oligomeric state. a) Chromatogram of control sample, with presence of two PARP1 forms, dimer bound to DNA (identified as 1) and monomer (identified as 2); b) Chromatogram from concentrated sample with identification of three main forms, dimer bound to DNA (1), monomer (2) and "free" dimer (identified as 3); c) Chromatogram from concentrated PARP1 "free" dimer (3).

Regarding the DNA bound form of PARP1 in Figure 4.3a, the estimated protein mass of 434 kDa points to a possible dimeric form of the protein. In the literature the protein dimerization is reported as a more enzymatically active form [41], that serves as a mean to increase repair efficiency by the DNA search "Monkey Bar" mechanism [42]. In the second protein batch (Figure 5.3b), we observe an additional oligomeric form (identified as peak 3) without DNA. This new form is eluted at 12.02 ml (Fig 5.3b) and translates into a protein mass of 317 kDa. Considering the PARP1 monomeric size (158 kDa) and the low absorbance at 254 nm, we believe that this new form is a "free" PARP1 dimer that has arisen due to the concentration procedure. Our analysis of the third protein batch (Figure 5.3c), verified that PARP1 "free" form was eluted at a similar volume (11.97 ml), thus confirming that protein dimerization occurs due to the concentration procedure. The elution volume of PARP1 in batch 3 corresponds to a molecular mass of 321 kDa and shows that purified protein is in one oligomeric state, free of

DNA and that dimerization occurs because of the concentration procedure. Previous reports [44] have shown that the PARP1 monomer is capable of self-association in high-concentration environments. The dimer formation probability is increased by 30 % when the protein concentration is above the 10 μM [44].

A DLS analysis (Figure 5.4 and Table 5.1) of the monomer (peak 2) and the dimer (peak 3) fractions shown in Figures 5.3a and 5.3c, respectively, reveal further information regarding possible quaternary structure and protein folding. Our results demonstrate that the monomer has a mean diameter of 345.05 ± 1.85 nm for the main population (> 91 %) and 118.4 ± 10.4 nm for the second population (8.2 %), with a low polydispersity index (PdI) of 0.29 ± 0.01. The dimeric form presents two populations with values of 268.3 ± 28.6 nm (> 76 %) and 56.32 ± 10.95 nm (< 15.2 %) with a PdI of 0.356 ± 0.002. The detection of two particle populations may be explained by possible orientations of the protein relative to the incident beam and detector. These results point to a more elongated and "sandwich-like" protein structure, for both monomer and dimer. However, it is verified that the dimer form appears to be more compact than the monomer, due to the reduced diameter values. The polydispersity index values (~0.3) indicate a low population heterogeneity and good protein quality in terms of population size distribution.

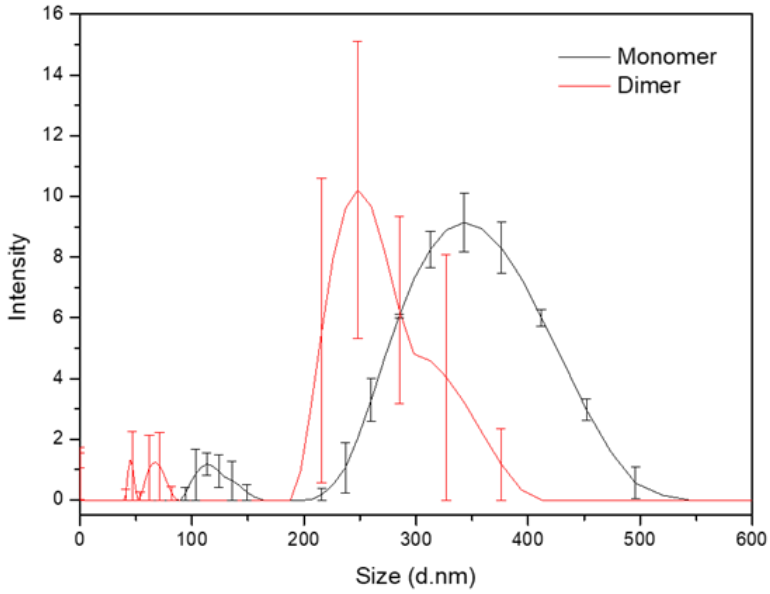

Figure 5.4 — DLS size distribution analysis of PARP1's monomer (black line) and dimer (red line) from. Identification of two main populations, one below the 150 nm in diameter and the other above 200 nm. Monomer presents greater values than dimer, suggesting that monomer exist in a more elongated form and dimer presents higher compaction. The detection of two populations indicate that protein does not behave as a globular protein but has more of an elongated shape.

Table 5.1 — DLS size distribution data regarding differences between monomer and dimer forms of PARP1.

DLS*	Monomer	Dimer
PdI	0.29 ± 0.01	0.356 ± 0.002
Population 1 (nm)	345.05 ± 1.85	268.3 ± 28.6
Population 2 (nm)	118.4 ± 10.4	56.32 ± 10.95
Area Population 1 (%)	91.8 ± 0.1	82 ± 5
Area Population 2 (%)	8.2 ± 0.1	11.65 ± 3.55

*mean values ± SD; PdI - Polydispersity

In sum, our results confirm that a "free" dimeric form of PARP1 arises due to the concentration procedure and that in its native biological state PARP1 appear to present only the "free" monomeric form and a DNA bound dimeric form, thus concluding that the free dimer is an artificial form. In its native biological environment, the PARP1s dimeric form arises by interaction with DNA and as mean to increase the repair kinetics. The plasticity that is shown here related to PARP1s oligomerization is closely related to its diverse biological activities [1].

5.3.3 Concentration Process assessment In Protein Oligomeric Shift

To improve our understanding of the dimerization process of PARP1's "free" form during the protein concentration procedure, we analysed the oligomerization process during a concentration procedure. Four equal volumes of one protein batch were individually concentrated to 5×, 10× and 20× and analysed by SEC. As observed in Figure 5.5, the PARP1 monomer peak shows a shift to lower elution volumes, from 12.99 ml (5×) to 12.38 ml (20×). This change is consistent with the range of elution volumes depicted here for PARP1 "free" monomer (13.95 ml) and "free" dimer form (11.97 ml) and serves as a confirmation of the protein dimerization during the concentration process.

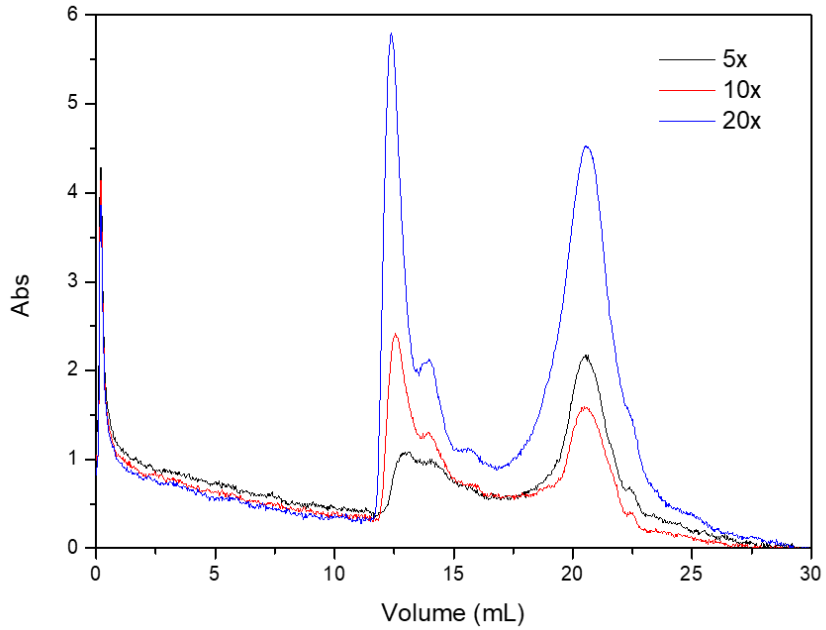

Figure 5.5 — Effect of centrifugal ultrafiltration process on PARP1 oligomeric state. The analysis was performed by measuring the maximum absorbance at 280nm, using the Superdex® 200 Increase 10/30 GL column. Samples were concentrated 5×, 10× and 20× and results show an increase in protein absorbance and a shift to lower elution volumes. PARP1 elution peaks in the 5× sample was elution volume at 12.99 ml (monomer), 10× sample was 12.55 ml (dimer) and 20× sample was 12.38 ml (dimer).

Complementary analysis of PARP1s amino acid sequence with the Aggrescan [45] prediction software, reveals that the protein presents a total of 28 segments that may be involved in inter-molecular interactions. These segments identified coincide with the core of each protein domain and could be an indication of putative protein regions that could be involved in protein-protein interactions. Previous reports have proposed that PARP1 dimerization occur through the BRCT-WGR domains [33] (387-646 aa) and we verify that 7 out of 28 hotspots identified, by the Aggrescan software, coincide with these domains (Figure B.4).

The DLS analysis of these samples (Table 5.2) shows a decrease in the particle Z-average diameter and PdI values, which served as an indication of protein self-association due to the concentration procedure. These results points to the possibility that (1) PARP1 dimer formation may act as a way to stabilize the monomer and that (2) increasing the microenvironment "crowdedness" of the sample by concentration, may aid in protein stabilization.

Table 5.2 — DLS analysis for the effect of protein concentration on protein particle diameter and population heterogeneity.

Concentration	Z-Average* (d.nm)	PdI*
1x	739.90 ± 7.70	0.435 ± 0.03
5x	683.70 ± 25.90	0.345 ± 0.03
10x	547.15 ± 15.05	0.343 ± 0.02
20x	572.35 ± 35.85	0.354 ± 0.04

* mean ± SD; PdI - Polydispersity

The behaviour displayed by the protein in this work has some similarities to those related to intrinsically disordered proteins/regions (IDPs/IDRs), namely the fact that IDP/Rs stabilization is conferred by the microenvironment, their activity, and stabilization chaperons (e.g. Heat-shock proteins) [46–49]. Also, some of their biological activities encompass differentiation, transcription, DNA condensation, cell cycle checkpoint, mRNA processing and splicing, among others, which are assigned due to their intrinsic disordered nature [47,49]. IDPs are considered key participants in intracellular signal pathways (e.g. assembly of large signal complexes and as components of self-assembly membraneless organelles) [47] and some of their typical features are : 1) lack of fixed or ordered 3D structure; 2) presence of highly flexible linkers; 3) presence of linear motifs; 4) transition to more ordered states upon binding to partners and 5) sequence enrichment in hydrophilic disorder-promoting amino acids (P, R, G, Q, S, E, K and A) [46,47]. In this sense, we theorise that PARP1's stability and folding may be regulated in a similar manner, because PARP1 checks the majority of IDP/Rs characteristic features. An analysis regarding the enrichment of PARP1's aa sequence with disorder-promoting residues reveal that these comprise 52.8 % of the total residues.

In eukaryotic proteomes most proteins described are close to those that present IDRs and structured regions [47,49]. Taking this into consideration we performed an IDR analysis of the PARP1 sequence, using the fIDPnn prediction server [50]. The server can analyse any protein sequence, predict and determine the propensity of a given residue to be disordered. The programme is also capable to point at potential participation of the residue in DNA, RNA, protein binding, and linker formation [50].

Six possible IDRs were identified in PARP1 (Figure 5.6), and they comprehend: 1) Zn1 (22-26 aa), 2) Zn1-Zn2 transition (91-105 aa), 3) Zn2-Zn3 transition (199-233 aa), 4) Linker

between Zn3 and BRCT (372-379 aa), 5) linker-WGR (495-520 aa) and 6) HD-ART/CAT (937-956 aa). Region 1-4 comprises the transitions between Zn and BRCT domains and are predicted as linker regions by the software (white boxes). Region 5 is also predicted as a linker region, which coincides with the amino acids associated with the linker preceding the WGR domain. Also, protein binding propensity is predicted in the second half of region 5 due to the dark blue colour (blue boxes), that corresponds to the WGR domain. This gives us another indication, and possible validation, for the hypothesis that this specific domain may be involved in the dimerization process of PARP1. Moreover, DNA and RNA binding propensity (green and red boxes, respectively) are indicated to the same portion of region 5, which coincides with a reported involvement of this domain in nucleic acid binding [1,5,51]. Additionally, region 1-3 are predicted to contain disorder-promoting residues (black boxes), as well as to be involved in DNA and RNA binding, which is indicated by the dark green and red colours. Based on this information we can say that PARP1s binding partners (itself, other proteins, and nucleic acids) appear to help in its stabilization and that the centrifugal induced "free" dimeric form could be a step for additional protein stabilization.

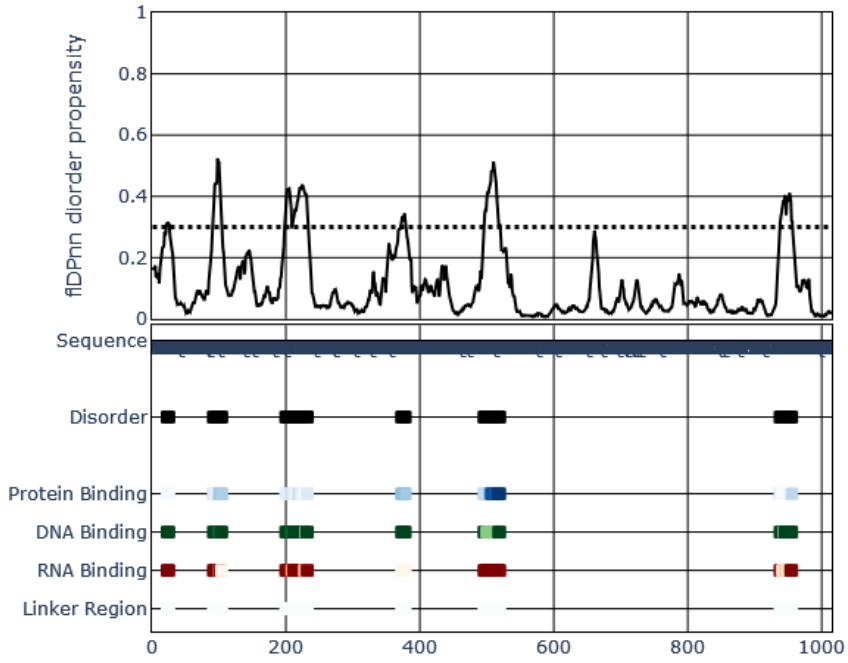

Figure 5.6 — Graphical representation for the prediction of intrinsically disordered regions (IDRs) in the amino acid sequence of human PARP1 using the fIDPnn prediction server [50].

We have previously reported high loss of protein during the concentration procedure, however no filamentous aggregates were visible during these processes [34]. This led us to propose that the protein loss is caused by an interaction with the cellulose membrane in the Amicon ultracentrifugal filters. Thus, the next stage was to identify conditions which increased the stabilization of PARP1 and reduced the losses during concentration.

5.3.4 Protein Stability Assessment

To identify a buffer condition which improved the stability of PARP1, several conditions such as salt concentration and additives were analysed using thermofluor shift (TFS) and nano differential scanning fluorimetry assays (Nano-DSF) (Table B.2). We have reported previously that 50 mM Tris-HCl pH 8.0 is the optimal buffer for stability of PARP1, which translated into a Tm value of 44.2 ± 0.3 °C [34]. Additionally, we verified an increase in the protein stability at high salt concentrations (500 mM NaCl) (Figure 5.7), with the observation of melting values of 48.80 ± 0.15 °C (Table B.3). However, the increased salt stabilization comes with a slight broadening of the derivative melting peaks (Figure 5.7). Due to this, selecting optimal salt concentration has to be weighted depending on buffer use (e.g. storage buffer, reaction buffer, activity buffer, or other). For example, if one is in need to mimic biological conditions and/or potentiate the protein enzymatic activity, it would be more advantageous to use salt concentrations close to 150 mM (where Tm = 45.10 ± 0.50 °C and peak broadening is still not perceived).

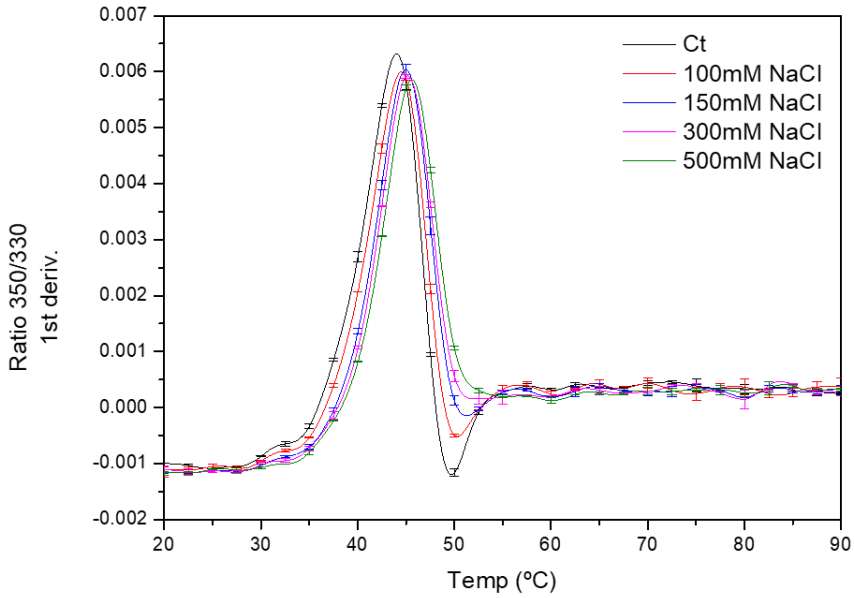

Figure 5.7 — Nano-DSF PARP1's stabilization assessment related to sodium chloride (NaCl) concentration in a 50mM Tris-HCl pH 8.0 buffer. Observed positive feedback relation between salt concentration and Tm value. Shift to high temperature value of the ratio 350/330 nm (1st derivative values).

A comparison of the Tm values determined by Nano-DSF and Thermofluor for purified PARP1 in 50 mM Tris-HCl pH 8.0, 150 mM NaCl, show a difference of approximately 2 degrees, with a Tm = 45.1 ± 0.5 °C and 47 ± 0 °C, respectively (Table 5.3). This difference can be explained by the methods used. One is associated with the protein's intrinsic fluorescence, specifically related to tryptophan (Trp - W) residues (Nano-DSF) and the other with the fluorescence emitted by an interacting dye due to the protein denaturation process [52].

Table 5.3 — Comparative analysis between Nano-DSF and Thermofluor of PARP1 giving melting temperatures of a variety of buffers.

Sample*	Nano-DSF⁺	Thermofluor⁺
150 mM NaCl	45.10 ± 0.50	47 ± 0
150 mM NaCl, 1 mM EDTA, 0.1 mM TCEP	42.65 ± 0.05	46 ± 0
500 mM NaCl, 1 mM EDTA, 0.1 mM TCEP	45.90 ± 0.05	46 ± 0

*50mM Tris-HCl pH8; ⁺ mean ± SD

To evaluate the stabilization effect of the reducing and chelating agents used in the Heparin purification, a stability analysis was performed in low (150 mM NaCl) and high salt condition (500 mM NaCl) using both TSF and nano DSF. The result demonstrated Tm values of 42.65 ± 0.05 °C (Nano-DSF) and 46 ± 0 °C (Thermofluor) in 50 mM Tris-HCl pH 8.0, 150 mM NaCl 1 mM EDTA, 0.1 mM TCEP, while at high salt concentration the Tm value was 45.9 ± 0.05 °C (Nano-DSF) and 46 ± 0 ºC (Thermofluor) (Table 5.3). These values present a reduction in Tm and some protein destabilization compared to equivalent buffers without the added agents. This result can possibly be explained by the properties of these agents, which are usually associated with protein destabilization [53]. Nevertheless, addition of the reducing agent is of outmost importance because it will help to prevent undesirable protein-protein interaction [53] and EDTA chelate metals that promote proteases activity and protein degradation [54]. Interestingly, there is a greater difference in the Tm values for PARP1 at low salt concentration in the Nano-DSF experiment than in TSF. This difference could be an indication that high salt concentration may help to compensate protein destabilization due to TCEP and EDTA presence. The disparity (> 3 °C) between the Tm values at 150mM NaCl is also an indication that reducing and chelating agents have a greater impact on residues with intrinsic fluorescence in the protein. This can give some indication to which protein regions that are involved in the stabilization (positive or negative) process.

Examining the three canonical residues in PARP1's aa sequence - tryptophan (Trp - W), tyrosine (Tyr - Y) and phenylalanine (Phe – F) -, we verify that they are present in all domains of PARP1 and that they represent 7.5 % of total residues (Figure B.5). From these, Y and F are the ones with highest contribution, 3.2 % and 3.0 %, respectively. While W residues, which are usually analysed by Nano-DSF, have a 1.3 % contribution to PARP1's full-length sequence. In terms of protein domain localization, the 13 W residues are found in: Zn 1-3 with 7 residues (53.8 %), BRCT with only 1 residue (7.7 %), WGR with 3 (23.1 %) while the HD-ART domain has 2 residues (15.4 %). As so, any results regarding PARP1's Nano-DSF thermostability analysis should be carefully interpreted and take into consideration that the data provided will have over 50 % input from only 36 % portion (Zn1-3) of full-length structure.

Nevertheless, one of the biggest advantages provided by Nano-DSF is its capability to analyse low amounts of protein (0.5-1 µg), which is of great assistance in the study of proteins with low yields [52]. Also, this technique can be helpful by circumventing thermofluor dye incompatibility with some stabilization additives and buffer formulations [55]. The data

presented so far give a strong indication that, in specific cases, thermostability techniques need to be used complement to each other, to ascertain the assessment of protein stabilization.

Additional additive compounds were tested, such as detergents (1 mM) (zwitterionic - Zwittergent 3-10 - and non-ionic - Mega 8 and n-octyl-β-D glucoside), glycerol (5, 10 and 15 %), amino acids (Glycine, D-Alanine, L-Lysine, L-Arginine and L-Proline), the denaturing agents guanidine hydrochloride (150 mM and 500 mM) and sucrose (25 mM). But unfortunately, the results did not show significant protein stabilization (Tables B.4 and B.5).

5.3.5 Ions as Stabilization Partners

In this section we focus on the assessment of divalent cations as potential stabilization partners of PARP1. Divalent cations are associated with enzyme activity and are considered essential for enzymatically active proteins to act in their biological environment [56] and have been suggested to work as natural "crowders" [57–59].

We focused mainly on the divalent cations: calcium (Ca^{2+}), magnesium (Mg^{2+}), manganese (Mn^{2+}), zinc (Zn^{2+}), iron (Fe^{2+}) and nickel (Ni^{2+}). Initial assessments involved the usage of ions in a final concentration of 1 mM in a 50 mM Tris-HCl pH 8.0, 150 mM NaCl buffer.

By Nano-DSF we observed that each of the selected ions interacted differently with the protein, revealing distinctive melting events. The profile of the melting curves indicates that Mg^{2+}, Ca^{2+} and Fe^{2+} contribute to a single denaturation event, while the remaining cations promote two or more denaturation steps (Figure 5.8a). The addition of Mg^{2+} or Ca^{2+} to the buffer results in an increase in the Tm of approximately 5 °C (Table 5.4), however a slight peak broadening occurs with the latter. Fe^{2+} increases PARP1's Tm with 3 °C, but because Fe^{2+} is easily oxidized to Fe^{3+}, this cation is not a good candidate for protein stabilization [60]. Although Mn^{2+}, Zn^{2+} and Ni^{2+} retrieves the highest increase in Tm (> 5 °C) (Table 5.4), the observed denaturation profiles (with indication of two distinguishable Tm values) exclude these ions as potential stabilizers for PARP1.

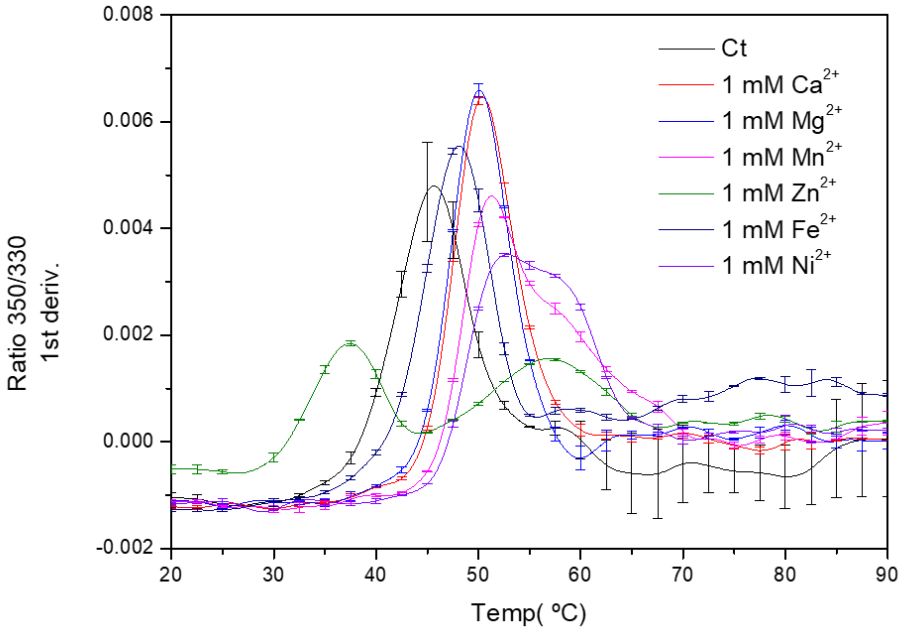

Figure 5.8 — Nano-DSF analysis of PARP1 stabilization with different divalent cations in a low salt concentration buffer (50 mM Tris-HCl pH 8.0, 150 mM NaCl).

Table 5.4 — Measurement of melting temperatures of PARP1 by Nano-DSF, assessing buffer (50 mM Tris-HCl pH 8.0, 150 mM NaCl) supplemented with divalent cations (Ca^{2+}, Mg^{2+}, Mn^{2+}, Zn^{2+}, Fe^{2+} and Ni^{2+}).

Divalent Cations*	Tm 1⁺	Tm 2⁺
Ct	45.70 ± 0.09	-
Ca^{2+}	50.50 ± 0.01	-
Mg^{2+}	50.20 ± 0.02	-
Mn^{2+}	51.60 ± 0.08	57.90 ± 1.13
Zn^{2+}	37.40 ± 0.22	56.90 ± 0.07
Fe^{2+}	48.10 ± 0.13	-
Ni^{2+}	53.60 ± 0.03	57.80 ± 0.29

* 50mM Tris-HCl pH 8.0; ⁺ mean ± SD (°C)

The metals impact on the activity of PARP1 was further analysed using the auto-modification assay (Figure B.6) [35]. The results demonstrated that the protein activity increased in presence of Mg^{2+}, Ca^{2+} and Mn^{2+}. The smear pattern observed with Ni^{2+} is perceived as partial protein modification and a slower reaction kinetic. Taking into consideration the Tm values, the melting profiles, and the activity assay results, we selected Mg^{2+} and Ca^{2+} as the best

candidates for protein stabilization. Although Mn^{2+} favours protein activity we don´t consider it for protein stabilization because of its multi-peak denaturation profile (Figure 5.8).

The divalent cations Mg^{2+}, Mn^{2+} and Ca^{2+} have significant biological roles intracellularly. Mg^{2+} is present at approximately 40 mM, while Mn^{2+} and Ca^{2+} are found in the micromolar range, 0.5 µM and 0.1 µM, respectively [61]. Magnesium and calcium homeostasis is strongly associated with basal and complex cellular processes, such as gene expression, transcription, differentiation, bioenergetics, cellular proliferation, neurotransmission, cellular death, among others [62–64]. And it's interesting to notice that there is a specific organelle compartmentalization/representation of these ions in the nuclei, cytosol, and mitochondria, where PARP1 is present and enzymatically active [5,65,66]. Any alteration in the metal concentration equilibrium can lead to intracellular stress and development of pathologies such as cancer. It has been shown that intracellular compartment flux, as well as intra- and extracellular flux alterations are involved in tumour initiation, progression, angiogenesis, and metastasis [62,64,67].

This information directs us to rationalize and inquire which optimal concentration should be used for PARP1 stabilization in vitro. A range from 0 to 5 mM of Mg^{2+} and Ca^{2+} were tested. The results showed that concentrations above 1 mM did not result in an increase in Tm (Table B.6). By combining Mg^{2+} and Ca^{2+} in buffers with varying salt concentrations also didn't result in a significant increase in Tm (> 3 °C). The PARP1 Tm values remained around 51 °C (Table B.7). However, the Nano-DSF melting curves showed a broadening of the 350/330 ratio (1st derivative) melting peak with the increase of salt concentration (Figure B.7). This is an indication that at high salt concentrations, $Mg^{2+}$and Ca^{2+} favour a differential denaturation process of PARP1 and that a combined optimal stabilization is achieved at low salt concentrations (≤ 150 mM).

Finally, the effect of salt (150 mM), ion (1 mM) and reducing agent (0.1 mM TCEP) was assessed by Nano-DSF. No significant alteration was observed between samples with (Table B.8) and without TCEP (Table 5.4) (Tm ≈ 50 °C) in the presence of Mg^{2+}or Ca^{2+}. TSF analysis indicates that the addition of Mg^{2+} resulted in a higher Tm in a reducing buffer than Ca^{2+} but the difference is not significant (1 °C) compared to the control sample. The result from the TSF experiments indicate that ions do not contribute to a global change in protein folding, due to the lack of significant Tm variation. However, the Nano-DSF results, points to a possible protein stabilization (Figure 5.8, Table 5.4, Figure B.7).

Considering, the presence and distribution of tryptophans in PARP1's aa sequence (see section 5.3.4, 4th paragraph), the stabilization conferred by Mg^{2+} and Ca^{2+} may be related to pin-point regions/domains in the protein. These could possibly be allosteric sites, where ions

act as modulators, and thus regulate small conformational changes that enhance e.g. the protein binding affinity to partners or its enzyme activity [68]. Keeping in mind this hypothesis, the activity results seen in Figure B.6 can serve as an indication for the divalent cations' action mode and stabilization effect observed by fluorimetry. Probably only by the presence and binding of a specific partner, like DNA/RNA or protein, we may be able to observe an overall conformational change.

Previous reports have shown allosteric modulation effects of Ca^{2+}, where the divalent cation interacts with two specific binding sites of the calcium sensing – receptor (CaSR) and counteracts structural negative charge to help the channel to open and activate the sensor [69]. Also, in calcium and integrin binding protein 2 (CIB2), Mg^{2+} has an important role as an interdomain connector. In active physiological conditions this ion leads to a non-covalent dimer oligomerization of CIB2. It is only in this dimeric form that CIB2 can interact to its physiologic target α7B integrin. Any mutation to the ion binding residue, abolishes any conformational change and target interaction [70]. Mg^{2+} is known to affect also enzyme activity, either by 1) ligand binding, 2) active site binding, 3) conformational change during enzymatic process, but even more curiously 4) in the promotion of multi-enzyme complex assembly (e.g. aldehyde dehydrogenase, ALDH) [56]. This is interesting in relation to the results we obtained by DLS, of a dialyzed PARP1 sample into a magnesium supplemented buffer (50 mM Tris-HCl pH 8.0, 150 mM NaCl, 0.1 mM TCEP, 1mM $MgCl_2$) (Table B.9). These results indicate that Mg^{2+} could be an association promoter factor in PARP1's oligomerization. Z-average values between control sample and magnesium sample did not show a significant change, but PdI values and population diameter values increased when Mg^{2+} was included in the buffer. PdI increased from 0.34 ± 0.02 to 0.41 ± 0.04 in the ion supplemented buffer, while the mean values for population 1 and 2 increased from 615.3 ± 37.1 nm to 754 ± 94 nm and 95.6 ± 95.4 nm to 286.1 ± 93.3 nm, respectively (Table B.9). The change in PdI and particle diameter values indicated that PARP1 has an apparent extended form in the absence of Mg^{2+}, while the presence particle volumetry increases. This is probably due to possible protein-protein interactions and/or the excluded volume effect, which we have discussed in the beginning of this section.

5.3.6 Binding partners for Protein Stabilization - DNA

PARP1's major binding partner is DNA. However, the interaction stoichiometry can vary depending on the type of damage [40,66,71,72]. Here we have analysed how DNA can stabilize PARP1 and have used small double stranded oligonucleotides (~15 nt) with different end

modifications and lesions: 1) Blunt ends (undamaged DNA), 2) double strand break DNA with 5′ and 3′ overhang strands (DSB), 3) nicked DNA (SSB), 4) abasic site (Ab) and 5) Ab in combination with DSB. First, we analysed how DSB and DSB+Ab damages would affect protein activity by using the Langelier et al., (2011) auto-modification assay, and 1 μM DNA and protein.

Our results demonstrated that PARP1 can auto-modify itself in the presence of both undamaged (blunt) and DSB (5′ and 3′ overhang) DNA (Figure 5.9a). Differences are observed between the DSBs, with the 3′- overhang sample presenting a modified PARP1 band after a 10-minute reaction in the 4 % stacking gel, while the 5′-overhang DNA reaction presents this band only at the 30-minute time point. This can be interpreted as a difference in activity kinetics. In the presence of 3′ DSB PARP1 appears to be more active, when compared to 5′ and blunt DNA reactions. Although PARP1 auto-modifies itself in the presence of undamaged DNA (blunt), the reactions with 3′ DSB indicate that reaction kinetics are increased, due to the intensity of the modified protein band in the limit of the separation gel and to the smear pattern in the concentration counterpart (Figure 5.9a). The presence of an abasic site did not introduce an apparent difference in PARP1's activity (Figure B.8a), compared to the controls in Figure 4.9a. In all conditions (Figure 5.9a and Figure B.8a) we observed the presence and maintenance of unmodified protein band, which led us to analyse PARP1's binding efficiency by EMSA.

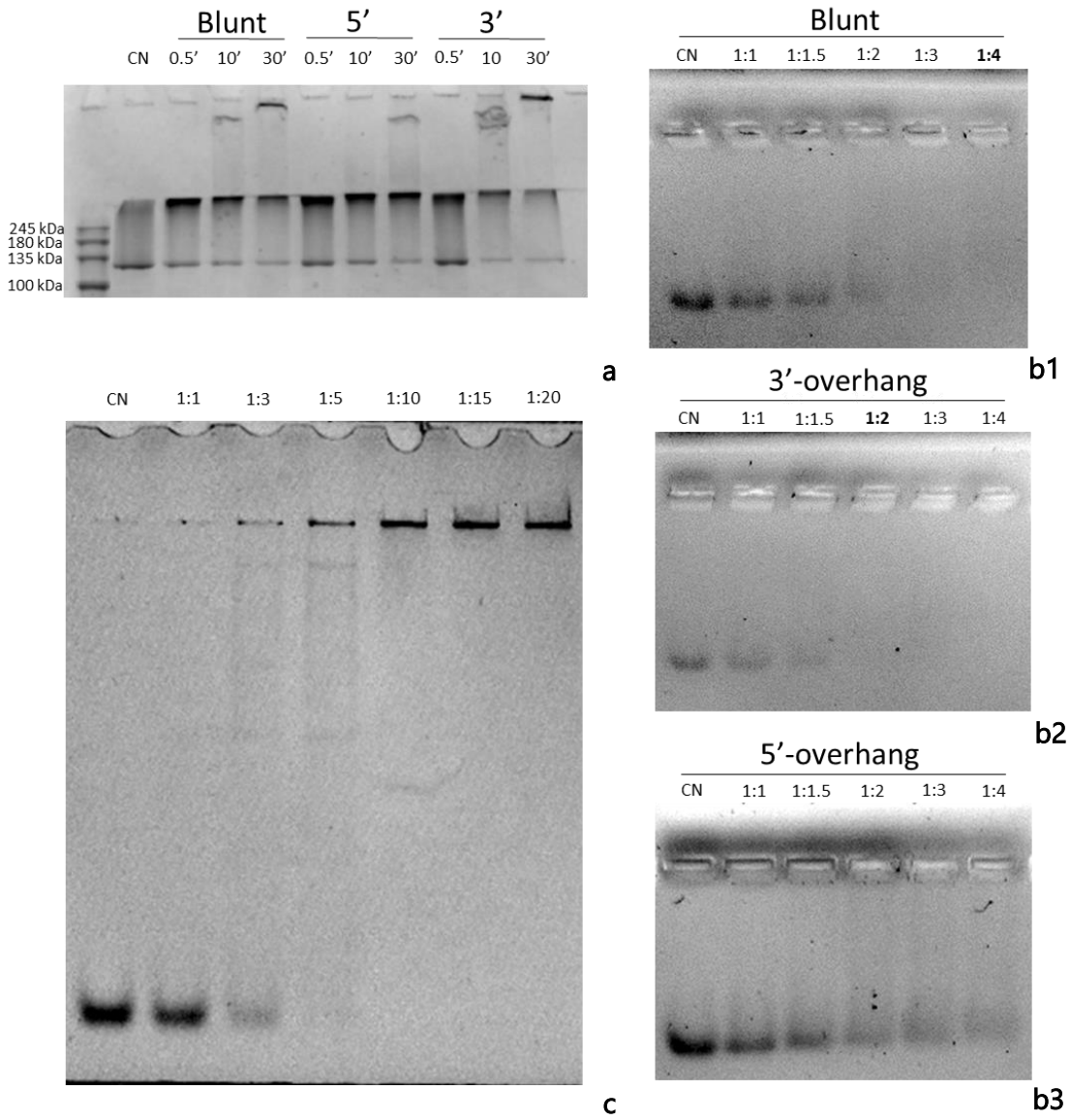

Figure 5.9 — DNA damage effect on PARP1 activity and binding affinity. a) Effect of different DSB damages on PARP1 activity and reaction kinetic. Assays were performed with 15 nucleotides dsDNA with different reaction timepoints. Blunt DNA represented undamaged DNA and DSB were represented by 5’- and 3’- overhang dsDNA. Observation of different reaction kinetics, with 3’ template incrementing PARP1 activity by the visualization of large, modified products in the concentration portion of the SDS-PAGE gel. 5’- overhang DSB presented the least increment in PARP1 activity, due to the surfacing of the large, modified protein only at 30-minute time reaction. b) EMSA results with unlabeled 15nt dsDNA in 1% agarose gels. Affinities of PARP1 to DSB templates are different, with highest affinity being verified with 3’- (1:2) (b3), followed by blunt (1:4) (b1) and 5’-onverhang (unreached binding value) (b2). c) EMSA assay with FAM - labelled 3’-obverhanged dsDNA (43nt). DNA-protein ratios were varied and analyzed in a 4% non-denaturant acrylamide gel. Results indicate a binding affinity ratio of 1:5.

The binding assays were performed with variable protein concentrations, in an incubation buffer consisting of 50 mM Tris-HCl pH 8.0, 150 mM NaCl, 25% glycerol. DNA templates

(1 μM) used for the EMSAs where the same as in the activity assays. What we uncovered was a difference in binding affinities, which was dependent on the type of DNA damage. We verified that PARP1 presented a higher binding affinity to 3′-overhang DSB, where complete DNA binding requires two protein molecules (1:2 ratio) (Figure 5.9b2). Blunt DNA retrieved a 1:4 ratio (Figure 5.9b1), while complete DNA binding was not achieved with 5′-overhang (Figure 5.9b3). Interestingly, the differences detected in binding affinity coincides with the ones observed in the PARP1 activity assay (Figure 5.9a), with the protein demonstrating highest activity on the 3′-overhang substrates. The coherence observed indicates that the enzyme kinetics of PARP1 is affected by the affinity to DNA molecules and the type of damage.

Previous reports have shown similar results, indicating that the binding affinities of PARP1 varies depending on the type of DSBs [40]. An analysis of PARP1 DNA binding domains (Zn 1-3) showed that the DNA-protein ratio was 1:2 with 3′-overhang and 1:1 with 5′-overhang/undamaged DNA [40]. Even though, our data coincides with reported 3′-overhang stoichiometries, there is a great discrepancy between the values of 5′ and undamaged DNA. This may be due to the DNA templates and the recombinant protein used. Regarding the first, in our analysis we employed an 15nt double DSB template, with a 1nt overhang, while Pion's study (2005) resorted to 66 nt DNA templates, with 32nt overhangs [40]. Also, while in our experiments we used a recombinant full-length PARP1, Pion analysed the binding effect with a smaller construct of PARP1 (Zn1-3). Although the DNA templates that were used by us were smaller, the results are still viable, because the minimal DNA length needed for PARP1 binding and activity is around 8bp [73].

To further analyse the binding properties, we proceeded to an EMSA analysis with a 43nt FAM-labelled 3′-overhang dsDNA, which contained one 3nt overhang. In this complementary assessment, the DNA:protein ratios (Figure 5.9c) were higher (1:3) than observed previously (1:2) (Figure 5.9b2). Total binding occurs at 1:5-10 (Figure 5.9c). Furthermore, assays with FAM labelled dsDNA control (blunt – 43nt) and SSB dsDNA (40nt), indicates that for control template PARP1 has a similar binding behaviour and ratio as 3′ overhang, while with SSB template ratio is of 1:15 (Figure B.9). Also, it is important to notice that the binding profile of PARP1 appears as a smear and multiple bands patter in all results, which is an indication that different size complexes are formed. This points to the central role of PARP1 in the formation of large repair complexes.

Additionally, our affinity assessments indicate that the way the activity protocol is designed (1:1 ratio of DNA-protein) optimal binding ratios were not used, which could partially justify the permanence of an unmodified PARP1 band (as seen in Figure 5.9a). Another

explanation can be related to the complete consumption of NAD+ in the assay. PARP1 among the PARP family is the one capable of generating long branched PAR chains [74–76], which in a small-scale assay may lead to great NAD+ consumption and conversion. Also due to its capability of cis and trans modification and activity in the monomer state [4,41,77], the theory of complete NAD^+ consumption is reinforced.

Further assessments were done combining the effect of divalent cations and DSB, where the affinity of PARP1 to a FAM-labelled 3'-overhang template was assessed, in the presence of Ca^{2+}, Mg^{2+}, Mn^{2+}, Zn^{2+} and Ni^{2+}. Assays were designed to give a final ion concentration of 5 mM and the binding buffer was composed of 50 mM Tris-HCl pH 8.0, 150mM NaCl and 25% glycerol. Complete binding ratios were 1:5 to 1:10, for all assessed ions (Figure 5.10a-e), with Zn^{2+} presenting the highest ratio/lowest affinity (Figure 5.10d). Differences were observed in terms of binding profiles and patterns. Mg^{2+}, Zn^{2+} and Ni^{2+} assays show that at 1:1 ratio binding occurs (Figure 5.10a, d and e), due to the decrease in band intensity of free DNA. Moreover, Ca^{2+} is the only cation where protein-DNA binding occurs as a "all-or-nothing" event (Figure 5.10c). All ion binding assays show smear and band patterns, indication the formation of large and different size complexes. Also, at ratios above 1:10 we verify difficulties for protein-DNA complexes to enter the gel, and in ratios above 1:15 the complexes remain in the well (Figure 5.10a-e).

Taking into consideration all the data that we have so far, we conclude that Mg^{2+} and Ca^{2+} are the best candidates for DNA-protein complex stabilization. However, among the two, Mg^{2+} is the preferable choice due to the moment of initial complex formation and the band intensity of "free" DNA (Figure 5.10a). Differences in binding affinity due to ion content were reported in other proteins, such as p53, where Mg^{2+} affects DNA binding and the sliding procedure of this protein [78]. As with PARP1, p53 interaction with DNA is sequence independent and even at low Mg^{2+} concentrations, p53 sliding velocity on DNA is regulated. An increase in ion concentration leads to positive feedback in sliding velocity [78] and at high concentrations like 8-10 mM, p53-DNA complexes tend to condensate and aggregate [78]. This event is due to the weakening effect of Mg^{2+} on protein-DNA binding, which in turn accelerates p53 sliding along the DNA strand. The increased acceleration leads to the aggregation of the moving proteins and consequently to the natural assembly of DNA-p53 large network structures. The aggregation tendency starts to appear even at 5 mM of Mg^{2+} [78]. Based on this observation and due to the discussed similarities between PARP1 and p53, we theorise that divalent cations may have a similar role in the binding/interaction of PARP1 and its biological partners.

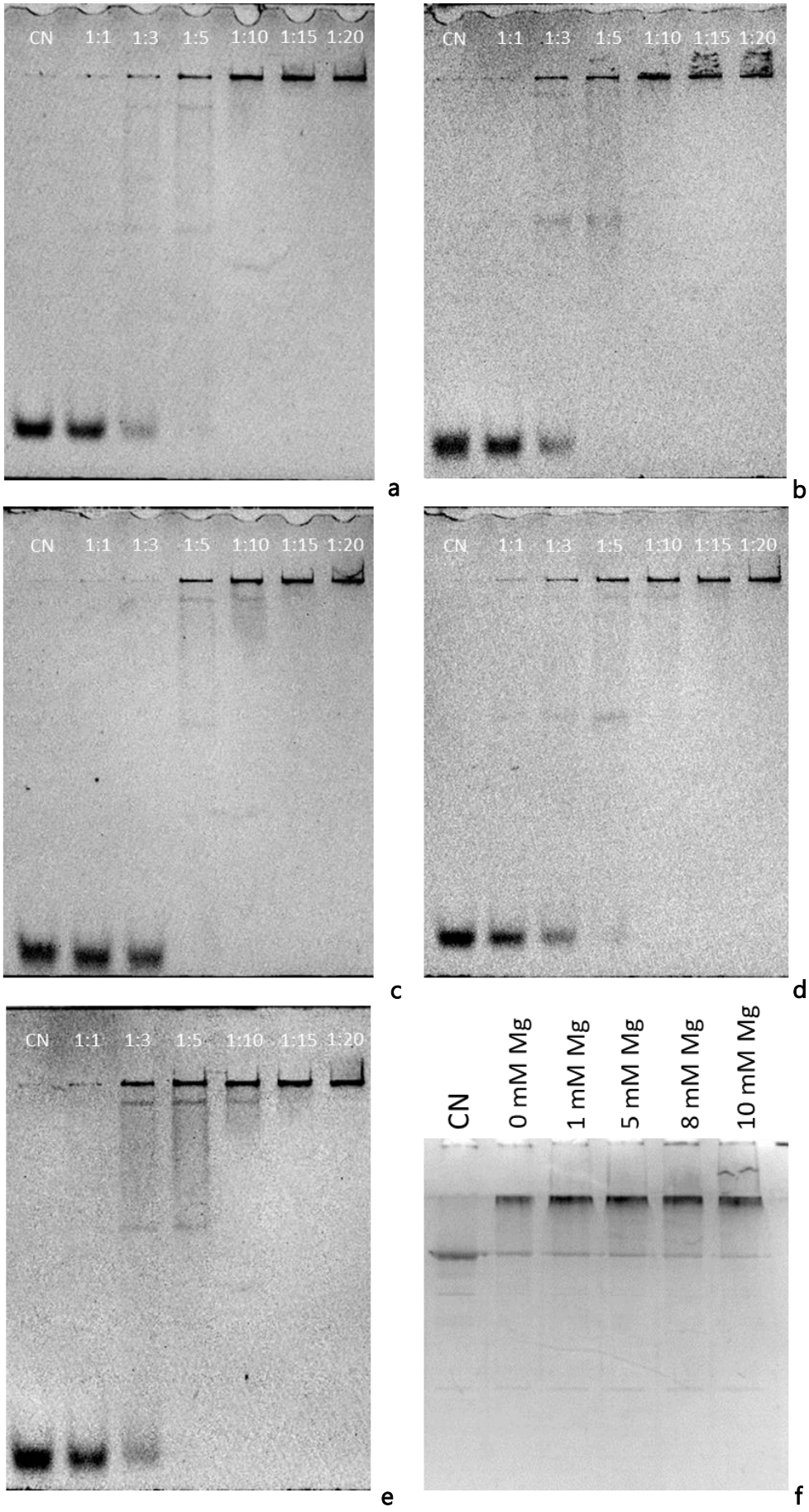
CN 1:1 1:3 1:5 1:10 1:15 1:20
a
CN 1:1 1:3 1:5 1:10 1:15 1:20
b
CN 1:1 1:3 1:5 1:10 1:15 1:20
c
CN 1:1 1:3 1:5 1:10 1:15 1:20
d
CN 1:1 1:3 1:5 1:10 1:15 1:20
e
CN
0 mM Mg
1 mM Mg
5 mM Mg
8 mM Mg
10 mM Mg
f

Figure 5.10 — Ion Effect on PARP1's binding affinity to 3'-overhang DSB and enzymatic activity. a) Mg^{2+} effect on PARP1 binding affinity to DSB (1:5); b) Mn^{2+} effect on PARP1 binding affinity to DSB (1:5); c) Ca^{2+} effect on PARP1 binding affinity to DSB (1:5); d) Zn^{2+} effect on PARP1 binding affinity to DSB (1:10); e) Ni^{2+} effect on PARP1 binding affinity to DSB (1:5); f) Mg^{2+} concentration effect on PARP1 auto-modification activity. PARP1 activity is increment in the presence Mg^{2+} and the use of concentrations above 1 mM do not produce significant differences in the un/modified bands of PARP1.

The effect of magnesium concentration on PARP1's binding affinity (Figure B.10) and enzymatic activity (Figure 5.10f) was assessed. Concentrations tested were 0 to 10 mM in both assays, the DNA-protein ratio was fixed to 1:5 and the reaction time of the activity assays were fixed at 10 minutes. In the EMSA assessment (Figure B.10), we did not observe any difference on PARP1 binding affinity to the FAM-labelled 3'-ovehang DNA, however an increase in PARP1's activity was verified in the presence of Mg^{2+} (Figure 5.10f). Ion concentrations above 1 mM do not appear to further increment PARP1 activity (Figure 5.10f), which is coherent with the thermostability assessments (Table B.6), where we verified that concentrations of Mg^{2+} and Ca^{2+} above 1 mM did not result in a significant Tm increase.

Mg^{2+} and Ca^{2+} ions are also known to have a great impact in DNA homeostasis and in the stabilization specific DNA structures [72]. These ions usually bind to the major grooves (rich in GC) and stabilize the bend [61,72]. Divalent cations can influence DNA and RNA tri-dimensional structures and transient metal ions can induce B- to Z- form transition in a poly[d(GC)] loci [61]. Moreover, reports have shown that the stabilization of G-quadruplex DNA structure by intracellular ions present the preferential order of: $K^+ > Ca^{2+} > Na^+ > Mg^{2+} > Li^+$ [79]. This evidence shows the importance and impact that intracellular ions may have on DNA homeostasis. Connecting this information with reported evidence that PARP1 interacts, binds, and stabilizes loops and G-quadruplex structures [72], we may say that divalent cations could play a role in these specific events.

To further understand how DNA and ions are affecting the stabilization of PARP1, we proceeded to a thermostability analysis of these complexes. All experiments were done in a 50 mM Tris-HCl pH 8.0 and 150mM NaCl buffer, where a 1:1 protein-DNA ratio was used and the effect of two divalent cations (Mg^{2+} and Ca^{2+}) was assessed. DNA used was the unlabelled 15nt dsDNA blunt and DSB templates (5' and 3') and concentrations were 1.76 µM and 1.16 µM in Nano-DSF and TSF, respectively.

Comparing the effect of the 5' and 3'-overhang DNA templates on the stabilization of PARP1, we observed tendencies in the Nano-DSF experiments (Table 5.5) which were in line with the activity assays and EMSAs. PARP1 presents higher Tm values with Blunt (47.30 ± 0.10

°C) and 3′-overhang DNA (47.70 ± 0.10 °C), than 5´-overhang (46.40 ± 0.10 °C). However, in comparison to the PARP1's control sample (without DNA) (46.40 ± 0.10 °C), the difference in Tm values is not biologically significant (≥ 3 °C). This could be related to the DNA-protein 1:1 stoichiometry used in the assay, which is different from the ratios verified earlier in this section. By TSF we verified a decrease in the Tm value for Blunt (2 °C) and 5′-overhang (1 °C), and no Tm variance with 3′-overhang, when compared to the control sample (Table 5.5).

Table 5.5 — Analysis of PARP1 stabilization by interaction with different DNA damage templates, by Nano-DSF and Thermofluor.

DNA Binding*	Nano-DSF+	Thermofluor+
Ct	46.20 ± 0.30	47 ± 0
Blunt	47.30 ± 0.10	44.50 ± 0.50
DSB 5′-overhanged	46.40 ± 0.10	46 ± 0
DSB 3′-overhanged	47.70 ± 0.10	47 ± 0

* 50 mM Tris-HCl pH 8.0, 150mM NaCl; + mean ± SD

Due to the results obtained by measuring PARP 1 activity and binding affinity using the unlabelled 3′-overhang templates, the joint effect with the Mg^{2+} and Ca^{2+} was assessed on PARP1's thermo-stabilization. 1:2 DNA-protein ratio and 1 mM ion concentration was used. The nano-DSF results (Figure 5.11) show that the Tm of PARP1 is increased in the presence of the DNA and it is possible to visualize a sharp denaturation peak (Figure 5.11) with a shift of 3.5 °C (Table 5.6), when compared to the control sample. PARP1's Tm values at 1:2 DNA-protein ratio provides better results than 1:1 (refer to Table 5.5). In the presence of the divalent cations the retrieved Tm values are above 50 ºC (Figure 5.11 and Table 5.6). Differences between Mg^{2+} and Ca^{2+} do not appear to be biologically significant. The melting curves of Prot + DSB + ion samples show that the presence of the divalent cations induces a change in the profile of the melting curves (350/330 ratio) (Figure 5.11). The presence of a negative peak around 45 °C and a positive peak at 50 °C, is an indication that the combined effect of DNA + ion appear to preferably stabilize hydrophilic exposed aromatics (positive peak, with Tm ≈ 51 °C). The Tm results observed in Prot + DSB + Ion samples are very similar to Tm values retrieved for Prot + Ion (Table 5.4). These results denote that Mg^{2+} and Ca^{2+} are preponderant PARP1 stabilizers in a complex system, with preferable hydrophilic aromatic stabilization.

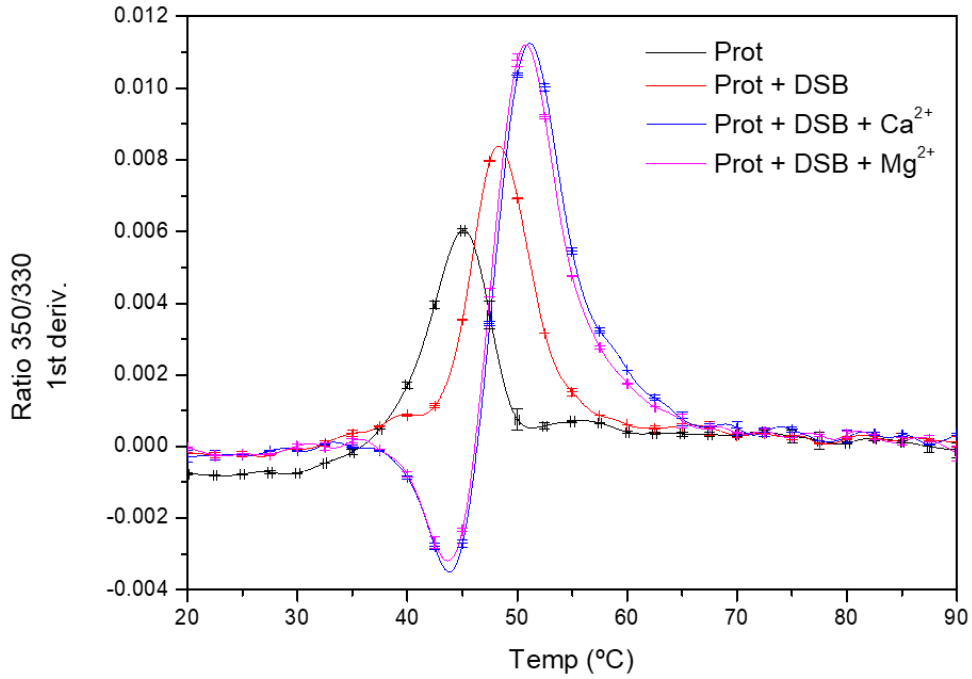

Figure 5.11 — Thermostability analysis on the stabilization effect of DNA binding, DNA damage and ions effects combined on PARP1. Unlabeled 3'-overhang DNA (14nt) was used in a 1:2 DNA-protein ratio and 1mM of $MgCl_2$/$CaCl_2$.

Table 5.6 — Melting temperature values determined by Nano-DSF regarding the effect of unlabeled 3'-overhang DSB (14nt) (1:2 DNA-protein ratio) and ion content (1 mM).

Sample*	Tm+
Prot	45.00 ± 0.18
Prot + DSB	48.50 ± 0.02
Prot + DSB + Ca^{2+}	51.30 ± 0.02
Prot + DSB + Mg^{2+}	50.90 ± 0.03

* 50 mM Tris-HCl pH 8.0, 150mM NaCl; + mean ± SD

The combined stabilizers assessments indicate the existence of a positive feedback between PARP1 enzymatic activity and the presence of DNA and the divalent cations Mg^{2+} and Ca^{2+}. However, thermostability analysis showed that an increase in the melting temperature is greatly related to the ion content. Results showed that PARP1 has a preferable binding affinity to 3'-overhang DSB templates and that differences in the DNA binding affinity impact PARP1's

enzyme kinetics. The ion content has an impact on PARP1-DNA binding and is probably associated with the complex DNA-protein formation and/or sliding (as with p53). The ion concentration did not appear to have an impact on the protein binding affinity, however PARP1 activity was enhanced upon addition of ions and the formation of large protein complexes was verified.

5.3.7 PARP Inhibitors In protein stabilization and structural assessments

In light of the results here depicted, the assessment of the stabilization effect of some known PARP1 inhibitors (PARPi) was performed. Among the compounds available we selected three molecules: 1) Niraparib (MK-4827); 2) Rucaparib (AG-014699) and 3) Veliparib (ABT-888). These inhibitors belong to the type III category of PARPi, where its inhibitor capability is related to protein allosteric regulation of PARP1 release from DNA [15].

A preliminary activity analysis confirmed the inhibitory ability for all compounds in the purified recombinant PARP1 protein (Figure 5.12a). A complete inhibition of PARP1 activity was obtained at equimolar (1:1) protein-inhibitor ratios with Rucaparib. (Figure 5.12a). However, this inhibition efficiency was not achieved with Niraparib and Veliparib (Figure 5.12a). The difference in the ability of the inhibitors to inhibit the PARP1 activity is associated to the inhibition/binding constants (IC50s and K_Is) of each of them to PARP1. Molecules such as Talazoparib, Olaparib and Rucaparib have been described as more potent inhibitors than Niraparib and Veliparib [80]. K_I values reported for Niraparib, Rucaparib and Veliparib were 7.9 nM [81], 1.4 nM [82] and 3.7 nM [81], respectively. Recent K_I assessments, that tried to minimize problems related to tight-binding limit the measurements of PARPi constants, have determined even lower values (1.2 nM, 0.09 nM and 0.96nM, respectively) [83].

The secondary structure of PARP1 upon association with Niraparib, Rucaparib and Veliparib was analysis by circular dichroism (CD). The results revealed a significant impact of the inhibitor on the PARP1 structure (Figure 5.12b). PARP1-inhibitor samples showed a major shift from a predominantly stabilized α-helical secondary structure to an apparent predominant β-sheet profile, when compared to native PARP1 (Figure 5.12b). The analysis of the CD spectra with the prediction software BeStSel [36,37] indicated that native PARP1 has a secondary contribution of 10.34 % for α-helixes, 34.58 % of anti-parallel β-sheets; 5 % of parallel β-sheets, 14.14 % of turns and 35.95 % of other structures (310-helix, π -helix, β-bridge, bends, loop/irregular and invisible regions) (Figure 5.12c and Table B.10). In the presence of PARPi, the secondary structure of PARP1 is altered by the absence of regular α-helixes (helix1) and a

reduction of distorted α-helixes (helix2). β-sheets also appeared to be affected, with the observation of a slight reduction in anti-parallel β-sheets and a more pronounced reduction in parallel sheets (Figure 5.12c and Table B.10). The reduced amounts of α-helixes in these structures appears to be compensated for, by the generation of alternative structures ("others" category) (Figure 5.12c and Table B.10). The contribution of these increases from 36 % up to 48% - 51.5 %, in native PARP1 to PARP1-inhibitor samples (Figure 5.12c). The structural shift that is verified in the secondary structure of PARP1 when bound to the clinical inhibitors appears to be related to destabilization of α-helixes, more predominantly in the regular helixes, that appear to shift to 3_{10}-helixes. This alteration can be induced by the solvent effect, which is a common event in low-polarity solvents [84]. Recurrent interconversion between these secondary structures has been observed in the amphiphilic peptide of the triacylglycerol lipase, derived from *Pseudomonas aeruginosa* [84]. Also, structural transition of α, 3_{10} and π helixes is possible, and it has been proved by simulations that drastic α to π transition is related to interactions between hydrophobic side chains [85]. Likewise, the presence of the reducing agent TCEP may have some effect on protein stabilization and folding, due to the reduction of disulfide bonds [86].

The differences observed between PARP1-inhibitor analysis (Figure 5.12c) demonstrates that protein-compound interactions have some distinctions. This is clearly illustrated in the crystal structures of PARP1's CAT domain and the analysed inhibitors. These three molecules share a conserved interaction within the catalytic domain of PARP1, which includes glycine (Gly – G) 863, serine (Ser – S) 904 and Y907 aa residues [80]. The inhibitor interacts with G863 through the formation of two hydrogen bonds to the bicyclic ring and the amide nitrogen, respectively, while the interaction with S904 is through a H-bond with the inhibitor bicyclic ring. These two interactions mimic the nicotinamide bond to the CAT domain of PARP1 [80]. In regard to Y907, this amino acid forms a π - π interaction with the aromatic ring of the inhibitors, and it is due this bond that clinical compounds present higher affinity (> 50 μM) than nicotinamide to PARP1 CAT domain [80]. Among Niraparib, Rucaparib and Veliparib the differentiated interactions with PARP1 are detected in the HD domain. Rucaparib (PDB: 4RV6 [12] and 6VKK [15]) only forms one H-bond with glutamate (Glu -E) 763 at the terminal secondary amine, while Niraparib (PDB: 7KK5 [14]) forms a water-mediated H-bond with glutamine (Gln – Q) 759 and a direct H-bond with aspartate (Asp – D) 766. As for Veliparib (PDB: 7KK6 [14]), only the previously mentioned G863, S904 and Y907 interactions are observed [80]. However, it is necessary to bear in mind that these crystal structures are only related to the catalytic domain and that we are comparing them with the spectra of a full-length protein.

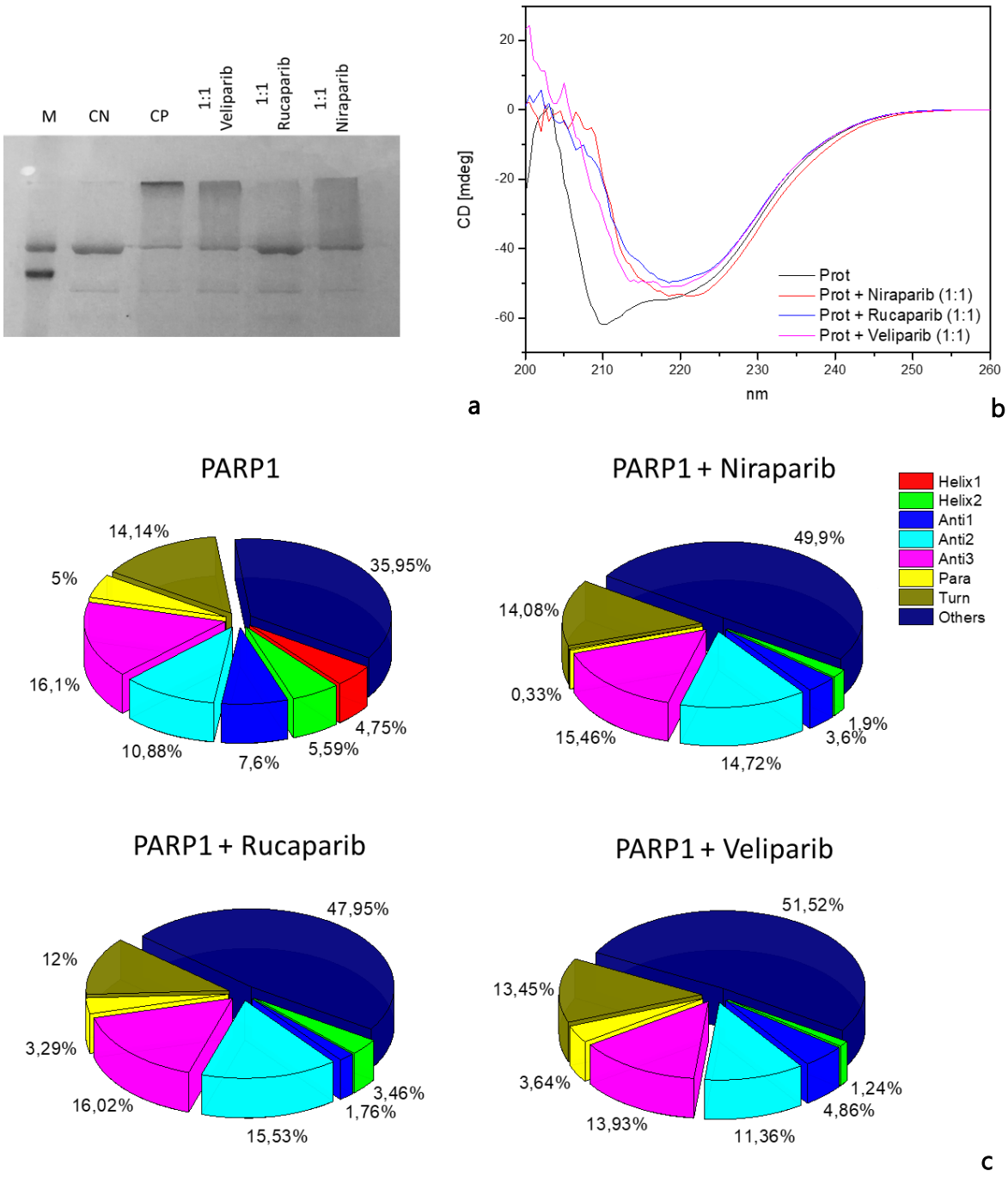

Figure 5.12 — Analysis of the effect of Niraparib, Rucaparib and Veliparib on the activity and secondary structure of PARP1. a) Auto-modification activity assay of PARP1 with PAPRi at equimolar ratios. Results display differences in the inhibitory efficiency of PARPi molecules; b) CD spectra of native PARP1 and PARP1 with inhibitors in 50 mM Tris-HCl pH 8.0, 500 mM NaCl, 1 mM EDTA, 0.1 mM TCEP; c) BeStSel secondary structure determination of native PARP1 and PARP1 bound to the inhibitors Niraparib, Rucaparib and Veliparib. Prediction was done with the CD spectra obtained for the protein samples.

Moreover, melting curves of native PARP1 and PARP1-inhibitor (1:1) samples were obtained by CD (Figure B.11) and their respective Tm values were calculated at 208 nm, 218 nm

and 222 nm (Table 5.7). The reference wavelengths analysed are related to the theoretical maximum ellipticity of α-helixes and β-sheets. The Tm values determined for native protein are in the range of 52 to 58 °C (Table 5.7), which indicates that both secondary structures appear to be stabilized in the incubation buffer, with a preferable stabilization of β structures (218 nm and 222 nm). These Tm values are superior to the ones determined in the same conditions by Nano-DSF and TSF, as seen in Figure 5.13 and Table 5.8. These differences in melting temperatures could be related to the heating system and the technique employed. Nevertheless, the three measurements are coherent in showing that native PARP1 is more or less, uniformly stabilized (Table 5.7, Figure 5.13, and Table 5.8). By CD, the presence of the three inhibitors appear to further stabilize PARP1, and Tm values as high as 62 °C are observed with Rucaparib. Interestingly, Niraparib and Veliparib appear to increase PARP1's Tm values to the same degree (≈ 60 °C), either at the 218 or 222 nm reference wavelengths. As for Rucaparib, Tm values are slightly higher (> 1 °C), and two Tm values were determined for 222 nm (Tm1= 38.97 ± 1.05 °C and Tm2 = 62.03 ± 0.33 °C) (Table 5.7). These results are an indication of the complexity of events occurring in the degradation of PARP1 and its overall structural plasticity.

Table 5.7 — Tm values of native PARP1 and PARP1 bound to inhibitors (1:1) determined by CD melting curves at 208, 218 and 222 nm.

CD* Melting curves	208nm⁺	218nm⁺	222nm⁺	R^2
Ct	52.56 ± 0.56	57.48 ± 0.26	58.03± 0.28	0.99
Veliparib (1:1)		60.01 ± 0.98	60.07 ± 0.84	0.99
Rucaparib (1:1)	N/A	61.71 ± 0.85	38.97 ± 1.05 62.03 ± 0.33	0.99
Niraparib (1:1)		59.67 ± 0.47	60.32 ± 0.56	0.99

* 50 mM Tris-HCl pH 8.0, 500 mM NaCl, 1 mM EDTA, 0.1 mM TCEP; ⁺ mean ± SD

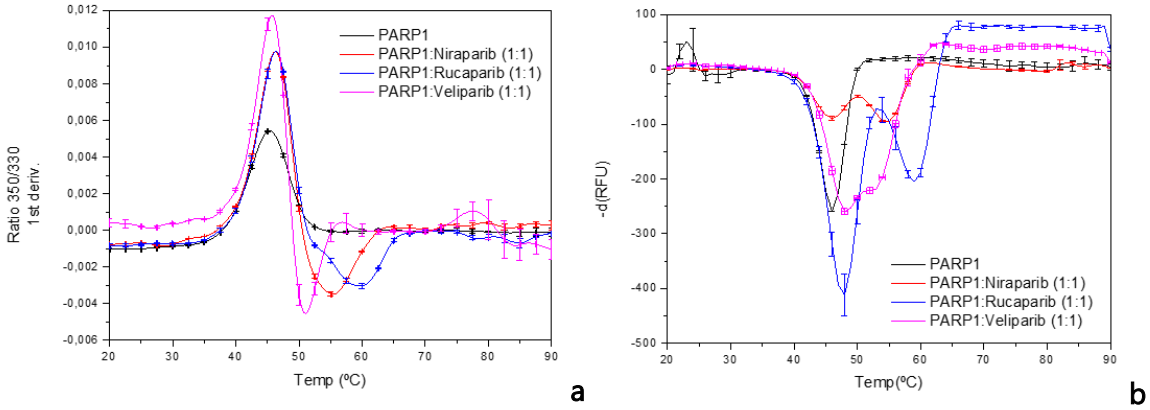

Figure 5.13 — Assessment of PARP1's thermo-stabilization with and without inhibitors (Niraparib, Rucaparib and Veliparib at 1:1 ratios). a) Nano-DSF 1st derivative of F350/F330 ratio; b) Thermofluor protein denaturation spectra.

Table 5.8 — Comparative analysis of Tm values of native PARP1 and PARP1 in the presence of clinical inhibitors (1:1 ratio). Data was obtained by Nano-DSF and thermofluor.

PARP1 inhibitors*	Nano-DSF⁺	Thermofluor⁺
Ct	45.30 ± 0.08	46.00 ± 0.00
Niraparib	46.00 ± 0.05	47.50 ± 0.50
	55.20 ± 0.04	55.00 ± 0.00
Rucaparib	46.20 ± 0.04	46.50 ± 0.50
	59.30 ± 0.02	59.00 ± 0.00
Veliparib	45.30 ± 0.04	48.00 ± 0.00
	51.70 ± 0.03	53.00 ± 0.00

* 50 mM Tris-HCl pH 8.0, 500 mM NaCl, 1 mM EDTA, 0.1 mM TCEP; ⁺ mean ± SD

BeStSel spectra analysis show the evolution and shift among secondary structures, during the denaturation process (Figure B.11b, d, f and h). Coincidently, the Tm values that were determined for native PARP1 appear to be the result of fluctuations in all secondary structures (Figure B.11 b). Here, helix 1, 2 and the parallel β-sheets are the ones that coincide with the Tm values determined (Figure B.11 b and Table 5.7). The Tms established in Table 5.7, when PARP1 interacts with the inhibitors, can thus be explained by loss of parallel β-sheets (Figure B.11d, f and h). In the crystal structures of the PARP1's CAT domain with these inhibitors (PDB IDs: Niraparib -7KK5, Rucaparib - 4RV6/6VKK, Veliparib - 7KK6) [12,14,15], we can see that

interactions occur in the α-helix, β-sheet and random coil structures that are buried in the CAT domain. Considering these data, we can say that our results are coherent regarding the preferable interaction between inhibitor and PARP1 in the β-sheets secondary structures. Moreover, our results suggest that the melting values of PARP1 reflect the structural plasticity and evolution of parallel β-sheets.

A thermostability assessment, with Nano-DSF and TSF, revealed that the inhibitors introduced additional stabilization to a portion of PARP1. This is made clear by the identification of more than one denaturation peaks (Figure 5.13). The Tm values are depicted in Table 5.8. Surprisingly, the additional stabilization observed by Nano-DSF is conferred to the hydrophobic aromatics, by the observance of a negative peak in Figure 5.13a. A comparison between the inhibitors, shows that Rucaparib is a better protein stabilizer, with Tm values of approximately 59 °C in both thermostability measurements. The order of protein stabilization in terms of Tm values is as follow: Rucaparib > Niraparib > Veliparib. These results are more or less, coherent with the tendency visualized in the activity assay results (Figure 5.12a) and reported K_I values. However, the prevalence of Niraparib over Veliparib in the activity assays and Tm results is not justified by the K_I values. However, if we take into consideration the structure of the inhibitors and the physical inter-molecular interaction with the catalytic domain of PARP1, this dominance can be explained. The way that Niraparib was designed, in comparison to Veliparib, provided the first with an extra pyridine ring that gives it the additional double interaction with PARP1' Q759 and D766 residues [80]. Because Veliparib has a simpler molecular structure, it can only interact with PARP1 through three aa residues, that are conserved interactions among the three inhibitors, which confers greater flexibility to Veliparib's interaction [80]. Although Niraparib presents less structural flexibility and limited interactions, the strong interaction with the HD-domain hinders the flexibility of the domain, which is needed for PARP1 activation [87]. Thus, this singular structural characteristic in Niraparib justifies the observed dominance over Veliparib, in our assays. Due to the unique interaction with the conserved HD-domain of PARP1-3 isoforms, Niraparib is considered the more selective inhibitor for PARP1 and 2, over other PARP members [87].

Additionally, to further clarify the stabilization capability of the three inhibitors, several protein-inhibitor ratios were tested (1:1, 1:3 and 1:5) by Nano-DSF and Thermofluor (Figure B.12 and Table B.11). The results showed positive feedback between inhibitor concentration and Tm values of PARP1 (Figure B.12 and Table B.11). The melting curves point to more than one denaturation step and the increase in inhibitor content did not alter this complex denaturation pattern (Figure B.12). The Nano-DSF results indicate that denaturation temperatures

of hydrophobic residues (negative peaks) are higher than hydrophilic (Figure B.12a, c and e), pointing to a potential partial stabilization effect of the inhibitors on PARP1. The increase of Veliparib content led to an apparent increase of the areas of the negative melting peaks and the determination of three Tm values at 1:3 and 1:5 ratio (Figure B.12e). This serves as an indication that this inhibitor is less desirable than Rucaparib and Niraparib, as a potential protein stabilizer. Also, Tm values show that maximum values in protein-Rucaparib mixtures are achieved at a 1:3 ratio. The highest Tm is of 61 °C for Nano-DSF and Thermofluor (Table B.11). Niraparib maximum effect is achieved at 1:5 ratio with the Tm being approximately 58 °C in both techniques. Veliparib stabilization effect appears to be more differentiated between Nano-DSF and TSF, with maximum values reached at 1:3 ratio in the first (57 ± 0 °C) and 1:5 in the latter (56 ± 0 °C) (Table B.11). These results are an additional confirmation of the less desirable use of Veliparib as a structural stabilizer, compared to Rucaparib and Niraparib. These two inhibitors appear to be more consistent and follow the same tendency in both techniques. The results and tendencies can be explained by K_I values, but they are also impacted by physical interactions between the protein and the inhibitor, as discussed above.

In sum, PARPi are good candidates for structural stabilizers and among Type III DNA pro-release allosteric regulators, Rucaparib presents the best choice. All inhibitors appeared to influence and change the protein secondary structures, with an apparent shift of regular α-helixes to 3_{10} – or π - helixes. β – sheets are also affected, with more pronounced alteration in parallel β – sheet content. All these structures appear to be shifted and compensated for by the increase of the alternative secondary structures. Nevertheless, Rucaparib presents more consensus in terms of determined Tm values. Maximum Tm values (61 °C) were accomplished at 1:3 ratio. Our results point to a protein stabilization tendency of: Rucaparib > Niraparib >Veliparib, which is justified by the inhibitors' unique molecular structure and subsequent physical interaction mode with PARP1 catalytic domain.

5.4 Conclusion

In this work we aimed to clarify the structural dynamic nature of PARP1, its oligomerization state and determine additional stabilization partners.

Our results showed that in the purification process we were able to separate different forms of PARP1: 1) DNA bound, 2) PARylated and 3) free and non-modified PARP1. A SEC analysis revealed specific chromatogram profiles and elution volumes for each form of PARP1, thus simplifying their identification and differentiation. Moreover, we have shown that purified

PARP1 following centrifugal concentration leads to protein self-association and generates a dimeric form. In its native biological state, the protein appears to be present as a "free" elongated monomer and in the presence of DNA, a bound dimeric form. Thus, we conclude that the free dimer is an artificial form of PARP1. In its native biological environment, the PARP's dimeric form is known to arise from the interaction with DNA and to increase the repair kinetics.

In terms of protein thermostability, we have here gathered relevant information about the effect of divalent cations. Among the ones that were tested, Mg^{2+} and Ca^{2+} presented the best option for protein stabilization at low salt concentrations. These ions appear to introduce point stabilization without global structural change, with PARP1 retaining its elongated form. Fluorometry data point to a possible positive allosteric modulation effect on PARP1 activity and binding, which is confirmed by the enhancement of protein enzymatic activity. Mg^{2+} appears to enhance PARP1 activity by favoring protein-protein interaction/association and facilitating the assembly of large enzymatic complexes.

Besides the divalent cations, DNA templates mimicking double strand breaks appeared to increase protein stabilization but only in an optimized DNA-protein ratio, and different binding affinities were determined for each type of damage. The combined effect on the enzymatic activity of PARP1 of ion content (Mg^{2+} and Ca^{2+}) and DNA damage indicated the existence of a positive feedback loop and thermostability analysis showed that an increase in the melting temperature is greatly related to the ion content. Results showed that PARP1 prefers binding to 3'-overhang DSB templates and that differences in the DNA binding affinity impact PARP1's enzyme activity. The ion content also has an impact on PARP1-DNA binding, probably associated with the formation of the DNA-protein complex and/or sliding (as with p53). The ion concentration did not appear to have an impact on the protein binding affinity, however PARP1 activity was enhanced upon increasing ion content and the formation of large protein complexes was verified.

The clinical inhibitors Veliparib, Rucaparib and Niraparib appear to partially stabilize full-length PARP1, and circular dichroism analysis revealed the profound effect the inhibitors have on PARP1's secondary structure. Among the Type III DNA pro-release allosteric regulators, Rucaparib presents the best choice for PARP1 stabilization. All inhibitors appeared to influence and change protein secondary structures, with an apparent shift of regular α-helixes to 3_{10} – or π - helixes. β – sheets are also affected, with more pronounced alterations in parallel β – sheet content. All these structures appear to be shifted and compensated for by the increase of the alternative secondary structure elements. Nevertheless, Rucaparib presents the most consensus in terms of determined Tm values and demonstrated a high Tm value (61 °C) 1:3 ratio.

Results point to a protein stabilization tendency of: Rucaparib > Niraparib >Veliparib, which is justified by the inhibitors' unique molecular structure and subsequent physical interaction mode with PARP1 catalytic domain.

5.5 Acknowledgments

This research was funded by the Portuguese National Funding Agency (FCT-MCTES), Radiation Biology and Biophysics Doctoral Training Programme (RaBBiT, PD/00193/2012), the Applied Molecular Biosciences Unit—UCIBIO (UIDB/04378/2020), the CEFITEC Unit (UIDB/00068/2020), UIDB/04559/2020 (LIBPhys) and UIDP/04559/2020 (LIBPhys), the FCT scholarships grant number PD/BD/142765/ 2018 and COVID/BD/152660/2022, to C.J.F.C. from the RaBBiT Doctoral Training Programme. and the project LISBOA-01-0145-FEDER007660 (Microbiologia Molecular, Estrutural e Celular) funded by FEDER funds through COMPETE2020. B.S. acknowledge the funding from (DOCTOrates 4 covid-19 2020.08066.BD) PhD Programme in Molecular Biosciences.

References

[1] J.D. Steffen, M.M. McCauley, J.M. Pascal, Fluorescent sensors of PARP-1 structural dynamics and allosteric regulation in response to DNA damage, Nucleic Acids Res. 44 (2016) 9771–9783. https://doi.org/10.1093/nar/gkw710.

[2] M.F. Langelier, J.L. Planck, S. Roy, J.M. Pascal, Structural Basis for DNA Damage–Dependent Poly(ADP-ribosyl)ation by Human PARP-1, Science (80-.). 336 (2012) 728–732. https://doi.org/10.1126/science.1216338.

[3] J.M. Dawicki-Mckenna, M. Langelier, J.E. Denizio, A. Riccio, C.D. Cao, K.R. Karch, M. Mccauley, J.D. Steffen, E. Ben, J.M. Pascal, PARP-1 activation requires local unfolding of an autoinhibitory domain, Mol. Cell. 60 (2015) 755–768. https://doi.org/10.1016/j.molcel.2015.10.013.PARP-1.

[4] L. van Beek, É. McClay, S. Patel, M. Schimpl, L. Spagnolo, T. Maia de Oliveira, Parp power: A structural perspective on parp1, parp2, and parp3 in dna damage repair and nucleosome remodelling, Int. J. Mol. Sci. 22 (2021) 1–23. https://doi.org/10.3390/ijms22105112.

[5] J.M. Dawicki-McKenna, M.F. Langelier, J.E. DeNizio, A.A. Riccio, C.D. Cao, K.R. Karch, M. McCauley, J.D. Steffen, B.E. Black, J.M. Pascal, PARP-1 Activation Requires Local Unfolding

of an Autoinhibitory Domain, Mol. Cell. 60 (2015) 755–768. https://doi.org/10.1016/j.molcel.2015.10.013.

[6] C.J. Lord, A. Ashworth, PARP Inhibitors: The First Synthetic Lethal Targeted Therapy Europe PMC Funders Group, Science (80-.). 355 (2017) 1152–1158. https://doi.org/10.1126/science.aam7344.PARP.

[7] C. Qin, Z. Ji, E. Zhai, K. Xu, Y. Zhang, Q. Li, H. Jing, X. Wang, X. Song, PARP inhibitor olaparib enhances the efficacy of radiotherapy on XRCC2-deficient colorectal cancer cells, Cell Death Dis. 13 (2022). https://doi.org/10.1038/s41419-022-04967-7.

[8] G. O'Sullivan Coyne, A. Chen, S. Kummar, Delivering on the promise: Poly ADP ribose polymerase inhibition as targeted anticancer therapy, Curr. Opin. Oncol. 27 (2015) 475–481. https://doi.org/10.1097/CCO.0000000000000238.

[9] E.A. Hobbs, J.K. Litton, T.A. Yap, Development of the PARP inhibitor talazoparib for the treatment of advanced BRCA1 and BRCA2 mutated breast cancer, Expert Opin. Pharmacother. 22 (2021) 1825–1837. https://doi.org/10.1080/14656566.2021.1952181.

[10] S.J. Baptista, M.M.C. Silva, E. Moroni, M. Meli, G. Colombo, T.C.P. Dinis, J.A.R. Salvador, Novel PARP-1 Inhibitor scaffolds disclosed by a dynamic structure-based pharmacophore approach, PLoS One. 12 (2017) 1–20. https://doi.org/10.1371/journal.pone.0170846.

[11] M. Mekhaeil, K.K. Dev, M.J. Conroy, Existing Evidence for the Repurposing of PARP-1 Inhibitors in Rare Demyelinating Diseases, Cancers (Basel). 14 (2022) 1–22. https://doi.org/10.3390/cancers14030687.

[12] H. Thorsell, A; Ekblad, T; Karlberg, T; Low, M; Pinto, AF; Trésaugues, L; Moche, M; Cohen, MS; Schuler, Structural Basis for Potency and Promiscuity in Poly(ADP-ribose) Polymerase (PARP) and Tankyrase Inhibitors, J. Med. Chem. 60 (2017) 1262–1271. https://doi.org/10.1021/acs.jmedchem.6b00990.

[13] T.E.H. Ogden, J.-C. Yang, M. Schimpl, L.E. Easton, E. Underwood, P.B. Rawlins, M.M. McCauley, M.-F. Langelier, J.M. Pascal, K.J. Embrey, D. Neuhaus, Dynamics of the HD regulatory subdomain of PARP-1; substrate access and allostery in PARP activation and inhibition, Nucleic Acids Res. 49 (2021) 2266–2288. https://doi.org/10.1093/nar/gkab020.

[14] K. Ryan, B. Bolaños, M. Smith, P.B. Palde, P.D. Cuenca, T.L. VanArsdale, S. Niessen, L. Zhang, D. Behenna, M.A. Ornelas, K.T. Tran, S. Kaiser, L. Lum, A. Stewart, K.S. Gajiwala, Dissecting the molecular determinants of clinical PARP1 inhibitor selectivity for tankyrase, J. Biol. Chem. 296 (2021) 1–13. https://doi.org/10.1074/JBC.RA120.016573.

[15] L. Zandarashvili, M. Langelier, U.K. Velagapudi, A. Mark, J.D. Steffen, R. Billur, Z.M. Hannan, A.J. Wicks, B. Krastev, S.J. Pettitt, C.J. Lord, T.T. Talele, J.M. Pascal, B.E. Black, Structural basis for allosteric PARP-1 retention on DNA breaks, Science (80-.). 368 (2020) 1–24. https://doi.org/10.1126/science.aax6367.Structural.

[16] L. Fu, S. Wang, X. Wang, P. Wang, Y. Zheng, D. Yao, M. Guo, L. Zhang, L. Ouyang, Crystal structure-based discovery of a novel synthesized PARP1 inhibitor (OL-1) with apoptosis-inducing mechanisms in triple-negative breast cancer, Sci. Rep. 6 (2016) 1–14. https://doi.org/10.1038/s41598-016-0007-2.

[17] X. Chen, X. Huan, Q. Liu, Y. Wang, Q. He, C. Tan, Y. Chen, J. Ding, Y. Xu, Z. Miao, C. Yang, Design and synthesis of 2-(4,5,6,7-tetrahydrothienopyridin-2-yl)-benzoimidazole carboxamides as novel orally efficacious Poly(ADP-ribose)polymerase (PARP) inhibitors, Eur. J. Med. Chem. 145 (2018) 389–403. https://doi.org/10.1016/j.ejmech.2018.01.018.

[18] A. Ruf, G. De Murcia, G.E. Schulz, Inhibitor and NAD+ binding to poly(ADP-ribose) polymerase as derived from crystal structures and homology modeling, Biochemistry. 37 (1998) 3893–3900. https://doi.org/10.1021/bi972383s.

[19] T.D. Penning, G.D. Zhu, J. Gong, S. Thomas, V.B. Gandhi, X. Liu, Y. Shi, V. Klinghofer, E.F. Johnson, C.H. Park, E.H. Fry, C.K. Donawho, D.J. Frost, F.G. Buchanan, G.T. Bukofzer, L.E. Rodriguez, V. Bontcheva-Diaz, J.J. Bouska, D.J. Osterling, A.M. Olson, K.C. Marsh, Y. Luo, V.L. Giranda, Optimization of phenyl-substituted benzimidazole carboxamide poly(ADP-ribose) polymerase inhibitors: Identification of (S)-2-(2-fluoro-4- (pyrrolidin-2-yl)phenyl)-1 H -benzimidazole-4-carboxamide (A-966492), a highly potent and efficacious inhibitor, J. Med. Chem. 53 (2010) 3142–3153. https://doi.org/10.1021/jm901775y.

[20] K. Hattori, Y. Kido, H. Yamamoto, J. Ishida, K. Kamijo, K. Murano, M. Ohkubo, T. Kinoshita, A. Iwashita, K. Mihara, S. Yamazaki, N. Matsuoka, Y. Teramura, H. Miyake, Rational approaches to discovery of orally active and brain-penetrable quinazolinone inhibitors of poly(ADP-ribose)polymerase, J. Med. Chem. 47 (2004) 4151–4154. https://doi.org/10.1021/jm0499256.

[21] T. Kinoshita, I. Nakanishi, M. Warizaya, A. Iwashita, Y. Kido, K. Hattori, T. Fujii, Inhibitor-induced structural change of the active site of human poly(ADP-ribose) polymerase, FEBS Lett. 556 (2004) 43–46. https://doi.org/10.1016/S0014-5793(03)01362-0.

[22] A. Iwashita, K. Hattori, H. Yamamoto, J. Ishida, Y. Kido, K. Kamijo, K. Murano, H. Miyake, T. Kinoshita, M. Warizaya, M. Ohkubo, N. Matsuoka, S. Mutoh, Discovery of quinazolinone and quinoxaline derivatives as potent and selective poly(ADP-ribose) polymerase-1/2 inhibitors, FEBS Lett. 579 (2005) 1389–1393. https://doi.org/10.1016/j.febslet.2005.01.036.

[23] A.R. Gangloff, J. Brown, R. De Jong, D.R. Dougan, C.E. Grimshaw, M. Hixon, A. Jennings, R. Kamran, A. Kiryanov, S. O'Connell, E. Taylor, P. Vu, Discovery of novel benzo[b][1,4]oxazin-3(4H)-ones as poly(ADP-ribose) polymerase inhibitors, Bioorganic Med. Chem. Lett. 23 (2013) 4501–4505. https://doi.org/10.1016/j.bmcl.2013.06.055.

[24] N. Ye, C.H. Chen, T. Chen, Z. Song, J.X. He, X.J. Huan, S.S. Song, Q. Liu, Y. Chen, J. Ding, Y. Xu, Z.H. Miao, A. Zhang, Design, synthesis, and biological evaluation of a series of benzo[de][1,7]naphthyridin-7(8 H)-ones bearing a functionalized longer chain appendage as novel PARP1 inhibitors, J. Med. Chem. 56 (2013) 2885–2903. https://doi.org/10.1021/jm301825t.

[25] S. Tomassi, J. Pfahler, N. Mautone, A. Rovere, C. Esposito, D. Passeri, R. Pellicciari, E. Novellino, M. Pannek, C. Steegborn, A. Paiardini, A. Mai, D. Rotili, From PARP1 to TNKS2 inhibition: A structure-based approach, ACS Med. Chem. Lett. 11 (2020) 862–868. https://doi.org/10.1021/acsmedchemlett.9b00654.

[26] G. Papeo, H. Posteri, D. Borghi, A.A. Busel, F. Caprera, E. Casale, M. Ciomei, A. Cirla, E. Corti, M. D'Anello, M. Fasolini, B. Forte, A. Galvani, A. Isacchi, A. Khvat, M.Y. Krasavin, R. Lupi, P. Orsini, R. Perego, E. Pesenti, D. Pezzetta, S. Rainoldi, F. Riccardi-Sirtori, A. Scolaro, F. Sola, F. Zuccotto, E.R. Felder, D. Donati, A. Montagnoli, Discovery of 2-[1-(4,4-Difluorocyclohexyl)piperidin-4-yl]-6-fluoro-3-oxo-2,3-dihydro-1H-isoindole-4-carboxamide (NMS-P118): A Potent, Orally Available, and Highly Selective PARP-1 Inhibitor for Cancer Therapy, J. Med. Chem. 58 (2015) 6875–6898. https://doi.org/10.1021/acs.jmedchem.5b00680.

[27] G. Papeo, P. Orsini, N.R. Avanzi, D. Borghi, E. Casale, M. Ciomei, A. Cirla, V. Desperati, D. Donati, E.R. Felder, A. Galvani, M. Guanci, A. Isacchi, H. Posteri, S. Rainoldi, F. Riccardi-Sirtori, A. Scolaro, A. Montagnoli, Discovery of Stereospecific PARP-1 Inhibitor

Isoindolinone NMS-P515, ACS Med. Chem. Lett. 10 (2019) 534–538. https://doi.org/10.1021/acsmedchemlett.8b00569.

[28] H. Wang, B. Ren, Y. Liu, B. Jiang, Y. Guo, M. Wei, L. Luo, X. Kuang, M. Qiu, L. Lv, H. Xu, R. Qi, H. Yan, D. Xu, Z. Wang, C.-X. Huo, Y. Zhu, Y. Zhao, Y. Wu, Z. Qin, D. Su, T. Tang, F. Wang, X. Sun, Y. Feng, H. Peng, X. Wang, Y. Gao, Y. Liu, W. Gong, F. Yu, X. Liu, L. Wang, C. Zhou, Discovery of Pamiparib (BGB-290), a Potent and Selective Poly (ADP-ribose) Polymerase (PARP) Inhibitor in Clinical Development, J. Med. Chem. 63 (2020) 15541–15563. https://doi.org/10.1021/acs.jmedchem.0c01346.

[29] M. Aoyagi-Scharber, A.S. Gardberg, B.K. Yip, B. Wang, Y. Shen, P.A. Fitzpatrick, Structural basis for the inhibition of poly(ADP-ribose) polymerases 1 and 2 by BMN 673, a potent inhibitor derived from dihydropyridophthalazinone, Acta Crystallogr. Sect. Struct. Biol. Commun. 70 (2014) 1143–1149. https://doi.org/10.1107/S2053230X14015088.

[30] A.E.G. Lindgren, T. Karlberg, A.G. Thorsell, M. Hesse, S. Spjut, T. Ekblad, C.D. Andersson, A.F. Pinto, J. Weigelt, M.O. Hottiger, A. Linusson, M. Elofsson, H. Schüler, PARP inhibitor with selectivity toward ADP-ribosyltransferase ARTD3/PARP3, ACS Chem. Biol. 8 (2013) 1698–1703. https://doi.org/10.1021/cb4002014.

[31] U.K. Velagapudi, M. Langelier, C. Delgado-martin, E. Morgan, S. Bakker, A. Ashworth, B.A. Patel, X. Shao, M. John, T.T. Talele, H. Sciences, U. States, H. Diller, F. Comprehensive, U. States, S. Francisco, U. States, Design and Synthesis of Poly(ADP-ribose) polymerase Inhibitors: Impact of Adenosine Pocket-Binding Motif Appendage to the 3-Oxo-2,3-dihydrobenzofuran-7-carboxamide on Potency and Selectivity, J. Med. Chem. 62 (2019) 5330–5357. https://doi.org/10.1021/acs.jmedchem.8b01709.Design.

[32] S. Bilokapic, M.J. Suskiewicz, I. Ahel, M. Halic, Bridging of DNA breaks activates PARP2–HPF1 to modify chromatin, Nature. 585 (2020) 609–613. https://doi.org/10.1038/s41586-020-2725-7.

[33] K. Kouyama, K. Mayanagi, S. Nakae, Y. Nishi, M. Miwa, T. Shirai, Single-particle analysis of full-length human poly(ADP-ribose) polymerase 1, Biophys. Physicobiology. 16 (2019) 59–67. https://doi.org/10.2142/biophysico.16.0_59.

[34] C.J.F. Conceição, B.A. Salgueiro, P.A. Ribeiro, M. Raposo, E. Moe, Advances in the expression and purification of human PARP1: A user-friendly protocol, Protein Expr. Purif. 211 (2023) 106336. https://doi.org/10.1016/j.pep.2023.106336.

[35] M.F. Langelier, J.D. Steffen, A.A. Riccio, M. McCauley, J.M. Pascal, Purification of DNA Damage-Dependent PARPs from E. coli for Structural and Biochemical Analysis, Methods Mol Biol. 1608 (2017) 431–444. https://doi.org/10.1007/978-1-4939-6993-7_27.

[36] A. Micsonai, F. Wien, L. Kernya, Y.-H. Lee, Y. Goto, M. Réfrégiers, J. Kardos, Accurate secondary structure prediction and fold recognition for circular dichroism spectroscopy, Proc. Natl. Acad. Sci. 112 (2015) E3095-103. https://doi.org/10.1073/pnas.1500851112.

[37] A. Micsonai, F. Wien, É. Bulyáki, J. Kun, É. Moussong, Y.-H. Lee, Y. Goto, M. Réfrégiers, J. Kardos, BeStSel: a web server for accurate protein secondary structure prediction and fold recognition from the circular dichroism spectra, Nucleic Acids Res. 46 (2018) W315–W322. https://doi.org/10.1093/nar/gky497.

[38] M. Miwa, T. Sugimura, Structure of poly(ADP-ribose), in: F. Wold, K. Moldave (Eds.), Methods Enzymol. - Posttranslational Modif. Part A, Academic Press, 1984: pp. 441–450. https://doi.org/10.1016/0076-6879(84)06048-1.

[39] M.I. Knight, P.J. Chambers, Problems associated with determining protein concentration: A comparison of techniques for protein estimations, Appl. Biochem. Biotechnol. - Part B Mol. Biotechnol. 23 (2003) 19–28. https://doi.org/10.1385/MB:23:1:19.

[40] E. Pion, G.M. Ullmann, J.C. Amé, D. Gérard, G. De Murcia, E. Bombarda, DNA-induced dimerization of poly(ADP-ribose) polymerase-1 triggers its activation, Biochemistry. 44 (2005) 14670–14681. https://doi.org/10.1021/bi050755o.

[41] E.E. Alemasova, O.I. Lavrik, Poly(ADP-ribosyl)ation by PARP1: Reaction mechanism and regulatory proteins, Nucleic Acids Res. 47 (2019) 3811–3827. https://doi.org/10.1093/nar/gkz120.

[42] J. Rudolph, J. Mahadevan, P. Dyer, K. Luger, Poly(ADP-ribose) polymerase 1 searches DNA via a 'monkey bar' mechanism, Elife. 7 (2018) 1–23. https://doi.org/https://doi.org/10.7554/eLife.37818.001.

[43] M.F. Langelier, D.D. Ruhl, J.L. Planck, W.L. Kraus, J.M. Pascal, The Zn3 domain of human poly(ADP-ribose) polymerase-1 (PARP-1) functions in both DNA-dependent poly(ADP-ribose) synthesis activity and chromatin compaction, J. Biol. Chem. 285 (2010) 18877–18887. https://doi.org/10.1074/jbc.M110.105668.

[44] P.I. Bauer, K.G. Buki, A. Hakam, E. Kun, Macromolecular association of ADP-ribosyltransferase and its correlation with enzymic activity, Biochem. J. 270 (1990) 17–26. https://doi.org/10.1042/bj2700017.

[45] O. Conchillo-Solé, N.S. de Groot, F.X. Avilés, J. Vendrell, X. Daura, S. Ventura, AGGRESCAN: A server for the prediction and evaluation of "hot spots" of aggregation in polypeptides, BMC Bioinformatics. 8 (2007). https://doi.org/10.1186/1471-2105-8-65.

[46] A.K. Dunker, J.D. Lawson, C.J. Brown, R.M. Williams, P. Romero, J.S. Oh, C.J. Oldfield, A.M. Campen, C.M. Ratliff, K.W. Hipps, J. Ausio, M.S. Nissen, R. Reeves, C. Kang, C.R. Kissinger, R.W. Bailey, M.D. Griswold, W. Chiu, E.C. Garner, Z. Obradovic, Intrinsically disordered protein, J. Mol. Graph. Model. 19 (2001) 26–59. https://doi.org/10.1016/S1093-3263(00)00138-8.

[47] P.E. Wright, H.J. Dyson, Intrinsically disordered proteins in cellular signalling and regulation, Nat. Rev. Mol. Cell Biol. 16 (2015) 18–29. https://doi.org/10.1038/nrm3920.

[48] L. Dubrez, S. Causse, N. Borges Bonan, B. Dumétier, C. Garrido, Heat-shock proteins: chaperoning DNA repair, Oncogene. 39 (2020) 516–529. https://doi.org/10.1038/s41388-019-1016-y.

[49] S.E. Bondos, A.K. Dunker, V.N. Uversky, On the roles of intrinsically disordered proteins and regions in cell communication and signaling, Cell Commun. Signal. 19 (2021) 1–9. https://doi.org/10.1186/s12964-021-00774-3.

[50] G. Hu, A. Katuwawala, K. Wang, S. Ghadermarzi, J. Gao, L. Kurgan, flDPnn : Accurate intrinsic disorder prediction with putative propensities of disorder functions, Nat. Commun. 12 (2021) 4438. https://doi.org/10.1038/s41467-021-24773-7.

[51] M.F. Langelier, L. Zandarashvili, P.M. Aguiar, B.E. Black, J.M. Pascal, NAD+ analog reveals PARP-1 substrate-blocking mechanism and allosteric communication from catalytic center to DNA-binding domains, Nat. Commun. 9 (2018). https://doi.org/10.1038/s41467-018-03234-8.

[52] V. Kotov, G. Mlynek, O. Vesper, M. Pletzer, J. Wald, C.M. Teixeira-Duarte, H. Celia, M. Garcia-Alai, S. Nussberger, S.K. Buchanan, J.H. Morais-Cabral, C. Loew, K. Djinovic-Carugo, T.C. Marlovits, In-depth interrogation of protein thermal unfolding data with MoltenProt, Protein Sci. 30 (2021) 201–217. https://doi.org/10.1002/pro.3986.

[53] D.L. Melnikova, V.D. Skirda, I. V Nesmelova, O. Sciences, The Effect of Reducing Agent TCEP on Translational Diffusion and Supramolecular Assembly in Aqueous Solutions of α - Casein, 123 (2019) 2305–2315. https://doi.org/10.1021/acs.jpcb.8b12511.

[54] A. Mónico, E. Martínez-Senra, F.J. Canada, S. Zorrilla, D. Pérez-Sala, Drawbacks of Dialysis Procedures for Removal of EDTA, 12 (2017) e0169843. https://doi.org/10.1371/journal.pone.0169843.

[55] T. Kroeger, B. Frieg, T. Zhang, F.K. Hansen, A. Marmann, P. Proksch, L. Nagel-steger, G. Groth, S.H.J. Smits, H. Gohlke, EDTA aggregates induce SYPRO orange-based fluorescence in thermal shift assay, (2017) 1–21.

[56] M.F. Ryan, The role of magnesium in clinical biochemistry: An overview, Ann. Clin. Biochem. 28 (1991) 19–26. https://doi.org/10.1177/000456329102800103.

[57] A. Irbäck, S. Mohanty, Protein folding/unfolding in the presence of interacting macromolecular crowders, Eur. Phys. J. Spec. Top. 226 (2017) 627–638. https://doi.org/10.1140/epjst/e2016-60316-9.

[58] K.A. Sharp, Analysis of the size dependence of macromolecular crowding shows that smaller is better, Proc. Natl. Acad. Sci. 112 (2015) 7990–7995. https://doi.org/10.1073/pnas.1505396112.

[59] K. Bielec, A. Kowalski, G. Bubak, E. Witkowska Nery, R. Hołyst, Ion Complexation Explains Orders of Magnitude Changes in the Equilibrium Constant of Biochemical Reactions in Buffers Crowded by Nonionic Compounds, J. Phys. Chem. Lett. 13 (2022) 112–117. https://doi.org/10.1021/acs.jpclett.1c03596.

[60] M.A. Esmaeilbeig, M. Khorram, S. Ayatollahi, A.R. Zolghadr, On the hydrolysis of iron ions: DFT-based molecular dynamics perspective, J. Mol. Liq. 367 (2022) 120323. https://doi.org/10.1016/j.molliq.2022.120323.

[61] C.A. Davey, T.J. Richmond, DNA-dependent divalent cation binding in the nucleosome core particle, Proc. Natl. Acad. Sci. U. S. A. 99 (2002) 11169–11174. https://doi.org/10.1073/pnas.172271399.

[62] L.J. Anghileri, Magnesium, calcium and cancer, Magnes. Res. 22 (2009) 247–255. https://doi.org/10.1684/mrh.2009.0173.

[63] A.M.P. Romani, Intracellular magnesium homeostasis, Magnes. Cent. Nerv. Syst. 512 (2011) 13–58. https://doi.org/10.1017/UPO9780987073051.003.

[64] C. Fernandez-Sanz, S. De la Fuente, S. Sheu, Mitochondrial Ca 2+ concentrations in live cells: quantification methods and discrepancies, FEBS Lett. 593 (2019) 1528–1541. https://doi.org/10.1002/1873-3468.13427.

[65] M.F. Langelier, R. Billur, A. Sverzhinsky, B.E. Black, J.M. Pascal, HPF1 dynamically controls the PARP1/2 balance between initiating and elongating ADP-ribose modifications, Nat. Commun. 12 (2021). https://doi.org/10.1038/s41467-021-27043-8.

[66] G.K. Herrmann, W.K. Russell, N.J. Garg, Y.W. Yin, Poly(ADP-ribose) polymerase 1 regulates mitochondrial DNA repair in an NAD-dependent manner, J. Biol. Chem. 296 (2021) 100309. https://doi.org/10.1016/J.JBC.2021.100309.

[67] A.G. Oliveira, E.S. Guimarães, L.M. Andrade, G.B. Menezes, M.F. Leite, Decoding calcium signaling across the nucleus, Physiology. 29 (2014) 361–368. https://doi.org/10.1152/physiol.00056.2013.

[68] T.P. Kenakin, Allosteric Drug Effects, in: Pharmacol. Drug Discov. Dev., Elsevier, 2017: pp. 101–129. https://doi.org/10.1016/B978-0-12-803752-2.00005-3.

[69] H. Liu, P. Yi, W. Zhao, Y. Wu, F. Acher, J.-P. Pin, J. Liu, P. Rondard, Illuminating the allosteric modulation of the calcium-sensing receptor, Proc. Natl. Acad. Sci. 117 (2020) 21711–21722. https://doi.org/10.1073/pnas.1922231117.

[70] R. Vallone, G. Dal Cortivo, M. D'Onofrio, D. Dell'Orco, Preferential Binding of Mg2+ Over Ca2+ to CIB2 Triggers an Allosteric Switch Impaired in Usher Syndrome Type 1J, Front. Mol. Neurosci. 11 (2018). https://doi.org/10.3389/fnmol.2018.00274.

[71] S. Eustermann, H. Videler, J.C. Yang, P.T. Cole, D. Gruszka, D. Veprintsev, D. Neuhaus, The DNA-binding domain of human PARP-1 interacts with DNA single-strand breaks as a monomer through its second zinc finger, J. Mol. Biol. 407 (2011) 149–170. https://doi.org/10.1016/j.jmb.2011.01.034.

[72] A.D. Edwards, K.D. Raney, J.C. Marecki, A.K. Byrd, G-Quadruplex loops regulate PARP-1 enzymatic activation, 49 (2021) 416–431. https://doi.org/10.1093/nar/gkaa1172.

[73] J.M.F. Fischer, O. Popp, D. Gebhard, S. Veith, A. Fischbach, M. Scheffner, E. Ferrando-may, S. Beneke, A. Leitenstorfer, Poly (ADP-ribose) -mediated interplay of XPA and PARP1

leads to reciprocal regulation of protein function, 281 (2014) 3625–3641. https://doi.org/10.1111/febs.12885.

[74] M. Rouleau, A. Patel, M.J. Hendzel, S.H. Kaufmann, G.G. Poirier, PARP inhibition: PARP1 and beyond, Nat. Rev. Cancer. 10 (2010) 293–301. https://doi.org/10.1038/nrc2812.

[75] M.O. Hottiger, SnapShot : ADP-Ribosylation Signaling SnapShot : ADP-Ribosylation Signaling, Mol. Cell. 58 (2015) 1134-1134.e1. https://doi.org/10.1016/j.molcel.2015.06.001.

[76] B. Matkarimov, D. Zharkov, M. Saparbaev, B. Matkarimov, D. Zharkov, M. Saparbaev, Mechanistic insight into the role of Poly (ADP-ribosyl) ation in DNA topology modulation and response to DNA damage To cite this version : HAL Id : hal-02392725 Mechanistic insight into the role of Poly (ADP-ribosyl) ation in DNA topology modulation a, (2019). https://doi.org/10.1093/mutage/gez045.

[77] A. Krüger, A. Bürkle, K. Hauser, A. Mangerich, Real-time monitoring of PARP1-dependent PARylation by ATR-FTIR spectroscopy, Nat. Commun. 11 (2020) 2174. https://doi.org/10.1038/s41467-020-15858-w.

[78] Y. Chen, T. Gao, Y. Wang, G. Yang, Investigating the Influence of Magnesium Ions on p53 – DNA Binding Using Atomic Force Microscopy, 18 (2017) 1585. https://doi.org/10.3390/ijms18071585.

[79] C.C. Hardin, T. Watson, M. Corregan, C. Bailey, Cation-dependent transition between the quadruplex and Watson-Crick hairpin forms of d(CGCG3GCG), Biochemistry. 31 (1992) 833–841. https://doi.org/https://doi.org/10.1021/bi00118a028.

[80] J. Rudolph, K. Jung, K. Luger, Inhibitors of PARP: Number crunching and structure gazing, Proc. Natl. Acad. Sci. U. S. A. 119 (2022) 1–10. https://doi.org/10.1073/pnas.2121979119.

[81] T.A. Hopkins, Y. Shi, L.E. Rodriguez, L.R. Solomon, C.K. Donawho, E.L. DiGiammarino, S.C. Panchal, J.L. Wilsbacher, W. Gao, A.M. Olson, D.F. Stolarik, D.J. Osterling, E.F. Johnson, D. Maag, Mechanistic Dissection of PARP1 Trapping and the Impact on In Vivo Tolerability and Efficacy of PARP Inhibitors, Mol. Cancer Res. 13 (2015) 1465–1477. https://doi.org/10.1158/1541-7786.MCR-15-0191-T.

[82] H.D. Thomas, C.R. Calabrese, M.A. Batey, S. Canan, Z. Hostomsky, S. Kyle, K.A. Maegley, D.R. Newell, D. Skalitzky, L.-Z. Wang, S.E. Webber, N.J. Curtin, Preclinical selection of a

novel poly(ADP-ribose) polymerase inhibitor for clinical trial, Mol. Cancer Ther. 6 (2007) 945–956. https://doi.org/10.1158/1535-7163.MCT-06-0552.

[83] J. Rudolph, G. Roberts, K. Luger, Histone Parylation factor 1 contributes to the inhibition of PARP1 by cancer drugs, Nat. Commun. 12 (2021) 736. https://doi.org/10.1038/s41467-021-20998-8.

[84] R.B. Nellas, Q.R. Johnson, T. Shen, Solvent-Induced α - To 310-Helix Transition of an Amphiphilic Peptide, Biochemistry. 52 (2013) 7137–7144. https://doi.org/10.1021/bi400537z.

[85] R. Armen, D.O. V Alonso, V. Daggett, The role of alpha, 3 10- and pi-helix in helix → coil transitions, 12 (2003) 1145–1157. https://doi.org/10.1110/ps.0240103.

[86] N.A. Ciaccio, J.S. Laurence, Effects of Disulfide Bond Formation and Protein Helicity on the Aggregation of Activating Transcription Factor 5, Mol. Pharm. 6 (2009) 1205–1215. https://doi.org/10.1021/mp900058t.

[87] S. Eustermann, W.-F. Wu, M.-F. Langelier, J.-C. Yang, L.E. Easton, A.A. Riccio, J.M. Pascal, D. Neuhaus, Structural Basis of Detection and Signaling of DNA Single-Strand Breaks by Human PARP-1, Mol. Cell. 60 (2015) 742–754. https://doi.org/10.1016/j.molcel.2015.10.032.

6

ENCAPSULATION OF PARPI IN LIPOSOME NANO-SYSTEMS

Liposome Formulations for the Strategic Delivery of PARP1 inhibitors: Development and Optimization[4]

Abstract

The development of a liposome nano-delivery system was attempted for three specific poly (ADP-ribose) polymerase 1 (PARP1) inhibitors: Veliparib, Rucaparib, and Niraparib. Simple lipid and dual lipid formulations with 1,2-dipalmitoyl-sn-glycero-3-phospho-rac-(10-glycerol) sodium salt (DPPG) and 1,2-dipalmitoyl-sn-glycero-3-phosphocoline (DPPC) were developed and tested following the thin-film method. DPPG-encapsulating inhibitors presented the best fit in terms of encapsulation efficiency (> 40 %, translates into concentrations as high as 100 μM), zeta potential values (below - 30 mV), and population distribution (single population profile). The particle size of the main population of interest was ~130 nm in diameter. Kinetic release studies showed that DPPG encapsulating PARP1 inhibitors present slower drug release rates than liposome control samples, and complex drug release mechanisms were identified. DPPG + Veliparib/Niraparib presented a combination of diffusion-controlled and non-Fickian diffusion, while anomalous and super case II transport was verified for DPPG + Rucaparib. Spectroscopic analysis revealed that PARP1 inhibitors interact with the DPPG lipid membrane, promoting membrane water displacement from hydration centers. A preferential membrane

[4] This chapter is based on the following publication:

Conceição, C.J.F., Moe, E., Ribeiro, P. A. and Raposo, M.. Liposome Formulations for the Strategic Delivery of PARP1 Inhibitors: Development and Optimization. Nanomaterials, 2023, 13 (10): 1613, DOI: 10.3390/nano13101613.

interaction with lipid carbonyl groups was observed through hydrogen bonding, where the inhibitors' protonated amine groups may be the major players in the PARP1 inhibitor encapsulation mode.

6.1 Introduction

Cancer, a multifactorial disease, has a standardized treatment strategy that resorts to the use of radiation therapy coupled with surgical intervention and chemotherapeutic agents [1]. Cytotoxic side effects from ionizing radiation on normal cells are also reported, which affect biological molecules directly through altered DNA moieties, and indirectly via the generation of reactive oxygen species (ROS) [2,3].

The efficiency of radiation therapy can be maximized with the use of molecules that can modulate radiation effects, among which DNA repair inhibitors are included [4,5]. These molecules have specific cellular targets that are involved in signaling pathways related to homologous repair (HR), base excision repair (BER), and non-homologous end joining (NHEJ), such as poly (ADP-ribose) polymerase1 (PARP1) [1,4,6,7]. PARP1 inhibitors, such as Veliparib, Niraparib, and Rucaparib, were developed to specifically interact with the protein's catalytic domain and prevent PARP1's enzymatic activity. In this way, PARP1's biological cycle and DNA repair process are stalled, undermining cellular viability [4,5]. However, some drawbacks are associated with this therapy, such as the cytotoxic effect on normal cells, high compound clearance rates in the organism, and drug interaction with plasma proteins. Values as high as 83% binding with human plasma protein have been reported for Niraparib after entering the blood through the digestive system [8].

Thus, a liposome-based delivery system may be the answer to surpassing these downsides and increasing therapeutic efficacy and efficiency [9]. Liposomes have been used and investigated as efficient transport systems and as a mean to achieve target delivery of therapeutic agents [9–13]. This ability is mostly due to its biocompatibility, biodegradability, low toxicity, lack of immune system activation, and incorporation capability for both hydrophilic and hydrophobic drugs [9–13]. Furthermore, liposomes can act as a protective barrier for photosensitive molecules, protecting the drug's structural molecular integrity and therapeutic activity [14,15]. Additionally, lipidic nanoparticles can be employed as a biomimetic system for lipid–drug interaction studies, as a mean to reduce drug cytotoxicity, and for the development of co-loading systems to attain a high degree of drug synergistic therapeutic effect [9].

In this work, the development of a lipid nano-delivery system was attempted for three specific PARP1 inhibitors: Veliparib, Rucaparib, and Niraparib. Simple lipid formulations were tested and developed following the thin-film method, coupled with two sonication methods (bath and tip sonicators). Liposome production, optimization, and compound encapsulation were extensively explained and discussed.

6.2 Materials and Methods

6.2.1 Chemicals

1,2-Dipalmitoyl-sn-glycero-3-phospho-rac-(1′-glycerol) sodium salt (DPPG) (MW 744.96 g/mol) and 1,2-dipalmitoyl-sn-glycero-3-phosphocoline (DPPC) (MW 734.05 g/mol) were purchased from AvantiPolar Lipids (Alabaster, AL, USA) and CordenPharma (Plankstadt, Baden-Wurttemberg, Germany), respectively. PARP1 inhibitors Veliparib (MW 244.3 g/mol), Rucaparib phosphate (MW 421.4 g/mol), and Niraparib (MW 320.4 g/mol) were purchased from AdooQ® Bioscience (Irvine, CA, USA).

6.2.2 Liposome Preparation

DPPG and DPPC liposomes were prepared using the dry thin-film method [16–18], where 1 mM of lipid was dissolved in a chloroform and methanol 4:1 (*v/v*) mixture. The solvents were evaporated using a gentle stream of nitrogen. To remove residual solvent traces, samples were left overnight in a desiccator, under vacuum. Lipid films were then hydrated at 47 °C for 2 h with Milli-Q ultrapure water (Millipore, Burlington, MA, USA) [16–18] to a final concentration of 1 mM. Bath and tip sonicators (UP200S (200 W, 24 kHz), Hielscher Ultrasonics, GmbH, Teltow, Germany) were used to sonicate vesicle suspensions to obtain small unilamellar vesicles (SUV) [16–18]. Different time intervals and cycles were tested: 1–3 cycles of 5 min and 15–25 cycles of 30 seconds with 1 min intervals between sonication cycles. Veliparib, Rucaparib, and Niraparib were added to the DPPG formulations at different final concentrations of 20, 100, and 200 µM during the lipid dissolution in the organic solvent mixture (organic phase) and the hydration (aqueous phase) steps of liposome preparation. For simplification, we will refer to the drug addition during the two steps of liposome preparation as organic phase supplementation and aqueous phase supplementation, respectively. Non-trapped inhibitor molecules were removed from liposomes by dialysis (Spectra/Por® 4 Dry Standard RC membrane, MWCO 12–14 kDa, Spectrum Labs, Biotech, San Francisco, CA, USA) for 48 h at 4 °C. The concentration

of PARP1 inhibitors encapsulated in DPPG/C liposomes was determined by UV–Vis spectroscopy, by measuring absorbance at 295 nm (Veliparib), 360 nm (Rucaparib), and 311 nm (Niraparib) using a Shimadzu UV-1800 UV/Visible Scanning Spectrophotometer (Kyoto, Kyoto, Japan). Liposome encapsulation efficiency ($EE\%$) and loading capacity ($LC\%$) were determined using the following equations:

$$EE\% = \frac{C_{encap}}{C_{total}} \times 100 \tag{6.1}$$

and

$$LC\% = \frac{C_{encap}}{C_{lipid}} \times 100 \tag{6.2}$$

where C_{encap} is the concentration of inhibitor encapsulated after dialysis, C_{total} is the concentration of inhibitor before dialysis, and C_{lipid} is lipid concentration.

6.2.3 Spectral measurements

Both UV–Vis and FTIR spectra were used to analyze drug encapsulation and interaction modes with liposomes. UV–Vis spectra were acquired with a Shimadzu UV-1800 UV/Visible Scanning Spectrophotometer (Shimadzu). FTIR spectra were recorded on a Bruker IFS 66/S (Billerica, MA, USA) spectrometer in absorbance mode, with a wavenumber range of 500 to 4000 cm^{-1}, a resolution of 4 cm^{-1}, and 128 scans. Samples were deposited on CaF_2 supports, and water was evaporated in a desiccator under vacuum conditions. CaF_2 clean support spectra were subtracted from all sample spectra.

6.2.4 Dynamic Light Scattering

Liposome size, polydispersity index, and zeta potential were determined by dynamic light scattering measurements using a Zetasizer Nano ZS (Malvern Instruments, 633 nm He-Ne laser, measuring angle θ = 173°) (Malvern, Worcestershire, United Kingdom). Size measurements were carried out using a 0.3 mm quartz cuvette (ZEN 2112) for low-volume samples, and the temperature was set to 25 °C. The analyzed liposomes were diluted to 10 μM and 200 μM concentrations for size and zeta potential analysis, respectively. At least three measurements per sample were undertaken, with a 1 min waiting time and a 30 s equilibration time. The lipid refractive index input was 1.45, and the dispersant was defined as 1.33. Zeta potential measurements were attained using the Smoluchowski equation and Malvern disposable sample cells (DTS1070). Intensity particle size distributions and zeta potential values were recorded with Zetasizer software v.7.11. Mean and standard deviation values are presented.

6.2.5 In vitro release of PARP1 inhibitors

Drug release studies [19] of DPPG-encapsulating PARP1 inhibitors Veliparib, Rucaparib, and Niraparib were performed following an adaptation of Sivadasan et al. [19] using Slide-A-Lyzer™ Mini Dialysis devices (MWCO 10K) (ThermoFisher, Waltham, Massachusetts, USA). It should be noted that other Slide-A-Lyzer™ systems, namely Slide-A-Lyzer™ Cassete, similar to those employed here, have previously been used to build a "Liposome Dialysis" system [20]; however, the sample volumes needed are greater (250–300 µL) than the device that was used in the present work (50 µL). The liposome formulation was applied (50 µL) to the mini dialysis devices, sealed, and immersed in 1.2 mL of PBS 1x pH 7.4. The dialysis system was incubated in a Thermoblock (Eppendorf, Hamburg, Germany) at 37 °C with gentle agitation. The temperature was selected taking into consideration typical human body temperature. At fixed time intervals, samples were collected from the dialysate buffer and replaced with fresh PBS. Dialysate was analyzed by UV–Vis spectroscopy, and absorbance at 295 nm, 360 nm, and 311 nm was measured for Veliparib, Rucaparib, and Niraparib, respectively. Control (pure drug) samples were also subjected to the dialysis process, and the concentration used was equivalent to the final drug concentration encapsulated in the liposome formulations. All formulations were analyzed in triplicate, and cumulative drug release percentages were determined.

6.2.6 Release Kinetic Models

Data obtained from in vitro drug release analyses were plotted using various kinetic models with the KinetDS software [21,22] to study drug release kinetics from DPPG. The best model criteria employed were empirical R^2:

$$R^2_{emp} = 1 - \frac{\sum_{i=1}^{N}(y_i - \hat{y}_i)^2}{\sum_{i=1}^{N}(y_i - y_{AV})^2} \tag{6.3}$$

and the Akaike information criterion (AIC) defined by

$$\mathrm{AIC} = 2K + N \cdot \left[\ln\left(\sum_{i=1}^{N}(y_i - \hat{y}_i)^2\right)\right] \tag{6.4}$$

where y_i is the observed value, $\hat{y}_i$ is the model-predicted value, and y_{AV} is the average output value.

The mathematical models used that presented best fit were Weibull:

$$Q = 1 - exp\left[\frac{-(t)^b}{a}\right] \tag{6.5}$$

modified Weibull with Lag Time (T_{LAG}):

$$Q = 1 - exp\left[\frac{-(t - T_{LAG})^b}{a}\right] \quad (6.6)$$

Michaelis–Menten:

$$Q = \frac{Q_{max} \cdot t}{k + t} \quad (6.7)$$

Michaelis–Menten (T_{LAG}):

$$Q = \frac{Q_{max} \cdot (t - T_{LAG})}{k + (t - T_{LAG})} \quad (6.8)$$

and Hixson–Crowell:

$$Q^{\frac{1}{3}} = k \cdot t + Q_0^{\frac{1}{3}} \quad (6.9)$$

where Q is the amount (%) of drug released at time t, Q_o is the start value of Q, Q_{max} is the maximum value of Q (100 %), t is time, T_{LAG} is lag time, and a and b are constants.

To determine the drug release mechanism, the obtained data were plotted using the Krosmeyer–Peppas equation:

$$Q = k \cdot t^n \quad (6.10)$$

where n (release exponent) was used as the drug release mechanism determinant parameter.

6.3 Results and Discussion

Lipidic formulation production, optimization, and compound encapsulation will be extensively explained and discussed in the following subsections.

6.3.1 Development of the PARP1i Lipidic Nano-Delivery System

The preparation of DPPG and DPPC single-lipid formulations followed the procedure described in Section 6.2. Once this procedure was completed, the sonication was optimized to reduce the particle size to a desired range.

6.3.2 Optimization of the Sonication Process

To optimize DPPG and DPPC liposome size, two sonication methods were used (bath-type and tip sonicators), and several time intervals and cycles were employed (1–3 cycles of 5

min and 15/20/25 cycles of 30 s). The bath-type sonicator produced unstable formulations in all conditions, while the tip sonicator was able to produce relatively stable populations. This may be related to the cavitation intensity and ultrasonic wave distribution, where the bath sonicator tends to have an uneven ultrasonic irradiation distribution and the tip sonicator tends to have a greater localized effect that translates into a higher intensity and efficiency in the process [23,24]. Cycles of 5 min revealed a non-homogeneous and unstable liposome population, with the occurrence of particle flocculation for both types. The best results were obtained with a reduced time (30 s cycles) and the tip sonicator (UP200S, 200 W, 24 kHz), since long sonication periods tend to hinder liposome stability through the promotion of lipid oxidation associated with elevated cavitation exposure [25]. Cycles of 30 s (15, 20, and 25) produced stable DPPC and DPPG liposomes, with the presence of two particle populations of small (< 95 nm) and large (> 0.5 μm) sizes (Figure 6.1 and Tables C.1 and C.2). The DPPG main population presented a high degree of size stabilization (approx. 55 nm) regardless of the number of cycles employed (Figure 6.1b), while DPPC showed a constant decrease in size value dependent on the number of cycles. This could be explained by the impact of the lipids' head-sites that govern hydrogen bonding, electrostatic interactions, and overall membrane mechanical stability [26]. Even though simulation data show that DPPC and DPPG present similar area per lipid values (62.0 $Å^2$ and 67.0 $Å^2$, respectively), their overall mechanical stability is quite distinct [26,27]. AFM analysis of the DPPG bilayer reported a mechanical stability of ~66 nM and that of DPPC had an intermediate value of ~19 nM [26]. The observed enhanced stabilization of the DPPG bilayers has been suggested to result from lipid coordination or is due to the effect of Na^+ counterions adsorbed in the membrane that reduce the repulsive effect of the negative charge in the headgroup [26], thus explaining why DPPG liposome particle size appears to be more stable than DPPC when subjected to a mechanical force/stimulus, such as ultrasound.

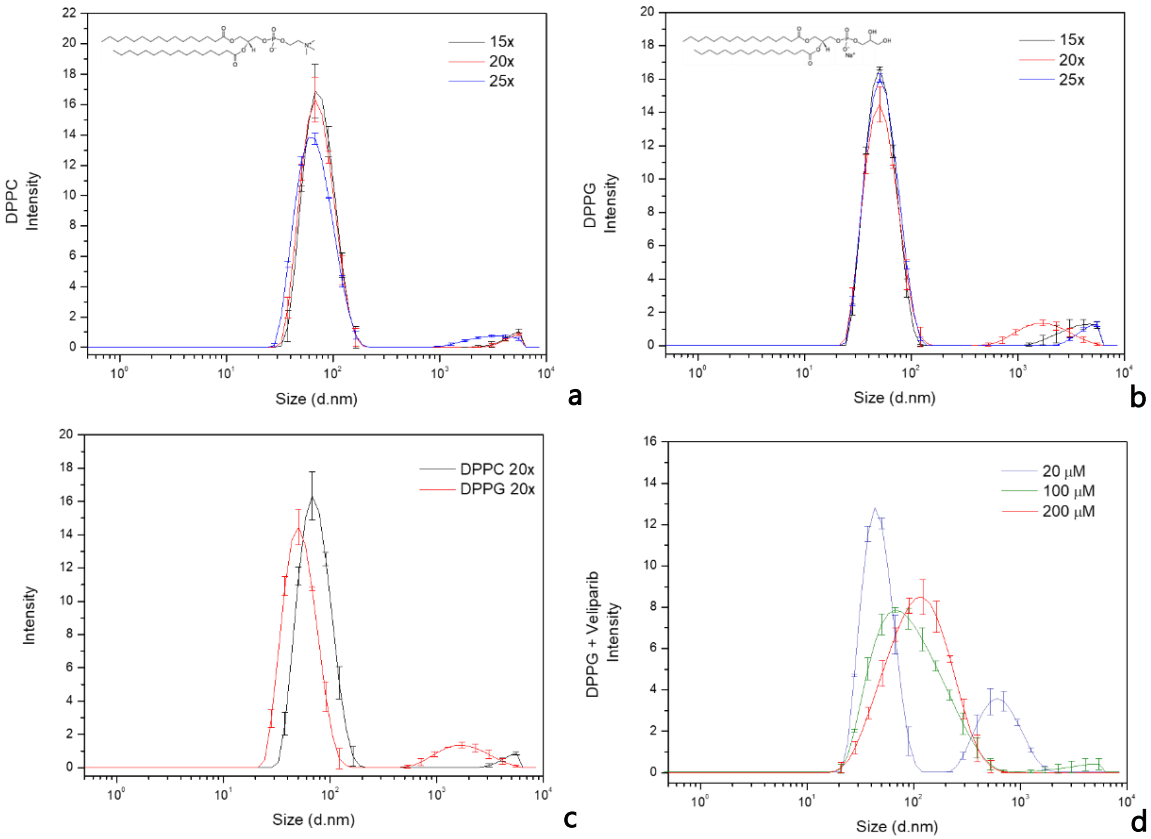

Figure 6.1 — Size distribution analysis of liposome formulations dependent on sonication cycles and drug encapsulation. Evaluation of the effect of sonication cycles (15×, 20× and 25×) on (a) DPPC and (b) DPPG liposome particle size distribution. Analysis was carried out by determining the intensity of each size population detected by dynamic light scattering (DLS), and particle diameter values are presented in nanometers. The lipids' structures are included in the respective graphs. The line in black refers to 15 repeats, the red line to 20 repeats, and the blue line to 25 repeats. c) Population and size distribution of DPPC (dark line) and DPPG (red line) liposome formulations, produced with 20 sonication cycles (20×). Observation of bimodal distribution in both liposomes, with DPPG presenting the main population smaller than DPPC. The large size population presented diameter values above 500 nm in both formulations. d) DPPG size distribution analysis dependent on supplemented Veliparib's concentration in the liposome production.

Considering the population number (one or more populations), size, and sonication time, the 20-cycle condition was selected for liposome preparation. This sonication cycle seemed to be the best compromise between population size distribution and time of exposure to cavitation. Under these conditions, DPPG and DPPC presented z-average values of 56.2 ± 0.4 nm and 71.0 ± 0.5 nm, respectively, and polydispersity index (PdI) values below 0.3 (Figure 6.1c and Table 6.1). Regarding the main population of interest (Pop.1 - population 1), a difference of approximately 19 nm in diameter is observed, as can be seen from the data displayed in Table 6.1. The small discrepancy could be explained by lipid interaction forces and the non-specificity of the sonication technique, which results in a broader particle size distribution. This

is also visualized in the main population peak broadening, where diameter values vary from 28 to 200 nm and 20 to 170 nm, respectively, for DPPC and DPPG (Figure 6.1c). However, the size distribution in both formulations coincides within the range of 28 to 170 nm, showing that a significant number of nanoparticles in the DPPC and DPPG main populations are similar. The presence of large size secondary populations also has an impact on size determination and distribution, influencing scattering events and scattering intensities. DPPG presents a second population with diameters above 0.5 μM and DPPC above 2.5 μM, as can be seen in the particle size distribution of Figure 6.1c.

Table 6.1 — Nanoparticle characterization of DPPC and DPPG liposome formulations produced by 20 sonication cycles (20×). Diameter values for each population, zeta average, polydispersity index, and zeta potential values are presented.

Lipid Formulation *	Z-Average (nm)	PdI	Pop. 1 (nm)	Pop. 2 (nm)	Zeta Potential (mV)
DPPC (20×)	71.0 ± 0.5	0.18 ± 0.01	75 ± 2	4700 ± 200	−17.9 ± 0.9
DPPG (20×)	56.2 ± 0.4	0.27 ± 0.01	56 ± 2	1900 ± 200	−43 ± 2 mV

* Mean ± SD values (n=3 to 4). Note: PdI—polydispersity index, Pop.1—population 1, and Pop.2—population 2.

6.3.3 Optimization of PARP1 Inhibitor Veliparib Encapsulation in DPPC and DPPG liposomes

Following the selection of the best DPPC and DPPG sonication conditions, encapsulation of the PARP1 inhibitor Veliparib was attempted using 100 μM of this inhibitor. The compound was added during the lipid dissolution in the organic solvent mixture step of liposome production (organic phase supplementation). Encapsulation of Veliparib ($\varepsilon_{295\ nm}$ = 8316.7 M^{-1} cm^{-1}) in the DPPG liposomes was observed with an efficiency (EE) of 49 ± 2% (Table C.3), while encapsulation in DPPC was unsuccessful. In fact, extreme liposome destabilization and flocculation starting in the hydration step were observed in DPPC samples. This could be related to charge compensation given by positively charged inhibitors, which, in turn, destabilized lipid bilayer organization. However, the negative charge of the DPPG molecule was able to maintain lipid bilayer stability. Through the zeta potential determination of DPPC and DPPG without inhibitors, this event can be further explained, and the values retrieved were −17.9 ± 0.9 mV and −43 ± 2 mV, respectively, for DPPC and DPPG (Table 6.1). These results are a clear indication of DPPC liposome instability prior to any type of drug encapsulation and the elevated

stability of DPPG (<−30 mV). The analysis of DPPG + Veliparib samples presented a zeta potential of −41 ± 2 mV, showing that inhibitor encapsulation led to an increase in liposome overall surface charge, confirming our previous theory.

Because of the very low loading capacity (LC) attained in the DPPG + Veliparib formulation (LC = 3.9 ± 0.2 %), displayed in Table C.3, different conditions were tested to increase EE and LC, thus further maximizing the drug load. For this, concentration and supplementation phases were varied. Concentrations of 20, 100, and 200 μM were assessed by organic phase supplementation, and an increase in EE and LC values is verified in Table 6.2. It was observed that loading capacity increases exponentially up to 10 % with 200 μM of Veliparib. EE values vary inversely with drug concentration. However, a stagnation is verified for this parameter around 50–55 % and occurs above the 100 μM supplementation, which indicates possible system saturation. Even though the highest concentration tested (200 μM) is far below the equimolar drug/lipid ratio, the saturation event can be related to the DMSO molecules. DMSO is the sole solvent used for the preparation of PARP1 inhibitor stocks, and it is known to interact with lipid membranes. DMSO is regularly used in cell cultures as a cryoprotectant, increasing membrane porosity and preventing water crystal formation through the promotion of vitrification at low temperatures [28]. This solvent is also known to be capable of interacting with lipids' headgroups, leading to water displacement. Neutron diffraction analysis has shown that the DMSO sulfur atom is attracted to LUVs' and MLVs' negatively charged phosphate groups, while DMSO methyl groups are capable of remaining inserted in lipids' head/pocket, which includes a phosphorus and four oxygen atoms. DMSO in PC lipids also presents a second interaction mechanism that is governed by DMSO oxygen attractive forces toward positively charged choline nitrogen moieties [29]. The water displacement mechanisms reported coincide with the DPPG (first mechanism) and DPPC (both mechanisms) expected lipophilic drug interaction regions, which clearly demonstrate the profound effect that DMSO could have on lipophilic drug encapsulation efficiency.

Table 6.2 — Veliparib encapsulation efficiency (EE) and loading capacity (LC) values in DPPG liposomes.

Veliparib (μM)	EE * (%)	LC * (%)
20	99.9 ± 0.2	1.99 ± 0.01
100	49± 2	3.9 ± 0.2
200	55 ± 1	10.20 ± 0.09

* Mean ± SD values (n=3 to 4).

Further DLS characterization showed that liposome size increases with Veliparib concentration (Figure 6.1d), and z-average values vary from approximately 60 to 90 nm, as seen in Table 6.3. The population and size distribution profile, shown in Figure 5.1d, appears to change with drug concentration. Condition 1 (20 μM) presents two populations and a distribution profile similar to the DPPG control condition without Veliparib, as shown in Figure 6.1c. The increase in drug concentration led to a change in the size distribution profile, the elimination of large size populations, and the main population shift to higher diameter values (Figure 6.1d). PdI reduces with drug concentration (Table 6.3) and is intrinsically associated with a more homogeneous sample and single population profile. The population of interest (Pop.1) shows a clear shift in size from the control sample (DPPG) (56 ± 2 nm) to encapsulation samples (>56 nm) (Table 6.3), where the greatest differences are observed at 200 μM supplementation (134 ± 6 nm). In terms of the liposome's surface charge, a decrease in value is observed dependent on drug concentration. Here, the values are not as straightforward, showing that 100 and 200 μM drug supplementation results in a similar shift to −40 mV, while the 20 μM condition presents a greater shift to −31 mV (Table 6.3). This may be explained by the presence of DMSO in the lipid membrane and the competition that occurs between Veliparib and DMSO molecules in the lipid's headgroup space. During the dialysis process, this competition event will be a determinant. Since Veliparib stocks are prepared in 100 % (*v/v*) DMSO solvent, drug supplementation dependent on concentration leads to positive feedback between DMSO and Veliparib final concentrations. This may explain why 100 % drug encapsulation takes place with 20 μM supplementation, where the system is not saturated and the DMSO percentage is reduced (~0.02 % *v/v*), thus allowing complete drug encapsulation. In the remaining concentrations, 100 μM and 200 μM, DMSO values were at 0.1 and 0.2 %, respectively, which explains the reduction and apparent stagnation in EE (< 55 %) through competitive events in higher inhibitor concentrations. These results show that an increase in DMSO to values of ~0.1–0.2 % fixes EE to approximately half the drug concentration input. By converting EE values to effective Veliparib concentration in DPPG membranes, it was possible to encapsulate approximately 48 μM and 100 μM in conditions 2 and 3, respectively. It was also interesting to verify that the same conditions appear to result in higher liposome stabilization with the determination of lower zeta potential values, as seen in Table 6.3.

Finally, it was also verified that after dialysis, the final DMSO percentage in the liposome stock formulations, 20 μM, 100 μM, and 200 μM supplementation, was in the range of 0.02–0.05 %, thus making the solvent content within the biocompatibility limit (0.05 %) for future cellular studies [30]. Moreover, this biocompatibility will be further increased by the reduction

of DMSO effective content upon liposome stock dilution when testing in vitro and in model organisms.

In summary, particle size is directly influenced by drug concentration, and a homogeneous liposome population is acquired at 200 μM drug supplementation. EE values are inversely related to initial drug-supplemented concentration; however, effective drug content in DPPG goes up to 100 μM of Veliparib. In terms of system stability, higher drug concentrations appear to result in a better fit, with zeta potential values around −40 mV. DMSO appears to be a competitor for drug encapsulation, and EE values appear to stagnate at 0.1–0.2 % *v/v* DMSO.

Taking this into consideration, DPPG supplementation with 200 μM Veliparib appears to be a good and stable system to employ in any type of test and system characterization for future applications.

Table 6.3 — DPPG liposomes' particle size and zeta potential variance dependent on Veliparib concentration.

Veliparib (μM)	Particle Size *				Zeta Potential * (mV)
	Z-Average (d.nm)	PdI	Pop.1 (d.nm)	Pop.2 (d.nm)	
20	60 ± 2	0.40 ± 0.04	48 ± 1	741 ± 86	−31 ± 2
100	79.4 ± 0.4	0.29 ± 0.02	116 ± 7	~2700	−41 ± 2
200	91 ± 2	0.28 ± 0.03	134 ± 6	---	−39 ± 2

* Mean ± SD values (n=3 to 4). Note: PdI—polydispersity index, Pop.1—population 1, and Pop.2—population 2.

Additionally, in an attempt to increase LC values, phase supplementation was varied. Since PARP1 inhibitors are insoluble in water (manufacturer recommendation), initial drug supplementation was performed in the organic phase, and afterwards, simultaneous organic and aqueous phase supplementation was tested. The 200 μM Veliparib concentration condition was used and divided into dual supplementation (100 μM + 100 μM). Results showed a clear difference in EE values between conditions, where dual supplementation achieved an efficiency of 31 ± 4 % (Table C.4) when compared to the organic phase condition (55 ± 1 %); see Table 6.2. A reduction of 5 % in loading capacity (LC) is observed from the organic phase to the dual phase (Table C.4), which, interestingly, is very similar to the 100 μM organic supplementation condition. Additionally, the dual phase EE value appears to be even lower than the 100 μM condition, but if we take into consideration the errors associated with these values, the differences do not appear to be that significant. The apparent coincidences lead to an indication for Veliparib's exclusive lipid bilayer encapsulation, which can be expected of a water-insoluble

drug. On the other hand, the dual phase z-average and main population size values (Table C.5) are similar to the 200 μM organic condition. However, the presence of a large size secondary population is consistent with the population profile from the 100 μM condition. This could be an indication that, even though the Veliparib dual system may be close to the 100 μM organic condition in EE and LC parameters, the increase in size of the main population could be related to DMSO integration on the lipid bilayer. Because DMSO addition to the lipid solution was of 0.2 % *v/v* in the 200 μM condition, this double difference for the 100 μM condition can explain the impact on liposome swelling. Previous studies have shown that DMSO has a profound effect on the lipid membrane, and a correlation was established between the DMSO mole fraction (DMSO/water mixture) and membrane behavior [29,31]. At molar fractions below 0.1 (X_{DMSO} < 0.1), DMSO does not appear to change the membrane structure or headgroup mobility, even though water displacement is verified by the competition and gain of lipid headgroups [28]. At these ratios, the lipid gel-to-fluid transition temperature increases, thus stabilizing the gel phase through changes in the surface hydration on the lipid headgroup [29]. Thermostability in this phase can be extended by DMSO up to a 5 °C increase [31]. DMSO is, thus, capable of altering the membrane's mechanical properties in a concentration-dependent manner. However, the DMSO effect is also variable, depending on the membrane composition and structure, which, in turn, affects membrane biological functions [31]. Infrared studies revealed that DMSO reduces the binary bilayers' free volume, while not affecting more complex liposome systems, specifically ones involving cholesterol. In POPC/ESM 1:1 GUVs systems, DMSO noticeably affected vesicle biophysical characteristics through a "membrane loosening" event, resulting from the increase in excess surface area in the vesicle. Again, this effect was not detected in complex liposome systems involving cholesterol (POPC/ESM/chol 1:1:3) [31]. The reported data reinforce our hypothesis of DMSO affecting DPPG + Veliparib encapsulation efficiency and vesicle size through interaction with the lipid headgroup and subsequent DMSO/Veliparib competition for the negatively charged phosphate groups.

The polydispersity quality evaluation for size distribution was 0.32 ± 0.02, which is an acceptable value for this type of sample. Zeta potential analysis of dual phase supplementation shows similar values to 100 and 200 μM organic phase, with an indication of −42 ± 3 (Table C.5). Making this a very stable system. In sum, organic supplementation retrieved the best results in terms of EE, LC, and sample homogeneity for Veliparib DPPG encapsulation.

Taking all this into consideration, the thin film encapsulation protocol of PARP1 inhibitors in DPPG should follow a 200 μM drug supplementation in the organic phase.

6.3.4 Ascertaining PARP1 Inhibitor Encapsulation in Single and Bi-Lipid Formulations

Encapsulation of PARP1 inhibitors Rucaparib ($\varepsilon_{360\ nm}$ = 14,144.4 M^{-1} cm^{-1}) and Niraparib ($\varepsilon_{311\ nm}$ = 13,200 M^{-1} cm^{-1}) was performed following the conditions previously optimized for Veliparib. DPPG drug encapsulation quality parameters retrieved slightly reduced EE values for 200 µM supplementation when compared to Veliparib values, as displayed in Table 6.4. A decrease of 5.8 % and 4.3 % for Rucaparib and Niraparib is observed, respectively. LC values are also reduced by 1 % when compared to Veliparib. Both parameters are similar between Rucaparib and Niraparib. Observed differences may be due to the molecular structure of the compound, the protonation state, the overall charge, and spatial hindrances based on the inhibitor's molecular size. Theoretical topological surface areas show an increase in calculated values in the following order: Niraparib (72.9 $Å^2$) < Veliparib (83.8 $Å^2$) < Rucaparib (135 $Å^2$) [32–34]. Even though differences between Niraparib and Veliparib do not follow the expected tendency (Veliparib < Niraparib), we must consider that this parameter is calculated taking into consideration only the N and O atoms, which have the same representativity in both molecules (five in total), as shown in Table 6.4. However, when comparing overall molecular structures, it is evident that the total atom composition is greater in Niraparib than Veliparib, which, in turn, translates into a greater atomic mass. The design of PARP1 inhibitors targeting the protein catalytic domain follows specific guidelines. They all have in common a benzamide moiety, while the remaining structure is adjustable and designed to best fit the catalytic hydrophobic pocket, which thus ensures high target specificity [5,35,36]. These compounds are designed to mimic NAD^+ molecules (specifically the nicotinamide core structure) that are essential for PARP1's transferase activity [5,36].

Nevertheless, for all three inhibitors, the determined EE values are exceptionally good (≥ 50 %) and translate into an effective drug cargo of 90 to 100 µM in DPPG liposomes.

Table 6.4 — Encapsulation efficiency (EE) and loading capacity (LC) values of PARP1 inhibitors in single- and dual-lipid formulations.

PARP1 Inhibitor	Molecular Structure	DPPG (200 µM) *		DPPG/DPPC 1:1 (100 µM) *	
		EE + (%)	LC + (%)	EE + (%)	LC + (%)
Veliparib	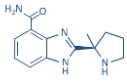	55 ± 1	10.20 ± 0.09	38 ± 2	3.3 ± 0.3
Rucaparib	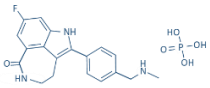	49.2 ± 0.3	9.2 ± 0.1	40 ± 1	2.80 ± 0.03
Niraparib	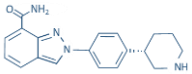	50.7 ± 0.9	9.0 ± 0.1	33.7 ± 0.9	3.1 ± 0.2

* Supplemented drug concentration; + mean ± SD values (n=3 to 4).

Since DPPC drug encapsulation was not successful, the development of a complementary liposome system was attempted. To ensure the presence of PC lipids and further increase biological compatibility in the liposome formulation, we developed an equimolar DPPG/DPPC complex following the protocol previously described. The bi-lipid liposome formulation was relatively stable (<−30 mV), presenting a surface area charge of −38.8 ± 0.7 mV. In comparison to DPPG control samples (see Table 6.1), the best stability results were observed in the single liposome formulation. The decreased stabilization of DPPG/DPPC can be expected if one considers the overall DPPC lipid charge and determined zeta potential values (−17.9 mV). DPPG/DPPC 1:1 size distribution analysis revealed a single population with a mean diameter size of 98.0 ± 1.76 nm, a z-average value of 77.0 ± 0.8 nm, and a PdI value of 0.22 ± 0.01. In comparison with DPPC and DPPG single-lipid formulations (Table 6.1), 20 sonication cycles resulted in an overall increment in size values of the complex liposome formulation. This can be related to the attractive and repulsive forces between DPPC and DPPG headgroups, as well as the Na+ counterion effect on the equilibrium of these forces.

Since the DPPG/DPPC 1:1 formulation presented a diminished degree of stabilization compared to PG liposomes, a 100 µM drug supplementation was employed. EE and LC values for the three inhibitors were low, which was expected. EE values were around 40 % (see Table 6.4), and close to the 100 µM Veliparib supplementation in DPPG liposomes (Table 6.2). Still, some differences are observed, with a decrease in efficiency that ranges from 9 to 15 %. Among PARP1 inhibitors, differences are also verified, with Rucaparib presenting the best

encapsulation values and Niraparib presenting the lowest EE value (33.7 ± 0.9 %). The differences in encapsulation efficiencies can be explained by the lipid formulation and the lower presence of DPPG lipids in the DPPG/DPPC liposome formulation. Additionally, liposome and inhibitor overall charge will be determinants of lipid–inhibitor interaction. Lipid susceptibility to DMSO presence can also explain EE differences between liposome formulations, with lower mechanical stabilization of DPPC over DPPG lipid [26]. LC values are like those observed with 100 μM supplementation in DPPG liposomes. These results are a clear indication that the DPPG/DPPC formulation has similar behavior to the DPPG 100 μM drug supplementation condition but does not present the same good EE values.

In the following section, liposome formulations with encapsulated PARP1 inhibitors will be extensively characterized and discussed. Additionally, a quality assessment of each formulation as a potential therapeutic alternative will be performed, and an effective lipid–inhibitor interaction will be determined.

6.3.5 Lipid Delivery System Characterization - Quality Assessment

DLS zeta potential characterization has shown that in terms of surface charge, DPPG encapsulating inhibitor liposomes have a better fit than the bi-lipid formulation, with values achieved being far below the −30 mV stability boundary. Binary DPPG/DPPC liposome encapsulating inhibitors presented values over −30 mV (Table 6.5), stating that the formulations are not as stable as would be desired. In terms of size distribution, DPPG and the bi-lipid formulation present similar z-average values around 90 to 100 nm. All formulations, except DPPG/DPPC (1:1) + Rucaparib, present only one population with a diameter above 100 nm, as seen in Table 6.5. The smallest particle size is verified in the Veliparib formulation, which would be expected if the molecular structure and topological surface areas of the inhibitors were taken into consideration, as discussed previously. Additionally, from the analysis of published PARP1 inhibitor crystal structures, it is possible to get an idea of each inhibitor's 2D dimensions [37,38]. This allows us to determine reference values for putative maximum lengths and widths of Veliparib, Niraparib, and Rucaparib using the RSCB PDB data treatment software [39–42]. The inhibitors' maximum values follow the tendency of Rucaparib > Niraparib > Veliparib for width, and Niraparib > Rucaparib > Veliparib for length (Figure C.1). These data are an indication of the putative spatial constrictions, and in which order they may occur.

Overall, DPPG liposomes appear to be the best formulation for PARP1 inhibitor encapsulation, presenting good EE and LC values, as well as a high degree of stabilization (zeta potential < −30 mV). In terms of liposome size distribution, a single population profile is attained,

and particle diameter values are somewhat coherent. Main population (Pop.1) particle size contribution is defined as 130 ± 3 nm, 135 ± 10 nm, and 132 ± 7 nm for each inhibitor (Table 6.5). Between the three formulations, size distribution appears to be more homogeneous in DPPG + Veliparib liposome particles (Figure C.2).

Table 6.5 — DLS particle size and zeta potential characterization of DPPG and PG/PC (1:1) formulations encapsulating PARP1 inhibitors.

Liposome	PARP1 Inhibitor	Particle Size *				Zeta Potential * (mV)
		Z-Average (d.nm)	PdI	Pop.1 (d.nm)	Pop.2 (d.nm)	
DPPG	Veliparib	91 ± 2	0.28 ± 0.02	130 ± 3	----	−39 ± 2
	Rucaparib	94 ± 8	0.25 ± 0.01	135 ± 10	----	−33 ± 1
	Niraparib	94 ± 4	0.25 ± 0.01	132 ± 7	----	−36 ± 2
DPPG/DPPC 1:1	Veliparib	88 ± 2	0.22 ± 0.01	115 ± 4	----	−29 ± 4
	Rucaparib	97 ± 3	0.28 ± 0.02	130 ± 40	~117	−25 ± 4
	Niraparib	101 ± 2	0.31 ± 0.05	156 ± 11	----	−25 ± 4

* Mean ± SD values (n=3 to 4). Note: PdI—polydispersity index, Pop.1—population 1, and Pop.2—population 2.

Since DPPG simple formulation presented the best fit for further exploitations as PARP1 inhibitor delivery system, an evaluation over time was performed concerning particle size stability along a 28-day time period. Samples were stored at 4 °C after production, with Z-average and main population size values taken into consideration and analyzed in parallel, seen in Figure 6.2. The DPPG control sample (without inhibitor) showed an initial increase in size values after 7 days of storage, with a return to approximately initial size values after 14 days, as it can be seen from Figure 6.2a. After 28 days of storage, liposome samples have shown a stabilization of the size of the main population, but z-average values increased significantly with detection of large size particles (> 0.5 μm). This was a clear indication of sample destabilization after approximately one month storage.

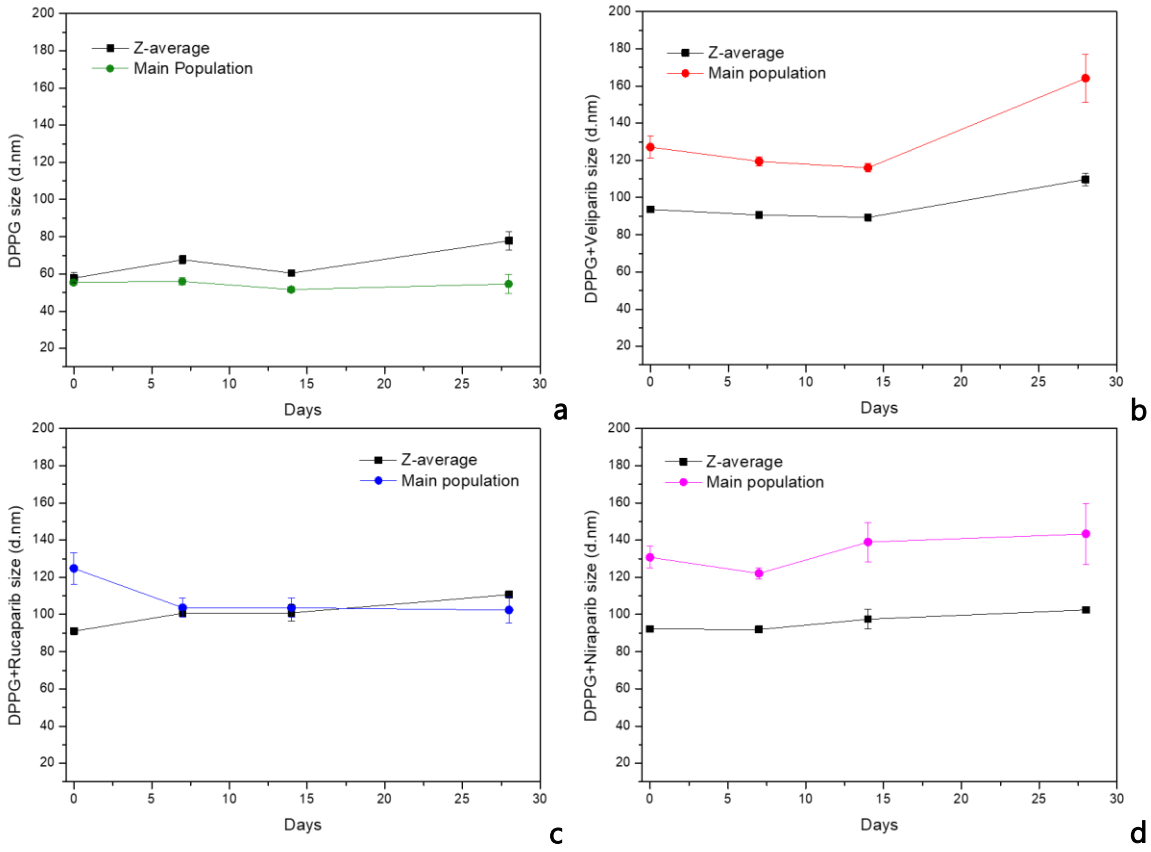

Figure 6.2 — Evaluation of particle size stability (z-average and main population size values, n=3 to 4) of DPPG-encapsulating PARP1 inhibitors, during 28 days of storage at 4 °C. a) Control sample without an inhibitor, b) DPPG with Veliparib, c) DPPG with Rucaparib, and d) DPPG with Niraparib. In all graphs, z-average (black line) and main population size values (colored line) are presented as mean values with standard deviation values (SD).

The observation of size variation of DPPG liposomes with time is not uncommon for simple liposome formulations. It has already been reported for DMPC, DPPC, and DSPC simple formulations that there are increases and decreases in liposome size distribution [43]. In these, particle size stabilization was enhanced and achieved with the introduction of cholesterol to the liposome formulations. Stabilization was due to increases in transition temperatures and membrane elasticity range, thus improving lipid organization, packing, and formulation robustness [43].

The liposome formulation containing PARP1 inhibitors revealed specific size variation patterns for each compound, different from the control. Veliparib appears to stabilize DPPG liposome size until 14 days of storage, for both z-average and main population values, which is an indication that the liposome product/formulation retained the same size characteristics as those observed after the production stage. Over 14 days, size distribution values show an increase in particle diameter with the surfacing of large size populations (Figure 6.2b). On the other hand, Rucaparib appears to have a profound effect on particle size distribution, with z-

average and main population values becoming closer to each other (Figure 6.2c). This may be an indication that Rucaparib increases sample homogeneity in terms of size population distribution. After 14 days of storage, it was verified that there was an increase in z-average values, while the main population size was maintained. This was related to the appearance of large size populations due to particle aggregation. The DPPG + Niraparib formulation, on the other hand, shows an inverted tendency from the DPPG control sample. Variance is observed in the main population size, while z-average size variation is more stable. The main population shows a decrease in particle size until 7 days of storage, which is followed by an increase until 14 days. Past this time, the particle size increase rate is slowed down. From a physical sample evaluation, it was observed that until 14 days of storage, all samples were translucid with no apparent deposit; however, after approximately one month, this event was observed. This indicates that after one month, DPPG liposome formulations present aggregation events, with large size particle destabilization. Nevertheless, for all drug formulations, it was verified that particle size stabilization occurred until 14 days of storage at 4 °C, with no deposit formation/flocculation. Taking into consideration cholesterol studies on liposome stability [43,44], it can be inferred that the tested inhibitors may be affecting DPPG stability in a similar manner. By putative electrostatic interaction and hydrogen bonding between the inhibitors and lipid headgroups, DPPG stabilization is being favored through the increase of membrane elasticity temperature range (increase in transition temperature leads to a more permanent gel-phase state) and promotion of lipid organization, thus translating into a high degree of system robustness and fit.

The DPPG formulations appear to be a good option for PARP1 inhibitors' encapsulation and future therapeutic applications. We verified that encapsulation is favored using negatively charged lipids and state that DPPG should be employed when designing a lipid carrier for these compounds. Furthermore, the produced liposome formulations can be used as a base for further liposome surface functionalization with coatings such as polymers, polyelectrolytes, antibodies, or even conjugation with other systems [15,44,45]. This will aid in overall system stability, biocompatibility, target specificity, and controlling drug release [15,45,46].

6.3.6 Drug Release Analysis and Kinetics - Time of Circulation Determination

The biophysical features of liposome-encapsulating lipophilic compounds are greatly affected and determined by their core–shell properties [43,44]. However, additional factors are also in play when we talk about drug release. Factors such as buffer/medium, the nanocarrier

units' physicochemical properties, and the nanocarrier's internal structure are of high importance for release rates and the determination of suitable delivery systems [47].

An *in vitro* analysis was performed with the three DPPG-encapsulating PARP1 inhibitor systems and compared to the respective standard drug solutions. Each control sample was prepared at the concentration that was present in the liposome system. PBS 1x was used as the dialysis buffer, and compound concentration was determined from the dialysate. Absorbance measurements were performed at the absorbance wavelengths of 295, 360, and 311 nm for Veliparib, Rucaparib, and Niraparib, respectively. It was verified in all samples that there was an initial burst release due to the dialysis system, thus contributing a lag time to the cumulative drug release profile, as can be seen in the plots in Figure 6.3. Release patterns are distinct for each inhibitor, with control samples presenting after 3 h at 37 °C values of 66 ± 1 %, 104 ± 1 %, and 68.5 ± 0.9 % for Veliparib, Rucaparib, and Niraparib, respectively. Corresponding DPPG drug release percentage values were 48 ± 9 %, 96 ± 2 %, and 54 ± 2 %. Differences observed between control and liposome formulations show that the presence of DPPG led to an overall decrease in drug release rates. Past 7 h, cumulative drug release values were as follows: 74 ± 15%, 100.0 ± 0%, and 59 ± 11% (Figure 6.3), showing that DPPG + Veliparib/Niraparib are best suited for long-term release. The DPPG + Rucaparib system was efficient in delaying drug release rates until 3 h; however, after this timepoint, cumulative values converged to one of the control samples (Figure 6.3b).

Drug release from nano-delivery systems is determined by the physical and chemical properties of the system, including the drug and nanocarrier. Features such as porosity, surface roughness, chemical composition, molecular weight, degradation rate, particle size, compound dosage, and drug–matrix interactions are of extreme importance [48]. In our case, the variability observed between systems may be related to the entrapment efficiency of the inhibitors in the nanocarrier bilayer, to the inhibitors orientation and mode of insertion in the bilayer, as well as to the membrane's rigidity, porosity, and gel–fluid state [44,47].

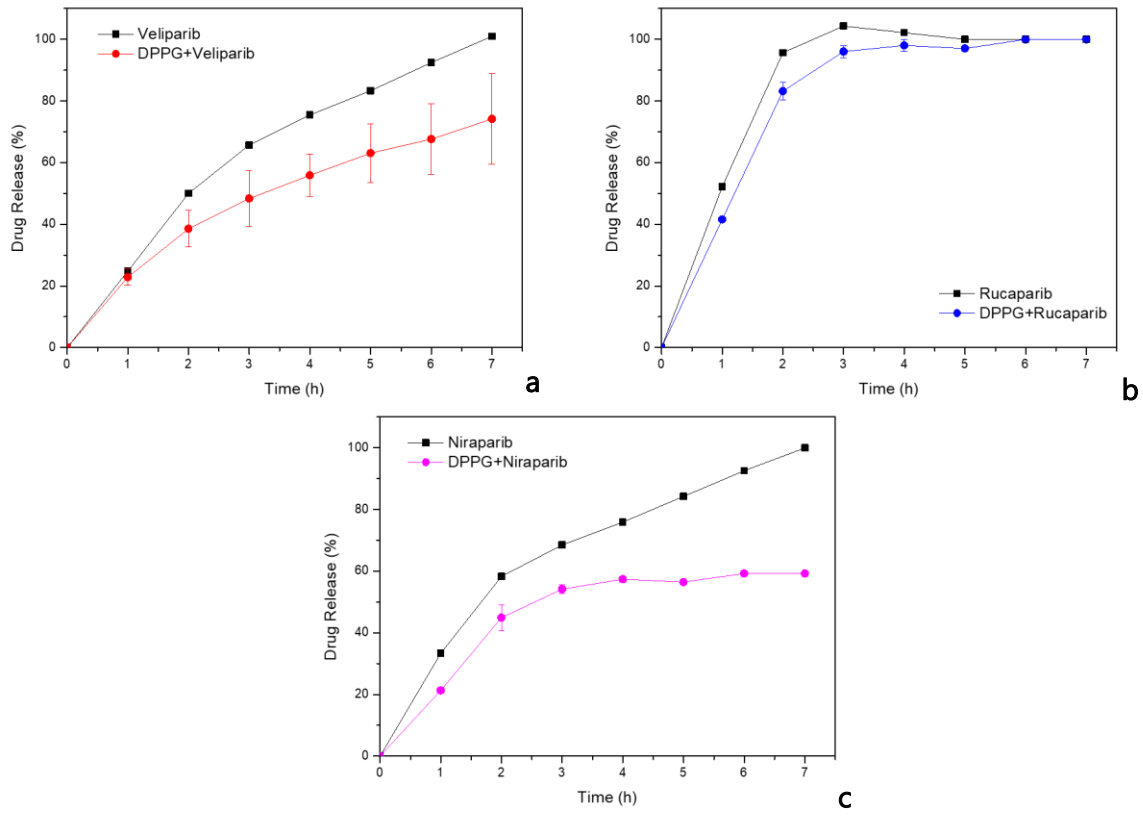

Figure 6.3 — In vitro cumulative drug release analysis from DPPG liposomes (colored line), with respective drug control samples (black line). a) Veliparib; b) Rucaparib; c) Niraparib.

To understand drug release kinetics and determine the DPPG potential nanocarrier applicability and efficiency, the data obtained were plotted following various mathematical models. Among them, Weibull (T_{LAG}) and Michaelis–Menten equations better explained drug release from DPPG, presenting the highest linearity with the highest value of R^2 and the lowest value of the Akaike information criterion (AIC), as can be seen from the data displayed in Table 6.6. The first equation gave the best fit for Veliparib and Niraparib release data, while the second equation explains the Rucaparib system. The Hixson–Cromwell model did not explain the drug release data. Krosmeyer–Peppas n values suggest that all systems present complex drug release mechanisms. Calculated values with best fit point to a non-Fickian diffusion mechanism ($0.45 < n < 0.89$) (Krosmeyer–Peppas (T_{LAG})) for all three inhibitors [49]. Further confirmation of transport complexity is given by the Weibull β (shape) parameter, with values < 1 for Veliparib and Niraparib, and >1 for Rucaparib (Table 6.6).

β values ≤ 0.75 are linked to Fickian diffusion mechanisms, while values between 0.75 and 1 are associated with combined mechanisms of Fickian diffusion and controlled transport by nanoparticle swelling. A shape factor above 1 implies very complex drug release mechanisms, characterized by an initial non-linear increase in drug rate release, followed by an equal

decrease event [50]. This mechanism is quite perceptible in Rucaparib's cumulative drug release graph (Figure 6.3b). Thus, our results state that the Veliparib and Niraparib release mechanisms in DPPG are governed by a combined system of Fickian and non-Fickian diffusion processes (n and β values), involving nanoparticle swelling and deswelling events. Rucaparib, on the other hand, presents a complex mechanism associated with anomalous diffusion with a possible link to super case II transport, if the n > 0.89 value for the conventional Krosmeyer–Peppas model is taken into consideration (Table 6.6) [49]. Super case II is mainly associated with stress and a polymer state transition due to swelling in water or biological fluids [51]. The combination of anomalous case II and super case II behaviors has previously been related to hydrogel porosity [49], which can give us some indications about the DPPG-encapsulating PARP1 inhibitor release system. Taking into consideration the DPPG transition temperatures (Tc = 41 °C), the release assay temperature (Ta = 37 °C), and the presence of DMSO, it is within reason to hypothesize that while performing the release assay, liposome samples could have been in their gel-state phase (Ta < Tc), presenting some pore structures resulting from the presence of DMSO, which is in line with the anomalous and porous theory. In this way, super case II transport, indicated by n values above 0.89, and anomalous transport verified in the liposome systems can be explained. All these are due to drug release mechanisms governed by membrane swelling transport due to osmotic pressure, membrane hydration, and a protonation state [48].

Table 6.6 — Release kinetics determined for PARP1 inhibitors from DPPG liposomes.

Model	Veliparib				Rucaparib				Niraparib			
	R^2	K	β	AIC	R^2	K	β	AIC	R^2	K	β	AIC
Weibull	0.999	4.33	0.94	31.76	0.992	0.75	1.02	60.29	0.999	4.63	0.93	54.15
Weibull (T_{LAG})	0.999	3.78	0.83	16.64	0.989	0.75	1.02	62.29	0.999	3.59	0.73	50.60
	R^2	Km		AIC	R^2	Km		AIC	R^2	Km		AIC
Michaelis–Menten	1.00	0.55		60.89	1.00	1.15		54.16	1.00	0.54		55.53
Michaelis–Menten (T_{LAG})	1.00	0.55		62.92	1.00	1.13		56.22	1.00	0.53		57.56
	R^2	Km		AIC	R^2	Km		AIC	R^2	Km		AIC

Hixson–Crowell	0.629	0.45	67.81	0.512	0.47	78.78	0.537	0.40	69.72
	R^2	n	AIC	R^2	n	AIC	R^2	n	AIC
Korsmeyer–Peppas	0.999	0.92	58.91	0.998	0.94	76.55	0.998	0.92	65.36
Korsmeyer–Pepas (T_{LAG})	0.999	0.72	47.65	0.999	0.73	72.48	0.999	0.72	60.68

Note: R^2 refers empirical coefficient of determination; AIC—Akaike information criterion; K—model release constants; β–shape parameter; Km—Michaelis–Menten constant; n—diffusion release exponent.

In summary, it has been shown that DPPG-encapsulated inhibitors presented slower release rates than control samples. DPPG + Veliparib/Niraparib were considered the most suitable formulations, with complete drug release delayed until 7 h. Rucaparib formulation was efficient until 3 h of dialysis; however, after this timepoint, cumulative values converged to those from the control sample. The three inhibitors presented complex release mechanisms, with Veliparib and Niraparib being governed by a combination of diffusion-controlled (Fickian) and non-Fickian diffusion mechanisms, while anomalous and super case II transport was verified for Rucaparib. Anomalous drug transport events could be related to membrane swelling events and the presence of porous structures due to DMSO. Further testing and optimization should be performed to enhance system stability in circulation and drug release rates. This could be achieved through the addition of stabilizer components to the liposome membrane, such as cholesterol or other lipidic components. The addition of polymeric stabilizers such as PEG or polyelectrolytes may help to increase membrane stability and decrease drug release rates [15,19]. In addition, the reduction in DMSO content could help with membrane porosity; however, this will be limited and related to drug solubility and dialysis procedures.

6.3.7 PARPi and Lipid Delivery System Biophysical Interaction - Spectroscopic Characterization

Spectroscopic characterization was performed for DPPG-encapsulating systems using UV–Vis and Fourier-transform infrared (FTIR) spectroscopies.

The UV–Vis spectra of DPPG liposomes in Figure 6.4 present a maximum absorption peak near 194 nm, which is consistent with a typical liposome band at 194.4 ± 0.7 nm [18,52]. This is assigned to the lone-pair transition of carbonyl oxygen to the antibonding π_{CO} valence orbital, to $n_O \rightarrow \pi^*_{CO}$, or to the valence shell electronic excitation of hydroxyl groups [18].

DPPG-encapsulating PARP1 inhibitors present characteristic inhibitor maximum absorbance peaks in the 224–450 nm region (Veliparib: 270 and 295 nm; Rucaparib: 238, 281, 323, and 360 nm; Niraparib: 239 nm, 311 nm, and 342 nm), confirming drug encapsulation (Figure 6.4). Upon drug incorporation into the lipid carrier, it is verified that Rucaparib's 278 nm and Niraparib's 306 nm pure drug maximum absorbance peaks, shown as colored dash lines in the UV–Vis spectra in Figure 6.4, present a significant change in the peak position toward higher wavelengths, i.e., a red shift, when DPPG is encapsulating these drugs. The observed shift could be a result of a higher protonation state [53] and/or the presence of a substituent (e.g., -OH) in the chromophore [54] in the inhibitor molecules. The DPPG + Veliparib sample does not present such significant shifts in its peaks in the UV–Vis spectra. The observed red shift of the maximum absorbance peaks in the case of Rucaparib and Niraparib molecules encapsulated into liposomes serves as an additional indication of the interaction of these inhibitors with the liposome membrane and the indication of drug encapsulation. Additionally, the characteristic absorbance peak of DMSO solvent (211 ± 6.0 nm) is also perceived in the region around 205–210 nm, due to the n → π* electronic transition from the unshared electron pair of the oxygen atom [55].

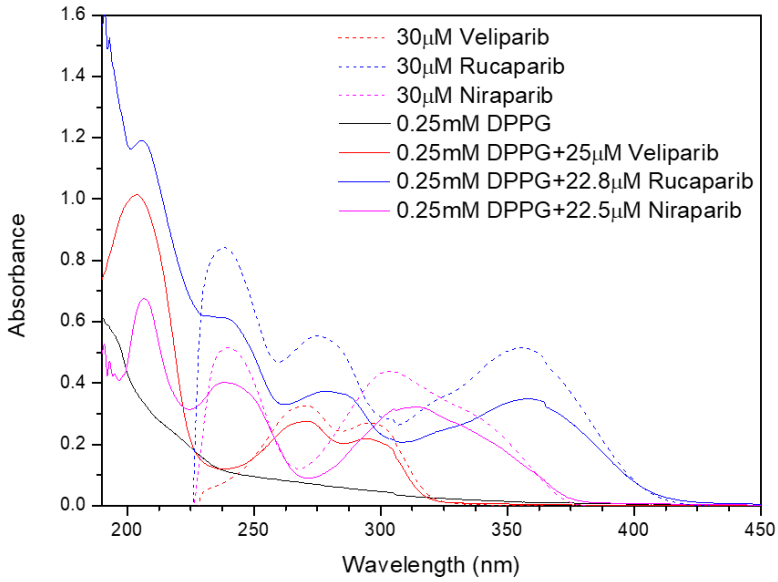

Figure 6.4 — Absorption spectra of DPPG (black line), DPPG+PARP1 inhibitor liposomes (colored line), and pure inhibitor solutions (colored dash line).

Characteristic infrared absorption bands and assignments are displayed in Table C.6 for DPPG (Figure 6.5) and Tables C.7–C.9 for PARP1 inhibitors (Veliparib, Rucaparib, and Niraparib) (Figure C.3).

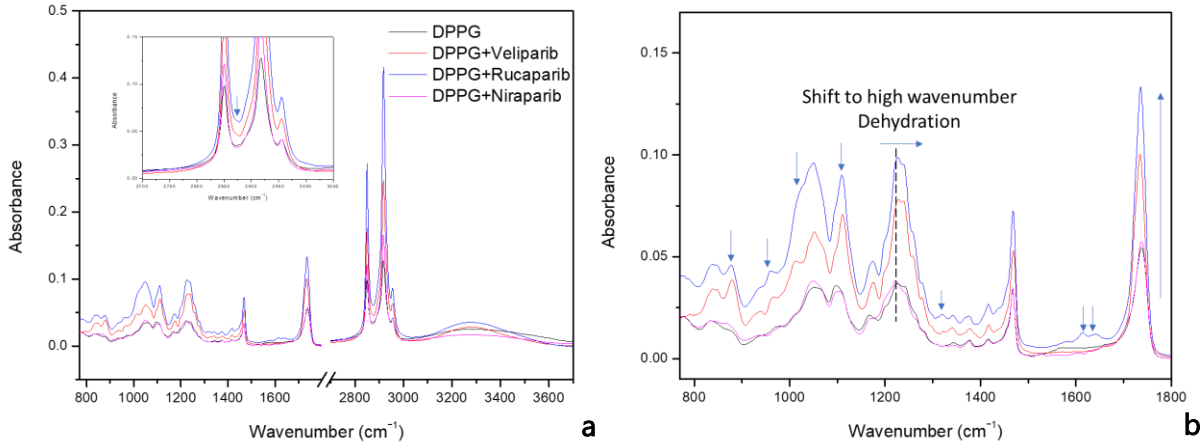

Figure 6.5 — FTIR analysis of DPPG liposomes with and without PARP1 inhibitors. a) Full spectra with the inset showing the presence of the inhibitor band in the 2800–3000 cm^{-1} region. b) Enlarged spectra, displaying the differences between the DPPG control and encapsulating samples. Identification of the major contributions to DPPG spectra changes due to inhibitor encapsulation in the lipid membrane. Arrows identifying the inhibitor contribution bands, absorbance increases in the carbonyl and phosphate bands, and the phosphate band at 1224 cm^{-1} shift toward higher values (indication of possible lipid membrane dehydration in the inhibitor encapsulating formulae).

The spectra for the DPPG formula were obtained by subtracting the CaF_2 support without the cast film. The control sample spectra (dark line), shown in Figure 6.5, present typical DPPG bands with a broad peak in the region above 3000 cm^{-1}, which is attributed to O-H and C-H vibrational modes, while the 2800–3000 cm^{-1} region refers to both symmetric and antisymmetric stretching vibrations of the CH_2 groups. Incorporation of PARP1 inhibitors is perceived in these regions with the narrowing and sharpening of the band above 3000 cm^{-1} (due to C-H and N-H absorbance contributions from inhibitor molecules) and the increased absorbance of CH_2 vibrational bands. Band narrowing above 3000 cm^{-1} indicates possible inhibitor incorporation through the exclusion/displacement of water molecules, due to the reduction of OH vibrational modes, as well as incorporation in the bilayer membrane by peak sharpening and absorbance increases above the 2800 cm^{-1} region (Figure 6.5a). Furthermore, in the Figure 6.5a inset, an additional band is detected at 2872 cm^{-1}, between liposome CH_2 vibrational modes, consistent with the inhibitor's CH_3 symmetric and asymmetric stretch and aromatic ring CH stretch (Tables C.7–C.9). Other similar compound incorporation contributions to the DPPG FTIR spectra are displayed and signaled in Figure 6.5b and correspond to characteristic inhibitor vibrational bands from the aromatic rings and functional groups. These comprise the signature-specific bands for each compound [56,57]. Overall, there is a verified increase in liposome band absorbance, with this being more preeminent in the DPPG methylene (2800–3000 cm^{-1}), carbonyl (1736 cm^{-1}), and phosphate (12243 and 1242 cm^{-1}) groups (Figure 6.5).

According to the literature, the phosphate and carbonyl groups are considered hydration centers, with band position and strength providing useful information about the lipids' hydration state when in contact with water [58–60]. Both regions are highly sensitive to local hydrogen bond interactions, and a decrease in hydrogen bonding (hydration state) results in a shift of phosphate and carbonyl bands to higher wavenumbers [59,60], thus providing great insight into the compounds' bilayer membrane interaction mode. In Figure 6.5b, marked with a dashed line, and Table 6.7, it is perceived that the phosphate hydrogen-bonded band (1224 cm^{-1}) presents a slight shift to higher wavenumbers around 1227 and 1228 cm^{-1} for Rucaparib and Veliparib, respectively, while Niraparib does not appear to significantly affect the phosphate hydrogen bond/hydration state.

DPPG carbonyl vibration modes can be evaluated by decomposition of the major band into three Gaussian peaks at 1699 cm^{-1}, 1725 cm^{-1}, and 1740 cm^{-1} (Figure C.4). The first two bands are assigned to hydrogen-bonded carbonyl groups and the third band to non-hydrogen-bonded carbonyl groups, respectively [60]. Differences are perceived in the carbonyl peak profile upon inhibitor incorporation. A small shift to lower wavelengths is observed as a result of alterations in the Gaussian areas and contributions (Figure C.4 and Table 6.8). An overall increase in the area of the non-hydrogen-bonded band (1740 cm^{-1}) is observed, with the inhibitor impact following the tendency: Veliparib > Rucaparib > Niraparib (Table 6.8). Veliparib membrane incorporation appears to have a more profound effect with the surfacing of an additional vibrational band at 1760 cm^{-1} (Figure C.4). More interestingly, it was verified that there was a significant alteration in the hydrogen-bonded bands, with a significant increase in the Gaussian area for the first peak and a decrease for the second peak (Figure C.4), which is better perceived in the area ratio analysis in Table 6.8. Inhibitor impacts follow the same tendency as the third peak. Analysis from the area ratio values of the peak at 1725 cm^{-1} depicts the effect of each compound in the liposome bilayer, with values of 0.373, 0.035, 0.038, and 0.340 for the control, Veliparib, Rucaparib, and Niraparib, respectively (Table 6.8).

The two low-frequency peaks for hydrogen-bonded carbonyls are attributed to different interaction modes, with the peak at 1699 cm^{-1} being associated with the presence of lipids' glycerol OH in the interaction [60] and the peak at 1725 cm^{-1} being attributed to water OH molecules [58,60]. The major observed decrease in the second peaks' area ratios indicates that the three compounds promote water displacement from the lipid membrane, while increasing another type of hydrogen-bond vibrational mode at lower wavelengths (1699 cm^{-1}); see Figure C.4 and Table 6.8. The increase in area and ratios of carbonyl's first Gaussian (1699 cm^{-1}) indicates a possible mode of interaction between all three compounds with the lipid membrane.

The membrane insertion of PARP1 inhibitors may be contributing to the formation of additional hydrogen bond interactions with the lipids' carbonyl groups, which may be orchestrated by the inhibitors' amine groups/aromatic rings (that will be in a higher protonated state due to the solvent pH). This amine–carbonyl interaction, in turn, promotes an apparent membrane hydration that is, in fact, a water substitution. Confirmation of this event is further anchored by the narrowing of the X-H stretch (> 3000 cm^{-1}), where DPPG IR absorbance in the O-H region is decreased (> 3440 cm^{-1}) and C-H and N-H are increased.

Even though Niraparib appears to have the least impact on DPPG infrared spectra and membrane dehydration, which could be related to encapsulation efficiency, it appears that the major interaction and effect are directed to the carbonyl group. Regarding Veliparib and Rucaparib, membrane dehydration is favored by both compounds in the phosphate and carbonyl centers; however, a significant impact is verified in the liposome carbonyl group. To summarize, PARP1 inhibitors interact with the DPPG lipid membrane, preferentially in the carbonyl group, through hydrogen bonding. This interaction may involve the inhibitors' protonated amine groups, which, in turn, leads to water displacement in the hydration centers.

Table 6.7 — Analysis of the hydrogen-bonded phosphate band (1224 cm^{-1}) shift dependent on inhibitor encapsulation in DPPG liposomes. Arrows indicate the direction of wavenumber band shift in the FTIR spectra upon inhibitor encapsulation.

Hydrogen-Bonded Phosphate Band (1224 cm^{-1}) Shift			
DPPG	**DPPG + Veliparib**	**DPPG + Rucaparib**	**DPPG + Niraparib**
1224	1227.7	1226.5	1223.4
(0)	(+3.7)	(+2.5)	(−0.6)
-	→	→	←

Table 6.8 — Area ratios of carbonyl groups deconvoluted with Gaussian curves, corresponding to hydrogen-bonded (maximum band at 1699 cm^{-1} and 1725 cm^{-1} wavenumbers) and non-hydrogen-bonded forms (maximum band at 1740 cm^{-1} wavenumbers).

DPPG Formulation	**Ratios ($A_{x\ cm^{-1}}/A_{total}$)**			
	$A_{1699\ cm^{-1}}$	**$A_{1725\ cm^{-1}}$**	**$A_{1699+1725\ cm^{-1}}$**	**$A_{1740\ cm^{-1}}$**
Control	0.066	0.373	0.439	0.560
Veliparib	0.179	0.035	0.214	0.774
Rucaparib	0.170	0.038	0.208	0.792

Niraparib	0.074	0.340	0.414	0.586

To summarize, PARP1 inhibitor encapsulation was achieved in DPPG liposomes, and encapsulation efficiency was optimized taking into consideration DMSO content and its presence in a biocompatible range (below 0.051 %). It was also observed that lipid–inhibitor interaction occurs preferentially in the carbonyl groups, thus confirming drug encapsulation in the lipidic membrane (Figure 6.6). The encapsulating DPPG formulation presented structural stabilization until 14 days of storage, which can be further increased by overall lipid formulation optimization (lipid conjugation) and liposome surface functionalization/coating. This work has shown that the devised DPPG + PARP1 inhibitor formulations present the best starting point and foundation for future target delivery design. By coating the surface of liposomes with polymers, polyelectrolytes, antibodies, and other compounds, greater stabilization, increased time circulation, increased control release, and drug target delivery may be achieved.

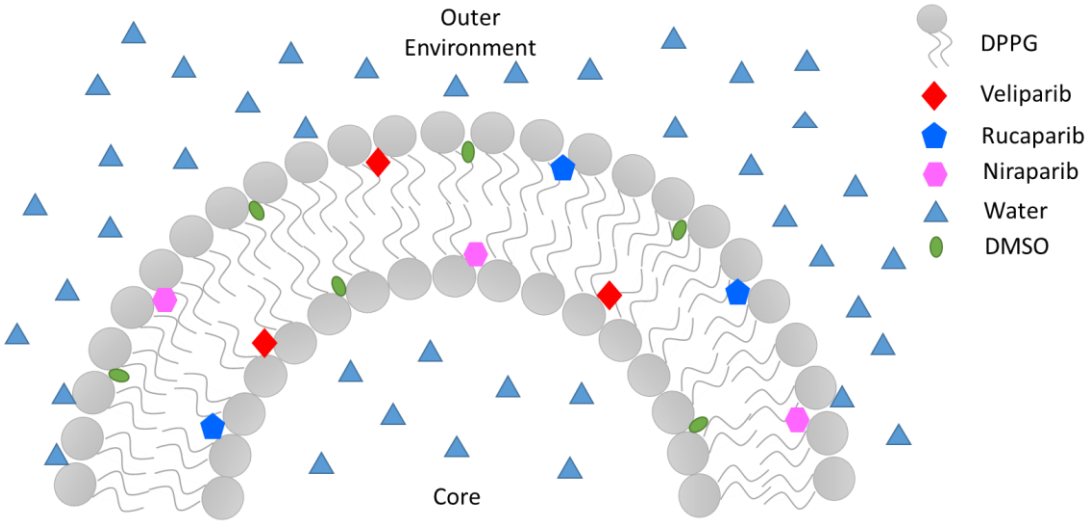

Figure 6.6 — Illustration of PARP1 inhibitors' Veliparib, Rucaparib, and Niraparib encapsulation mode in a sectionized DPPG liposome's lipid bilayer.

6.4 Conclusion

In this work, lipid nano-delivery systems for three PARP1 inhibitors (Veliparib, Rucaparib, and Niraparib) were implemented and characterized. Simple lipid and dual lipid formulations with DPPG and DPPC were developed and tested following the thin-film method. Conditions were optimized for inhibitor encapsulation, where good values of encapsulation efficiency were attained (> 40 %), which translate to drug concentration values as high as 100

μM. DPPG-encapsulating inhibitors presented the best fit in terms of particle stabilization by retrieval of zeta potential values below −30 mV and good particle population distribution (single population profile). The size of the main population of interest was ~130 nm in diameter. DPPG/DPPC (1:1) formulations presented zeta potential values above −30 mV, indicative of particle destabilization, thus making DPPG liposomes the best formulation for PARP1 inhibitor encapsulation. An evaluation of the storage stabilization of DPPG formulations led to the verification of particle size stabilization until 14 days of storage at 4 °C. No particle deposition or flocculation was observed.

Kinetic release studies showed that DPPG-encapsulating inhibitors presented slower release rates than drug control samples, and DPPG + Veliparib/Niraparib were considered the most suitable formulations, with complete drug release delayed until 7 h. The Rucaparib formulation was efficient until 3 h of dialysis; however, after this timepoint, cumulative values converged to those of the control sample. In all three DPPG drug formulations, complex release mechanisms were identified, with Veliparib and Niraparib being governed by a combination of diffusion-controlled (Fickian) and non-Fickian diffusion, while anomalous and super case II transport was verified for Rucaparib, indicating that further optimization should be carried out to enhance system stabilization in circulation and drug release rates. This can be achieved using liposome membrane stabilization components such as cholesterol, PEG, polyelectrolytes, and other lipidic components.

Spectroscopic analysis revealed that PARP1 inhibitors interact with the DPPG lipid membrane, which may explain the complex release mechanism unveiled. Infrared analysis indicated a preferential membrane interaction with the lipid carbonyl groups through hydrogen bonding, where the inhibitors' protonated amine groups may be major players in the drug encapsulation mode. These interactions appear to have a profound effect on lipid membrane hydration, where efficient PARP1 inhibitor encapsulation results in water displacement from phosphate and carbonyl hydration centers. Differences in the impact on membrane water displacement are perceived, with a tendency to follow the order from highest to lowest: Veliparib > Rucaparib > Niraparib. This could be explained by the encapsulation efficiencies of each drug, their molecular structure, and their composition.

To summarize, stable single-lipid formulations for PARP1 inhibitors with high encapsulation values have been developed for therapeutic drug delivery. The type of interaction mode between the drug and lipid in the encapsulation process was determined, and an impact tendency among compounds was verified. Further optimization is needed to increase liposome membrane stabilization and optimize release rates and mechanisms in circulation.

6.5 Funding Statement

This research was funded by the Portuguese National Funding Agency (FCT-MCTES), the Radiation Biology and Biophysics Doctoral Training Programme (RaBBiT, PD/00193/2012), the Applied Molecular Biosciences Unit—UCIBIO (UIDB/04378/2020), the CEFITEC Unit (UIDB/00068/2020), UIDB/04559/2020 (LIBPhys), and UIDP/04559/2020 (LIB-Phys)), and the scholarships grant numbers PD/BD/142765/2018 and COVID/BD/152660/2022 to C.J.F.C. from the RaBBiT Doctoral Training Programme.

6.6 Acknowledgements

The authors acknowledge the availability and usage of the UP200S tip sonicator from the Bacterial Energy Metabolism Lab (ITQB NOVA, Oeiras, Portugal), spectroscopic equipment (UV–Vis) from the Macromolecular Crystallography Unit (ITQB NOVA, Oeiras, Portugal), and spectroscopic equipment (DLS and FTIR) from the Institute of Chemical and Biological Technology (ITQB NOVA) (Oeiras, Portugal), The New University of Lisbon (Portugal).

References

[1] D.E. Citrin, J.B. Mitchell, Altering the Response to Radiation: Sensitizers and Protectors, Semin. Oncol. 41 (2014) 848–859. https://doi.org/10.1053/j.seminoncol.2014.09.013.

[2] S.K. Liu, P.L. Olive, R.G. Bristow, Biomarkers for DNA DSB inhibitors and radiotherapy clinical trials, Cancer Metastasis Rev. 27 (2008) 445–458. https://doi.org/10.1007/s10555-008-9137-8.

[3] G.I. Mun, S. Kim, E. Choi, C.S. Kim, Y.S. Lee, Pharmacology of natural radioprotectors, Arch. Pharm. Res. 41 (2018) 1033–1050. https://doi.org/10.1007/s12272-018-1083-6.

[4] C.J. Lord, A. Ashworth, PARP Inhibitors: The First Synthetic Lethal Targeted Therapy Europe PMC Funders Group, Science (80-.). 355 (2017) 1152–1158. https://doi.org/10.1126/science.aam7344.PARP.

[5] G. O'Sullivan Coyne, A. Chen, S. Kummar, Delivering on the promise: Poly ADP ribose polymerase inhibition as targeted anticancer therapy, Curr. Opin. Oncol. 27 (2015) 475–481. https://doi.org/10.1097/CCO.0000000000000238.

[6] J.D. Steffen, M.M. McCauley, J.M. Pascal, Fluorescent sensors of PARP-1 structural dynamics and allosteric regulation in response to DNA damage, Nucleic Acids Res. 44 (2016) 9771–9783. https://doi.org/10.1093/nar/gkw710.

[7] H.H.W. Chen, M.T. Kuo, Improving radiotherapy in cancer treatment: Promises and challenges, Oncotarget. 8 (2017) 62742–62758. https://doi.org/10.18632/oncotarget.18409.

[8] N. Gan, Q. Sun, P. Tang, D. Wu, T. Xie, Y. Zhang, H. Li, Determination of interactions between human serum albumin and niraparib through multi-spectroscopic and computational methods, Spectrochim. Acta - Part A Mol. Biomol. Spectrosc. 206 (2019) 126–134. https://doi.org/10.1016/j.saa.2018.07.100.

[9] Y. Cheng, P. Zhao, S. Wu, T. Yang, Y. Chen, X. Zhang, C. He, C. Zheng, K. Li, X. Ma, G. Xiang, Cisplatin and curcumin co-loaded nano-liposomes for the treatment of hepatocellular carcinoma, Int. J. Pharm. 545 (2018) 261–273. https://doi.org/10.1016/j.ijpharm.2018.05.007.

[10] C. Has, S.M. Phapal, P. Sunthar, Rapid single-step formation of liposomes by flow assisted stationary phase interdiffusion, Chem. Phys. Lipids. 212 (2018) 144–151. https://doi.org/10.1016/j.chemphyslip.2018.01.007.

[11] B.-H. Chen, B. Stephen Inbaraj, Nanoemulsion and Nanoliposome Based Strategies for Improving Anthocyanin Stability and Bioavailability, Nutrients. 11 (2019) 1052. https://doi.org/10.3390/nu11051052.

[12] D. Cai, X. Li, J. Chen, X. Jiang, X. Ma, J. Sun, L. Tian, S.K. Vidyarthi, J. Xu, Z. Pan, W. Bai, A comprehensive review on innovative and advanced stabilization approaches of anthocyanin by modifying structure and controlling environmental factors, Food Chem. 366 (2022) 130611. https://doi.org/10.1016/j.foodchem.2021.130611.

[13] J.M. Al-Khayri, W. Asghar, A. Akhtar, H. Ayub, I. Aslam, N. Khalid, M.Q. Al-Mssallem, F.M. Alessa, H.S. Ghazzawy, M. Attimarad, Anthocyanin Delivery Systems: A Critical Review of Recent Research Findings, Appl. Sci. 12 (2022) 12347. https://doi.org/10.3390/app122312347.

[14] G. Ioele, M. De Luca, A. Garofalo, G. Ragno, Photosensitive drugs: a review on their photoprotection by liposomes and cyclodextrins, Drug Deliv. 24 (2017) 33–44. https://doi.org/10.1080/10717544.2017.1386733.

[15] M. Ruano, A. Mateos-Maroto, F. Ortega, H. Ritacco, J.E.F. Rubio, E. Guzmán, R.G. Rubio, Fabrication of Robust Capsules by Sequential Assembly of Polyelectrolytes onto Charged Liposomes, Langmuir. 37 (2021) 6189–6200. https://doi.org/10.1021/acs.langmuir.1c00341.

[16] M.L. Moraes, P.J. Gomes, P.A. Ribeiro, P. Vieira, A.A. Freitas, R. Köhler, O.N. Oliveira, M. Raposo, Polymeric scaffolds for enhanced stability of melanin incorporated in liposomes, J. Colloid Interface Sci. 350 (2010) 268–274. https://doi.org/10.1016/j.jcis.2010.06.043.

[17] A.A. Duarte, A.M. Botelho do Rego, M. Salerno, P.A. Ribeiro, N. El Bari, B. Bouchikhi, M. Raposo, DPPG Liposomes Adsorbed on Polymer Cushions: Effect of Roughness on Amount, Surface Composition and Topography, J. Phys. Chem. B. 119 (2015) 8544–8552. https://doi.org/10.1021/acs.jpcb.5b02384.

[18] F. Pires, V.P.N. Geraldo, A. Antunes, A. Marletta, O.N. Oliveira, M. Raposo, On the role of epigallocatechin-3-gallate in protecting phospholipid molecules against UV irradiation, Colloids Surfaces B Biointerfaces. 173 (2019) 312–319. https://doi.org/10.1016/j.colsurfb.2018.09.065.

[19] D. Sivadasan, M.H. Sultan, O.A. Madkhali, S.H. Alsabei, A.A. Alessa, Stealth Liposomes (PEGylated) Containing an Anticancer Drug Camptothecin: In Vitro Characterization and In Vivo Pharmacokinetic and Tissue Distribution Study, Molecules. 27 (2022) 1086. https://doi.org/10.3390/molecules27031086.

[20] K. Adamala, A.E. Engelhart, N.P. Kamat, L. Jin, J.W. Szostak, Construction of a liposome dialyzer for the preparation of high-value, small-volume liposome formulations, Nat. Protoc. 10 (2015) 927–938. https://doi.org/10.1038/nprot.2015.054.

[21] A. Mendyk, R. Jachowicz, Unified methodology of neural analysis in decision support systems built for pharmaceutical technology, Expert Syst. Appl. 32 (2007) 1124–1131. https://doi.org/10.1016/j.eswa.2006.02.019.

[22] A. Mendyk, R. Jachowicz, K. Fijorek, P. Dorozyński, P. Kulinowski, S. Polak, KinetDS: An open source software for dissolution test data analysis, Dissolution Technol. 19 (2012) 6–11. https://doi.org/10.14227/DT190112P6.

[23] C.C. Nascentes, M. Korn, C.S. Sousa, M.A.Z. Arruda, Use of ultrasonic baths for analytical applications: a new approach for optimisation conditions, J. Braz. Chem. Soc. 12 (2001) 57–63. https://doi.org/10.1590/S0103-50532001000100008.

[24] N.P. Dhanalakshmi, R. Nagarajan, Ultrasonic Intensification of the Chemical Degradation of Methyl Violet: An experimental Study, Int. J. Chem. Mol. Eng. 5 (2011) 1019–1024. https://doi.org/scholar.waset.org/1307-6892/13939.

[25] A. Akbarzadeh, R. Rezaei-Sadabady, S. Davaran, S.W. Joo, N. Zarghami, Y. Hanifehpour, M. Samiei, M. Kouhi, K. Nejati-Koshki, Liposome: classification, preparation, and applications, Nanoscale Res. Lett. 8 (2013) 102. https://doi.org/10.1186/1556-276X-8-102.

[26] S. Garcia-Manyes, L. Redondo-Morata, G. Oncins, F. Sanz, Nanomechanics of Lipid Bilayers: Heads or Tails?, J. Am. Chem. Soc. 132 (2010) 12874–12886. https://doi.org/10.1021/ja1002185.

[27] J. Pan, F.A. Heberle, S. Tristram-Nagle, M. Szymanski, M. Koepfinger, J. Katsaras, N. Kučerka, Molecular structures of fluid phase phosphatidylglycerol bilayers as determined by small angle neutron and X-ray scattering., Biochim. Biophys. Acta. 1818 (2012) 2135–48. https://doi.org/10.1016/j.bbamem.2012.05.007.

[28] C.T. Wohnhaas, G.G. Leparc, F. Fernandez-Albert, D. Kind, F. Gantner, C. Viollet, T. Hildebrandt, P. Baum, DMSO cryopreservation is the method of choice to preserve cells for droplet-based single-cell RNA sequencing, Sci. Rep. 9 (2019) 1–14. https://doi.org/10.1038/s41598-019-46932-z.

[29] C.Y. Cheng, J. Song, J. Pas, L.H.H. Meijer, S. Han, DMSO Induces Dehydration near Lipid Membrane Surfaces, Biophys. J. 109 (2015) 330–339. https://doi.org/10.1016/j.bpj.2015.06.011.

[30] M. Gallardo-Villagrán, L. Paulus, D.Y. Leger, B. Therrien, B. Liagre, Dimethyl Sulfoxide : A Bio-Friendly or Bio-Hazard Chemical ? The Effect of DMSO in Human Fibroblast-like Synoviocytes, Molecules. 27 (2022) 4472. https://doi.org/https://doi.org/10.3390/molecules27144472.

[31] B. Gironi, Z. Kahveci, B. McGill, B.D. Lechner, S. Pagliara, J. Metz, A. Morresi, F. Palombo, P. Sassi, P.G. Petrov, Effect of DMSO on the Mechanical and Structural Properties of Model and Biological Membranes, Biophys. J. 119 (2020) 274–286. https://doi.org/10.1016/j.bpj.2020.05.037.

[32] National Center for Biotechnology Information, PubChem Compound Summary for CID 24958200, Niraparib., PubChem Compd. Summ. CID 24958200, Niraparib. (n.d.). https://pubchem.ncbi.nlm.nih.gov/compound/Niraparib (accessed February 14, 2023).

[33] National Center for Biotechnology Information., PubChem Compound Summary for CID 9931953, Rucaparib phosphate., (n.d.). https://pubchem.ncbi.nlm.nih.gov/compound/Rucaparib-phosphate (accessed February 14, 2023).

[34] National Center for Biotechnology Information., PubChem Compound Summary for CID 11960529, Veliparib., (n.d.). https://pubchem.ncbi.nlm.nih.gov/compound/Veliparib (accessed February 14, 2023).

[35] I.T. Kirby, M.S. Cohen, Small-Molecule Inhibitors of PARPs: From Tools for Investigating ADP-Ribosylation to Therapeutics., Curr. Top. Microbiol. Immunol. 420 (2019) 211–231. https://doi.org/10.1007/82_2018_137.

[36] L. Yu, Z. Yan, Y. Wang, H. Miao, J. Zhao, C. Pang, S. Li, Recent advances in structural types and medicinal chemistry of PARP-1 inhibitors, Med. Chem. Res. 31 (2022) 1265–1276. https://doi.org/10.1007/s00044-022-02919-6.

[37] H. Thorsell, A; Ekblad, T; Karlberg, T; Low, M; Pinto, AF; Trésaugues, L; Moche, M; Cohen, MS; Schuler, Structural Basis for Potency and Promiscuity in Poly(ADP-ribose) Polymerase (PARP) and Tankyrase Inhibitors, J. Med. Chem. 60 (2017) 1262–1271. https://doi.org/10.1021/acs.jmedchem.6b00990.

[38] T.E.H. Ogden, J.-C. Yang, M. Schimpl, L.E. Easton, E. Underwood, P.B. Rawlins, M.M. McCauley, M.-F. Langelier, J.M. Pascal, K.J. Embrey, D. Neuhaus, Dynamics of the HD regulatory subdomain of PARP-1; substrate access and allostery in PARP activation and inhibition, Nucleic Acids Res. 49 (2021) 2266–2288. https://doi.org/10.1093/nar/gkab020.

[39] RCSB Protein Data Banck, (n.d.). http://www.rcsb.org/ (accessed February 14, 2023).

[40] H.M. Berman, J. Westbrook, Z. Feng, G. Gilliland, T.N. Bhat, H. Weissig, I.N. Shindyalov, P.E. Bourne, The Protein Data Bank, 28 (2000) 235–242. https://doi.org/10.1093/nar/28.1.235.

[41] S.K. Burley, C. Bhikadiya, C. Bi, S. Bittrich, L. Chen, G. V Crichlow, C.H. Christie, K. Dalenberg, L. Di Costanzo, J.M. Duarte, S. Dutta, Z. Feng, S. Ganesan, D.S. Goodsell, S. Ghosh, R.K. Green, D. Guzenko, B.P. Hudson, C.L. Lawson, V. Guranovi, Y. Liang, R. Lowe, H. Namkoong, E. Peisach, I. Persikova, C. Randle, A. Rose, Y. Rose, A. Sali, J. Segura, M. Sekharan, C. Shao, Y. Tao, M. Voigt, J.D. Westbrook, J.Y. Young, C. Zardecki, M. Zhuravleva, RCSB Protein Data Bank : powerful new tools for exploring 3D structures of biological macromolecules for basic and applied research and education in fundamental biology ,

biomedicine , biotechnology , bioengineering and energy sciences, 49 (2021) 437–451. https://doi.org/10.1093/nar/gkaa1038.

[42] D. Sehnal, S. Bittrich, M. Deshpande, R. Svobodov, K. Berka, S. Velankar, S.K. Burley, A.S. Rose, Mol * Viewer : modern web app for 3D visualization and analysis of large biomolecular structures Jaroslav Ko ca, 49 (2021) 431–437. https://doi.org/doi.org/10.1093/nar/gkab314.

[43] M.L. Briuglia, C. Rotella, A. McFarlane, D.A. Lamprou, Influence of cholesterol on liposome stability and on in vitro drug release, Drug Deliv. Transl. Res. 5 (2015) 231–242. https://doi.org/10.1007/s13346-015-0220-8.

[44] N. Dan, Core–shell drug carriers: liposomes, polymersomes, and niosomes, in: E. Andronescu, A.M. Grumezescu (Eds.), Nanostructures Drug Deliv., Elsevier, Cambridge, USA, 2017: pp. 63–105. https://doi.org/10.1016/B978-0-323-46143-6.00002-6.

[45] F. Pires, J.F. Santos, D. Bitoque, G. Araujo, A. Marletta, V.A. Nunes, P.A. Ribeiro, J.C. Silva, M. Raposo, Polycaprolactone / Gelatin Nano fi ber Membranes Containing EGCG- Loaded Liposomes and Their Potential Use for Skin Regeneration, ACS Appl. Bio Mater. 2 (2019) 4790–4800. https://doi.org/10.1021/acsabm.9b00524.

[46] S. Hama, M. Sakai, S. Itakura, E. Majima, K. Kogure, Rapid modification of antibodies on the surface of liposomes composed of high-affinity protein A-conjugated phospholipid for selective drug delivery, Biochem. Biophys. Reports. 27 (2021). https://doi.org/https://doi.org/10.1016/j.bbrep.2021.101067.

[47] Y.-C. Chang, I.-M. Chu, Methoxy poly(ethylene glycol)-b-poly(valerolactone) diblock polymeric micelles for enhanced encapsulation and protection of camptothecin, Eur. Polym. J. 44 (2008) 3922–3930. https://doi.org/10.1016/j.eurpolymj.2008.09.021.

[48] J.M. Unagolla, A.C. Jayasuriya, Drug transport mechanisms and in vitro release kinetics of vancomycin encapsulated chitosan-alginate polyelectrolyte microparticles as a controlled drug delivery system, Eur. J. Pharm. Sci. 114 (2018) 199–209. https://doi.org/10.1016/j.ejps.2017.12.012.

[49] Y. Danyuo, C.J. Ani, A.A. Salifu, J.D. Obayemi, S. Dozie-Nwachukwu, V.O. Obanawu, U.M. Akpan, O.S. Odusanya, M. Abade-Abugre, F. McBagonluri, W.O. Soboyejo, Anomalous Release Kinetics of Prodigiosin from Poly-N-Isopropyl-Acrylamid based Hydrogels for

The Treatment of Triple Negative Breast Cancer, Sci. Rep. 9 (2019) 1–14. https://doi.org/10.1038/s41598-019-39578-4.

[50] C. Corsaro, G. Neri, A.M. Mezzasalma, E. Fazio, Weibull Modeling of Controlled Drug Release from Ag-PMA Nanosystems, Polymers (Basel). 13 (2021) 2897. https://doi.org/10.3390/polym13172897.

[51] M.L. Bruschi, Mathematical models of drug release, in: M.L. Bruschi (Ed.), Strateg. to Modify Drug Release from Pharm. Syst., 1st ed., Elsevier, 2015: pp. 63–86. https://doi.org/10.1016/B978-0-08-100092-2.00005-9.

[52] A.A. Duarte, P.J. Gomes, J.H.F. Ribeiro, P.A. Ribeiro, S. V. Hoffmann, N.J. Mason, O.N. Oliveira, M. Raposo, Characterization of PAH/DPPG layer-by-layer films by VUV spectroscopy, Eur. Phys. J. E. 36 (2013) 98. https://doi.org/10.1140/epje/i2013-13098-7.

[53] I. Grante, A. Actins, L. Orola, Protonation effects on the UV/Vis absorption spectra of imatinib: A theoretical and experimental study, Spectrochim. Acta Part A Mol. Biomol. Spectrosc. 129 (2014) 326–332. https://doi.org/10.1016/j.saa.2014.03.059.

[54] J.W. Springer, K.M. Faries, J.R. Diers, C. Muthiah, O. Mass, H.L. Kee, C. Kirmaier, J.S. Lindsey, D.F. Bocian, D. Holten, Effects of Substituents on Synthetic Analogs of Chlorophylls. Part 3: The Distinctive Impact of Auxochromes at the 7- versus 3-Positions, Photochem. Photobiol. 88 (2012) 651–674. https://doi.org/10.1111/j.1751-1097.2012.01083.x.

[55] T. Zhao, F. Sha, J. Xiao, Q. Xu, X. Xie, J. Zhang, X. Wei, Absorption, desorption and spectroscopic investigation of sulfur dioxide in the binary system ethylene glycol+dimethyl sulfoxide, Fluid Phase Equilib. 405 (2015) 7–16. https://doi.org/10.1016/j.fluid.2015.06.047.

[56] J. Coates, Interpretation of Infrared Spectra, A Practical Approach, in: R.A. Meyers (Ed.), Encycl. Anal. Chem., John Wiley & Sons, Ltd, Chichester, UK, 2006: pp. 1–23. https://doi.org/10.1002/9780470027318.a5606.

[57] P.J. Larkin, General Outline for IR and Raman Spectral Interpretation, in: K. Morrissey (Ed.), Infrared Raman Spectrosc., 2nd ed., Elsevier, Stamford, USA, 2018: pp. 135–151. https://doi.org/10.1016/B978-0-12-804162-8.00007-0.

[58] F. Pires, V.P.N. Geraldo, A. Antunes, A. Marletta, O.N. Oliveira, M. Raposo, Effect of blue light irradiation on the stability of phospholipid molecules in the presence of

epigallocatechin-3-gallate, Colloids Surfaces B Biointerfaces. 177 (2019) 50–57. https://doi.org/10.1016/j.colsurfb.2019.01.042.

[59] N.E. Levinger, R. Costard, E.T.J. Nibbering, T. Elsaesser, Ultrafast energy migration pathways in self-assembled phospholipids interacting with confined water, J. Phys. Chem. A. 115 (2011) 11952–11959. https://doi.org/10.1021/jp206099a.

[60] L.B. Dreier, M. Bonn, E.H.G. Backus, Hydration and Orientation of Carbonyl Groups in Oppositely Charged Lipid Monolayers on Water, J. Phys. Chem. B. 123 (2019) 1085–1089. https://doi.org/10.1021/acs.jpcb.8b12297.

[61] J.L.R. Arrondo, F.M. Goñi, J.. Macarulla, Infrared spectroscopy of phosphatidylcholines in aqueous suspension a study of the phosphate group vibrations, Biochim. Biophys. Acta - Lipids Lipid Metab. 794 (1984) 165–168. https://doi.org/10.1016/0005-2760(84)90310-2.

[62] A. Dicko, H. Bourque, M. Pézolet, Study by infrared spectroscopy of the conformation of dipalmitoylphosphatidylglycerol monolayers at the air-water interface and transferred on solid substrates, Chem. Phys. Lipids. 96 (1998) 125–139. https://doi.org/10.1016/S0009-3084(98)00084-X.

[63] V.M. Wallace, N.R. Dhumal, F.M. Zehentbauer, H.J. Kim, J. Kiefer, Revisiting the Aqueous Solutions of Dimethyl Sulfoxide by Spectroscopy in the Mid- and Near-Infrared: Experiments and Car-Parrinello Simulations, J. Phys. Chem. B. 119 (2015) 14780–14789. https://doi.org/10.1021/acs.jpcb.5b09196.

[64] W. Jastrzbski, M. Sitarz, M. Rokita, K. Bułat, Infrared spectroscopy of different phosphates structures, Spectrochim. Acta - Part A Mol. Biomol. Spectrosc. 79 (2011) 722–727. https://doi.org/10.1016/j.saa.2010.08.044.

[65] M. Kim, S. Hwang, J.S. Yu, Novel ordered nanoporous graphitic C3N4 as a support for Pt-Ru anode catalyst in direct methanol fuel cell, J. Mater. Chem. 17 (2007) 1656–1659. https://doi.org/10.1039/b702213a.

7

COMBINING RADIATION AND LIPOSOMES WITH PARPI: EFFECTS ON INHIBITORY CAPABILITY AND DEGRADATION

Understanding the effect of UVC irradiation on PARP1 inhibitor Veliparib with and without encapsulation in liposomes[5]

Abstract

Poly (ADP-ribose) polymerase inhibitors (PARPi) are often used in complementary cancer therapy with conventional approaches (e.g. radiotherapy and chemotherapy). However, these present some limitations that may be circumvented with nano-systems such as liposomes. Since PARPi increases cell sensitization to UVC radiation, our aims were to evaluate the effect of UVC on the degradation process and inhibitory capability of Veliparib encapsulated and not encapsulated in DPPG liposomes, as well as to determine putative degradation products. Results demonstrate that Veliparib is sensitive to UVC radiation, leading to the degradation of the benzamide ring and carbonyl functional group. This event coincides with the loss of inhibitory capability of Veliparib on PARP1's auto-modification activity. Furthermore, DPPG encapsulation protects Veliparib from UVC irradiation up until 30 min of exposure, due to the delay in the appearance of a degradation band at 330 nm. Infrared analysis revealed that the surfacing of the UV-vis 330 nm absorbance band is associated to the degradation of the benzamide ring and the carbonyl functional group. This group presents several C=O infrared vibrational bands, which are associated with isomerization and degradation of the functional group. These results allowed to infer the potential degradation process of Veliparib, due to UVC irradiation, that is associated to a linear

[5] This chapter is based on a manuscript that is in preparation for submission for publication:
Conceição, C.J.F., Moe, E., Ribeiro, P. A. and Raposo, M.. Understanding the effect of UVC radiation on PARP1 inhibitor Veliparib with and without encapsulation in liposomes.

unsaturated aldehyde and conjugated ketone structures that arise from the degradation of the benzamide pharmacophore.

7.1 Introduction

PARP proteins have a great interest in therapeutic approaches, due to their many and extensive cellular roles. The PARP family that englobes 17 members present broad cellular localization and cellular roles [1]. PARP1 belongs to the DNA dependent sub-group of proteins and is involved directly and/or indirectly in DNA repair, transcription, replication, cell cycle progression and other pathways [2,3].

PARPi therapy is often employed as a complement to more conventional cancer therapies. Using analogous NAD^+ molecules, PARP1 enzymatic activity is hindered [4,5]. Molecules such as Veliparib act by interacting with the polymerase's catalytic domain (CAT), preventing the modification of target proteins through the addition of ADP-ribose polymeric chains (PARylation) [4,6]. These inhibitors take advantage of the compromised DNA repair pathways in cancer cells, and therefore prevent the repair of DNA strand breaks. The inhibition of PARP1's auto-PARylation prevents its release from the DNA strand breaks and consequently hinders the allocation of Base Excision Repair (BER) proteins to these loci [4,6]. However, several drawbacks are pointed to PARPi cancer therapy [7,8], which may be circumvented by nano-delivery systems such as liposomes [9]. PARP1 inhibitors can be used in synergistic lethal strategies, in combinational therapies employing DNA damage agents (e.g. radiation or chemotherapeutics), or as mono-therapy agents [10–12].

Conventional PARPi therapy was proved to increase cell sensitization to UV irradiation [13] and positive feedback was reported when irradiation was combined with PARPi, leading to cancer cell death [10–12,14–16]. Moreover, it was verified that even low-energy sources, such as UVC light, were capable of activating PARylation, due to intracellular DNA damage, and in turn PARP1 inhibition further sensitized cells to UVC irradiation [17].

The main goal of this work is to ascertain the applicability of DPPG liposomes and UVC conjugated therapy in Veliparib's nano-delivery approach for cancer treatment. The effect of UVC radiation exposure on Veliparib was analyzed, and the protective effect of DPPG liposomes on the inhibitor molecule was also verified. In addition, the degradation process, and products of Veliparib, due to irradiation, as well as their inhibitory capacity on PARP1 enzymatic activity were determined, allowing us to infer about the degradation process.

7.2 Materials and Methods

7.2.1 Chemicals

1,2-Dipalmitoyl-sn-glycero-3-phospho-rac-(1'-glycerol) sodium salt (DPPG) (MW 744.96 g/mol) was purchased from AvantiPolar Lipids (Alabaster, AL, USA) and PARP1 inhibitor Veliparib (ABT-888) (MW 244.3 g/mol) was purchased from AdooQ® Bioscience (Irvine, CA, USA). Veliparib stock solutions (100 mM) were prepared in DMSO anhydrous (99.9 %) (Sigma-Aldrich, Missouri, USA).

7.2.2 Liposome Preparation

DPPG liposomes were prepared following our previously described method [18]. Veliparib stock solution was added at a final concentration of 200 µM during lipid dissolution (1 mM DPPG) in the organic solvent mixture (chloroform and methanol 4:1 (*v/v*) mixture). Lipid formulations were evaporated using a gentle stream of nitrogen and left overnight in a desiccator under vacuum. Lipid films were hydrated for 2 h at 47 °C, with Milli-Q ultrapure water (Millipore, Burlington, MA, USA). Afterwards sonicated using tip-sonicator (UP200S (200 W, 24 kHz), Hielscher Ultrasonics, GmbH, Teltow, Ger-many) to obtain small unilamellar vesicles (SUV). 20 cycles of 30 seconds and 1 minute interval between sonication cycles was employed. Inhibitor molecules that were not encapsulated were removed dialysis (Spectra/Por® 4 Dry Standard RC membrane, MWCO 12–14 kDa, Spectrum Labs, Biotech, San Francisco, CA, USA) for 48 h at 4 °C. Encapsulation efficiency of 50 % was estimated by calculation of the ratio between the absorbance at 275 nm of DPPG + Veliparib before and after dialysis.

7.2.3 Irradiation experiments

Irradiation assessments were performed using aqueous solutions of 50 µM and 500 µM Veliparib, and vesicle suspension of 0.5 mM DPPG and 0.5 mM DPPG + 50 µM Veliparib. Samples were placed in quartz cuvettes and irradiated with a 254 nm UVC germicide lamp (Philips TUV PL-S 5 W/2 P 1CT) at a radiance of 28.9 W/m^2. Samples were analyzed by UV-Visible and Fourier transform infrared (FTIR) spectroscopies. Three independent replicates were used per assay.

7.2.4 Spectral Measurements

Both UV–Vis and FTIR spectra were used to analyse drug encapsulation and irradiation effect. UV–Vis spectra were acquired with a Shimadzu UV-1800 UV/Visible Scanning Spectrophotometer (Kyoto, Kyoto, Japan). FTIR spectra were recorded on a Bruker IFS 66/S (Billerica, MA, USA) spectrometer in absorbance mode, with a wavenumber range of 500 to 4000 cm^{-1}, a resolution of 4 cm^{-1}, and 128 scans. Samples were deposited on CaF_2 supports, and water was evaporated in a desiccator under vacuum conditions. CaF_2 clean support spectra were subtracted from all sample spectra. Three independent replicates were analysed per assay.

The principal component analysis (PCA) was carried out considering the UV-vis spectra irradiated at different times. This allowed us to reduce the size of data while obtaining a new area of orthogonal components, whose different irradiation period patterns could be examined and explained.

7.2.5 Human PARP1 gene cloning, protein expression and purification

Human PARP1 protein was obtained following the previously described protocol [19]. Purified protein was concentrated to approximately 1mg/mL using an Amicon® Ultra-4 (10 kDa MWCO) (Merck Millipore, München, Germany), flash frozen in liquid nitrogen and stored at -80 °C. Storage buffer composition was 50 mM Tris-HCl pH 8.0, 400-500 mM NaCl, 0.1 mM TCEP and 1mM EDTA.

7.2.6 PARP1 auto-modification activity assay

PARP1 auto-modification activity reactions were conducted following the protocol described by Langelier [16]. Activity reactions were all prepared on ice and incubated at room temperature for 10 min. Reaction solutions used 1 μM protein, 1 μM blunt non-labelled DNA template (Seq.Fw: 5′-AGTACGGTCATCGCG-3′ and Seq.Rv: 5′-CGCGATGACCGTACT-3′), 5 mM beta - nicotinamide adenine dinucleotide (β-NAD^+) and incubation buffer (20 mM Tris-HCl pH 7.5, 50 mM NaCl, 5 mM MgCl2). Auto-modification reactions were stopped by adding SDS-loading buffer (15.6 mM Tris, 100 mM EDTA, 2.5 % glycerol, 0.2 M β -mercaptoethanol, 0.26 % SDS, 0.001 % bromophenol blue). The inhibitory capacity of irradiated Veliparib (500 μM) was assessed by adding the inhibitor to a 1 μM final concentration, in the reaction mixtures prepared on ice. Reactions were analysed in 10 % SDS-PAGE gel, stained with BlueSafe (NZYTech, Lisbon, Portugal) and images were acquired using the Gel Doc EZ System (BIORAD, Hercules, CA, USA).

7.3 Results and Discussion

7.3.1 Analysis of UV damage on Veliparib and DPPG encapsulating Veliparib via UV-vis spectroscopy

Analysis of UVC (254 nm) damage on 50 μM and 0.5mM DPPG encapsulating 50 μM Veliparib was done by UV-Vis spectroscopy. The absorption spectra of Veliparib (Figure 7.1a) presents two peaks at 270 nm and 295 nm, which are assigned to π - π * transitions from benzene [20] and imidazole [21–23], respectively. The spectra of DPPG liposomes display the typical maximum absorption peak near 194 nm (Figure D.1a), which is consistent with the characteristic liposome band at 194.4 ± 0.7 nm [24,25]. This is assigned to the lone-pair transition of carbonyl oxygen to the antibonding π_{CO} valence orbital, $n_O \rightarrow \pi^*_{CO}$, or to the valence shell electronic excitation of hydroxyl groups [18,25]. DPPG encapsulating Veliparib presents the characteristic absorption peaks of the inhibitor, as well as the DMSO band around 205-210 nm (Figure 7.1b and Figure D.1b).

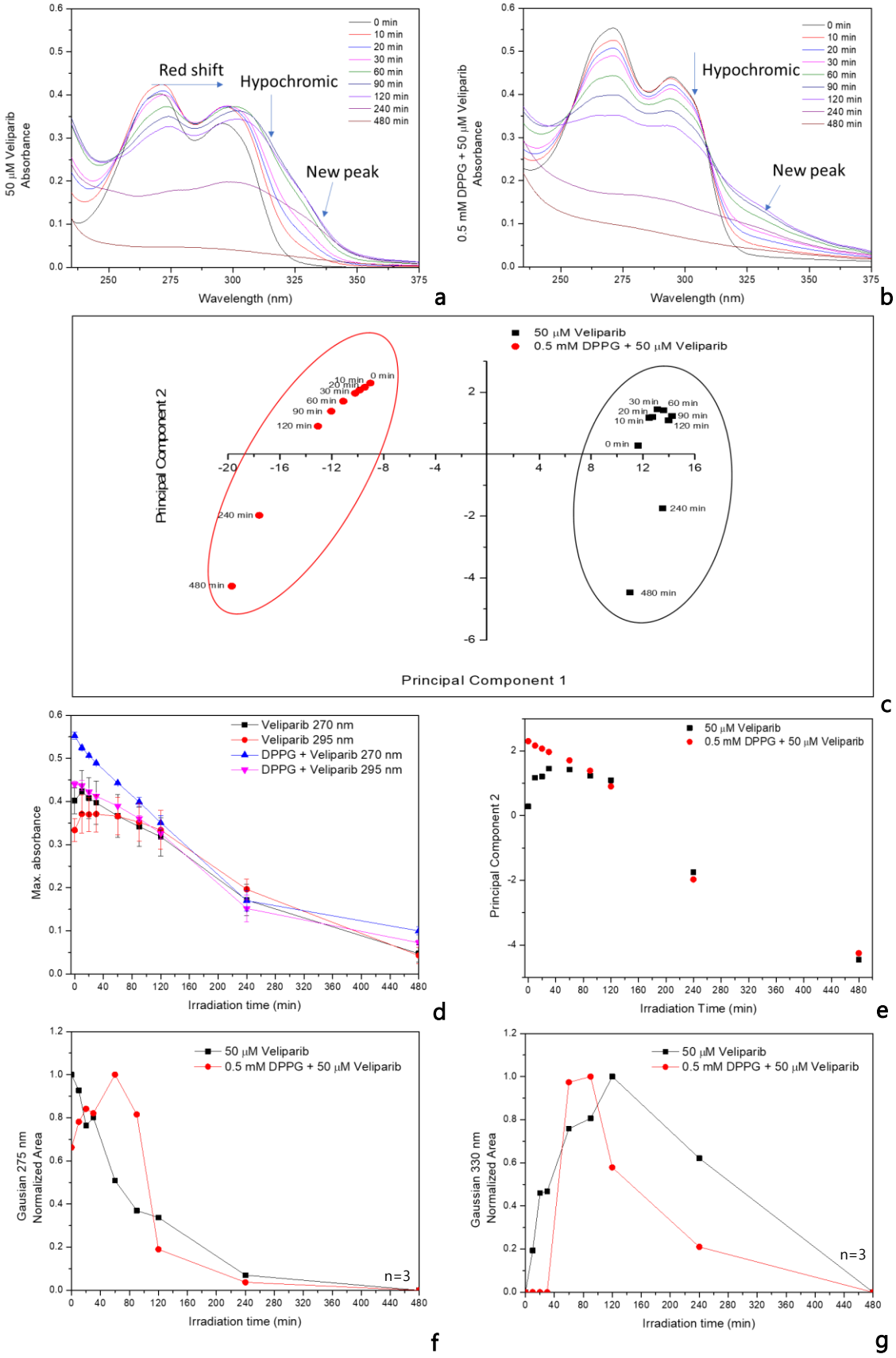
50 μM Veliparib Absorbance
Red shift
Hypochromic
New peak
0 min
10 min
20 min
30 min
60 min
90 min
120 min
240 min
480 min
Wavelength (nm)
a
0.5 mM DPPG + 50 μM Veliparib Absorbance
Hypochromic
New peak
Wavelength (nm)
b
50 μM Veliparib
0.5 mM DPPG + 50 μM Veliparib
Principal Component 2
Principal Component 1
c
Veliparib 270 nm
Veliparib 295 nm
DPPG + Veliparib 270 nm
DPPG + Veliparib 295 nm
Max. absorbance
Irradiation time (min)
d
Principal Component 2
Irradiation Time (min)
e
Gausian 275 nm Normalized Area
n=3
f
Gaussian 330 nm Normalized Area
n=3
g

Figure 7.1 — Evaluation of the effect of UVC irradiation on Veliparib and DPPG encapsulating Veliparib. a) UV-Vis spectra of 50 μM Veliparib at different irradiation periods of time; b) UV-Vis spectra of 0.5 mM DPPG + 50 μM Veliparib at different irradiation times; c) PCA plot of UV-Vis spectra of 50 μM Veliparib and of 0.5 mM DPPG + 50 μM Veliparib solutions at different irradiation times; d) Analysis of maximum absorbance at 270 nm and 295 nm for Veliparib and DPPG + Veliparib samples at different irradiation times; e) Plot of PC2 values versus irradiation time of Veliparib and DPPG + Veliparib samples; f) Analysis of normalized areas of Gaussian 2 (~ 275 nm) from irradiated Veliparib and DPPG + Veliparib spectra; g) Analysis of normalized areas of Gaussian 5 (~ 330 nm) from irradiated Veliparib and DPPG + Veliparib spectra.

Upon irradiation, the samples presented a gradual degradation process (Figure 7.1a-b and Figure D.1). Liposome formulation presented a new peak around 210 nm, which may be related to lipid peroxidation [25]. Lipids degradation may occur by two processes, either hydrolysis and/or oxidation. Exposure to ionizing irradiation triggers the formation of water radicals (e.g. hydroxyl (OH), hydrogen peroxide (H_2O_2) and hydroperoxyl), that attack methylene groups from polyunsaturated lipids. The oxidation process can then be monitored by the absorption band of conjugated dienes (215 nm and 250 nm band), resultant from lipid oxidation [25,26]. In the case of saturated phospholipids, the ester bonds and hydroxyl groups are attacked, and common DPPG degradation products are dipalmitoylphosphatidic acid, 1,2-dipalmitoyl-sn-glycerol-3-phospho-(1,3-dihydroxyacetone), dipalmitoyl-sn-glycerol-3-phosphoryl, (1,2-dihydroxypropaldehyde), 1-palmitoyl-snpropanediol-3-phosphorylglycerol and 1,2-dipalmitoyl-snglycerol-3-phosphorylethanol [25,27]. Because DPPG+Veliparib samples present a significant DMSO band (Figure D.1b), that coincides with the region of lipid peroxidation, one cannot infer on the effect of the inhibitor compound in the degradation process of DPPG.

Veliparib presents an overall change in its UV-vis spectra upon radiation exposure (Figure 7.1a and b). It was observed an overall shift to higher wavelengths (red-shift) and the appearance of a new absorbance band around 330 nm (Figure 7.1a). On the other hand, encapsulated Veliparib apparently did not present a red-shift of the spectra, but a band around 330 nm also surfaces upon radiation exposure (Figure 7.1b). Principal component analysis of UV-vis spectra revealed a complete segregation among the irradiated samples, confirming that they behave independently from each other in the irradiation assessment (Figure 7.1c).

Because no significant differences were detected after plotting maximum absorbance values versus time of irradiation at 270 nm and 295 nm (Figure 7.1d), in both samples, a complementary analysis was done regarding gaussian content. Additionally, the plot of PCA2 vs irradiation time revealed that differences in the degradation process are detected at initial irradiation time-points (Figure 7.1e).

Gaussian analysis of Veliparib's UV-vis spectra (Figure D.2) reveals that these comprise four gaussians and that after DPPG encapsulation a shift to higher wavelength values is verified (Figure D.2 and Table 7.1). The shift may be a result of a higher protonation state and /or the presence of a substituent (e.g. -OH) in the chromophore of the inhibitor, resultant from the encapsulation and interaction with the liposome membrane [18]. The data revealed in this work constitutes an update to our previous assessments, regarding the encapsulation of PARPi in DPPG liposomes. In our previous work we verified a red-shift on Rucaparib and Niraparib UV-Vis spectra after encapsulation, while in Veliparib this event was not detected [18]. The reason behind the difficulty in verifying the red-shift on Veliparib spectra could be due to an overall "masking effect", since only the major wavelength shift is detected in gaussian 1 (+ 5 nm), while remaining gaussians present discrete differences (1 - 2 nm), as depicted in Table 7.1.

Table 7.1 — Gaussian analysis of UV-vis spectra of Veliparib and DPPG + Veliparib samples.

	Peak Position (nm)	
Drug **Gaussian Analysis**	Veliparib*	DPPG + Veliparib*
1	259.8 ± 0.8	264.9 ± 0.3 (+5)
2	273.6 ± 0.4	275.2 ± 0.1 (+2)
3	292.6 ± 0.2	294.3 ± 0.1 (+2)
4	305.1 ± 0.3	306.3 ± 0.1 (+1)

* wavelength ± SD

Spectra deconvolution revealed that the effects of UVC irradiation on Veliparib, either encapsulated and non-encapsulated, are most significant in Gaussian 2 (~ 275 nm) and in the band that arises above 300 nm (Figure 7.1f-g).

Analysis of Gaussian 2 reveals that with irradiation maximum wavelength value is roughly stable, shifting from 273.7 ± 0.4 nm to 275.2 ± 0.5 nm and 275.3 ± 0.1 to 278.7 ± 0.6 in Veliparib and DPPG + Veliparib, respectively (Table D.1). Analysis of normalized gaussian areas (Figure 7.1f) reveals that inhibitor degradation is delayed in DPPG + Veliparib, in the

initial periods of irradiation (0 to 90 min). One verifies that the area of gaussian 2 in Veliparib decreases with time of exposure to UVC, while the normalized areas of encapsulated Veliparib samples appear to be sustained or even increased until 90 min of irradiation (Figure 7.1f). In both samples gaussian 2 disappears completely after 480 min of UVC exposure, which translates in complete compound degradation (Figure 7.1a and b).

The detection of the new absorbance band after UVC exposure can be hypothesized as related to a degradation product of Veliparib. The wavelength at maximum absorbance of this product (Gaussian 5) shifts from 325.2 ± 0.8 nm to 330.3 ± 0.9 nm and 317.2 ± 3.1 nm to 331.3 ± 0.4 nm in Veliparib and DPPG + Veliparib, respectively (see Table D.1). But more interestingly, we verified that the surface of this new band occurs at different irradiation times, depending on the encapsulation status. Analysis of Veliparib normalized gaussian areas shows that even after 10 min of UVC exposure the degradation product is detected, and that area values increase gradually until 120 min of irradiation (Figure 7.1g). On the other hand, in DPPG + Veliparib samples, Gaussian 5 appears only after 60 min (1h) of UVC exposure (Figure 7.1g), thus proving that encapsulation into DPPG liposomes contributes to the delay of the degradation process of Veliparib. Continued UVC exposure led to the disappearance of Gaussian 5, which was verified after 480 min of irradiation (Figure 7.1g). The final 330 nm electronic excitation band may be attributed to n- π * transition of the carbonyl group in a linear unsaturated aldehyde [28]. High absorption above 290 nm, that is linked to this specific electronic transition, is pointed to serve as an indication that compounds could be degraded by photolysis [28].

The results confirm that Veliparib encapsulation in DPPG liposomes protected the inhibitor from UVC degradation and are in line with PCA analysis (Figure 7.1e), that highlighted differences in the degradation process at the initial periods of irradiation. Also, the new absorbance band that emerges around 330 nm, in the UV-Vis spectra, can be associated to a degradation product of the Veliparib's carbonyl group. However, to determine the degradation process and products of Veliparib due to UVC irradiation, infrared analysis was conducted.

7.3.2 Analysis of UV damage on Veliparib via UV-vis and FTIR - compound degradation process

To confirm the effect of UVC irradiation on the degradation process and on products of Veliparib, a complementary analysis with UV-vis and FTIR spectroscopies was performed. Veliparib samples were used at a final concentration of 500 μM, and UV-vis analysis was employed to follow the degradation process and compare it with the one from the 50 μM samples

(Figure 7.1a). In this way we want to pinpoint key degradation moments of Veliparib. The degradation process is similar for both samples at 50 μM (Figure 7.1a) and 500 μM (Figure 7.2a), however at higher concentrations it appears that the process is slower. Since the absorbance values at 270 nm and 295 nm is above 2, with 500 μM Veliparib sample (Figure 7.2a), one cannot consider these wavelengths for analysis because of signal saturation. However, the region of interest showcasing the degradation product (330 nm absorbance band), is within the unitary value thus making the comparative analysis between samples feasible. The normalized areas of gaussians 5 (330 nm) from 50 μM and 500 μM Veliparib, seen in Figure 7.2b, show that this new band occurs in both samples even after 10 min of irradiation. These results thus state that the appearance of this new band is a direct result of Veliparib exposure to UVC sources. Moreover, one verifies that maximal areas are attained at different irradiation time periods, showcasing that the degradation process is slowed down at high concentrations of inhibitor (Figure 7.2b). This could be due to the reduced number of water molecules and/or photons.

Additionally, irradiated 500 μM Veliparib samples were analyzed for their inhibitory capability on PARP1's enzymatic activity. In this sense auto-modification activity assays were done following a previously described method [16]. Results are visualized in a SDS-PAGE gel, where modified protein presents a shift of PARP1 band (114 kDa) to higher weight regions of the gel. In Figure 7.2c we confirmed that PARP1 activity was completely inhibited with not irradiated Veliparib (0 min of UVC exposure), while samples of irradiated inhibitor appeared to have lost their inhibitory capability. The loss of inhibitory capability is identified due to the observation of shifted protein band to regions above 114 kDa. The increase in UVC exposure led to a progressive loss of Veliparib's inhibitory capability. The effect was maximum after 480 min of UVC exposure (Figure 7.2c), with the visualization of almost complete shift of PARP1 band to regions above 114 kDa. In Figure 7.2b and 7.2c, we identify irradiation timepoints that coincide with major alterations in Veliparib's inhibitory capability (yellow, blue, and red arrows) and maximum area of gaussian 5 (red arrow). These samples were the ones that were used in FTIR analysis, to determine the alterations that occurred in the structure of Veliparib and led to the loss of its inhibitory capacity.

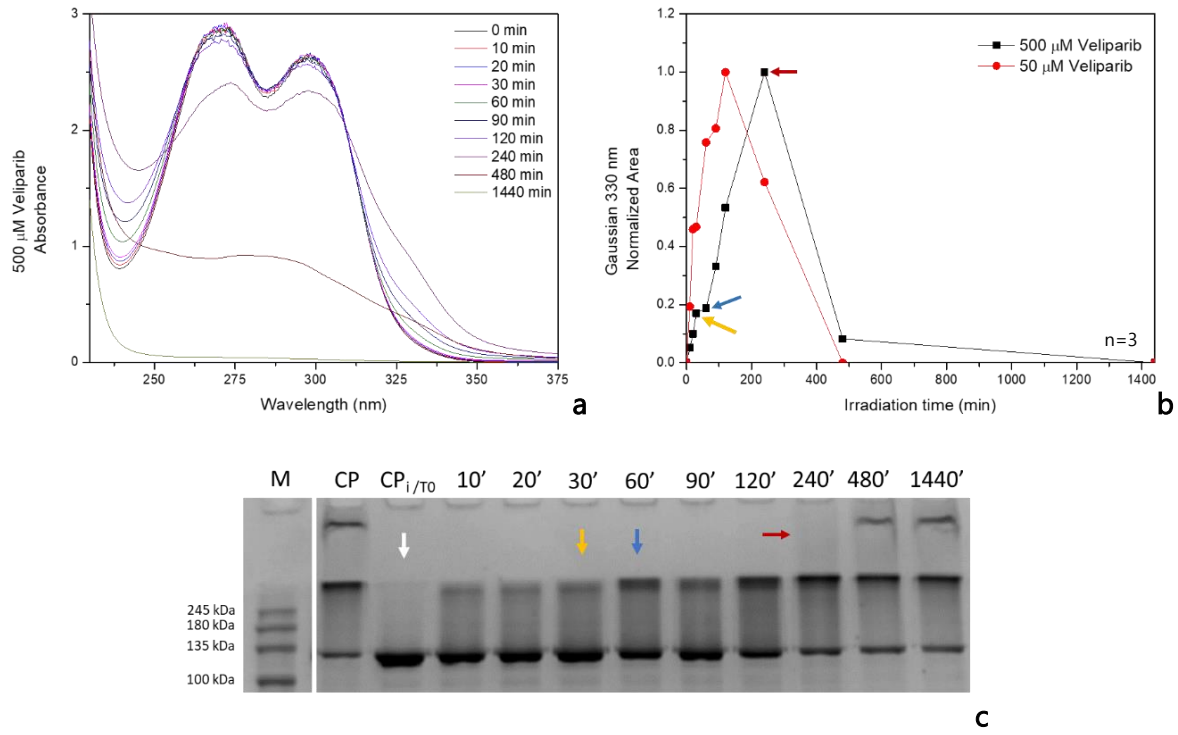

Figure 7.2 — Evaluation of the effect of UVC irradiation on Veliparib's degradation process. a) UV-vis spectra of 500 μM Veliparib solution at different irradiation time periods; b) Comparative analysis of the normalized areas of UV-Vis spectra Gaussians 5 (330 nm) of irradiated 50 μM and 500 μM Veliparib samples; c) SDS-PAGE gel analysis of the effect of irradiated Veliparib samples (500 μM) on the auto-modification activity of PARP1. M – NZYColour Protein Marker II (NZYTech); CP – positive control without inhibitor; CPi/T0 – positive control with non-irradiated inhibitor; X′ – Veliparib's irradiation (min). Colored arrows are used to identify the irradiation time-points that showcase major alterations in the inhibitory capability of Veliparib and when the normalized area of gaussian 5 attained maximum value. These samples were the ones that were further analyzed by infrared spectroscopy.

Veliparib samples analyzed by FTIR were irradiated for 30, 60 and 240 min. Also, a non-irradiated sample was used as a control. Veliparib control sample presents the typical infrared bands, that we have assigned previously [18], while in the irradiated samples we verified significant alterations in various regions of the spectra (Figure 7.3a-d).

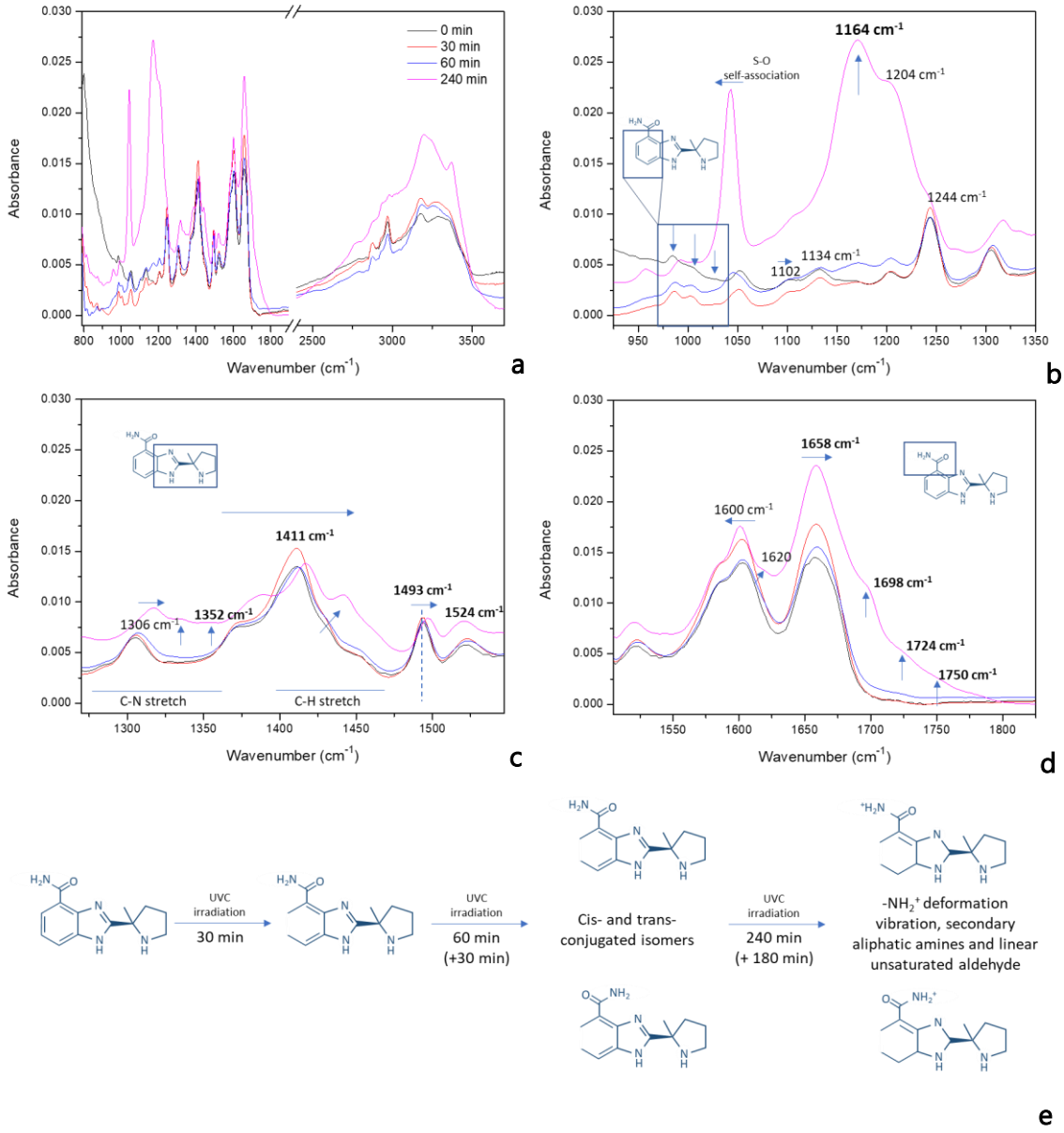

Figure 7.3 — Infrared spectroscopy analysis of UVC irradiated Veliparib samples. a) Complete FTIR spectra of 500 µM Veliparib at various irradiation periods of time; b) FTIR spectra comprising 900 to 1350 cm^{-1} region; c) FTIR spectra comprising 1275 to 1550 cm^{-1} region; d) FTIR spectra comprising 1500 to 1825 cm^{-1} region; e) Scheme illustrating a putative degradation process and products of irradiated Veliparib, taking into consideration FTIR and UV-vis analysis.

In Figure 7.3b, the absorbance bands at 984, 1004 and 1022 cm^{-1} (identified with blue arrows) present some alteration in their absorbance ratios, with band at 1022 cm^{-1} not being detected after 30 min of UVC exposure. This band is assigned to C-C stretch from the cyclo-hexane ring of Veliparib [18]. Structural alterations in the benzamide ring of PARPi molecules constitute a severe impact on the therapeutic effectiveness of these molecules since it is the core of their inhibitory capability on the activity of PARP1. Most PARPi were designed to mimic

and compete with the cofactor NAD^+ for the catalytic domain of PARP1 [10,13,29,30]. They belong to the monoaryl amides and bi-/tri-/tetracyclic lactam compound group [29], and their common pharmacophore features are the aromatic ring and carboxamide moiety (benzamide) [31]. It was verified through PARP1's activity assay that even after 10 min of irradiation Veliparib loses some of its inhibitory capability, and that the effect remains the same until 30 min of UVC exposure (Figure 7.2c). This data and the loss of cyclohexane vibrational band are coherent and explains one another, thus confirming UVC effect on the core structure of Veliparib. Additionally, we verified that the bands assigned to the C-N stretch of the aromatic rings (1102, 1134 and 1164 cm^{-1}) are also profoundly altered, with bands 1102 cm^{-1} and 1134 cm^{-1} shifted to higher wavenumbers and absorbance of band 1164 cm^{-1} increased significantly (Figure 7.3b). Maximum absorbance of band 1164 cm^{-1} is observed in the sample irradiated for 240 min. This band is also associated to secondary amine group [32], thus indicating hinderance/alteration of aromatic rings that contain nitrogen atoms, more specifically the imidazole ring. The increase of absorbance in the 3330-3400 cm^{-1} region points to a possible primary or secondary aliphatic amine (N-H stretch) [32], thus reinforcing the indication of UVC impact on the aromatic rings with nitrogen.

The vibration band at 1244 cm^{-1}, associated to C-C/C-O stretch [18], appears diminished in relation to the preceding bands (1164 cm-1 and 1204 cm^{-1}) after 240 min irradiation, and the band associated to DMSO solvent is shifted to a lower wavenumber, when compared com the control samples. This shift is associated to S-O band vibration when DMSO is self- associated [18,33].

The analysis regarding the aromatics C-N and C-H stretch, seen in Figure 7.3c, reveals that the spectra is shifted to higher wavenumbers, and we verified the appearance of a new vibrational band at 1352 cm^{-1}. This band could be assigned to C-C stretch, C-N stretch from a secondary aromatic amine or to a C-H bend from a methine functional group [32]. The latter could be the result form a possible opening of the benzamide ring, that we verified by the loss of the cyclohexane vibration band in Figure 7.3b. DMSO vibrational bands (1375 and 1410 cm^{-1}) and the band associated to Veliparib's C-H asymmetric bend of methyl ($-CH_3$) functional group (1438 cm^{-1}) [18], are shifted to higher wavenumbers, with the last presenting an increase in absorbance. This increase could be a result of the degradation process of the aromatic rings. However, the maintenance of C=C-C aromatic stretch bonding (1493 cm^{-1}) may indicate that some aromatic species are maintained even after 240 min of UVC irradiation. The same can be inferred with the maintenance of the 1524 cm^{-1} band, previously assigned to aromatic amine CH_2 scissoring/C-N and C-C ring stretch [18].

Finally, the spectra region comprising the benzamide functional groups (amine and carbonyl), seen in Figure 7.3d, indicates that these groups sustain another degree of structural alterations. The vibrational band at 1600 cm^{-1}, assigned to -NH_2 scissoring, is slightly shifted to lower wavenumbers and a shoulder band surfaces after 240 min of irradiation. The latter appears at 1620 cm^{-1} and is associated to -NH_2^+ deformation vibrations [34], showing how the amine functional group is affected by UVC exposure. Additionally, the band assigned to the carboxyl functional group is slightly shifted and three new vibrational bands appear at higher wavenumbers. In Figure 7.3d, the new band at 1724 cm^{-1} arises only after 60 min of UVC exposure and is assigned to a cis conjugated C=O functional group, while the canonical C=O of Veliparib (1658 cm^{-1}) is assigned to a trans conjugated form [35]. Additionally, it is interesting to notice that the rise of the carbonyl isomer coincides with one of the irradiation periods of time that shows major alterations in the shift pattern of PARP1's activity assay (Figure 7.2c). This led us to infer that the isomer form leads to a reduction in the inhibitory capability of Veliparib.

The new vibrational band at 1698 cm^{-1}, if taken into consideration with the conjugated double bond band, points to a carbonyl group from a conjugated ketone [32]. This band only appears after 240 min of UVC exposure, and its appearance is further reinforced by the degradation of the cyclohexane ring and points to a putative degradation product resultant from the aromatic ring-opening. Additionally, the band that is detected at 1750 cm^{-1} reveals another degradation product, with this vibrational band being associated to an aldehyde or an ester functional group [32]. Interestingly, this data is coherent with the assignment of the 330 nm UV-Vis band, thus showing that UVC has a profound effect on the benzamide ring and the carbonyl functional group. Moreover, we verify that the pharmacophore of Veliparib is readily affected by UVC irradiation, leading to its degradation and the formation of a linear unsaturated aldehyde structure. Moreover, the degradation process points to the loss of double bonds in the imidazole ring and its saturation with hydrogens, which is also perceived by the increase of absorbance in the N-H stretch spectra region (> 3200 cm^{-1}).

Taking all this data into consideration we propose in Figure 7.3e, a putative degradation scheme for 500 µM Veliparib due to UVC irradiation. In this scheme, after 30 min of irradiation the cyclohexane ring becomes an open structure and upon further irradiation time a new isomer arises. After 240 min of UVC irradiation the imidazole ring becomes an aliphatic secondary amine, and the protonation and deformation of the amine functional group in the benzamide is verified. Also, due to the various C=O vibrational bands present in the 240 min spectra, we

propose that the amine group may be removed/lost from the benzamide open structure, thus appearing aldehyde and conjugated ketone structures as degradation products.

Complementing this analysis with the data from the previous section, we conclude that the protection that is conferred against UVC degradation through the encapsulation of Veliparib in DPPG liposomes, is mainly associated to the benzamide ring and its functional groups. The DPPG protection against degradation is shown to be related to a delay up to 30 min (Figure 1e and f) in the benzene ring-opening reactions and the surfacing of the linear unsaturated aldehyde degradation product. Veliparib's protection against irradiation could be further increased by the functionalization of DPPG liposomes surface. Coatings such as polymers (e.g. PEG), polyelectrolytes, or even conjugation with other systems could be employed [36–38].

7.4 Conclusion

The effect of UVC radiation on Veliparib either encapsulated or not encapsulated was analyzed, as well as the degradation process of this molecule.

Results demonstrated that Veliparib is sensitive to UVC irradiation, and that exposure leads to compound degradation and loss of inhibitory capability on PARP1 auto-modification activity. Furthermore, DPPG encapsulation protects Veliparib from UVC irradiation, up to 30 min of exposure. The protective effect on Veliparib is mainly associated to the benzene ring and the delay on the appearance of a linear unsaturated aldehyde degradation product. It was also verified that even though the degradation process appeared slowed down at high concentrations of Veliparib, the surfacing of the band at 330 nm is a result from UVC exposure.

Infrared analysis revealed that the surfacing of the UV-vis 330 nm absorbance band is associated to the degradation of the benzamide ring and the carbonyl functional group. The latter presents several C=O vibrational bands, which are associated to isomerization and degradation of the functional group. Through the analysis of PARP1's auto-modification activity, we verified that these structural alterations were responsible for major losses in Veliparib's inhibitory capability.

Moreover, taking into consideration the infrared results we have proposed a putative degradation process due to UVC irradiation, and we have identified possible degradation products such as aldehyde and conjugated ketone structures that arise from the degradation of the benzamide pharmacophore.

In this way the UVC degradation effect on Veliparib and the protective effect given by the encapsulation of this compound in DPPG liposomes was confirmed. This allows us to infer

that some drawbacks that are associated to the use of these molecules in PARPi therapy as a complement to more conventional cancer therapies can be circumvented by liposomes nano-systems encapsulating these molecules.

7.5 Acknowledgments

This research was funded by the Portuguese National Funding Agency (FCT-MCTES), Radiation Biology and Biophysics Doctoral Training Programme (RaBBiT, PD/00193/2012), the Applied Molecular Biosciences Unit—UCIBIO (UIDB/04378/2020), the CEFITEC Unit (UIDB/00068/2020), UIDB/04559/2020 (LIBPhys) and UIDP/04559/2020 (LIBPhys), the FCT scholarships grant number PD/BD/142765/ 2018 and COVID/BD/152660/2022, to C.J.F.C. from the RaBBiT Doctoral Training Programme.

References

[1] S. Vyas, M. Chesarone-Cataldo, T. Todorova, Y. Huang, P. Chang, A systematic analysis of the PARP protein family identifies new functions critical for cell physiology, Nat. Commun. 4 (2013) 1–13. https://doi.org/10.1038/ncomms3240.

[2] J.D. Steffen, M.M. McCauley, J.M. Pascal, Fluorescent sensors of PARP-1 structural dynamics and allosteric regulation in response to DNA damage, Nucleic Acids Res. 44 (2016) 9771–9783. https://doi.org/10.1093/nar/gkw710.

[3] S.J. Baptista, M.M.C. Silva, E. Moroni, M. Meli, G. Colombo, T.C.P. Dinis, J.A.R. Salvador, Novel PARP-1 Inhibitor scaffolds disclosed by a dynamic structure-based pharmacophore approach, PLoS One. 12 (2017) 1–20. https://doi.org/10.1371/journal.pone.0170846.

[4] C.J. Lord, A. Ashworth, PARP Inhibitors: The First Synthetic Lethal Targeted Therapy Europe PMC Funders Group, Science (80-.). 355 (2017) 1152–1158. https://doi.org/10.1126/science.aam7344.PARP.

[5] C. Qin, Z. Ji, E. Zhai, K. Xu, Y. Zhang, Q. Li, H. Jing, X. Wang, X. Song, PARP inhibitor olaparib enhances the efficacy of radiotherapy on XRCC2-deficient colorectal cancer cells, Cell Death Dis. 13 (2022). https://doi.org/10.1038/s41419-022-04967-7.

[6] G. O'Sullivan Coyne, A. Chen, S. Kummar, Delivering on the promise: Poly ADP ribose polymerase inhibition as targeted anticancer therapy, Curr. Opin. Oncol. 27 (2015) 475–481. https://doi.org/10.1097/CCO.0000000000000238.

[7] C.E. Knezevic, G. Wright, L.L. Remsing Rix, W. Kim, B.M. Kuenzi, Y. Luo, J.M. Watters, J.M. Koomen, E.B. Haura, A.N. Monteiro, C. Radu, H.R. Lawrence, U. Rix, Proteome-wide Profiling of Clinical PARP Inhibitors Reveals Compound-Specific Secondary Targets, Cell Chem. Biol. 23 (2016) 1490–1503. https://doi.org/10.1016/j.chembiol.2016.10.011.

[8] N. Gan, Q. Sun, P. Tang, D. Wu, T. Xie, Y. Zhang, H. Li, Determination of interactions between human serum albumin and niraparib through multi-spectroscopic and computational methods, Spectrochim. Acta - Part A Mol. Biomol. Spectrosc. 206 (2019) 126–134. https://doi.org/10.1016/j.saa.2018.07.100.

[9] L. Cai, X. Xu, W. Chen, The Current State of the Art in PARP Inhibitor-Based Delivery Nanosystems, Pharmaceutics. 14 (2022) 1647. https://doi.org/10.3390/pharmaceutics14081647.

[10] B. Carney, S. Kossatz, T. Reiner, Molecular imaging of PARP, J. Nucl. Med. 58 (2017) 1025–1030. https://doi.org/10.2967/jnumed.117.189936.

[11] S. Boussios, P. Karihtala, M. Moschetta, A. Karathanasi, A. Sadauskaite, E. Rassy, N. Pavlidis, Combined Strategies with Poly (ADP-Ribose) Polymerase (PARP) Inhibitors for the Treatment of Ovarian Cancer: A Literature Review, Diagnostics. 9 (2019) 87. https://doi.org/10.3390/diagnostics9030087.

[12] M. Yi, B. Dong, S. Qin, Q. Chu, K. Wu, S. Luo, Advances and perspectives of PARP inhibitors, Exp. Hematol. Oncol. 8 (2019) 29. https://doi.org/10.1186/s40164-019-0154-9.

[13] N. V Malyuchenko, E.Y. Kotova, O.I. Kulaeva, M.P. Kirpichnikov, V.M. Studitskiy, PARP1 Inhibitors: antitumor drug design., Acta Naturae. 7 (2015) 27–37. http://www.ncbi.nlm.nih.gov/pubmed/26483957.

[14] T. Hirai, S. Saito, H. Fujimori, K. Matsushita, T. Nishio, R. Okayasu, M. Masutani, Radiosensitization by PARP inhibition to proton beam irradiation in cancer cells, Biochem. Biophys. Res. Commun. 478 (2016) 234–240. https://doi.org/10.1016/j.bbrc.2016.07.062.

[15] S.A. Jannetti, B.M. Zeglis, M.R. Zalutsky, T. Reiner, Poly(ADP-Ribose)Polymerase (PARP) Inhibitors and Radiation Therapy, Front. Pharmacol. 11 (2020) 170. https://doi.org/10.3389/fphar.2020.00170.

[16] S.J. Derby, A.J. Chalmers, R.D. Carruthers, Radiotherapy-Poly(ADP-ribose) Polymerase Inhibitor Combinations: Progress to Date, Semin. Radiat. Oncol. 32 (2022) 15–28. https://doi.org/10.1016/j.semradonc.2021.09.005.

[17] J.M.F. Fischer, O. Popp, D. Gebhard, S. Veith, A. Fischbach, M. Scheffner, E. Ferrando-may, S. Beneke, A. Leitenstorfer, Poly (ADP-ribose) -mediated interplay of XPA and PARP1

leads to reciprocal regulation of protein function, 281 (2014) 3625–3641. https://doi.org/10.1111/febs.12885.

[18] C.J.F. Conceição, E. Moe, P.A. Ribeiro, M. Raposo, Liposome Formulations for the Strategic Delivery of PARP1 Inhibitors: Development and Optimization, Nanomaterials. 13 (2023) 1613. https://doi.org/10.3390/nano13101613.

[19] C.J.F. Conceição, B.A. Salgueiro, P.A. Ribeiro, M. Raposo, E. Moe, Advances in the expression and purification of human PARP1: A user-friendly protocol, Protein Expr. Purif. 211 (2023) 106336. https://doi.org/10.1016/j.pep.2023.106336.

[20] J.M. Antosiewicz, D. Shugar, UV–Vis spectroscopy of tyrosine side-groups in studies of protein structure. Part 1: basic principles and properties of tyrosine chromophore, Biophys. Rev. 8 (2016) 151–161. https://doi.org/10.1007/s12551-016-0198-6.

[21] J. Jayabharathi, M. Sundharesan, A. Prabhakaran, C. Karunakaran, Understanding the binding interaction of imidazole with ZnO nanomaterials and clusters, RSC Adv. 5 (2015) 9518–9531. https://doi.org/10.1039/C4RA15957H.

[22] W. Abd El-Fattah, N.Y. Elamin, Synthesis, Spectroscopic Characterization, Molecular Docking and Biological Activity of Novel Secnidazole Metal Complexes, Inorganics. 10 (2022) 156. https://doi.org/10.3390/inorganics10100156.

[23] M. Mohsen, A. Baraka, I. Naeem, H. Tantawy, M. Awaad, O. Abuzalat, Effect of sulfur doping of zinc-imidazole coordination polymer (ZnIm CP) as a novel photocatalyst for degradation of ionic dyes, BMC Chem. 16 (2022) 86. https://doi.org/10.1186/s13065-022-00877-z.

[24] A.A. Duarte, P.J. Gomes, J.H.F. Ribeiro, P.A. Ribeiro, S. V. Hoffmann, N.J. Mason, O.N. Oliveira, M. Raposo, Characterization of PAH/DPPG layer-by-layer films by VUV spectroscopy, Eur. Phys. J. E. 36 (2013) 98. https://doi.org/10.1140/epje/i2013-13098-7.

[25] F. Pires, V.P.N. Geraldo, A. Antunes, A. Marletta, O.N. Oliveira, M. Raposo, On the role of epigallocatechin-3-gallate in protecting phospholipid molecules against UV irradiation, Colloids Surfaces B Biointerfaces. 173 (2019) 312–319. https://doi.org/10.1016/j.colsurfb.2018.09.065.

[26] R.O. Recknagel, E.A. Glende, Spectrophotometric detection of lipid conjugated dienes, Methods Enzymol. 105 (1984) 331–337. https://doi.org/10.1016/S0076-6879(84)05043-6.

[27] N.J. Zuidam, C. Versluis, E.A.A.M. Vernooy, D.J.A. Crommelin, Gamma-irradiation of liposomes composed of saturated phospholipids. Effect of bilayer composition, size, concentration and absorbed dose on chemical degradation and physical destabilization of

liposomes, Biochim. Biophys. Acta - Biomembr. 1280 (1996) 135–148. https://doi.org/10.1016/0005-2736(95)00275-8.

[28] C. Kalalian, B. Samir, E. Roth, A. Chakir, UV absorption spectra of trans-2-pentenal, trans-2-hexenal and 2-methyl-2-pentenal, Chem. Phys. Lett. 718 (2019) 22–26. https://doi.org/10.1016/j.cplett.2019.01.028.

[29] E. Kotova, A.D. Pinnola, A. V. Tulin, Small-molecule collection and high-throughput colorimetric assay to identify PARP1 inhibitors., Methods Mol. Biol. 780 (2011) 491–516. https://doi.org/10.1007/978-1-61779-270-0_29.

[30] T. Zhu, J.-Y. Zheng, L.-L. Huang, Y.-H. Wang, D.-F. Yao, H.-B. Dai, Human PARP1 substrates and regulators of its catalytic activity: An updated overview, Front. Pharmacol. 14 (2023) 1137151. https://doi.org/10.3389/fphar.2023.1137151.

[31] G.F. Elmasry, E.E. Aly, F.M. Awadallah, S.M. El-Moghazy, Design and synthesis of novel PARP-1 inhibitors based on pyridopyridazinone scaffold, Bioorg. Chem. 87 (2019) 655–666. https://doi.org/10.1016/j.bioorg.2019.03.068.

[32] J. Coates, Interpretation of Infrared Spectra, A Practical Approach, in: R.A. Meyers (Ed.), Encycl. Anal. Chem., John Wiley & Sons, Ltd, Chichester, UK, 2006: pp. 1–23. https://doi.org/10.1002/9780470027318.a5606.

[33] V.M. Wallace, N.R. Dhumal, F.M. Zehentbauer, H.J. Kim, J. Kiefer, Revisiting the Aqueous Solutions of Dimethyl Sulfoxide by Spectroscopy in the Mid- and Near-Infrared: Experiments and Car-Parrinello Simulations, J. Phys. Chem. B. 119 (2015) 14780–14789. https://doi.org/10.1021/acs.jpcb.5b09196.

[34] R.A. Heacock, L. Marion, THE INFRARED SPECTRA OF SECONDARY AMINES AND THEIR SALTS, Can. J. Chem. 34 (1956) 1782–1795. https://doi.org/10.1139/v56-231.

[35] N.L. Rockley, B.A. Halley, M.G. Rockley, E.C. Nelson, Infrared spectroscopy of retinoids, Anal. Biochem. 133 (1983) 314–321. https://doi.org/10.1016/0003-2697(83)90090-8.

[36] F. Pires, J.F. Santos, D. Bitoque, G. Araujo, A. Marletta, V.A. Nunes, P.A. Ribeiro, J.C. Silva, M. Raposo, Polycaprolactone / Gelatin Nano fi ber Membranes Containing EGCG- Loaded Liposomes and Their Potential Use for Skin Regeneration, ACS Appl. Bio Mater. 2 (2019) 4790–4800. https://doi.org/10.1021/acsabm.9b00524.

[37] M. Ruano, A. Mateos-Maroto, F. Ortega, H. Ritacco, J.E.F. Rubio, E. Guzmán, R.G. Rubio, Fabrication of Robust Capsules by Sequential Assembly of Polyelectrolytes onto Charged Liposomes, Langmuir. 37 (2021) 6189–6200. https://doi.org/10.1021/acs.langmuir.1c00341.

[38] S. Hama, M. Sakai, S. Itakura, E. Majima, K. Kogure, Rapid modification of antibodies on the surface of liposomes composed of high-affinity protein A-conjugated phospholipid for selective drug delivery, Biochem. Biophys. Reports. 27 (2021). https://doi.org/https://doi.org/10.1016/j.bbrep.2021.101067.

8

CONCLUDING REMARKS

8.1 Conclusion

In this section it will be summarized the main conclusions of the present doctoral thesis.

This work was focused on PARP1 therapeutic inhibitors and understanding how the combination of liposome and low-energy radiation (UVC) therapy would impact the inhibitory capability of set inhibitors. Additionally, in this work one wanted to unveil the degradation profile and products of PARPi Veliparib and ascertain the potential protective effect of liposome encapsulation. In this way the work intended to infer on the potential of PARPi combination therapy with liposomes and UVC irradiation.

To achieve this, the first step was to produce our own PARP1 protein samples for unveiling the inhibitory capability of irradiated compound samples. In this way, in Chapter 4 was described a fast and easy procedure for the purification of PARP1 constructs, full-length and WGR-CAT. A two and three-step purification protocols were established for the first and second construct, respectively. Biologically active full-length protein was purified to an apparent purity > 95 %, with only two purification steps. Additionally, the protein obtained was capable of binding DNA and did not present inhibitor molecules bound to its active site, contrary to other protocols. This new protocol is more efficient and produces similar protein quantities in less time, with yields sufficient for biochemical, biophysical, and structural analysis.

Furthermore, due to the complexity of PARP1's nature and to guarantee proper enzymatic activity and stability, it was done an assessment regarding protein oligomerization state and stabilization. In Chapter 5, it was demonstrated the formation of a dimeric form of PARP1 not bound to DNA, that arouse from the concentration process. And so, we have proved that protocols following a centrifugal concentration process will lead to the obtention of this new

PARP1 form. Additionally, in this chapter, oligomerization evaluations proved that PARP1 native forms are: 1) a "free" form and a 2) DNA bound form. The native form of PARP1 without DNA appears as an elongated monomer and in its DNA bound form it exists as a dimer. In this way, the assessments done in chapter 5 constitutes an additional information to PARP1 nature and may be helpful to understand its intrinsic and complex behaviour. Moreover, the results provided by the protein stabilization analysis proved that higher degree of structural stability can be attained when Mg^{2+} and Ca^{2+} ions are added to the protein, in complex with oligonucleotides with double strand breaks (Tm ≥ 50 °C). CD data revealed that Veliparib, Rucaparib and Niraparib have a significant impact on the secondary structure of PARP1, leading to an apparent shift of regular α-helixes to 3_{10} – or π - helixes, that translates in an overall enriched β-sheet CD spectrum. Moreover, thermostability assessments revealed that PARPi confer an uneven stabilization to PARP1 structure, and that each inhibitor has different stabilization potential. Values as high as 60 °C were attained. The data provided by this chapter may be helpful for other researchers when attempting to combine stabilization partners for PARP1, which can be of major importance in biochemical, biophysical, and structural analysis.

Concerning PARPi encapsulation in liposomes, the work done in this thesis provided the first evidence that points to DPPG as the best lipid, from the ones analysed, for the encapsulation of these molecules. Encapsulation efficiencies were above 40 %, which translates in concentrations as high as 100 μM. Moreover, zeta-potential values indicated that liposome particles were stable, with a single population profile and particle diameter values around 130 nm (main population of interest). It was proved that drug release rates were slowed-down when PARPis were encapsulated in DPPG liposomes, and that the release mechanisms in play were diffusion-controlled and non-Fickian diffusion processes, in most of the systems. The interaction studies done in this work, constitutes the first evidence that reports PARPi encapsulation mode in DPPG. And it was proved that the studied inhibitors interact with the lipid membrane of DPPG liposomes and promote membrane water displacement. Moreover, preferential interaction was verified with the carbonyl groups of DPPG, through hydrogen bonding. It is believed that the protonated amine groups from the inhibitor could be the major players in PARPis' encapsulation mode.

Finally, the effect of UVC exposure was assessed in Veliparib and DPPG+Veliparib samples. In chapter 7, it was demonstrated that Veliparib is sensitive to UVC irradiation, which results in the degradation of the benzamide ring and carbonyl functional group. The degradation of these structures coincides with the loss of inhibitory capability of Veliparib, on the automodification enzymatic activity of PARP1. DPPG encapsulation conferred a degree of

protection to Veliparib upon UVC exposure, which was verified by the delay in the appearance of a degradation band at 330 nm in the UV-vis spectra. By FTIR it was proven that this product was associated to the degradation of the benzamide ring and the carbonyl functional group. Moreover, during the degradation process of Veliparib several C=O bands are detected and associated to functional group isomerization and degradation. In this way, a putative degradation process and products were proposed, namely a linear unsaturated aldehyde and conjugated ketone structures that arose from the benzamide pharmacophore.

In sum, the work presented in this thesis strengthens the idea that PARPi combination therapy is a desirable alternative to more conventional approaches in the treatment of cancer. It was proved that the combination of liposomes with PARPi provides a mean to protect the inhibitory capability of PARPi, that can be lost due to UVC degradation. Moreover, this thesis provides the first evidence that PARPi liposome formulations should include negatively charged lipids, such as DPPG, so that high levels of encapsulation are achieved. Moreover, the present work provides a significant input onto the fundamental knowledge about PARP1's native state. And also directs future researchers to how protein assessments should take into consideration different components for the structural stabilization of PARP1.

8.2 Future Work and Perspectives

About the future developments and directions in the field of PARP1 fundamental studies and PARP1 directed cancer therapy, one believes that these will encompass the following points.

In Protein studies:

- The determination of full-length PARP1 structure through cryo-EM. This will mostly pass through the stabilization of PARP1 flexible structure with the combination of stabilization partners such as ions, DNA and/or protein interactors;
- Regarding new signalling pathways interaction, it is believed that soon more information will be available with PARP1 being at its centre, but also new developments in the understanding of PARP1 interactions and interaction partners.

In Liposome studies:

- The use of molecular simulations to predict and understand the interaction of PARPi and lipid bilayer. These will come as a complement to the experimental data obtained in this work;

- Development of more complex liposome formulations, through the combination of different phospholipids and varying their proportions. In this way, it is possible to obtain more biocompatible liposome formulations and possibly increase cell specificity and cellular uptake (more complex formulations were developed during this work, but the data generated is not included in this thesis because it is in processing stage);
- Liposomes surface functionalization with polymers, polyelectrolytes, glycans and antibodies. It is important to understand how surface functionalization would affect drug content, particle stabilization and delivery. But also, liposome functionalization would help to increase circulation time, protect drug pharmacokinetic properties, confer target specificity and increase cellular uptake;
- Co-loading DPPG based liposome formulations with PARPi and other cancer therapeutic compounds (experiments done, but still under data processing).

Irradiation studies:

- It would be necessary to understand the effect of UVC on PARP1 and PARP1+inhibitor. These experiments were already performed but were not included in this work because it is in the processing stage;
- Study the effect of UVC radiation in other solutions/media, pH conditions and salt concentrations;
- Test the effect of other radiation sources/energies on the degradation and therapeutic capability of PARPi.

PARPi Cancer Therapy:

- *In vitro* analysis to understand the impact and efficiency of PARPi + liposomes + radiation combination therapy;
- Design liposomes that mimic the lipidic membranes of cancer cell, so that cell recognition is more efficient and cell uptake is promoted;
- Design of new specific inhibitors of PARP1's intracellular activity, redirection of known clinical therapy molecules to PARPi therapy and focus on natural molecules that may be useful in PARP1-target cancer treatment.

General future perspectives on Cancer treatment:

- Future approaches to cancer treatment will pass through the combination of nanotechnology, chemotherapy, radiotherapy and immunotherapy;
- Moreover, one points that science and medical fields are evolving in the sense that future treatments will take under consideration the biological, biochemical, and metabolic features of each cancer type and patient, so that tailor made treatments can be applied. In this way cancer therapy will respond to the specific needs of each pathology, localization, and respective cellular microenvironment.

A

APPENDIX: PRODUCTION OF HUMAN PARP1: PROTOCOL DEVELOPMENT AND OPTIMIZATION

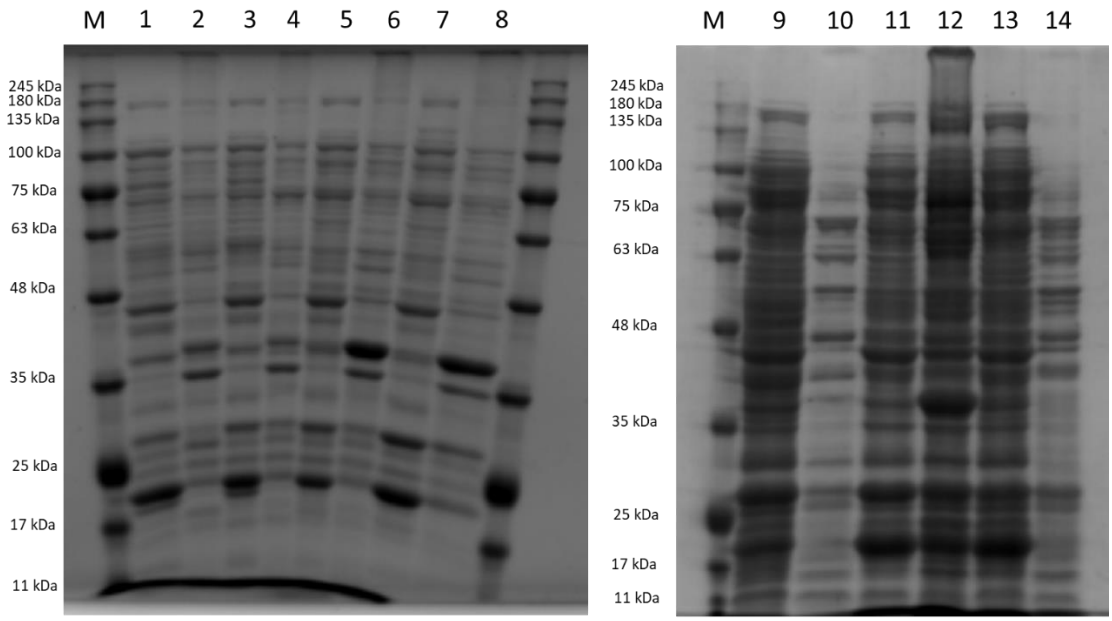

Figure A.1 — SDS- PAGE results for PARP1 Full-length expression tests in various cell lines and media conditions (cont.). M – NZYColour Protein Marker II (NZYTech); 1 – Gami 2 LB (soluble fraction); 2 - Gami 2 LB (insoluble fraction); 3 - Gami 2 PB (soluble fraction); 4 - Gami 2 PB (insoluble fraction); 5 - pLysS 2 LB (soluble fraction); 6 - pLysS 2 LB (insoluble fraction); 7 - pLysS 2 PB (soluble fraction); 8 - pLysS 2 PB (insoluble fraction); 9 – pLysS* PB (soluble fraction); 10 – pLysS* PB (insoluble fraction); 11 – Lemo 21 PB (soluble fraction); 12 – Lemo 21 PB (insoluble fraction); 13 - Lemo 21 LB (soluble fraction); 14 - Lemo 21 PB (insoluble fraction).

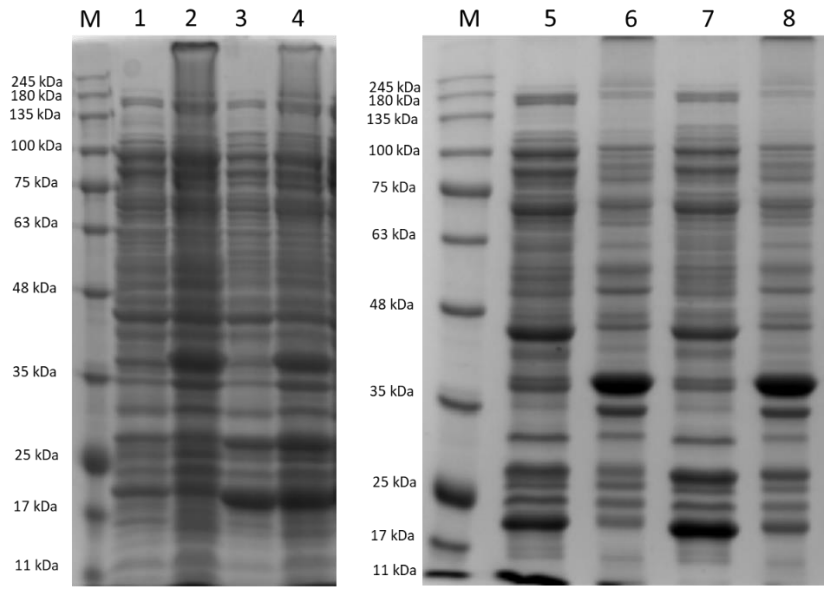

Figure A.2 — SDS- PAGE results for PARP1 Full-length expression tests in various cell lines and media conditions (cont.). M – NZYColour Protein Marker II (NZYTech); 1 – Rosetta 2 Auto-induction (soluble fraction); 2 - Rosetta 2 Auto-induction (insoluble fraction); 3 - Rosetta 2 PB (soluble fraction); 4 - Rosetta 2 PB (insoluble fraction); 5 - Tuner LB (soluble fraction); 6 - Tuner LB (insoluble fraction); 7 - Tuner PB (soluble fraction); 8 - Tuner PB (insoluble fraction).

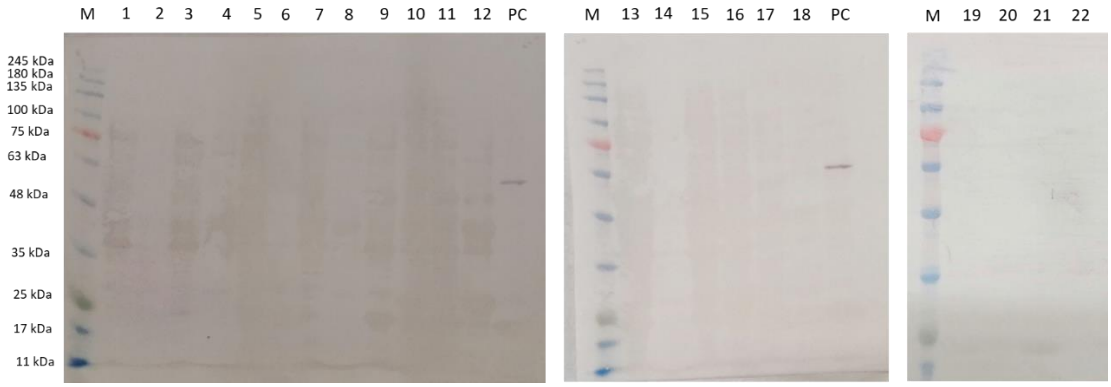

Figure A.3— Western blot results for PARP1 Full-length expression tests in various cell lines and media conditions previously shown in figures A.1 and A.2. M – NZYColour Protein Marker II (NZYTech); 1 – Tuner LB (soluble fraction); 2 - Tuner LB (soluble infraction); 3 - Tuner PB (soluble fraction); 4 - Tuner PB (insoluble fraction); 5 – Rosetta 2 Auto-induction medium (soluble fraction); 6 - Rosetta 2 Auto-induction medium (insoluble fraction); 7 – Rosetta 2 PB (soluble fraction); 8 – Rosetta 2 PB (insoluble fraction); 9 – pLysS* PB (soluble fraction); 10 – pLysS* PB (insoluble fraction); 11 – Lemo21 LB (soluble fraction); 12 – Lemo21 LB (insoluble fraction); 13 - Lemo21 PB (soluble fraction); 14 - Lemo21 PB (insoluble fraction); 15 – Gami2 LB (soluble fraction); 16 – Gami2 LB (insoluble fraction); 17 – Gami2 PB (soluble fraction); 18 - Gami2 PB (soluble fraction); 19 – pLysS2 LB (soluble fraction); 20 – pLysS2 LB (insoluble fraction); 21 – pLysS2 PB (soluble fraction); 22 – pLysS2 PB (insoluble fraction); PC – positive control (PARP1 WGR-CAT construct).

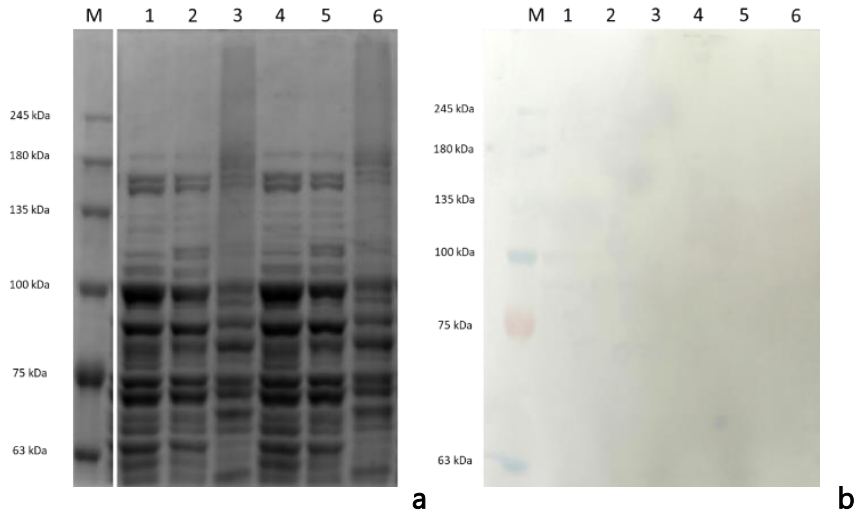

Figure A.4 — PARP1 Full-length expression incubation test for 2- and 3-hours growth in LB medium at 37º C, in Rosetta 2. a) SDS-PAGE results; b) Western blot results. M – NZYColour Protein Marker II (NZYTech); 1 – Negative control 2h incubation (soluble fraction); 2 – 2h incubation (soluble fraction); 3 -2h incubation (insoluble fraction); 4 - Negative control 3h incubation (soluble fraction); 5 – 3h incubation (soluble fraction); 6 - 3h incubation (insoluble fraction).

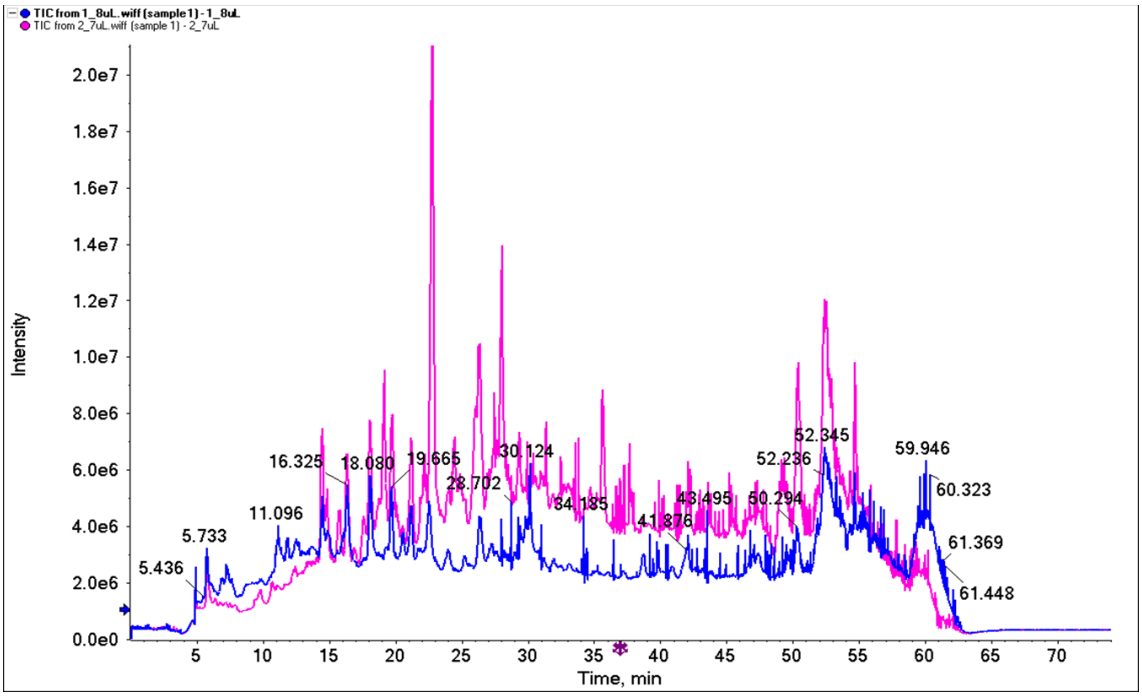

Figure A.5 — Mass Spectrometer total ion current chromatogram generated from the analysis of two target proteins. Identification of band 1 (blue line) as recombinant Human PARP1 and band 2 (pink line) as E. coli maltodextrin phosphorylase protein.

Table A.1 — MS analysis of Band 1 identified as human full-length PARP1 protein (identified as Band1 human).

N	Unused	Total	% Cov (95)	Accession #	Name	Species	Peptides(95%)
1	77,74	77,74	37	sp|Sequence	Band 1|Band1 human		88
2	16,98	16,99	11	sp|P00490|PHSM_ECOLI	Maltodextrin phosphorylase OS=Escherichia coli (strain K12) OX=83333 GN=malP PE=1 SV=7	ECOLI	11
3	4,15	4,15	1,4	sp|Q0TA77|RPOC_ECOL5	DNA-directed RNA polymerase subunit beta' OS=Escherichia coli O6:K15:H31 (strain 536 / UPEC) OX=362663 GN=rpoC PE=3 SV=1	ECOL5	2
4	4,02	4,02	13,6	sp|Q1RB79|RL20_ECOUT	50S ribosomal protein L20 OS=Escherichia coli (strain UTI89 / UPEC) OX=364106 GN=rplT PE=3 SV=1	ECOUT	4
5	4,01	4,01	6,8	sp|Q1R636|RS4_ECOUT	30S ribosomal protein S4 OS=Escherichia coli (strain UTI89 / UPEC) OX=364106 GN=rpsD PE=3 SV=1	ECOUT	2
6	3,38	3,4	0,8	sp|B7MRB3|RPOB_ECO81	DNA-directed RNA polymerase subunit beta OS=Escherichia coli O81 (strain ED1a) OX=585397 GN=rpoB PE=3 SV=1	ECO81	1
7	2,64	2,64	3,9	sp|Q7BSW8|KATG2_ECO57	Catalase-peroxidase 2 OS=Escherichia coli O157:H7 OX=83334 GN=katG2 PE=3 SV=1	ECO57	3
8	2,38	2,39	0,7	sp|P39321|TAMB_ECOLI	Translocation and assembly module subunit TamB OS=Escherichia coli (strain K12) OX=83333 GN=tamB PE=1 SV=2	ECOLI	1
9	2,33	2,33	6,2	sp|Q19NJ4|CH602_ECOK1	60 kDa chaperonin 2 OS=Escherichia coli O1:K1 / APEC OX=405955 GN=groL2 PE=3 SV=1	ECOK1	3
10	2,24	2,25	2,6	sp|Q1R607|RL2_ECOUT	50S ribosomal protein L2 OS=Escherichia coli (strain UTI89 / UPEC) OX=364106 GN=rplB PE=3 SV=1	ECOUT	1
11	2,16	2,16	2,6	sp|Q8FBC3|GLPK_ECOL6	Glycerol kinase OS=Escherichia coli O6:H1 (strain CFT073 / ATCC 700928 / UPEC) OX=199310 GN=glpK PE=3 SV=3	ECOL6	1
12	2,05	2,05	2,4	sp|Q1R7A6|E4PD_ECOUT	D-erythrose-4-phosphate dehydrogenase OS=Escherichia coli (strain UTI89 / UPEC) OX=364106 GN=epd PE=3 SV=2	ECOUT	2
13	2,02	2,03	6,8	sp|Q1R633|RS13_ECOUT	30S ribosomal protein S13 OS=Escherichia coli (strain UTI89 / UPEC) OX=364106 GN=rpsM PE=3 SV=1	ECOUT	1
14	2,02	2,02	1,9	sp|B7NQW3|ADEC_ECO7I	Adenine deaminase OS=Escherichia coli O7:K1 (strain IAI39 / ExPEC) OX=585057 GN=ade PE=3 SV=1	ECO7I	1
15	2,01	2,01	1,4	sp|Q1R7R4|ENO_ECOUT	Enolase OS=Escherichia coli (strain UTI89 / UPEC) OX=364106 GN=eno PE=3 SV=1	ECOUT	1
16	2,01	2,01	1,2	sp|Q0T8V3|OPGB_ECOL5	Phosphoglycerol transferase I OS=Escherichia coli O6:K15:H31 (strain 536 / UPEC) OX=362663 GN=mdoB PE=3 SV=1	ECOL5	1
17	2,01	2,01	7,3	sp|Q1R617|RL14_ECOUT	50S ribosomal protein L14 OS=Escherichia coli (strain UTI89 / UPEC) OX=364106 GN=rplN PE=3 SV=1	ECOUT	2
18	2,01	2,01	6,4	sp|Q1R610|RL22_ECOUT	50S ribosomal protein L22 OS=Escherichia coli (strain UTI89 / UPEC) OX=364106 GN=rplV PE=3 SV=1	ECOUT	1
19	2,01	2,01	8,7	sp|Q1R609|RS19_ECOUT	30S ribosomal protein S19 OS=Escherichia coli (strain UTI89 / UPEC) OX=364106 GN=rpsS PE=3 SV=1	ECOUT	1
20	2	2	3,4	sp|Q1RF98|CLPP_ECOUT	ATP-dependent Clp protease proteolytic subunit OS=Escherichia coli (strain UTI89 / UPEC) OX=364106 GN=clpP PE=3 SV=1	ECOUT	1

21	2	2	4,1	sp|P41069|TRAV_ECOLI	Protein TraV OS=Escherichia coli (strain K12) OX=83333 GN=traV PE=1 SV=1	ECOLI	1
22	2	2	3	sp|P0AG78|SUBI_ECOLI	Sulfate-binding protein OS=Escherichia coli (strain K12) OX=83333 GN=sbp PE=1 SV=1	ECOLI	1
23	2	2	2,7	sp|P0AGH6|SAPC_ECOL6	Peptide transport system permease protein SapC OS=Escherichia coli O6:H1 (strain CFT073 / ATCC 700928 / UPEC) OX=199310 GN=sapC PE=3 SV=1	ECOL6	1
24	1,92	1,96	3,8	sp|P0AEK5|FABI_ECO57	Enoyl-[acyl-carrier-protein] reductase [NADH] FabI OS=Escherichia coli O157:H7 OX=83334 GN=fabI PE=3 SV=2	ECO57	1
25	1,77	1,82	2,7	sp|Q47141|HCAR_ECOLI	Hca operon transcriptional activator HcaR OS=Escherichia coli (strain K12) OX=83333 GN=hcaR PE=1 SV=2	ECOLI	1
26	1,73	1,78	1,6	sp|Q6XGD8|DNCV_ECOLX	Cyclic GMP-AMP synthase OS=Escherichia coli OX=562 GN=dncV PE=1 SV=1	ECOLX	1
27	1,68	1,72	2,1	sp|P20083|PARE_ECOLI	DNA topoisomerase 4 subunit B OS=Escherichia coli (strain K12) OX=83333 GN=parE PE=1 SV=3	ECOLI	1
28	1,65	1,7	0,9	sp|P76272|YEBT_ECOLI	Intermembrane transport protein YebT OS=Escherichia coli (strain K12) OX=83333 GN=yebT PE=1 SV=2	ECOLI	1
29	1,65	1,69	2,3	sp|P0A9X5|MREB_ECOL6	Cell shape-determining protein MreB OS=Escherichia coli O6:H1 (strain CFT073 / ATCC 700928 / UPEC) OX=199310 GN=mreB PE=3 SV=1	ECOL6	1
30	1,62	1,68	1	sp|P31224|ACRB_ECOLI	Multidrug efflux pump subunit AcrB OS=Escherichia coli (strain K12) OX=83333 GN=acrB PE=1 SV=1	ECOLI	1
31	1,54	1,58	1,6	sp|B7M3D0|TREF_ECO8A	Cytoplasmic trehalase OS=Escherichia coli O8 (strain IAI1) OX=585034 GN=treF PE=3 SV=1	ECO8A	1

Table A.2 — MS analysis of Band 2 identified as E. coli maltodextrin phosphorylase protein.

N	Unused	Total	% Cov (95)	Accession #	Name	Species	Peptides(95%)
1	272,16	272,16	85,7	sp|P00490|PHSM_ECOLI	Maltodextrin phosphorylase OS=Escherichia coli (strain K12) OX=83333 GN=malP PE=1 SV=7	ECOLI	562
2	4,23	4,23	3,2	sp|P15977|MALQ_ECOLI	4-alpha-glucanotransferase OS=Escherichia coli (strain K12) OX=83333 GN=malQ PE=1 SV=2	ECOLI	2
3	2,85	2,85	2,8	sp|Sequence	Band 1|Band1 human		2
4	2,04	2,04	3,4	sp|Q1R636|RS4_ECOUT	30S ribosomal protein S4 OS=Escherichia coli (strain UTI89 / UPEC) OX=364106 GN=rpsD PE=3 SV=1	ECOUT	1
5	2	2	1,6	sp|Q1R3B6|CH60_ECOUT	60 kDa chaperonin OS=Escherichia coli (strain UTI89 / UPEC) OX=364106 GN=groL PE=1 SV=1	ECOUT	1
6	2	2	6,8	sp|Q1RB79|RL20_ECOUT	50S ribosomal protein L20 OS=Escherichia coli (strain UTI89 / UPEC) OX=364106 GN=rplT PE=3 SV=1	ECOUT	1
7	2	2	8,7	sp|Q1R609|RS19_ECOUT	30S ribosomal protein S19 OS=Escherichia coli (strain UTI89 / UPEC) OX=364106 GN=rpsS PE=3 SV=1	ECOUT	1
8	2	2	2,7	sp|P0AGH6|SAPC_ECOL6	Peptide transport system permease protein SapC OS=Escherichia coli O6:H1 (strain CFT073 / ATCC 700928 / UPEC) OX=199310 GN=sapC PE=3 SV=1	ECOL6	1

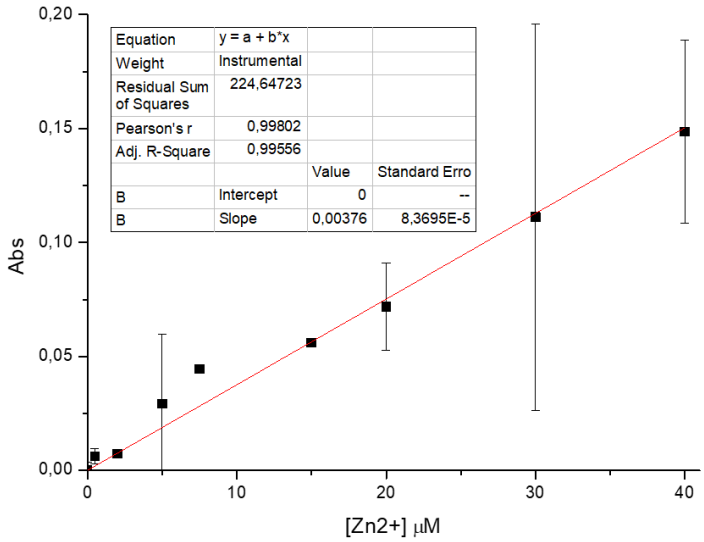

Figure A.6 — Zincon Assay plot of $Zinc^{2+}$ concentration versus absorbance at 628nm, with equation and confidence values.

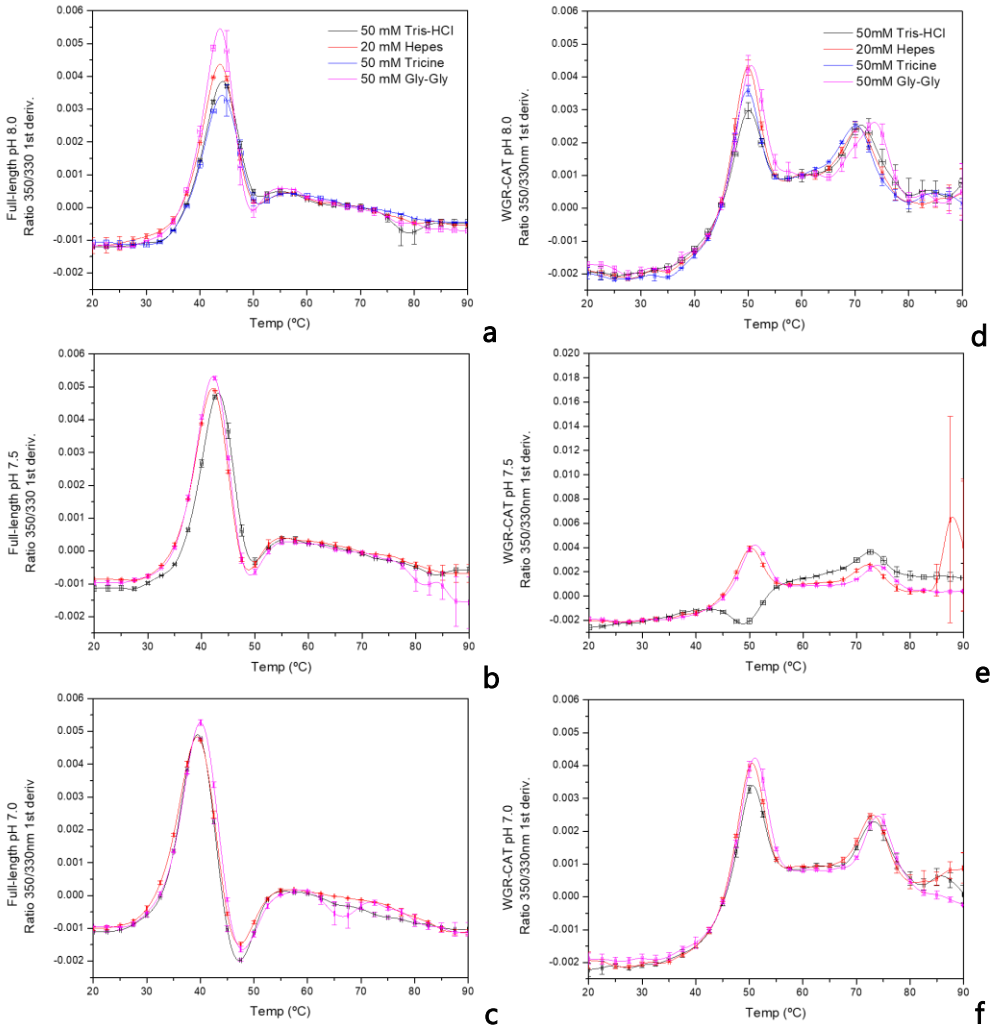

Figure A.7 — Full-length and WGR-CAT PARP1 buffer and pH stabilization assessment by Nano-DSF. a) Full-length PARP1 stabilization curves (1st derivative 350/330 nm ratio) with buffer at pH 8.0; b) Full-length PARP1 stabilization curves (1st derivative 350/330 nm ratio) with buffer at pH 7.5; c) Full-length PARP1 stabilization curves (1st derivative 350/330 nm ratio) with buffer at pH 7.0; d) WGR-CAT stabilization curves (1st derivative 350/330 nm ratio) with buffer at pH 8.0; e) WGR-CAT stabilization curves (1st derivative 350/330 nm ratio) with buffer at pH 7.5; f) WGR-CAT stabilization curves (1st derivative 350/330 nm ratio) with buffer at pH 7.0.

Table A.3 — Statistical significance values for Tm variation on Nano-DSF results for PARP1 buffer stabilization.

Full-length PARP1					
p-Values					
pH 8.0					
Tris-HCl vs Hepes	Tris-HCl vs Tricine	Tris-HCl vs Gly-Gly	Hepes vs Tricine	Hepes vs Gly-Gly	Tricine vs Gly-Gly
1,87E-02	7,25E-01	8,95E-03	1,19E-01	2,52E-01	4,52E-02

p-Values		
50 mM Tris-HCl		
pH 8.0 vs pH 7.5	**pH 8.0 vs pH 7.0**	**pH 7.5 vs pH 7.0**
1,48E-03	3,50E-06	3,28E-06

WGR-CAT PARP1		
Tm1 p-Values		
pH 7.5		
Gly-Gly vs Tris-HCl	Gly-Gly vs Hepes	Tris-HCl vs Hepes
6,27E-03	1,32E-03	9,94E-03

Tm1 p-Values		
50 mM Gly-Gly		
pH7.5 vs pH7	**pH7.5 vs pH8**	**pH7 vs pH8**
8,73E-01	8,73E-01	1,97E-03

Tm2 p-Values

pH 7.5		
Gly-Gly vs Tris-HCl	Gly-Gly vs Hepes	Tris-HCl vs Hepes
4,92E-02	2,33E-03	2,48E-01

Tm2 p-Values 50 mM Gly-Gly		
pH7.5 vs pH7	pH7.5 vs pH8	pH7 vs pH8
7,58E-01	6,16E-02	4,63E-02

Table A.4 — WGR-CAT PARP1 onset values determined by Nano-DSF with 50 mM Gly-Gly buffer.

Buffer	T_{onset} (°C)	SD
50mM Gly-Gly pH 7.0	41.4	5.4
50mM Gly-Gly pH 7.5	45.2	0.4
50mM Gly-Gly pH 8.0	37.0	5.5

B

APPENDIX: UNDERSTANDING THE INTRINSIC NATURE OF PARP1: STABILITY AND OLIGOMERIZATION

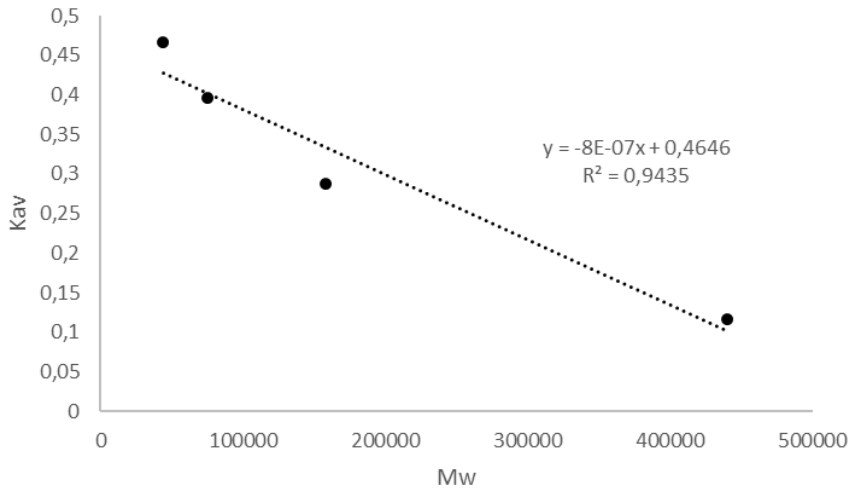

Figure B.1 — Superdex S200 Increase 10/300 GL calibration curve performed in the AKTA Explorer system, with buffer 50 mM Tris-HCl pH 8.0, 150 mM NaCl.

Table B.1 — Nucleotide sequence of the unlabelled and FAM-labelled oligos used in the Electrophoretic Mobility Shit Assays (EMSA), PARP1 activity assays and thermostability assessments.

Type	Name	Sequence
Unlabelled	Blunt DNA	F: 5′ – AGTACGGTCATCGCG – 3′ R: 5′ – CGCGATGACCGTACT – 3′
	5′ – overhang DSB	F: 5′ – GAGTACGGTCATCGC – 3′ R: 5′ – CGCGATGACCGTACT – 3′
	3′- overhang DSB	F: 5′ – GTACGGTCATCGCGA – 3′ R: 5′ – CGCGATGACCGTACT – 3′
	Abasic Blunt DNA	F: 5′ – AGTACGGTCATCGCG – 3′ R: 5′ – CGCGATGACAbGTACT – 3′
	Abasic 5′ - overhang	F: 5′ – GAGTACGGTCATCGC – 3′ R: 5′ – CGCGATGACAbGTACT – 3′
	Abasic 3′- overhang	F: 5′ – GTACGGTCATCGCGA – 3′ R: 5′ – CGCGATGACAbGTACT – 3′
FAM labelled	SSB	F1: 5' - CGATACTTTGTCCACTCAAT [FAM] -3' F2: 5'- TATCCACCAATACTACCCTA –3′ R: 5′- ATTGAGTGGACAAAGTATCGTAGGGTAGTATTGGTGGATA - 3′
	Blunt DNA	F: 5′ – AGCTACCATGCCTGCACGAACTAAGCAATTCGTAATCATGGTCAT – 3′ R: 5′ – ATGACCATGATTACGAATTGCTTAGTTCGTGCAGGCATGGTAGCT – 3′
	3′- overhang DSB	F: 5′ – AGCTACCATGCCTGCACGAACTAAGCAATTCGTAATCATGGTCAT – 3′ R: 5′ – CCATGATTACGAATTGCTTAGTTCGTCCAGGCATGGTAGCT – 3′

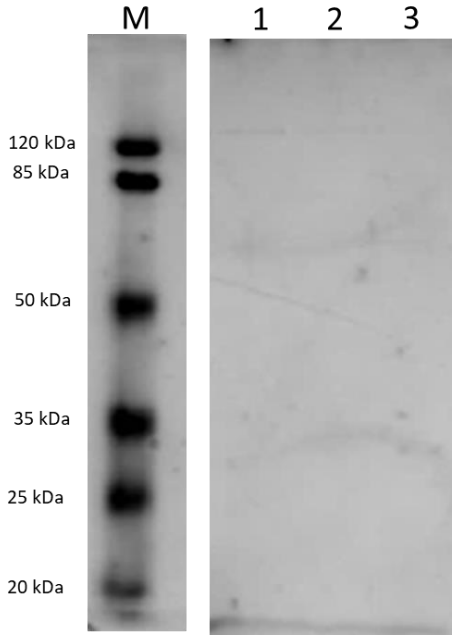

Figure B.2 — SDS-Page analysis of eluted fractions from size exclusion chromatography of sample peak 4 (PARP1 "free" form).

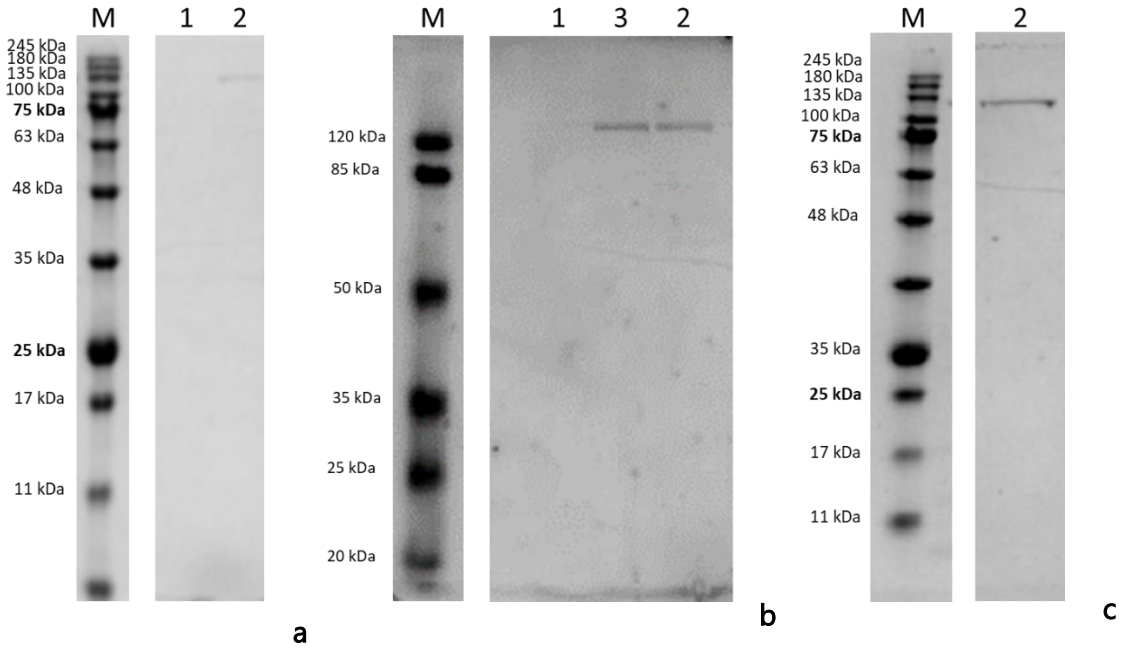

Figure B.3 — SDS-PAGE analysis of eluted fractions from the size exclusion chromatography of PARP1 oligomeric assessment regarding the concentration effect. a) Protein eluted peaks 1 and 2 from the control sample; b) Eluted peaks from the sample concentrated with Amicon; c) eluted peak from the concentrated PARP1 "free" dimer.

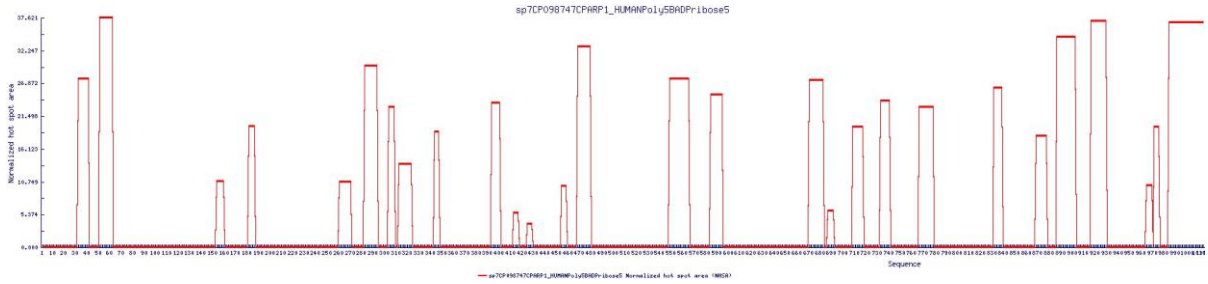

Figure B.4 — Graphical representation of the 28 hotspot regions identified in the amino acid sequence of human PARP1 (sequence retrieved from Uniprot: P09874·PARP1 _HUMAN) given by the Aggrescan Server [43]. Results are presented as the normalized hotspot area vs aa sequence.

Table B.2 — List of additives used in the thermostability assessments of human PARP1.

Group	Compound	Concentrations
Salt	NaCl	100, 150, 300 and 500 mM
Chelating Agent	EDTA	1 mM
Reducing Agent	TCEP	0.1 mM
Detergents	Zwittergent 3-10	1 mM
	Mega 8	
	n-octyl-β-D glucoside (OG)	
Triols	glycerol	5, 10 and 15%
Amino acids	Glycine	1mM
	D-Alanine	
	L-Lysine	
	L-Arginine	
	L-Proline	
Denaturing agents	Guanidine hydrochloride	150 mM and 500 mM
Sugars	Sucrose	25mM
Divalent Cations	$CaCl_2$	0 – 5 mM
	$MgCl_2$	
	$MnSO_4$	1 mM
	$ZnSO_4$	
	$FeCl_2$	
	$NiCl_2$	

Table B.3 — Thermostability assessment of PARP1 in different concentrations of sodium chloride.

NaCl Concentration*	Nano-DSF⁺ (°C)
0 mM	44.2 ± 0.3
100 mM	44.60 ± 0.48
150 mM	45.10 ± 0.50
300 mM	46.93 ± 0.15
500 mM	48.80 ± 0.15

*50mM Tris-HCl pH 8.0; ⁺ mean ± SD

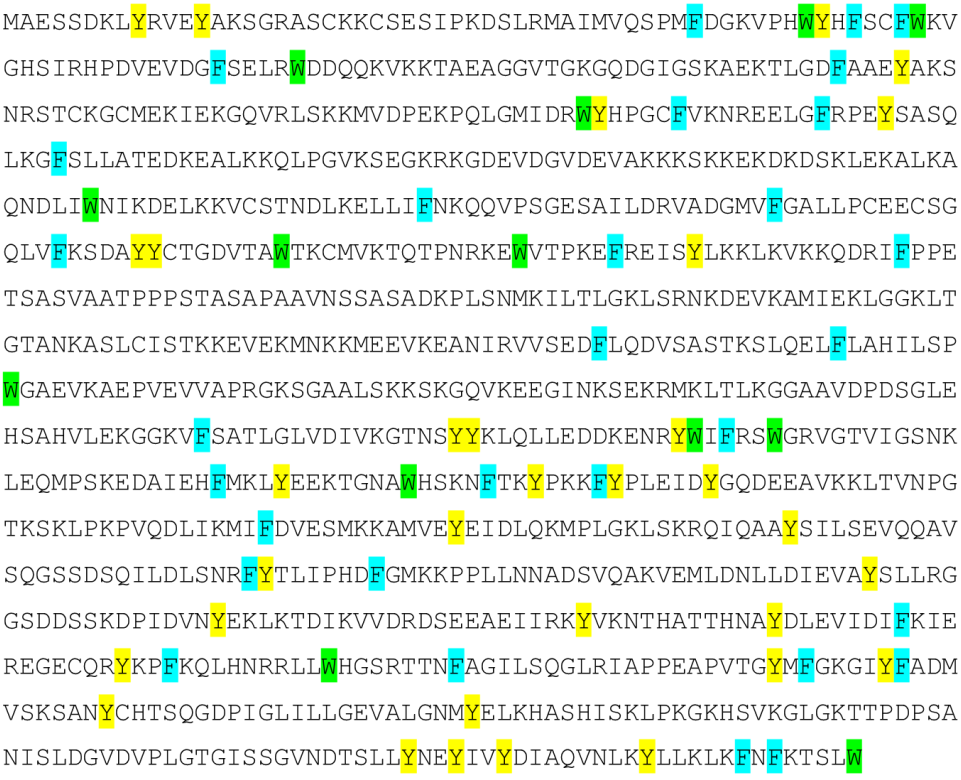

Figure B.5 — Amino acid sequence of PARP1 with identification of tryptophan (W) (green), tyrosine (Y) (yellow) and phenylalanine (F) (blue) residues.

Table B.4 — Nano-DSF PARP1 thermostability assessments with additives in buffer 50 mM Tris-HCl pH8.0, 150mM NaCl.

Additive	Melting Temperatures (°C)*
Ct	45.80 ± 0.18
1 mM Zwittergent 3-10	45.60 ± 0.01
1 mM Mega 8	45.60 ± 0.02
1 mM n-octyl-β-D glucoside (OG)	46.60 ± 0.12
1 mM D-Alanine	44.40 ± 0.04
1 mM L-Lysine	44.40 ± 0.05
1 mM L – Arginine	43.70 ± 0.16
1 mM Glycine	42.90 ± 0.08
1 mM L-Proline	45.00 ± 0.03

* mean ± SD

Table B.5 — Thermofluor PARP1 thermostability assessments with glycerol in buffer 50 mM Tris-HCl pH 8.0, 150 mM NaCl, 1 mM EDTA, 0.1 mM TCEP; sucrose and guanidine in buffer 50 mM Tris-HCl pH 8.0, 150 mM NaCl, 0.1 mM TCEP.

Additive	Melting Temperatures (°C)*
Ct (50 mM Tris-HCl pH8.0, 150 mM NaCl, 1 mM EDTA, 0.1 mM TCEP)	45.5 ± 0.5
5 % glycerol	46 ± 0
10 % glycerol	47 ± 0
15 % glycerol	47 ± 0
Ct (50 mM Tris-HCl pH8.0, 150 mM NaCl, 0.1 mM TCEP)	46.5 ± 0.5
25 mM sucrose	46 ± 0
150 mM guanidine hydrochloride	45 ± 0
500 mM guanidine hydrochloride	38 ± 0

*mean ± SD

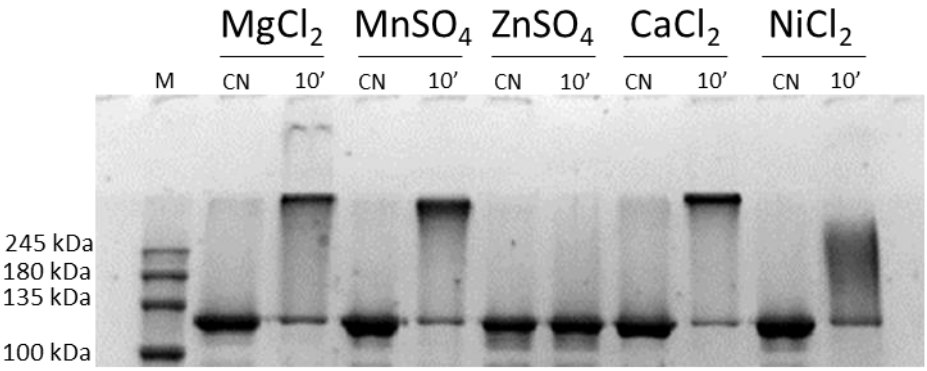

Figure B.6 — PAPR1 auto-modification activity assay testing different divalent cations.

Table B.6 — Calcium and magnesium concentration assessment regarding PARP1 melting temperature by Nano-DSF (in 50 mM Tris-HCl pH 8.0, 150mM NaCl).

Concentration (mM)	Ca^{2+} (°C) *	Mg^{2+} (°C)*
0	45.90 ± 0.13	45.90 ± 0.13
0.25	46.90 ± 0.02	47.70 ± 0.03
0.5	50.20 ± 0.03	49.90 ± 0.01
1	50.60 ± 0.01	50.10 ± 0.04
2.5	50.60 ± 0.10	50.40 ± 0.05
5	50.80 ± 0	50.50 ± 0.02

* mean ± SD

Table B.7 — Combined effect of salt and divalent cations (Ca^{2+} and Mg^{2+}) concentration on PARP1's melting temperature, using the Nano-DSF system (in 50 mM Tris-HCl pH 8.0, X mM NaCl, 1mM Ca/$MgCl_2$).

Buffer	Ca^{2+} + Mg^{2+} (°C)*
150mM NaCl	51.30 ± 1.03
300mM NaCl	51.90 ± 1.15
500mM NaCl	51.20 ± 0.31

* mean ± SD

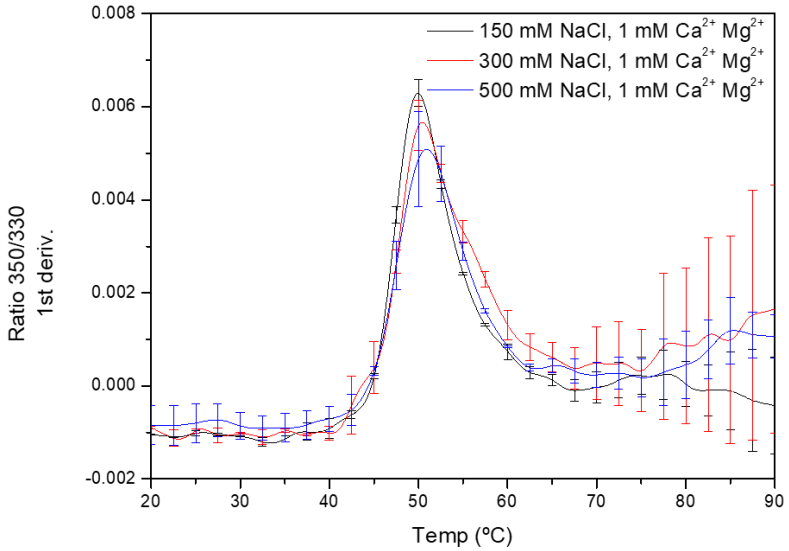

Figure B.7 — Nano-DSF PARP1 melting curves regarding the combined effect salt and divalent cations (Ca^{2+} and Mg^{2+}) concentration.

Table B.8 — Combined effect of salt, divalent cations (Ca^{2+} and Mg^{2+}) and TCEP on PARP1's melting temperature (in 50 mM Tris-HCl pH 8.0).

Buffer	Nano-DSF (°C)*	Thermofluor (°C)*
150 mM NaCl, 0.1 mM TCEP	44.75 ± 0.05	46.50 ± 0.50
150 mM NaCl, 0.1 mM TCEP, 1 mM Mg^{2+}	50.10 ± 0.10	48 ± 0
150 mM NaCl, 0.1 mM TCEP, 1mM Ca^{2+}	50.55 ± 0.05	47 ± 0

* mean ± SD

Table B.9 — DLS analysis for the effect of magnesium salt on protein particle diameter and population heterogeneity in 50 mM Tris-HCl pH 8.0, 150 mM NaCl, 0.1 mM TCEP and X mM $MgCl_2$.

Ion Content	Z-Average* (d.nm)	PdI*	Population 1* (d.nm)	Population 2* (d.nm)
0 mM	555.7 ± 16.1	0.35 ± 0.02	615.3 ± 37.1	95.6 ± 95.4
1 mM	534.87 ± 27.09	0.41 ± 0.04	754 ± 94	286.1 ± 93.3

* mean ± SD

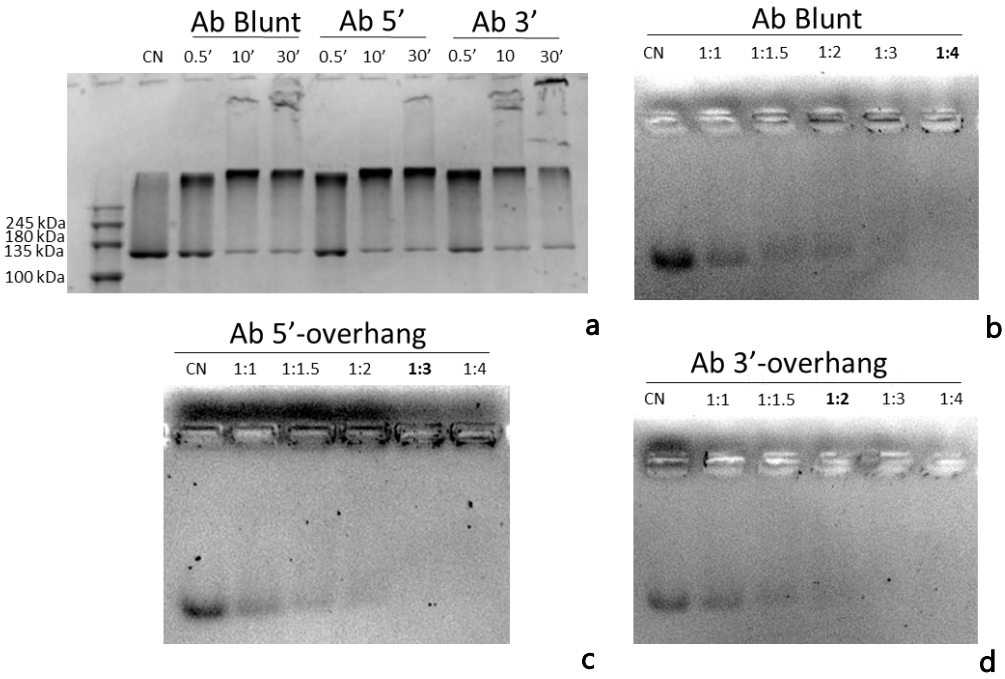

Figure B.8 — PARP1 activity assay (a) and EMSA (b -c) results in 1% agarose gels, where an abasic site was introduced in unlabeled 15nt dsDNA.

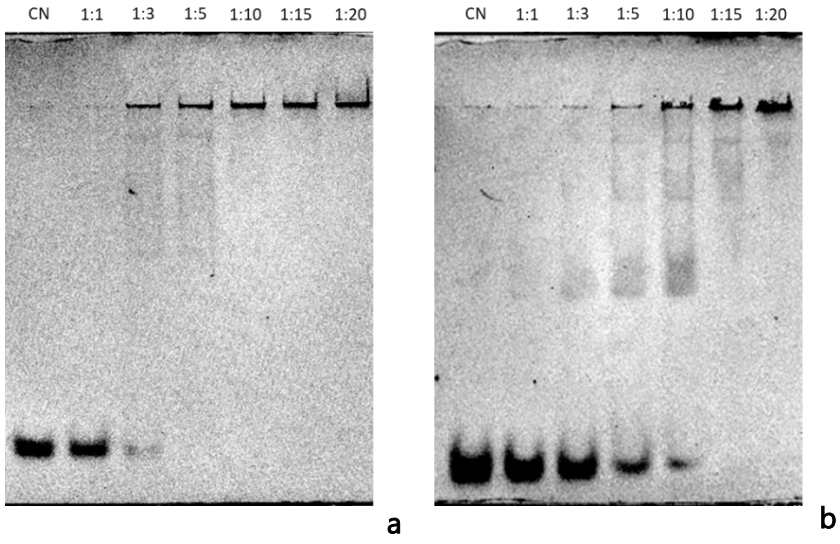

Figure B.9 — PARP1 EMSA with FAM labelled dsDNA control (blunt – 43nt) (a) and SSB dsDNA (40nt) (b) used at a final concentration of 0.1 µM.

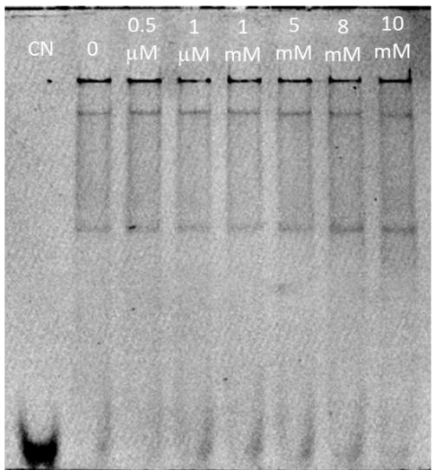

Figure B.10 — Assessment on the effect of magnesium concentration (0 – 10 mM) on PARP1 binding affinity to FAM labelled 3'-overhang dsDNA (43nt). DNA-protein ratio was fixed at 1:5.

Table B.10 — Results from the secondary structure analysis with the BeStSel prediction software, of the CD spectra obtained for PARP1 and PARP1+inhibitor samples. The different secondary structures are identified, as well as contribution to the analyzed spectra (in percentage).

Structures	PARP1	PARP1 +Rucaparib	PARP1 +Veliparib	PARP1 +Niraparib
α - helix	10.34 %	1.90 %	3.46 %	1.24%
Anti – β sheets	34.58 %	33.78 %	33.31 %	30.15%
Parallel	5.00 %	0.33 %	3.29 %	3.64 %
Turn	14.14 %	14.08 %	12.00 %	13.45 %
Others	35.95 %	49.90 %	47.95 %	51.53 %
NRMSD	0.02	0.05	0.03	0.08

Note: NRMSD – normalized root mean square deviation ("Goodness-of-fit" parameter. Good values are bellow 0.1); Others comprehend: 3_{10}-helix, π-helix, β-bridge, bends, loop/irregular and invisible regions.

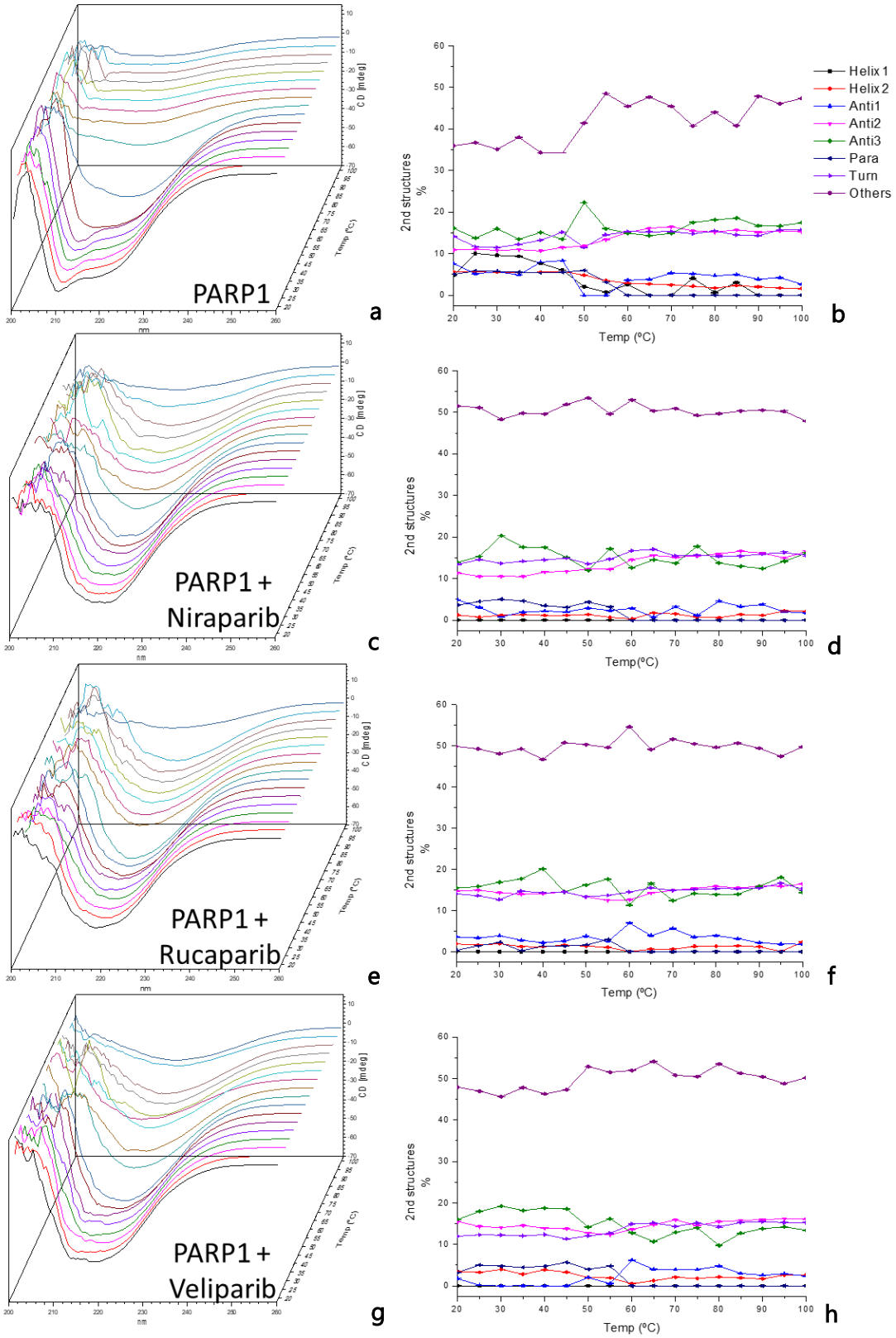
PARP1
a
Helix 1
Helix 2
Anti1
Anti2
Anti3
Para
Turn
Others
2nd structures %
Temp (ºC)
b
PARP1 + Niraparib
c
Temp(ºC)
d
PARP1 + Rucaparib
e
f
PARP1 + Veliparib
g
h

Figure B.11 — Evaluation of native PARP1 and PARP1-inhibitor (1:1) denaturation process by circular dichroism (CD) and respective secondary structure (using the BeStSel software). a) Native PARP1 CD melting curves; b) Native PARP1 secondary structure analysis with temperature variation; c) PARP1-Niraparib CD melting curves; d) PARP1 - Niraparib secondary structure analysis with temperature variation; e) PARP1-Rucaparib CD melting curves; f) PARP1-Rucaparib secondary structure analysis with temperature variation; g) PARP1-Veliparib CD melting curves; h) PARP1-Veliparib secondary structure analysis with temperature variation.

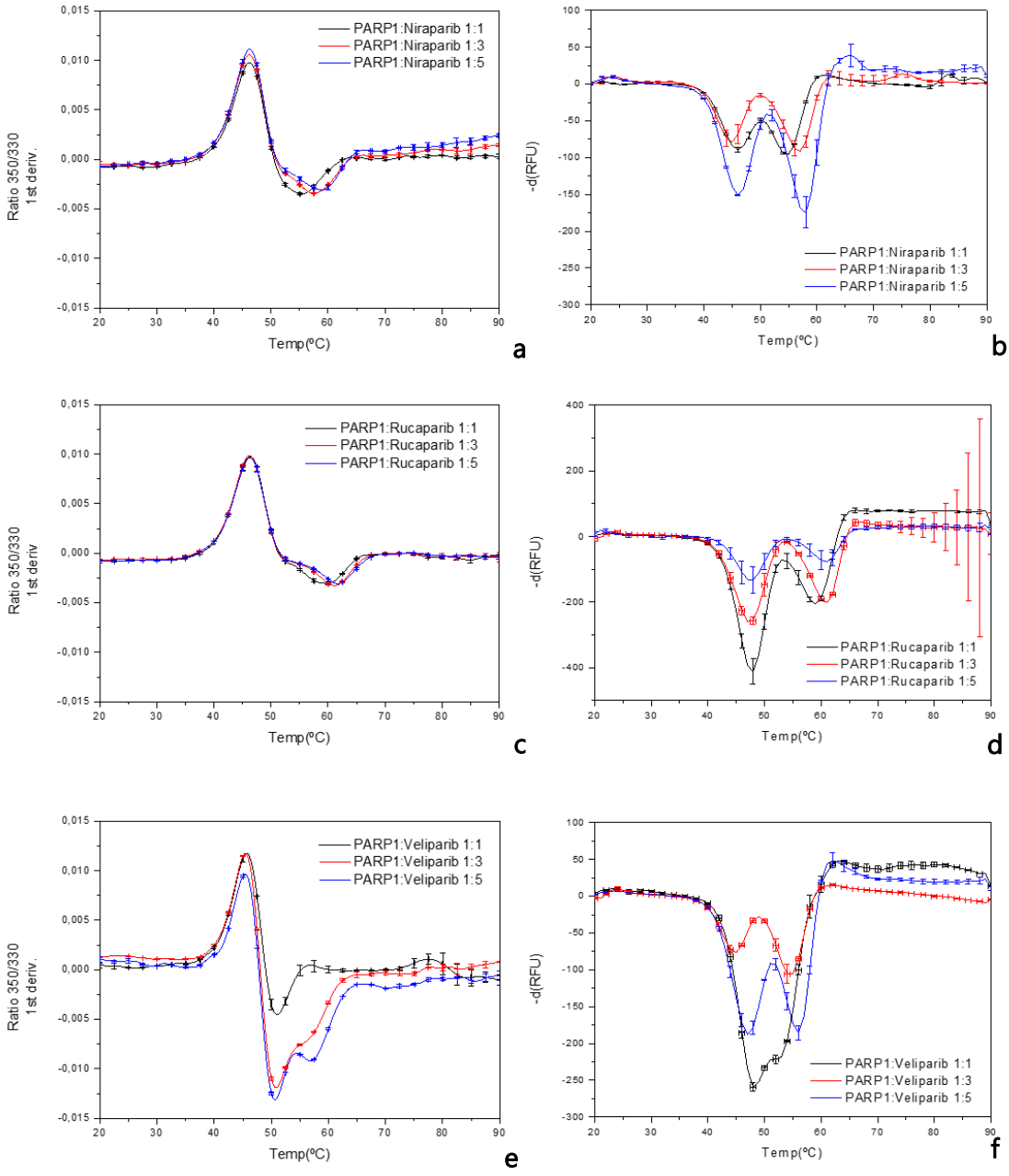

Figure B.12 — Thermo-stability assessments of PARP1 in various protein-inhibitor ratios (1:1, 1:3 and 1:5). a) Nano-DSF assessment of PARP1-Niraparib samples; b) Thermofluor assessment of PARP1-Niraparib samples; c) Nano-DSF assessment of PARP1-Rucaparib samples; d) Thermofluor assessment of PARP1-Rucaparib samples; e) Nano-DSF assessment of PARP1-Veliparib samples; f) Thermofluor assessment of PARP1-Veliparib samples.

Table B.11 — Nano-DSF and Thermofluor determined melting temperatures for PARP at different protein-inhibitor ratios (1:1, 1:3 and 1:5). All assays were performed in 50 mM Tris-HCl pH 8.0, 500 mM NaCl, 1 mM EDTA, 0.1 mM TCEP buffer.

Nano-DSF (°C)*			
Ratio	**Niraparib**	**Rucaparib**	**Veliparib**
1:1	46.00 ± 0.05 55.20 ± 0.04	46.20 ± 0.04 59.30 ± 0.02	45.30 ± 0.04 51.70 ± 0.03
1:3	46.00 ± 0.03 57.5 ± 0.08	46.10 ± 0.06 61.00 ± 0.03	44.90 ± 0.01 51.70 ± 0.02 57.10 ± 0.00
1:5	46.00 ± 0.01 58.40 ± 0.12	46.20 ± 0.04 61.50 ± 0.04	44.90 ± 0.02 51.40 ± 0.02 57.00 ± 0.00

Thermofluor (°C)*			
Ratio	**Niraparib**	**Rucaparib**	**Veliparib**
1:1	46.00 ± 0.00 55.00 ± 0.00	48.00 ± 0.00 59.00 ± 0.00	48.00 ± 0.00 52.50 ± 0.50
1:3	45.00 ± 0.00 57.00 ± 0.00	47.50 ± 0.50 61.00 ± 0.00	45.00 ± 0.00 54.40 ± 0.50
1:5	46.00 ± 0.00 58.00 ± 0.00	48.00 ± 0.00 61.00 ± 0.00	47.00 ± 0.00 56.00 ± 0.00

* mean ± SD

C

APPENDIX: ENCAPSULATION OF PARPI IN LIPOSOME NANO-SYSTEMS

Table C.1 — DPPC size distribution evaluation dependent on the number of sonication cycles.

Sonication Cycle	Z-Average * (nm)	PdI *	Pop.1 * (nm)	Pop.2 * (nm)
15×	74.2 ± 0.3	0.19 ± 0.01	77 ± 2	4650 ± 230
20×	71.0 ± 0.5	0.18 ± 0.01	75 ± 2	4693± 220
25×	67.6 ± 0.3	0.21 ± 0.01	71.4 ± 0.9	3163 ± 150

* Mean ± SD values (n=3 to 4). Note: PdI—polydispersity index, Pop.1—population 1, and Pop.2—population 2.

Table C.2 — DPPG size distribution evaluation dependent on the number of sonication cycles.

Sonication Cycle	Z-Average * (nm)	PdI *	Pop.1 * (nm)	Pop.2 * (nm)
15×	55 ± 1	0.25 ± 0.03	54.0 ± 0.5	3830± 560
20×	56.2 ± 0.4	0.27 ± 0.01	56± 2	1925 ± 240
25×	54.0 ± 0.6	0.21 ± 0.01	55.6 ± 0.2	4460 ± 30

* Mean ± SD values (n=3 to 4). Note: PdI—polydispersity index, Pop.1—population 1, and Pop.2—population 2.

Table C.3 — Veliparib organic phase encapsulation efficiencies (EE) and lipid capacity (LC) in DPPG, dependent on concentration.

Inhibitor Concentration (μM)	EE * (%)	LC * (%)
100	49± 2	3.9 ± 0.2
200	55 ± 1	10.20 ± 0.09

* Mean ± SD values (n=3 to 4).

Table C.4 — Veliparib (200 μM) encapsulation efficiencies (EE) and lipid capacity (LC) in DPPG, dependent on phase supplementation.

Phase (200 μM)	EE * (%)	LC * (%)
Organic phase	55 ± 1	10.20 ± 0.09
Both phases	31± 4	4.9 ± 0.7

* Mean ± SD values (n=3 to 4).

Table C.5 — Effect of Veliparib (200 μM) phase supplementation on DPPG size distribution and zeta potential.

Veliparib (μM)	Particle Size *				Zeta Potential * (mV)
	Z-Average (d.nm)	PdI	Pop.1 (d.nm)	Pop.2 (d.nm)	
Organic phase	91± 2	0.28 ± 0.03	134 ± 6	---	−39 ± 2
Both phases	93 ± 2	0.32 ± 0.02	135 ± 11	~36,805	−42 ± 3

* Mean ± SD values (n=3 to 4). Note: PdI—polydispersity index, Pop.1—population 1, and Pop.2—population 2.

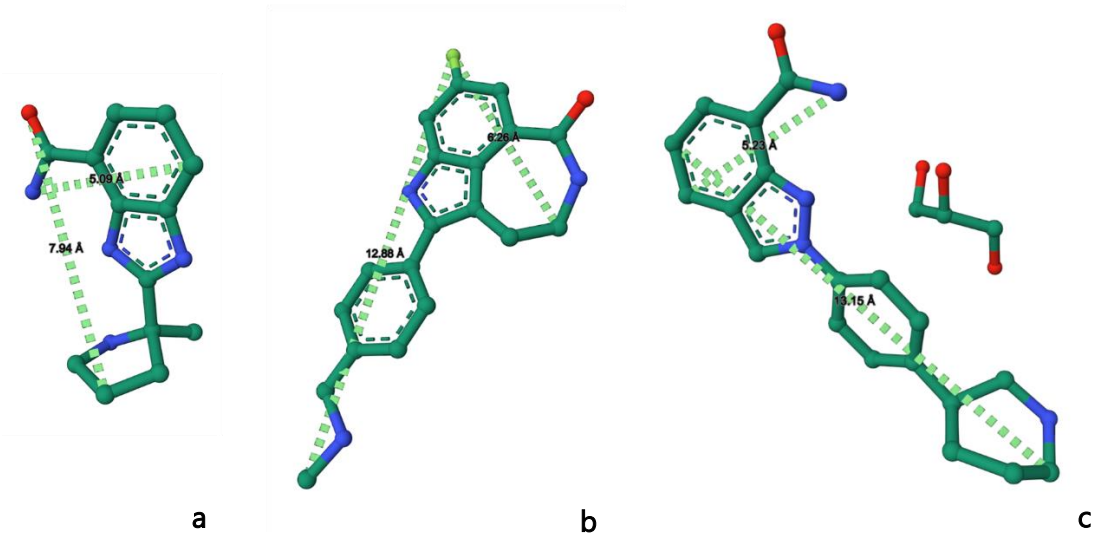

Figure C.1 — PARP1 inhibitor maximum length and width spatial distance values (Å) determined with RCSB PDB online tools [39–42] and protein inhibitor published crystal structures. a) Veliparib molecule structure with spatial values (PDB: 7AAC) [38]; b) Rucaparib molecule structure with spatial values (PDB: 4RV6) [37]; c) Niraparib molecular structure with spatial values (PDB: 4R6E) [37].

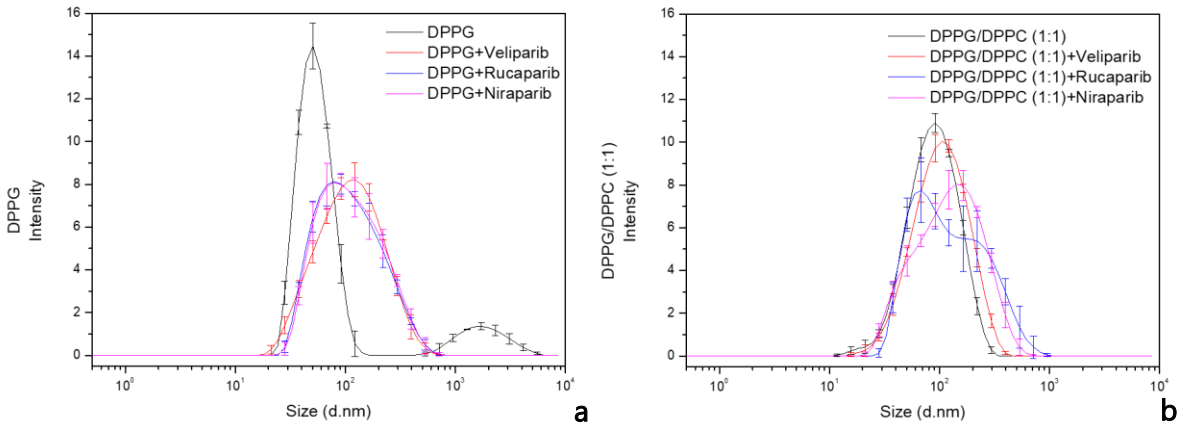

Figure C.2 — DPPG (a) and DPPG/DPPC 1:1 (b) liposome size distribution analysis upon encapsulation of PARP1 inhibitors Veliparib, Rucaparib, and Niraparib.

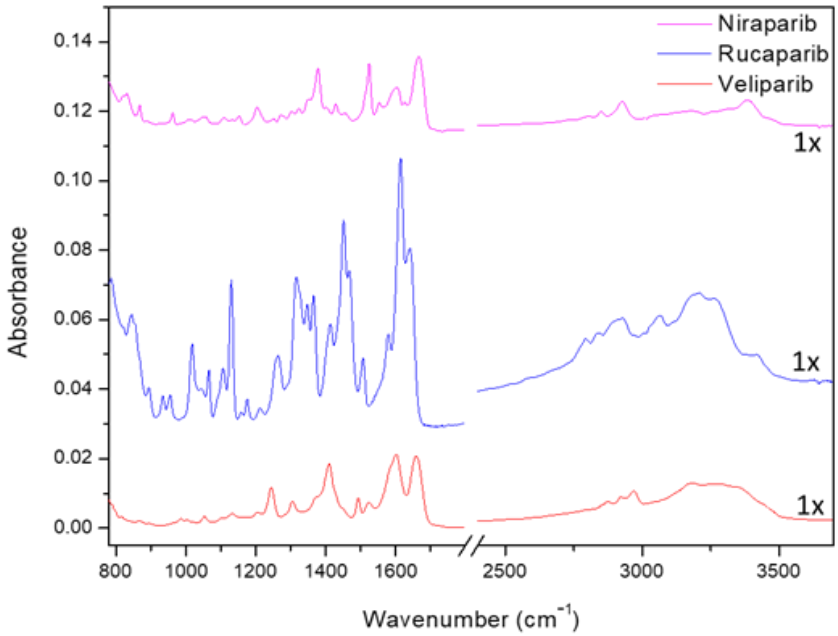

Figure C.3 — FTIR spectra of PARP1 inhibitors Veliparib, Rucaparib, and Niraparib.

Table C.6 — Characteristic infrared absorption bands of DPPG cast films in CaF_2 supports. Assignments carried out taking into account [18,56,59–62] and references therein.

DPPG Band Frequency (cm^{-1})	Assignment
1052	Symmetric stretch of C-O-C
1097	PO_2^- symmetric stretch
1166	C-O stretch
1224	PO_2^- asymmetric stretch hydrogen-bonded
1242	PO_2^- asymmetric stretch
1416	In-plane bend of C-O-H group
1468	CH_2 scissoring
1736	Stretch of carbonyl group (C=O)
2850	Symmetric C-H stretch of phospholipid hydrocarbon (CH_2)
2917	Anti-symmetric C-H stretch of phospholipid hydrocarbon (CH_2)
2956	Asymmetric stretch C-H (CH_3)
3286	OH group from glycerol and H_2O retained in liposomes

Table C.7 — Characteristic infrared absorption bands of Veliparib cast films in CaF_2 supports. Assignments carried out taking into account [56,57,63] and references therein.

Veliparib Band Frequency (cm^{-1})	Assignment
790 and 868	Aromatic C-H out-of-plane bend
986	Aromatic C-H in-plane bend
1008	C-C stretch, cyclohexane ring vibrations
1054	S-O stretch and CH_3 rocking vibrations from not self-associated DMSO
1134	C-N stretch from aromatic rings
1244	C-O/C-C stretch
1306	C-N stretch from aromatic secondary amine
1375 and 1410	S-O stretch and C-H bending from DMSO
1439	C-H asymmetric bend from -CH_3 methyl functional group
1493	C=C-C aromatic stretch
1524	Aromatic amine CH_2 scissoring/C-N and C-C ring stretch
1600	Secondary amine N-H weak bending and NH_2 scissoring from amine group in benzamide
1660	C=O stretch from benzamide
2850–3000	C-H symmetric and asymmetric stretch from CH_3 and C-H stretch from aromatic ring
3180	N-H symmetric stretch from benzamide
>3200	N-H stretch from aromatic ring and OH group from H_2O

Table C.8 — Characteristic infrared absorption bands of Rucaparib cast films in CaF_2 supports. Assignments carried out taking into account [56,57,63,64] and references therein.

Rucaparib Band Frequency (cm^{-1})	Assignment
843	Aromatic C-H out-of-plane bend
934; 954	Aromatic C-H in-plane bend
1016	P-O asymmetric stretch from phosphate ion
1042	S-O stretch and CH_3 rocking vibrations from self-associated DMSO

1130	C-F stretch from Fluorobenzene
1263	C-N stretch from aromatic secondary amine
1315	C-C vibrations and C-N stretch from aromatic secondary amine
1349	C-H bend from -CH- functional group
1366	C-H symmetric bend from -CH_3 functional group
1413	In-plane C-H bend from vinyl functional group in N-methylbenzylamine
1453	C-H bend from aromatic ring
1507	C=C-C aromatic stretch
1614	C=C stretch from conjugated double bonds in aromatic rings
1642	C=O stretch from Cycloheptanone
2740–2980	C-H symmetric and asymmetric stretch from CH_3
>3000	N-H stretch from aromatic ring and OH group from H_2O

Table C.9 — Characteristic infrared absorption bands of Niraparib cast films in CaF_2 supports. Assignments carried out taking into account [56,57,64,65] and references therein.

Niraparib Band Frequency (cm^{-1})	Assignment
830	Aromatic C-H out-of-plane bend
960	Aromatic C-H in-plane bend
1054	S-O stretch and CH_3 rocking vibrations from not self-associated DMSO
1205	C-C stretch aromatic skeletal vibration
1275 and 1303	C-N stretch from aromatic secondary amine
1323	C-N stretch from aromatic secondary and tertiary amine
1352	C-N stretch from aromatic tertiary amine
1413	In-plane C-H bend from vinyl functional group in N-methylbenzylamine
1378	S=O stretch and C-H bending from DMSO
1428	C-N stretching from aromatic ring
1511	C=C-C aromatic stretch
1524	Aromatic amine CH_2 scissoring, C-N and C-C ring stretching
1553	C=C-C stretch and C=N stretch from aromatic ring

1602	N-H bend from secondary and primary amine
1627	In-plane NH_2 scissoring
1642	C=O stretch from benzamide
2690–2980	C-H symmetric and asymmetric stretch from CH_3
>3000	N-H stretch from aromatic ring and OH group from H_2O

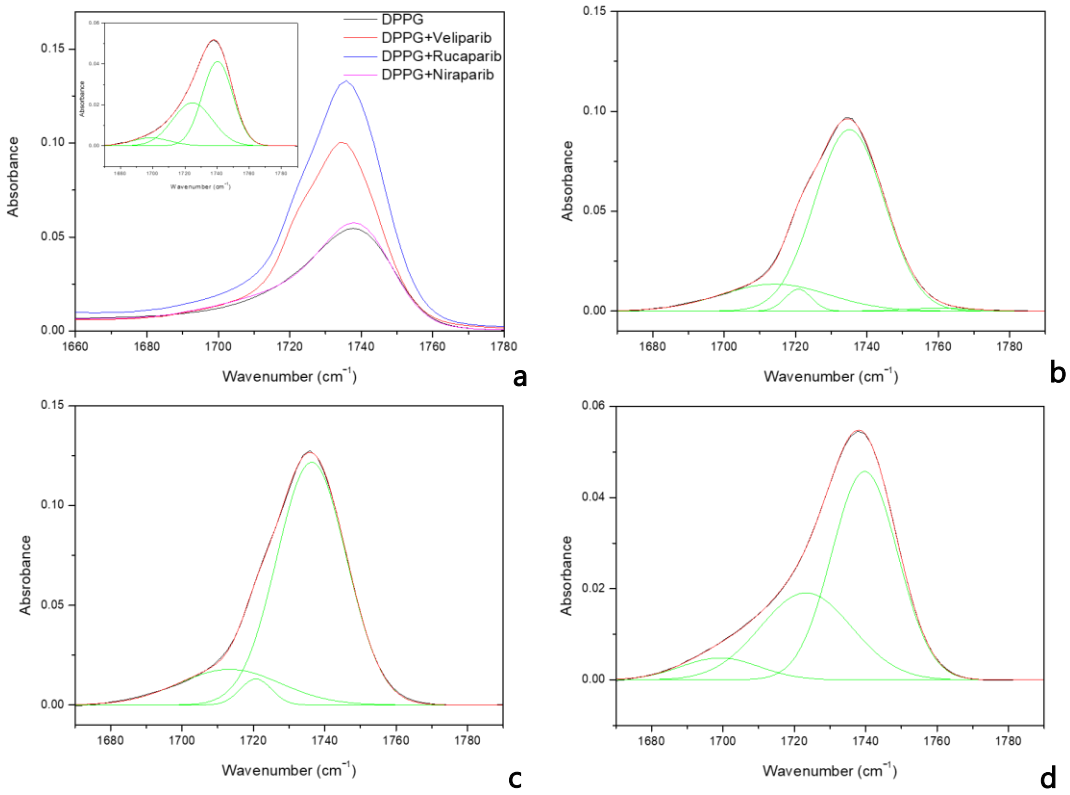

Figure C.4 — FTIR spectra of DPPG formulations comprising the carbonyl group vibration region and respective deconvoluted Gaussians (green lines) for hydrogen bond/hydration state evaluation. a) DPPG formulations with the DPPG carbonyl deconvoluted spectrum as the inset; b) DPPG + Veliparib deconvoluted spectrum; c) DPPG + Rucaparib deconvoluted spectra; d) DPPG + Niraparib deconvoluted spectra.

D

APPENDIX: COMBINING RADIATION AND LIPOSOMES WITH PARPI: EFFECTS ON INHIBITOR CAPABILITY AND DEGRADATION

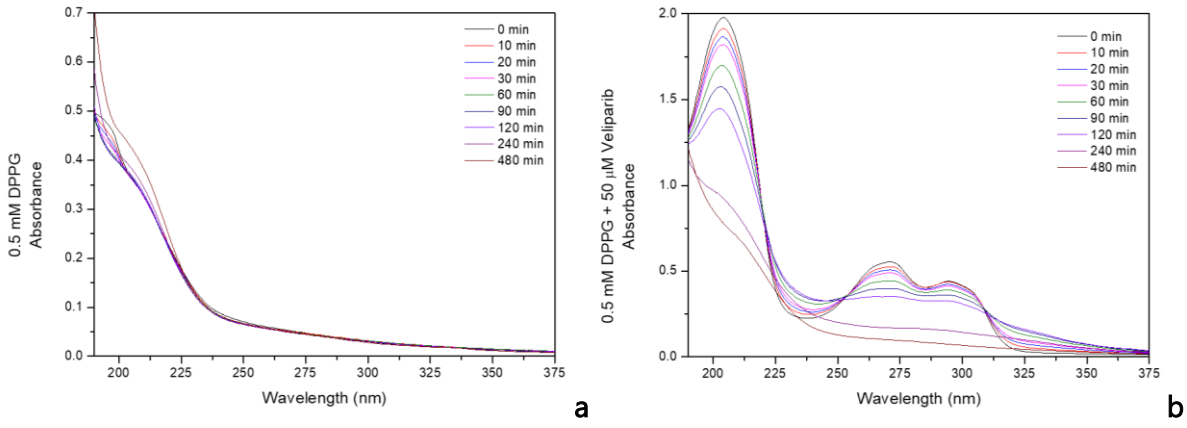

Figure D.1 — DPPG and DPPG encapsulating Veliparib irradiation assay with UVC lamp. a) 0.5 mM DPPG formulation; b) 0.5 mM DPPG + 50 µM Veliparib.

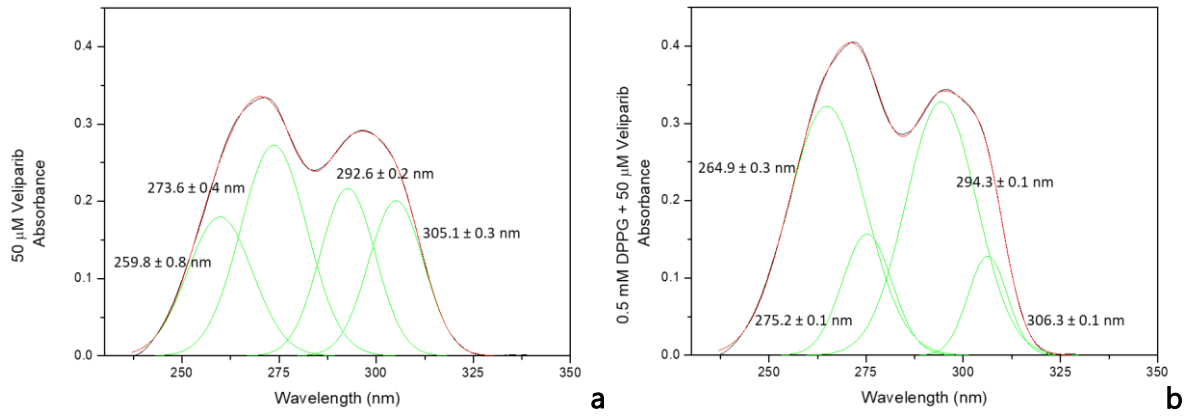

Figure D.2 — Gaussian analysis of Veliparib and DPPG+Veliparib samples. Data reveals that Veliparib spectra comprises four gaussians and that after drug encapsulation in DPPG liposomes, these gaussians present a red-shift on wavelength number. a) UV-vis spectra of 50 µM Veliparib; b) UV-vis spectra of 0.5 mM DPPG + 50 µM Veliparib.

Table D.1 — Analysis of Veliparib and DPPG + Veliparib wavelength shift of Gaussian 2 and 5 upon UVC irradiation.

Irradiation Time (min)	Gaussian 2 Wavelength (nm)*		Gaussian 5 Wavelength (nm)*	
	Veliparib	DPPG + Veliparib	Veliparib	DPPG + Veliparib
0	273.7 ± 0.4	275.3 ± 0.1	n.d.	n.d.
10	273.9 ± 0.3	274.9 ± 0.2	325.2 ± 0.8	n.d.
20	273.5 ± 0.2	274.5 ± 0.1	325.4 ± 0.7	n.d.
30	273.4 ± 0.2	274.1 ± 0.2	327.1 ± 0.4	n.d.
60	273.04 ± 0.32	273.8 ± 0.3	327.8 ± 0.5	317.2 ± 3.1
90	273.4 ± 0.2	273.7 ± 0.2	328.5 ± 0.5	324.3 ± 0.9
120	274.1 ± 0.3	273.9 ± 0.2	328.1 ± 0.7	329.5 ± 0.1
240	275.2 ± 0.5	278.7 ± 0.6	330.3 ± 0.9	331.3 ± 0.4
480	n.d.	n.d.	n.d.	n.d.

Note: n.d. means not detected. * wavelength ± SD

2023

CARLOTA JOSÉ FERNANDES
DA CONCEIÇÃO

PARP1 INHIBITORS FOR CANCER COMBINATION THERAPY:
merging liposome encapsulation and UVC irradiation